Acoustical Physics, Vol. 50, No. 1, 2004, pp. 1–8. Translated from Akusticheskiĭ Zhurnal, Vol. 50, No. 1, 2004, pp. 5–13.
Original Russian Text Copyright © 2004 by Boĭko, Tyutekin.

A Planar Active Sound Control System Using Two-Dimensional Spatial Harmonics

A. I. Boĭko and V. V. Tyutekin
Andreev Acoustics Institute, Russian Academy of Sciences, ul. Shvernika 4, Moscow, 117036 Russia
e-mail: Tytekin@akin.ru

Received April 4, 2003

Abstract—An active sound control system based on the extraction of orthogonal spatial harmonics is considered. The system comprises two parallel planar rectangular receiving arrays consisting of small monopole receivers and two planar rectangular transmitting arrays (installed parallel to the receiving arrays) consisting of small monopole transmitters. The field received by the receiving arrays is approximated by a finite number of propagating plane waves with the help of the Fourier transform. The transmitting arrays excite the same set of plane waves outside the system, their amplitudes being chosen so as to cancel the incident external field in a certain region near the system behind the transmitting arrays. The performance of the system is considered for both continuous and discrete distributions of transmitters and receivers. Allowance is made for random errors in the transmitters and receivers, individual to each device. *© 2004 MAIK “Nauka/Interperiodica”.*

This paper presents a further development of methods for designing active sound control systems based on the so-called Huygens surfaces, which exhibit the property of being unidirectional in both transmitting and receiving. Therefore, the system has no acoustic feedback and, consequently, is resistant to self-excitation. Another feature of the active systems considered here is that they apply, where possible, expansions of the acoustic fields in orthogonal spatial harmonics, which is extremely convenient for processing the primary (received by the system) and secondary (reradiated by the system) signals. Fundamentals of the development of such active sound control systems are described in detail in [1–3].

Planar active systems [4–7] give a sufficiently simple and illustrative example of the cancellation of plane wave fields in a given region in space. These systems are also convenient in practical realization. On the other hand, planar systems can be used as an instrument that reveals the main properties of more complex sound control systems depending on their wave dimensions, positions of transmitting and receiving elements, number of spatial harmonics used, and other factors.

The active field control systems are capable of operating at low frequencies, at which passive noise cancellation systems show a low efficiency, and this fact determines the considerable theoretical and practical interest in active systems. The latter statement is confirmed by the great number of publications devoted to this problem [8–12].

The sound control system considered in this paper can be treated as one of identical modules constituting a planar active system of sufficiently large dimensions (compared to the module dimensions).

The structure of an individual module is schematically shown in Fig. 1. It can be described mathematically as follows. Let the plane wave

$$v = P_0\exp\{ik[z\cos\beta + (x\cos\alpha + y\sin\alpha)\sin\beta]\} \quad (1)$$

be incident on the receiving side of a sound control system consisting of four identical parallel planar antennas. In formula (1), P_0 is the amplitude of the wave, $k = \omega/c$ is the wave number, ω is the circular frequency, c is the velocity of sound in the medium, and the angles α and β describe the direction of incidence. The antennas occupy the area $-D_x \le x \le D_x$, $-D_y \le y \le D_y$, are perpendicular to the z axis of the Cartesian coordinate system, and lie at $z = 0$ and l (receiving antennas) and at $z = L - l$ and L (transmiting antennas).

First, we consider the case when the antennas are continuously filled with monopole transmitters or receivers and are transparent to the fields incident on them.

Let us apply the Fourier transform to the field incident on the surface of the first receiving antenna (at $z = 0$) using the exponential harmonics

$$\Psi_{nm}(x, y) = \exp\left[i\pi\left(\frac{n}{D_x}x + \frac{m}{D_y}y\right)\right], \quad (2)$$

where m and n are integers. As a result, we obtain

$$\begin{aligned} &c_{1nm}(\alpha, \beta) \\ &= \frac{P_0a_0}{4D_xD_y}\int_{-D_x}^{D_x}\int_{-D_y}^{D_y}\exp[ik(x\cos\alpha + y\sin\alpha)\sin\beta] \\ &\quad\times\Psi_{nm}(-x, -y)\,dx\,dy \\ &= P_0a_0\,\mathrm{sinc}[X_n(\alpha, \beta)]\,\mathrm{sinc}[Y_m(\alpha, \beta)], \end{aligned} \quad (3)$$

where

$$X_n(\alpha, \beta) = \frac{2D_x}{\lambda}(\cos\alpha\sin\beta - \cos\alpha_n)\pi,$$

1063-7710/04/5001-0001$26.00 © 2004 MAIK “Nauka/Interperiodica”

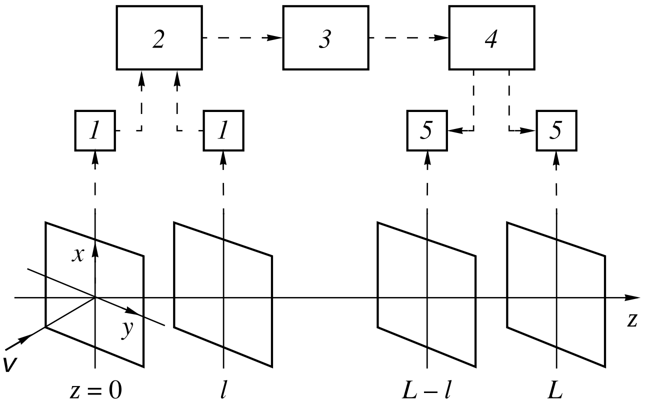

Fig. 1. Flow chart of a planar active sound control system: (*1*) analyzers of spatial harmonics; (*2*) unidirectional receiver; (*3*) intermediate unit; (*4*) unidirectional transmitter; (*5*) synthesizers of spatial harmonics.

$$Y_m(\alpha, \beta) = \frac{2D_y}{\lambda}(\sin\alpha\sin\beta + \sin\alpha_m)\pi.$$

Here, a_0 is the receiver sensitivity, λ is the wavelength, $\mathrm{sinc}(X) = \frac{\sin X}{X}$, $\cos\alpha_n = \frac{n\lambda}{2D_x}$, and $\sin\alpha_m = \frac{m\lambda}{2D_y}$.

The goal of transformation (3) is to represent an arbitrary field (in our case, the plane wave) incident on the system as a superposition of a finite number of normal harmonics of the system. It is clear that these harmonics are mutually orthogonal and do not interact with each other at the transmitting and receiving elements. Owing to this fact, we can represent the active sound control system as a parallel arrangement of independent channels, the number of the channels being equal to the number of propagating normal modes.

The number of harmonics that affect the performance of the system is given by the expressions $|\cos\alpha_n| \le 1$ and $|\sin\alpha_m| \le 1$, which yield N = integer part of $\max\left(\frac{2D_x}{\lambda}\right)$ and M = integer part of $\max\left(\frac{2D_y}{\lambda}\right)$. The quantities $2D_x$ and $2D_y$, which determine the dimensions of the antennas should be further chosen from the required performance of the system.

A similar procedure applied to the field at the second receiving antenna with the use of Eqs. (1)–(3) yields

$$c_{2nm}(\alpha, \beta) = \exp(ikl\cos\beta)c_{1nm}(\alpha, \beta). \tag{4}$$

Thus, the functions $c_{1nm}(\alpha, \beta)$ and $c_{2nm}(\alpha, \beta)$ are amplitudes of the Fourier harmonics of the fields at the receiving antennas. Transformations (3) and (4) are performed electronically by spatial harmonics analyzers 1 of the active sound control system.

Below, we describe the operation principle of a channel that processes a normal wave of number (n, m). The number of such channels is equal to the number of normal waves propagating at this frequency. All of these channels of the sound control system work simultaneously and in parallel.

Let us introduce the designations

$$\sin^2\beta_{nm} = \sin^2 a_m + \cos^2 a_n, \quad \cos\beta_{nm} = \sqrt{1 - \sin^2\beta_{nm}}$$

and consider the quantity

$$\begin{aligned} A_{1nm}(\alpha, \beta) &= c_{2nm}(\alpha, \beta)\exp(ikl\cos\beta_{nm}) \\ &\quad - c_{1nm}(\alpha, \beta) \qquad (5) \\ &= c_{1nm}(\alpha, \beta)\{\exp[ikl(\cos\beta + \cos\beta_{nm})] - 1\}. \end{aligned}$$

Linear transformation (5) is performed by the unidirectional receiving unit 2 whose output voltage is

$$V_{nm}(\alpha, \beta) = A_{1nm}(\alpha, \beta). \tag{6}$$

As follows from formulas (5) and (6), for the inverse wave incidence at the angle $\beta = \pi - \beta_{nm}$, we have $V_{nm}(\alpha, \beta) = 0$.

In accordance with the processing algorithm, the voltage $V_{nm}(\alpha, \beta)$ is applied to the intermediate unit 3 characterized by the complex transfer coefficient W_{nm}.

This unit links the receiving and transmitting antennas in the (n, m)th channel. The complex transfer coefficient W_{nm} will be determined later. The quantity $u_{nm}(\alpha, \beta) = V_{nm}(\alpha, \beta)W_{nm}$ is further fed to the transmitting antennas according to the linear transformation, which provides the unidirectional radiation of the (n, m)th harmonic. This procedure is realized by the unidirectional transmitting unit 4 as follows. The transmitting units 5 form traveling waves of the form of Eq. (2) on the surfaces of the transmitting antennas, each wave with its individual amplitude. These amplitudes are specified for each (n, m)th normal wave by the unidirectional transmitter 4. The amplitude of the (n, m)th wave for the first antenna located at $z = L - l$ is $u_{nm}(\alpha, \beta)\exp(ikl\cos\beta_{nm})$; for the second antenna located at $z = L$, it equals $-u_{nm}(\alpha, \beta)$. Then, the sound pressure amplitude of the (n, m)th harmonic for $-D_x \le x \le D_x$, $-D_y \le y \le D_y$, and $z = L$ is

$$p_{nm}(\alpha, \beta) = b_0 u_{nm}(\alpha, \beta)[\exp(2ikl\cos\beta_{nm}) - 1]. \tag{7}$$

Here, b_0 is the radiator sensitivity and the sound pressure depends on x and y according to Eq. (2). For $z \le L - l$, the amplitude of the (n, m)th harmonic is zero.

The quantity W_{nm} can be evaluated from the fundamental principle of the method of spatial harmonics: a plane wave incident on the system at the angle β_{nm} must be completely canceled. With Eqs. (1) and (7), this condition can be written as

$$P_0\exp(ikL\cos\beta_{nm}) + p_{nm}(\alpha, \beta) = 0. \tag{8}$$

By substituting all quantities involved in $p_{nm}(\alpha, \beta)$ into Eq. (8), we obtain the expression for W_{nm}:

$$W_{nm} = -\frac{1}{a_0 b_0}\frac{\exp(ikL\cos\beta_{nm})}{[\Phi_{nm}(\beta_{nm})]^2}, \tag{9}$$

where $\Phi_{nm}(\beta_{nm}) = \exp(2ikl\cos\beta_{nm}) - 1$.

Thus, when the active sound control system operates, the total acoustic pressure is distributed over the aperture of the second transmitting antenna ($z = L$, $|x| \le D_x$, and $|y| \le D_y$) as follows:

$$\begin{aligned} &F(x, y, z, L, \alpha, \beta) \\ &= P_0 \exp\{ik[L\cos\beta + (x\cos\alpha + y\sin\alpha)\sin\beta]\} \\ &\quad - \sum_{n=-N}^{N}\sum_{m=-M}^{M} a_0^{-1}\exp(ikL\cos\beta_{nm}) \\ &\quad \times \frac{\Phi_{nm}(\beta)}{\Phi_{nm}(\beta_{nm})} c_{1nm}(\alpha, \beta)\Psi_{nm}(x, y), \end{aligned} \qquad (10)$$

where $\Phi_{nm}(\beta) = \exp[ikl(\cos\beta + \cos\beta_{nm})] - 1$.

To describe the efficiency of a planar active sound control system, we use the amplitude of the sound pressure (10) transmitted in the direction of incidence of the plane wave (1). This amplitude has the form

$$\Delta = \frac{1}{4D_xD_y}\left| \int_{-D_x}^{D_x}\int_{-D_y}^{D_y} F(x, y, L, \alpha, \beta) \times \exp[-ik(x\cos\alpha + y\sin\alpha)\sin\beta]\,dxdy \right|.$$

From this expression, by using formula (10) and expanding all quantities that enter into it, we ultimately obtain the following expression for the system's efficiency:

$$\begin{aligned} \Delta = P_0 \Bigg| &\exp(ikL\cos\beta) \\ &- \sum_{n=-N}^{N}\sum_{m=-M}^{M} \exp(ikL\cos\beta_{nm})\frac{\Phi_{nm}(\beta)}{\Phi_{nm}(\beta_{nm})} \\ &\times \{\operatorname{sinc}[X_n(\alpha, \beta)]\operatorname{sinc}[Y_m(\alpha, \beta)]\} \Bigg|^2. \end{aligned} \qquad (11)$$

Calculations by Eq. (11) will be presented below.

Now, let us consider the antennas composed of discrete transmitters and receivers. Without a loss of generality, we can assume that each antenna contains the same number of transmitters or receivers located at points with the coordinates (x_q, y_t, Z), where

$$x_q = D_x\left[-1 + \frac{2(q-1)}{Q-1}\right], \quad y_t = D_y\left[-1 + \frac{2(t-1)}{T}\right],$$

and $Z = 0$, l, $L - l$, or L depending on which antenna is considered. Thus, each antenna contains a total of QT elements uniformly spaced in the x and y directions, the step size being individual for each direction.

For the first receiving antenna ($z = 0$), the analyzers of spatial harmonics perform the following procedure:

$$\begin{aligned} c^*_{1nm}(\alpha, \beta) &= \frac{1}{QT}\sum_{q=1}^{Q}\sum_{t=1}^{T} v(x_q, y_t, 0)\Psi_{nm}(x_q, y_t) \\ &= P_0\sum_{q=1}^{Q}\sum_{t=1}^{T} a_{1qt}R_{nmqt}(\alpha, \beta). \end{aligned} \qquad (12)$$

Here,

$$\begin{aligned} R_{nmqt}(\alpha, \beta) = (QT)^{-1}\exp\Bigg\{ &iX_n(\alpha, \beta)\left[-1 + \frac{2(q-1)}{Q-1}\right] \\ &+ iY_m(\alpha, \beta)\left[-1 + \frac{2(t-1)}{T-1}\right]\Bigg\}, \end{aligned}$$

the functions $v(x, y, z)$ and $\Psi_{nm}(x, y)$ are defined by Eqs. (1) and (2), respectively; and the random functions a_{1qt} determine the measurement error for each receiver. If this error is zero, we have $a_{1qt} \equiv 1$. Here and below, we omit both receiver sensitivity a_0 and transmitter sensitivity b_0, because they do not enter into the final formula for the system's efficiency.

A similar procedure applied to the second receiving antenna yields

$$\begin{aligned} c^*_{2nm}(\alpha, \beta) &= \frac{1}{QT}\sum_{q=1}^{Q}\sum_{t=1}^{T} v(x_q, y_t, l)\Psi_{nm}(x_q, y_t) \\ &= P_0\exp(ikl\cos\beta)\sum_{q=1}^{Q}\sum_{t=1}^{T} a_{2qt}R_{nmqt}(\alpha, \beta). \end{aligned} \qquad (13)$$

In Eq. (13), a_{2qt} is also a random quantity, which equals unity when measurements on the second receiving antenna are error-free.

From Eqs. (12) and (13), we compose the quantity

$$\begin{aligned} &A^*_{1nm}(\alpha, \beta) \\ &= c^*_{2nm}(\alpha, \beta)\exp(ikl\cos\beta_{nm}) - c^*_{1nm}(\alpha, \beta). \end{aligned} \qquad (14)$$

Procedure (14) is performed in the (n, m)th channel by the unidirectional receiver. As in the continuous case, the transfer coefficient of the intermediate unit in the (n, m)th channel has the form of Eq. (9). Thus, the quantity $u^*_{nm}(\alpha, \beta) = A^*_{1nm}(\alpha, \beta)W^*_{nm}$ applied to the inputs of the unidirectional transmitter is given by the expression

$$\begin{aligned} u^*_{nm}(\alpha, \beta) &= \frac{P_0\exp(ikL\cos\beta_{nm})}{[\Phi_{nm}(\beta_{nm})]^2} \\ &\times \sum_{q=1}^{Q}\sum_{t=1}^{T}\{a_{2qt}[\Phi_{nm}(\beta) + 1] - a_{1qt}\}R_{nmqt}(\alpha, \beta). \end{aligned} \qquad (15)$$

Here, the functions $\Phi_{nm}(\beta_{nm})$ and $\Phi_{nm}(\beta)$ are defined by Eqs. (9) and (10), respectively.

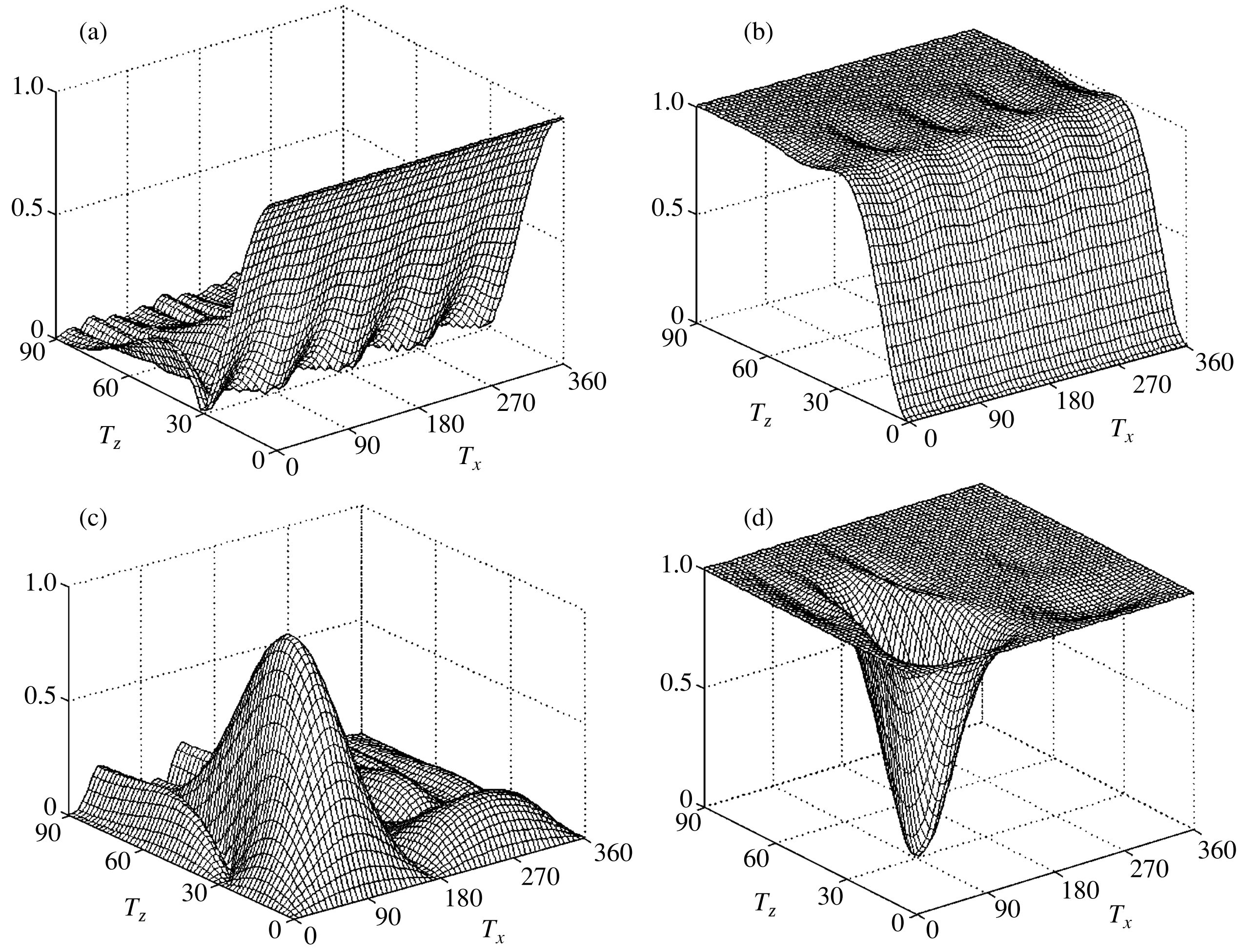

Fig. 2. (a, c) Amplitudes of spatial harmonics and (b, d) and the degree of sound suppression versus the angles of incidence (in degrees) of the plane wave at $Q_x = Q_y = 1$ and $F = 2$: (a, b) harmonic (0, 0) and (c, d) harmonic (0, 1).

As in the continuous case, from the outputs of the unidirectional transmitters, the quantities $u^*_{nm}(\alpha, \beta) \times \exp(ikl\cos\beta_{nm})$ and $-u^*_{nm}(\alpha, \beta)$, are supplied to the transmitting antennas, which consist of discrete radiators, so that the amplitude of the (q, t)th radiator in the (n, m)th channel on the first transmitting antenna is

$$\begin{aligned} & f_{1nm}(x_q, y_t, L-l) \\ &= b_{1qt}u^*_{nm}(\alpha, \beta)\exp(ikl\cos\beta_{nm})\Psi_{nm}(x_q, y_t) \\ &= b_{1qt}u^*_{nm}(\alpha, \beta)\exp(ikl\cos\beta_{nm}) \\ &\times \exp\left\{\frac{2\pi i}{\lambda}\left[D_x\left[-1+\frac{2(q-1)}{Q-1}\right]\cos\alpha_n\right.\right. \\ &\left.\left. + D_y\left[-1+\frac{2(t-1)}{T-1}\right]\sin\alpha_m\right]\right\}, \end{aligned} \quad (16)$$

for the second antenna, the corresponding amplitudes is

$$\begin{aligned} & f_{2nm}(x_q, y_t, L) \\ &= -b_{2qt}u^*_{nm}(\alpha, \beta)\Psi_{nm}(x_q, y_t) = -b_{2qt}u^*_{nm}(\alpha, \beta) \\ &\times \exp\left\{\frac{2\pi i}{\lambda}\left[D_x\left[-1+\frac{2(q-1)}{Q-1}\right]\cos\alpha_n\right.\right. \\ &\left.\left. + D_y\left[-1+\frac{2(t-1)}{T-1}\right]\sin\alpha_m\right]\right\}. \end{aligned} \quad (17)$$

Here, b_{1qt} and b_{2qt} determine the random measurement error for the (q, t)th radiator of each antenna. In the absence of error, $b_{1qt} = b_{2qt} = 1$.

Thus, Eqs. (16) and (17) yield the following expression for the efficiency of the discrete monopole active

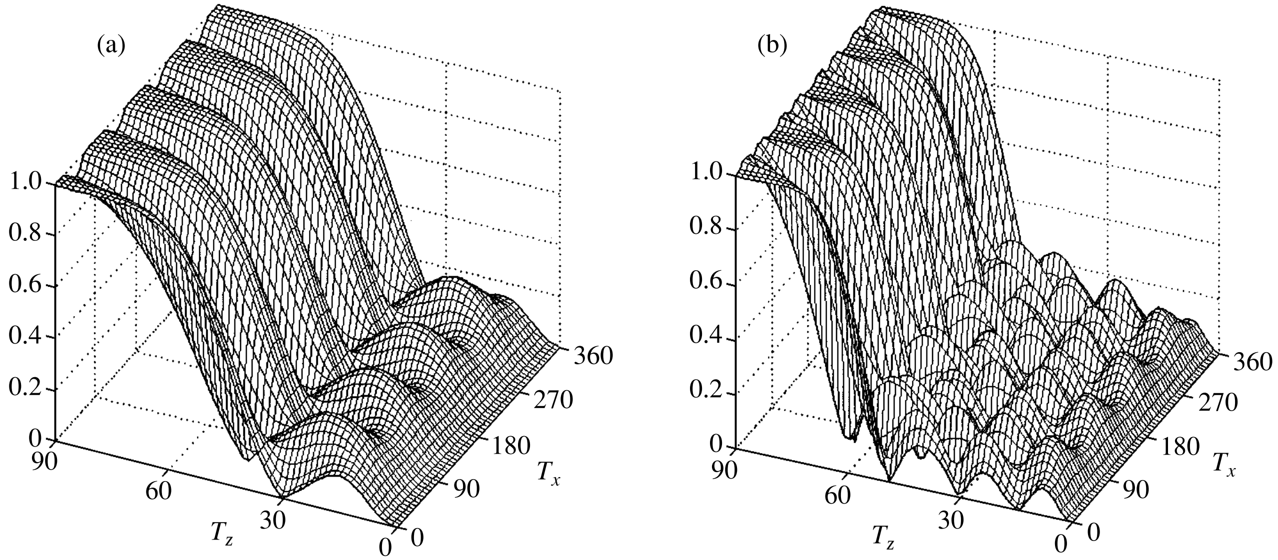

Fig. 3. System's efficiency versus the angles of incidence at $Q_x = Q_y = 1$: (a) $F = 2$, the total number of harmonics is 13; (b) $F = 4$, the total number of harmonics is 49.

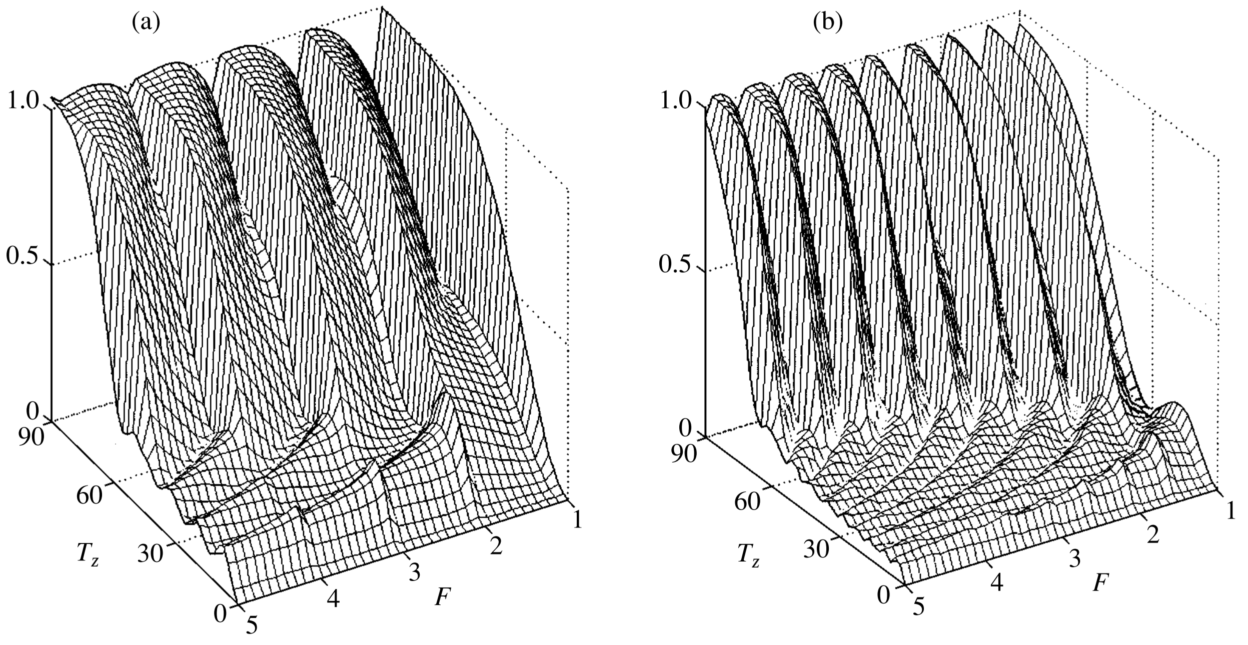

Fig. 4. System's efficiency versus the frequency and angle of incidence at $Q_x = Q_y$ = (a) 1 and (b) 2.

sound control system:

$$\Delta^*(\alpha, \beta) = P_0\left|\exp(ikl\cos\beta) + \sum_{n=-N}^{N}\sum_{m=-M}^{M} u^*_{nm}(\alpha, \beta) \times \sum_{q=1}^{Q}\sum_{t=1}^{T}\{b_{1qt}[\Phi_{nm}(\beta_{nm}) + 1] - b_{2qt}\}R_{nmqt}(\alpha, \beta)\right|. \tag{18}$$

From Eq. (18) it follows that, when the number of transmitters and receivers grows, i.e., when passing to the continuous case with no transmitting and receiving errors, the function $\Delta^*(\alpha, \beta)$ transforms to the function $\Delta(\alpha, \beta)$.

The efficiency of the control system calculated from Eqs. (11) and (18) is considered to be good if $\Delta(\alpha, \beta)$ or $\Delta^*(\alpha, \beta)$ normalized by the amplitude of the plane wave

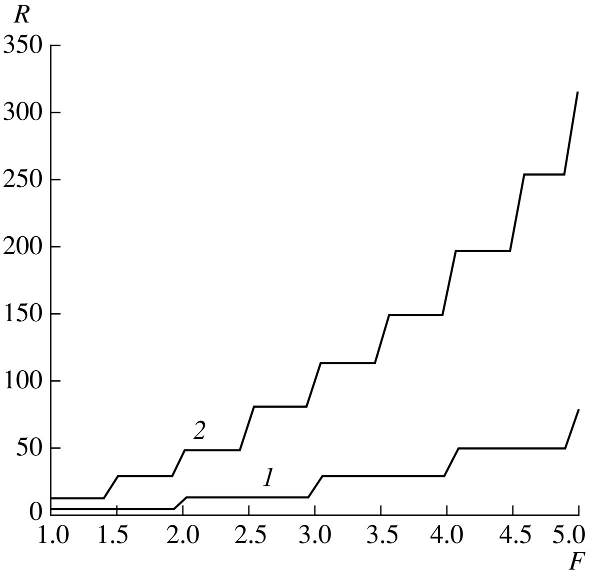

Fig. 5. Number of harmonics versus frequency range at $Q_x = Q_y =$ (*1*) 1 and (*2*) 2.

P_0 is below a specified threshold in a given range of angles of incidence α and β. This fact agrees with the results obtained in [13], where the silent zone conditions are fulfilled for large values of the parameter R of the spherical coordinate system, i.e., in the far-field zone.

The analytical formulas obtained above were used to calculate the efficiency of the active sound control system. The effects of the system's parameters (wave dimensions, number of two-dimensional spatial harmonics, frequency range, distance l between transmitters and receivers, system's size L, etc.), parameters of the incident plane wave (frequency and incidence angles), and number of transmitters and receivers and the difference in their sensitivities (in the discrete case) on the system's efficiency were investigated.

The figures below use the following designations: $Q_x = \frac{2D_x}{\lambda_0}$ is the wave dimension along the x axis; $Q_y = \frac{2D_y}{\lambda_0}$ is the wave dimension along the y axis; $F = \frac{f}{f_0}$ is the dimensionless frequency; f_0 and λ_0 are the lower frequency limit of the frequency range and the acoustic wavelength at this frequency, respectively; and T_x and T_z are the angles of incidence of the primary plane wave in the horizontal and vertical planes, where $0° \le T_x \le 360°$ and $0° \le T_z \le 90°$. Each harmonic is described by two numbers (m, n). All results refer to $L = 0.15$ and $l = 0.05$ (Fig. 1) and are normalized by the amplitude P_0 of the incident plane wave.

Figure 2 illustrates the structure of several harmonics and the efficiency of the system operating at each of them. Figures 2a and 2c show the amplitudes of harmonics versus the angles of incidence T_x and T_z, and Figs. 2b and 2d show the efficiency of the system for these harmonics. The parameters of the system are given in the figure caption. As can be seen from Fig. 2, the amplitudes of the normal waves have maxima equal to unity, at which the efficiency of the system is maximal (the field transmitted through the system is zero). Therefore, it becomes clear that, to attain a high efficiency at various incidence angles, the system should use a sufficiently high number of spatial harmonics.

This conclusion is illustrated by calculations of the system's efficiency shown in Fig. 3a ($Q_x = Q_y = 1$, $F = 2$) and in Fig. 3b ($Q_x = Q_y = 1$, $F = 4$). In Fig. 3a, the system uses 13 normal waves to cancel the external field. These are the waves numbers (–2, 0), (–1, –1), (–1, 0), (–1, 1), (0, –2), (0, –1), (0, 0), (0, 1), (0, 2), (1, –1), (1, 0), (1, 1), and (2,0). For the case illustrated in Fig. 3b, the number of normal waves and, consequently, of independent channels that take part in the field cancellation is 49. Consider the quantities $px = Q_xF$ and $py = Q_yF$, which describe the wave dimensions of the system along the x and y axes, respectively. As we noted above, $N = E(px)$ and $M = E(py)$, where E is the integral part of a number. Then, for the current maximum number max(m) on the y axis, the following formula is valid:

$$\max(m) = E\left(\frac{px}{py}\sqrt{N^2 - n^2}\right),$$

where n is the current number of the harmonic on the x axis, which varies within $-N \le n \le N$.

As seen from Fig. 3, the dependence of the system efficiency on the angle T_x is weak. Therefore, it is reasonable to average this quantity over the T_x angle (from 0° to 360°) at each frequency used in the calculations to obtain the dependences of the efficiency on the dimensionless frequency F and the angle T_z. These dependences are shown in Fig. 4 for various $Q_x = Q_y$. As we can see from Figs. 4a and 4b, new normal waves taking part in the sound control appear with increasing frequency, which increases the number of system's channels and, hence, enhances the efficiency in a wider range of the T_z angle. The frequency dependence of the number of normal waves R for cases illustrated in Figs. 4a and 4b is given in Fig. 5. The plots show that, for square antennas, an n-fold increase in their linear wave dimension leads to an increase in the number of normal waves by a factor of approximately n^2.

The data presented above refer to the continuous distributions of transmitters and receivers over the respective antennas. Practically, discrete distributions are important. The case of a discrete structure is illustrated in Fig. 6, which presents the efficiency calculated for different (sufficiently small) numbers of receivers (transmitters) with $Q = T = 10$ (Fig. 6a) and $Q = T = 8$ (Fig. 6b). At the lower frequency $F = 1$, the number of

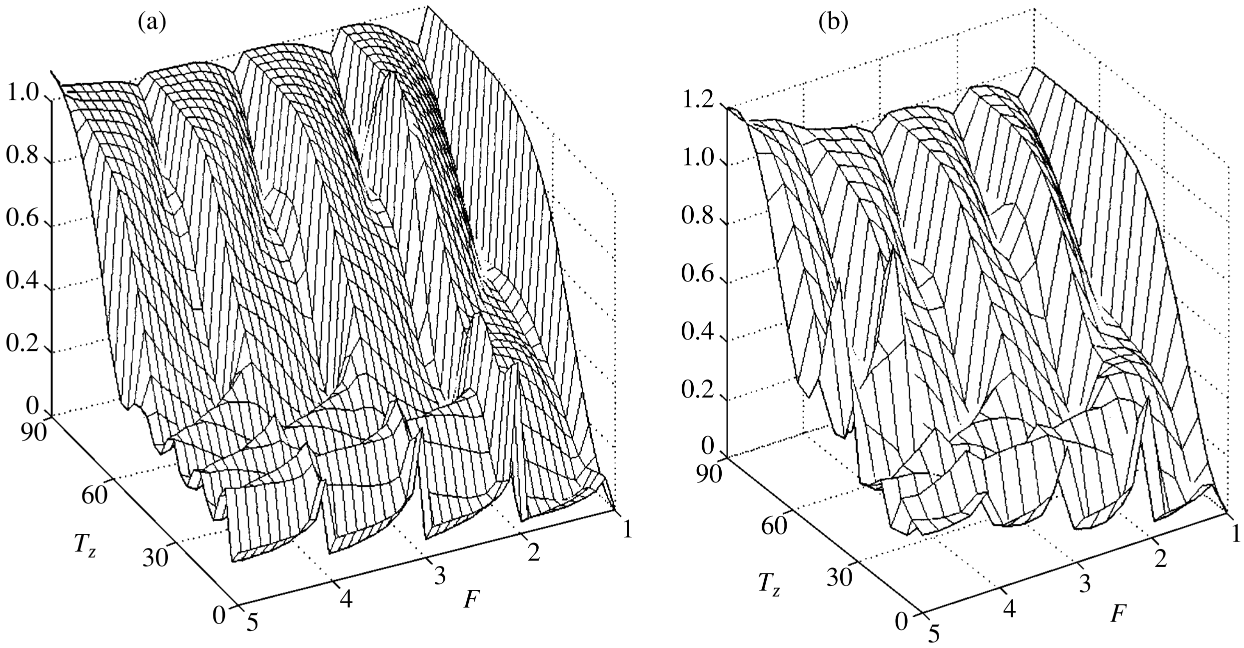

Fig. 6. Efficiency of a discrete system versus the frequency and angle of incidence at $Q_x = Q_y = 1$ and $Q = T =$ (a) 10 and (b) 8.

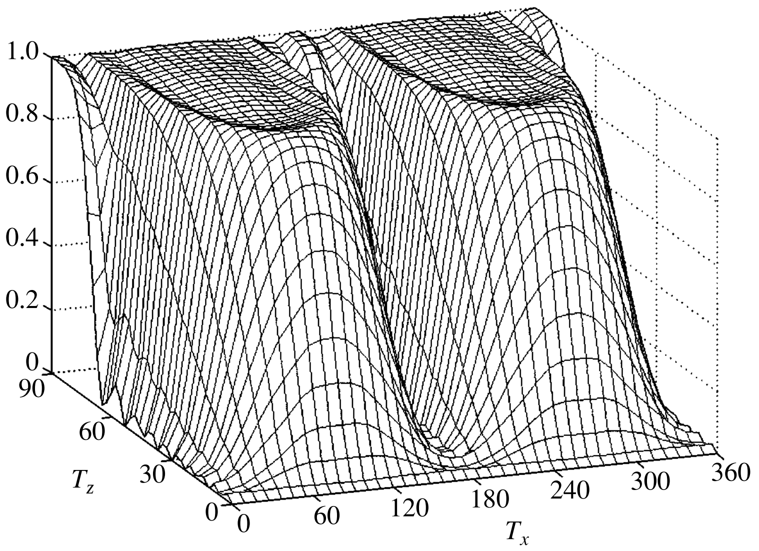

Fig. 7. System's efficiency versus the angles of incidence at $Q_x = 5$, $Q_y = 1$, and $F = 2$.

antenna elements per wavelength is 10 in the first case and 8 in the second case. As the frequency increases, this number decreases to 2 and 1.6, respectively, at the highest frequency $F = 5$. Therefore, the smaller the number of receivers per wavelength is, the greater the loss in the system's efficiency (compare with Fig. 4a).

Thus far, only square antennas were considered. If sound should be canceled in a small range of angles T_x, the efficiency can be increased using rectangular antennas with a relatively large side ratio. Our calculations showed that when, for example, $Q_x = 5$, $Q_y = 1$, and $F = 2$, the system's efficiency at $T_x = 0°$ and 180° remains high in the angular range of $0° \leq T_z \leq 70°$ (Fig. 7). At the same time, for any other angles of incidence, a high efficiency remains only at $T_z \approx \pm 10°$. In this case, all the necessary harmonics on the x axis, whose number was $N = 21$, and only one zero harmonic on the y axis were employed, so that the total number of harmonics was $R = 21$.

REFERENCES

1. A. I. Boĭko and V. V. Tyutekin, Akust. Zh. **45**, 454 (1999) [Acoust. Phys. **45**, 402 (1999)].
2. I. A. Urusovskiĭ, Akust. Zh. **27**, 585 (1981) [Sov. Phys. Acoust. **27**, 325 (1981)].
3. I. A. Urusovskiĭ, Akust. Zh. **32**, 560 (1986) [Sov. Phys. Acoust. **32**, 354 (1986)].
4. E. V. Korotaev and A. A. Mazanikov, Akust. Zh. **31**, 539 (1985) [Sov. Phys. Acoust. **31**, 323 (1985)].
5. V. V. Tyutekin, Akust. Zh. **43**, 238 (1997) [Acoust. Phys. **43**, 202 (1997)].
6. E. V. Korotaev and V. V. Tyutekin, Akust. Zh. **46**, 84 (2000) [Acoust. Phys. **46**, 71 (2000)].
7. A. I. Boĭko and V. V. Tyutekin, in *Architectural and Building Acoustics. Noise and Vibration: Proceedings of XI Session of the Russian Acoustical Society* (Geos, Moscow, 2001), Vol. 4, p. 168.
8. T. A. Beauvilain and J. S. Bolton, J. Acoust. Soc. Am. **107**, 1189 (2000).
9. S.-M. Kim and M. J. Brennan, J. Acoust. Soc. Am. **107**, 2523 (2000).
10. D.-B. Yoon and Y.-H. Kim, J. Acoust. Soc. Am. **107**, 3226 (2000).
11. C. D. Kestell, B. S. Cazzolato, and C. H. Hansen, J. Acoust. Soc. Am. **109**, 232 (2001).
12. S. K. Lau and S. K. Tang, J. Acoust. Soc. Am. **110**, 925 (2001).
13. W. K. Tseng, B. Rafaely, and S. J. Elliot, J. Sound Vibr. **234** (3), 427 (2000).

Translated by A. Khzmalyan

Acoustical Physics, Vol. 50, No. 1, 2004, pp. 100–106. Translated from Akusticheskiĭ Zhurnal, Vol. 50, No. 1, 2004, pp. 116–122.
Original Russian Text Copyright © 2004 by Tereshchenko, Rychagov.

Acoustical Multipath Flow Measurements Based on Quadrature Integration Methods

S. A. Tereshchenko and M. N. Rychagov

Moscow State Institute of Electronic Engineering (Technical University),
Zelenograd, Moscow, 124498 Russia

e-mail: tsa@miee.ru; mrychagov@miee.ru

Received February 28, 2003

Abstract—A systematic description of a new approach to determining the flow rates of liquids or gases transported through pipelines of circular cross sections is presented. The approach is based on multipath ultrasonic time-of-flight measurements. A mathematical technique for processing pulsed acoustic signals recorded in several measuring planes is developed. The technique provides precision estimates of flow rates owing to the use of quadrature integration methods. Several variants of realizing the multipath measurements are suggested. Tables of nodes and weights of the corresponding quadrature formulas, including both known values and values calculated for the first time, are presented. © *2004 MAIK "Nauka/Interperiodica".*

INTRODUCTION

Determination of the characteristics of liquids or gases pumped through pipelines of different (in particular, circular) cross sections is an urgent theoretical, computational, and engineering problem of considerable practical interest [1–6]. The most important characteristic of such flows is the flow rate, i.e., the volume of liquid or gas passing through a pipe cross section per unit time. The efforts of individual researchers and companies manufacturing the measuring equipment are aimed at reducing the measurement errors, which are determined primarily by the spatial inhomogeneity of the flows under measurement. One of the most promising approaches to solving this problem is based on the so-called multipath measurements. In this case, for estimating the flow characteristics, a number of measurements are performed in several measuring planes parallel to the longitudinal axis of the pipe. In addition to the evident gain in accuracy due to the increase in the volume of the input data, this approach makes it possible to apply the quadrature integration formulas, which provide a considerable increase in the accuracy of the final estimates of the flow rate. Moreover, multipath measurements allow one to formulate and solve the problem of reconstructing the symmetric distribution of the axial component of flow velocity on the basis of the Abel transform [7]. A further advancement of the multipath approach is connected with the development of instruments and algorithms for a complete reconstruction of an arbitrary two-dimensional distribution of the axial component of flow velocity in a pipe cross section by using the Radon transform [8].

1. THE MULTIPATH APPROACH TO ULTRASONIC FLOW MEASUREMENTS

In the general case, for determining the flow rate Q, it is necessary to calculate the two-dimensional integral

$$Q = \int\limits_{S(z)} v_z(x, y, z)dS = \int\limits_{-R}^{+R}\left[\int\limits_{-\sqrt{R^2-x^2}}^{+\sqrt{R^2-x^2}} v_z(x, y, z)dy\right]dx, \tag{1}$$

where $v_z(x, y, z)$ is the axial (along the tube) component of the flow velocity, $S(z)$ is the cross section of tube by a plane perpendicular to the tube axis, and (x, y, z) are the Cartesian coordinates: z is along the tube axis and x and y are in the plane of the cross section $S(z)$.

To determine the flow rate, it is possible to use the measurement of the time of flight of ultrasonic pulses in several measuring planes perpendicular to the tube cross section and parallel to the tube axis (Fig. 1). Here, it is assumed that, within the length L, the flow velocity does not change, i.e., $v_z(x, y, z) = v_z(x, y)$.

We consider the relation of the upstream and downstream times of flight of the signal to the distribution of the flow velocity over the tube cross section. We assume that the line of the signal passage makes an angle α with the tube axis (Fig. 2). Then, the time t_{AB} of the signal passage from point A to point B and the time t_{BA} of the signal passage from point B to point A are

1063-7710/04/5001-0100$26.00 © 2004 MAIK "Nauka/Interperiodica"

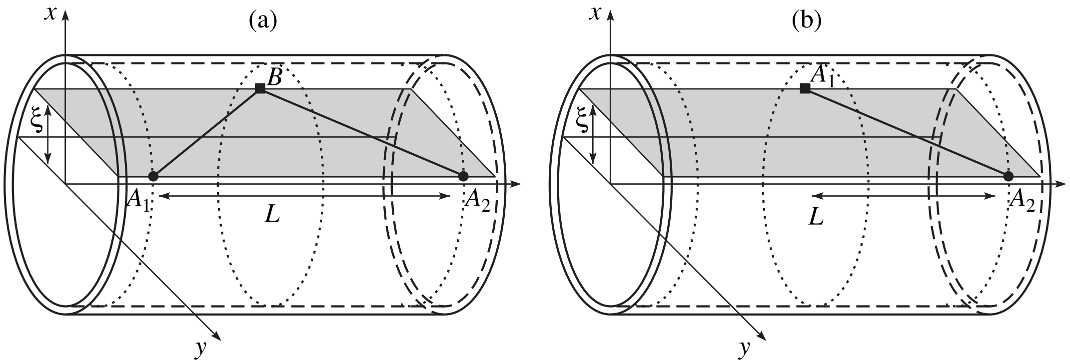

Fig. 1. A measuring plane lying at a distance ξ from the tube axis for measuring the time of flight of an ultrasonic pulse between the transmitting–receiving elements A_1 and A_2 located (a) on one side of the tube and (b) on different sides of the tube; *B* is a reflecting element and *L* is the distance between the transmitting–receiving elements A_1 and A_2 along the tube axis.

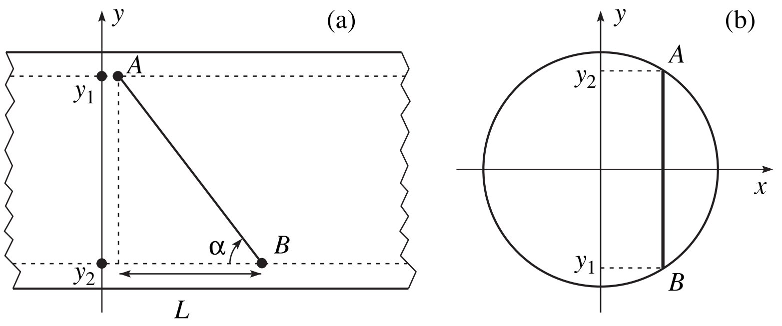

Fig. 2. Geometry of measuring the time of flight of an ultrasonic pulse between the transmitting–receiving elements *A* and *B*: (a) in the measuring plane and (b) in the projection on the tube cross section.

expressed as

$$t_{AB} = \int_A^B \frac{dl_1}{c_0 + v_z(l_1)\cos\alpha}, \qquad (2)$$

$$t_{BA} = \int_B^A \frac{dl_2}{c_0 + v_z(l_2)\cos\alpha}, \qquad (3)$$

where $v_z(l_m) = v_z(x(l_m), y(l_m))$, c_0 is the sound velocity in the stationary medium, and m is the index characterizing the measuring trajectory. The difference in the times of flight is

$$\Delta t = t_{BA} - t_{AB}$$
$$= \int_B^A \frac{2v_z(l)\cos\alpha dl}{c_0^2 - v_z^2(l)\cos^2\alpha} \approx \frac{2\cos\alpha}{c_0^2}\int_B^A v_z(l)dl. \qquad (4)$$

Here, the smallness of the ratio $\frac{v_z^2}{c^2}$ is taken into account.

We emphasize that, traditionally [9–12], flow measurements are performed with the use of the mean velocity $\bar{v}_z(x) \approx \frac{1}{|AB|}\int_B^A v_z(l)dl$, which is determined by the measured values of Δt:

$$\bar{v}_z(x) = \frac{c_0^2}{2|AB|\cos\alpha}\Delta t. \qquad (5)$$

The design of the majority of instruments is intended for measuring the mean flow velocities along one or several directions. Then, the flow rate is determined by multiplication of the mean velocity by the tube cross section with a correction factor introduced in the case of one measuring plane or with integration of the mean velocity estimates for several measuring planes. However, in general, obtaining the mean velocity estimates is not necessary when one deals with high-precision flow rate measurements. By contrast, it is sufficient to apply only the integration of the data of the time of flight measurements for ultrasonic pulses.

Expression (4) relates the integral over the spatial distribution of the axial flow velocity component, which is directed along the line connecting the transmitting–receiving elements (transducers), to the measured values of the times of flight of ultrasonic pulses. Similarly, by using the sum of these values, it is possible to determine the sound velocity c_0 in the stationary medium as a moving characteristic of the flow:

$$\begin{aligned}\sigma_t &= t_{BA} + t_{AB}\\ &= \int_B^A \frac{2c_0 dl}{c_0^2 - v_z^2(l)\cos^2\alpha} \approx \frac{2}{c_0}\int_B^A dl = \frac{2|AB|}{c_0}.\end{aligned} \tag{6}$$

Changing to the coordinates in the plane of the cross section $S(z)$ (Fig. 2b), we obtain

$$\begin{aligned}\int_B^A v_z(l)dl &= \frac{1}{\sin\alpha}\int_{y_1}^{y_2} v_z(x,y)dy\\ &= \frac{1}{\sin\alpha}\int_{-\sqrt{R^2-x^2}}^{+\sqrt{R^2-x^2}} v_z(x,y)dy.\end{aligned} \tag{7}$$

Then, the flow rate will be determined by one of the following expressions, depending on the quantities taken as input data. If the input data are Δt and c_0, the flow rate is determined as

$$\begin{aligned}Q &= \int_{-R}^{+R}\left[\int_{-\sqrt{R^2-x^2}}^{+\sqrt{R^2-x^2}} v_z(x,y)dy\right]dx\\ &= \frac{c_0^2\tan\alpha}{2}\int_{-R}^{+R}\Delta t(x)dx,\end{aligned} \tag{8a}$$

if the quantity $\bar{v}_z(x)$ is preset, we have

$$\begin{aligned}Q &= \int_{-R}^{+R}\bar{v}_z(x)|AB|\sin\alpha dx\\ &= 2\int_{-R}^{+R}\sqrt{R^2-x^2}\,\bar{v}_z(x)dx,\end{aligned} \tag{8b}$$

and if Δt and σ_t are used as initial data, the flow rate is

$$Q = \frac{2}{\sin\alpha\cos\alpha}\int_{-R}^{+R}(R^2-x^2)\frac{\Delta t(x)}{\sigma_t^2}dx. \tag{8c}$$

Formula (1) is valid for an arbitrary function $v_z(x, y)$. At the same time, in the flow measurements and flow monitoring, some additional conditions are imposed on the velocity $v_z(x, y)$, which restrict the class of admissible functions. Naturally, if the accepted assumption does not fit the real flow, an additional error is introduced in the results of calculations based on the measured data. The following classes of functions can be distinguished according to the significance of the imposed conditions:

(i) the velocity $v_z(x, y)$ is described by a given analytical dependence;

(ii) the velocity $v_z(x, y)$ is axially symmetric, $v_z(x, y) = v_z(\sqrt{x^2+y^2}) = v_z(r)$;

(iii) the velocity $v_z(x, y)$ is an arbitrary function of the coordinates.

In the first case, for calculating the flow rate, only one measurement in the diametrical measuring plane ($\xi = 0$) may be sufficient. For example, for a velocity that does not vary over a cross section, $v_z(x, y) = v_0 =$ const, we have

$$Q = v_0\pi R^2 = \bar{v}_z(0)\pi R^2. \tag{9}$$

For a Poiseuille flow $v_z(x, y) = v_0\left(1 - \frac{x^2+y^2}{R^2}\right)$, we have

$$Q = \frac{1}{2}v_0\pi R^2 = \frac{3}{4}\bar{v}_z(0)\pi R^2. \tag{10}$$

More complicated velocity profiles, such as the Salami profiles [13], are used mainly for testing the accuracy of various methods.

In the second case, for a numerical calculation of integral (1), it is necessary to make several measurements in various measuring planes (Fig. 3). Note that the measurements in a plane lying at a distance x from the tube axis do not depend on the orientation of the measuring plane relative to the tube: for instance, a parallel geometry of measurements is identical to a fan geometry (Fig. 4).

In this case, a diversity of methods of multipath measurements can be used, including the methods of quadrature integration. In addition, it becomes possible to solve the problem of reconstructing the complete velocity profile $v_z(r)$ on the basis of the Abel transform [7].

The last case is the most complex and most interesting one. Although the methods of quadrature integration are suitable for calculating the flow rate, all measuring planes should be parallel to each other. A fan geometry does not admit an accurate application of quadrature formulas. However, it is possible to pose the problem of reconstructing an arbitrary velocity profile $v_z(r)$ on the basis of the Radon transform [8].

2. QUADRATURE INTEGRATION

For calculating integrals (8a)–(8c), it is possible to use the formulas of numerical integration, such as the rectangle rule or Simpson's rule [14]. However, for a limited number of the integrand samples, quadrature formulas of higher orders give much more accurate estimates.

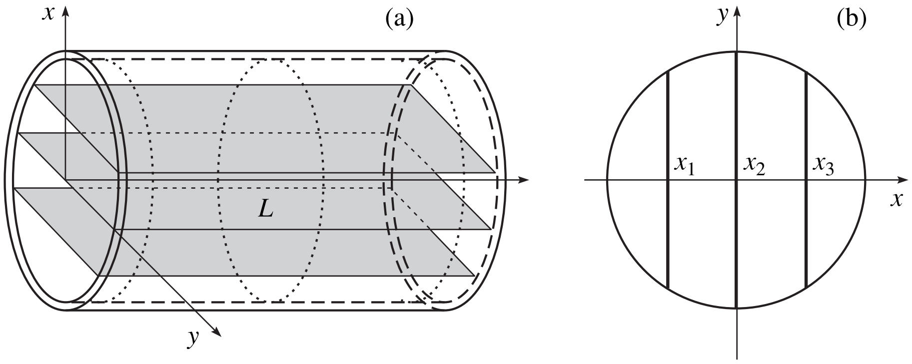

Fig. 3. Multipath ultrasonic measurements: (a) parallel measuring planes and (b) the tube cross section.

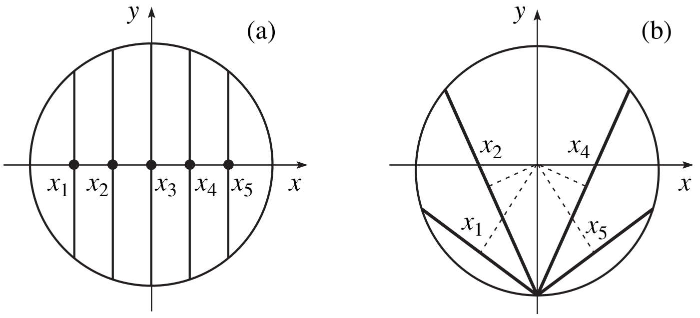

Fig. 4. (a) Parallel and (b) fan geometries of measurements.

The theory of quadrature integration considers the most efficient methods of calculating the integrals of the following form on a standard interval $\xi \in [-1, +1]$:

$$G = \int_{-1}^{+1} p(\xi) f(\xi) d\xi, \tag{11}$$

where $p(\xi) > 0$ is an arbitrary weight function.

It is evident that, after the substitution $\xi = x/R$, formulas (8a)–(8c) are reduced to the form of Eq. (11) with $p(\xi) = 1$, $p(\xi) = \sqrt{1-\xi^2}$, and $p(\xi) = 1 - \xi^2$ and with $f(\xi) = \dfrac{c_0^2 R \tan\alpha}{2}\Delta t(\xi)$, $f(\xi) = 2R^2 \bar{v}_z(\xi)$, and $f(\xi) = \dfrac{2R^3 \Delta t(\xi)}{\sigma_t^2 \sin\alpha\cos\alpha}$, respectively. For a fixed number of discreet measurements n, integral (11) transforms to the sum

$$G = \sum_{j=1}^{n} \lambda_j f(\xi_j), \tag{12}$$

where λ_j are the quadrature weights and ξ_j are the nodes (abscissas) of the quadrature formula.

In the framework of the theory of quadrature formulas, three variants of the problem statement are possible.

Newton's problem. For a given arrangement of nodes ξ_j find the best values of the coefficients λ_j. The best known problem of this kind is the problem with equidistant nodes ξ_j, i.e., the Newton–Cotes quadrature integration formulas.

Chebyshev's problem. For given values of the coefficients λ_j find the best arrangement of nodes ξ_j. The best known problem of this kind is the problem with equal constant coefficients $\lambda_j = \dfrac{2}{n}$, i.e., the Chebyshev approach to quadrature integration.

Gauss' problem. Find the best arrangement of nodes ξ_j and the corresponding values of the coefficients λ_j. This problem corresponds to the Gaussian quadrature formulas.

Obviously, the best accuracy is achieved with Gaussian formulas. Nevertheless, Newton's problem is the most flexible, because for an arbitrary arrangement of nodes it allows one to find the optimum values of quadrature coefficients. When a statistical error occurs in the results of measurements, Chebyshev's formulas are the most stable ones.

Table 1. Nodes and coefficients of the quadrature formula for the weight function $p(\xi) = 1$

n	Newton's problem		Chebyshev's problem		Gauss' problem	
	ξ_j	λ_j	ξ_j	λ_j	ξ_j	λ_j
3	–0.6667	0.7500	–0.7071	0.6667	–0.7746	0.5556
	+0.0000	0.5000	0.0000	0.6667	0.0000	0.8889
	+0.6667	0.7500	0.7071	0.6667	0.7746	0.5556
4	–0.7500	0.5417	–0.7947	0.5000	–0.8611	0.3479
	–0.2500	0.4583	–0.1876	0.5000	–0.3400	0.6521
	+0.2500	0.4583	0.1876	0.5000	0.3400	0.6521
	+0.7500	0.5417	0.7947	0.5000	0.8611	0.3479
5	–0.8000	0.4774	–0.8325	0.4000	–0.9062	0.2369
	–0.4000	0.1736	–0.3745	0.4000	–0.5385	0.4786
	+0.0000	0.6979	0.0000	0.4000	0.0000	0.5689
	+0.4000	0.1736	0.3745	0.4000	0.5385	0.4786
	+0.8000	0.4774	0.8325	0.4000	0.9062	0.2369

For any weight function $p_0(\xi)$, it is possible to use the formulas for another weight function $p_1(\xi)$ by multiplying the integrand by $\frac{p_0(\xi)}{p_1(\xi)}$, because the following equality is valid:

$$\int_{-1}^{+1} p_0(\xi) f(\xi) d\xi = \int_{-1}^{+1} p_1(\xi)\left[\frac{p_0(\xi)}{p_1(\xi)} f(\xi)\right] d\xi = \int_{-1}^{+1} p_1(\xi) f_1(\xi) d\xi. \tag{13}$$

Therefore, in particular, for calculating integral (11), it is possible to use the coefficients λ_j of the quadrature formula for $p(\xi) = 1$. Then, formula (12) can be written as

$$G = \sum_{j=1}^{n} \lambda'_j p(\xi_j) f(\xi_j) = \sum_{j=1}^{n} \lambda''_j f(\xi_j). \tag{14}$$

The solution to Newton's problem for an arbitrary arrangement of nodes has the form

$$\lambda_k = \frac{1}{\prod\limits_{\substack{j=1\\ j\neq k}}^{n} (\xi_k - \xi_j)} \int_{-1}^{+1} p(\xi) \prod_{\substack{j=1\\ j\neq k}}^{n} (\xi - \xi_j) d\xi. \tag{15}$$

Chebyshev's problem is less studied. Solutions for the case of $p(\xi) = 1$ and $n = 2, 3, 4, 5, 6, 7$, and 9 are known. It is interesting that, for $p(\xi) = \frac{1}{\sqrt{1-\xi^2}}$, Chebyshev's and Gaussian formulas coincide, while for other weight functions, in particular for $p(\xi) = \sqrt{1-\xi^2}$, they are different.

The solution to Gauss' problem for $p(\xi) = 1$ corresponds to the positions of the nodes ξ_j of quadrature formulas at the zero points of the Legendre polynomials $P_n(\xi_j) = 0$ and to $\lambda_j = \frac{2}{(1-\xi_j^2)\left[\frac{d}{d\xi}P_n(\xi)\right]^2_{\xi=\xi_j}}$.

For $p(\xi) = 1$, the solutions to Newton's (for equidistant positions of nodes), Chebyshev's, and Gauss' problems [15] are given in Table 1. Note that this case corresponds to the processing of the differences in the times of flight of ultrasonic pulses, Δt, rather than of the mean velocity $\bar{v}_z(x)$.

For other weight functions, the corresponding coefficients can be calculated by formula (14). However, the solutions obtained directly from the corresponding weight functions will be more accurate. Although not all these solutions can be found in reference sources, the methods of their derivation are well known [14] and can be used in every specific case. For instance, the calculation of the coefficients of quadrature formula λ_j (Eq. (15)) in Newton's problem for the weight function $p(\xi) = \sqrt{1-\xi^2}$ amounts to calculating the integrals of the form

$$I_k = \int_{-1}^{+1} \xi^k \sqrt{1-\xi^2} d\xi = \begin{cases} 0, & k = 2m+1 \\ \dfrac{(2m-1)!!}{2^{m+1}(m+1)!}\pi, & k = 2m. \end{cases} \tag{16}$$

In particular, $I_0 = \frac{1}{2}\pi$; $I_2 = \frac{1}{8}\pi$; $I_4 = \frac{1}{16}\pi$; $I_6 = \frac{5}{128}\pi$; $I_8 = \frac{7}{256}\pi$, and $I_{10} = \frac{21}{1024}\pi$.

Let us consider n measuring planes in a Newtonial measuring module based on the solution of Newton's problem (Fig. 5). Equidistant arrangement requires that $\Delta\xi_1 = \Delta\xi_2 = \ldots = \Delta\xi_n = \Delta\xi$. The length of the extreme segments $\Delta\xi_0$ and $\Delta\xi_{n+1}$ remains an open question. Assuming that they are equal, we set $\Delta\xi_0 = \Delta\xi_{n+1} = \alpha\Delta\xi$. The two limiting cases are $\Delta\xi_0 = \Delta\xi_{n+1} = 0$ ($\alpha = 0$) and $\Delta\xi_0 = \Delta\xi_{n+1} = \Delta\xi$ ($\alpha = 1$). In addition, intermediate variants are possible, and the preferable case is apparently $\alpha = 0.5$.

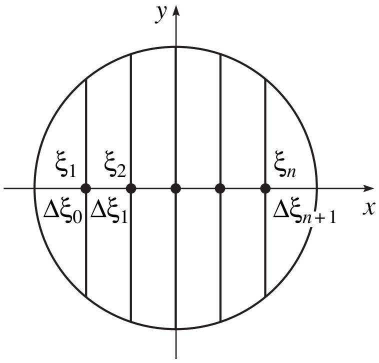

Fig. 5. Arrangement of the measuring planes in a Newtonian module.

The solutions to Newton's problem for $p(\xi) = \sqrt{1-\xi^2}$ and $\alpha = 0.0$, 0.5, and 1.0 were calculated for the first time, and they are given in Table 2.

The solution to Chebyshev's problem can be obtained in a similar way. The solution to Gauss' problem for the case of $p(\xi) = \sqrt{1-\xi^2}$ (i.e., when the quantity $\overline{v}_z(x)$ is taken as the measured input data) is known (see, e.g., [17]). The nodes of quadrature formula are $\xi_j = \cos\left(\frac{\pi}{n+1}\right)$, and the corresponding coefficients are $\lambda_j = \frac{\pi}{n+1}\sin^2\frac{\pi j}{n+1}$.

Multipath measurements make it possible to use a variety of realizations of the measuring modules. Taking that a measuring scheme is determined by a set of distances between the measuring planes and the tube axis together with a set of coefficients of quadrature formulas used for calculating the flow rate, at least three variants of measuring modules may be suggested, depending on the type of the problem on which they are based: a Newtonian module with an equidistant arrangement of measuring planes, a Chebyshev module, and a Gaussian module. Any of these types of measuring modules can be based on the solution to the corresponding problem with three weight functions for each of Eqs. (8a)–(8c). In addition, Newtonian modules, as indicated earlier, may have modifications with different extreme segments.

Further improvements are possible through increasing the order of quadrature formula with the same number of measuring planes, as well as through introducing the so-called skew measuring planes [16]. Thus, the choice of the optimal structure of a measuring module is a nontrivial scientific and engineering problem, a successful solution of which is determined by the spe-

Table 2. Nodes and coefficients of the quadrature formula for Newton's problem, for the weight function $p(\xi) = \sqrt{1-\xi^2}$

n	$\alpha = 0.0$		$\alpha = 0.5$		$\alpha = 1.0$	
	ξ_j	λ_j	ξ_j	λ_j	ξ_j	λ_j
3	–1.0000	0.1963	–0.6667	0.4418	–0.5000	0.7854
	+0.0000	1.1781	+0.0000	0.6872	+0.0000	0.0000
	+1.0000	0.1963	+0.6667	0.4418	+0.5000	0.7854
4	–1.0000	0.1227	–0.7500	0.2945	–0.6000	0.5154
	–0.3333	0.6627	–0.2500	0.4909	–0.2000	0.2700
	+0.3333	0.6627	+0.2500	0.4909	+0.2000	0.2700
	+1.0000	0.1227	+0.7500	0.2945	+0.6000	0.5154
5	–1.0000	0.0654	–0.8000	0.2173	–0.6667	0.5154
	–0.5000	0.5236	–0.4000	0.3579	–0.3333	0.2945
	+0.0000	0.3927	+0.0000	0.4203	+0.0000	1.1290
	+0.5000	0.5236	+0.4000	0.3579	+0.3333	0.2945
	+1.0000	0.0654	+0.8000	0.2173	+0.6667	0.5154

cific conditions of manufacturing such a module and by the requirements imposed on the data processing unit.

ACKNOWLEDGMENTS

This work was supported in part by the American Civil Research and Development Foundation, project CRDF RP1-517.

We are grateful to L.C. Lynnworth (GE Panametrics Inc., Waltham, USA) for fruitful discussions.

REFERENCES

1. L. C. Lynnworth, *Ultrasonic Measurements for Process Control: Theory, Techniques, Applications* (Academic, New York, 1989).
2. V. K. Khamidullin, *Ultrasonic Control-and-Measurement Instruments and Systems* (Leningr. Gos. Univ., Leningrad, 1989).
3. L. C. Lynnworth and V. Magori, in *Ultrasonic Instruments and Devices: Reference for Modern Instrumentation, Techniques and Technology*, Ed. by E. P. Papadakis (Academic, New York, 1998), Chap. 4, p. 275.
4. M. N. Rychagov, Akust. Zh. **44**, 829 (1998) [Acoust. Phys. **44**, 722 (1998)].
5. L. Le Brusquet and J. Oksman, Meas. Sci. Technol. **10**, 559 (1999).
6. T. T. Yeh, P. I. Espina, and S. A. Osella, in *Proceedings of 19th IEEE Instrumentation and Measurement Technology Conference* (IMTC, Budapest, 2001), p. 3112.
7. M. N. Rychagov and S. A. Tereshchenko, Inverse Probl. **16** (2), 495 (1999).
8. M. N. Rychagov, S. A. Tereshchenko, V. M. Podgaetskiĭ, and S. V. Selishchev, RF Patent No. 2177623 (25 July 2000).
9. G. A. Jackson, J. R. Gibson, and R. Holmes, Meas. Sci. Technol. **2**, 635 (1991).
10. C. N. Pannel, W. A. Evans, and D. A. Jackson, Flow Meas. Instrum. **1**, 216 (1990).
11. P. I. Moore, G. J. Brown, and B. P. Simpson, Meas. Sci. Technol. **11**, 1802 (2000).
12. A. E. Brown and L. C. Lynnworth, in *Flow Measurement: Practical Guides for Measurement and Control*, 2nd ed., Ed. by D. W. Spitzer (ISA, Research Triangle Park, NC, 2001), Chap. 20, p. 515.
13. L. A. Salami, Trans. Inst. Meas. Control (London) **6**, 197 (1984).
14. N. S. Bakhvalov, *Numerical Methods* (Nauka, Moscow, 1973).
15. *Handbook of Mathematical Functions: with Formulas, Graphs and Mathematical Tables*, Ed. by M. Abramowitz and I. Stegun (National Bureau of Standards, Washington, 1964; Nauka, Moscow, 1979), NBS Appl. Math. Ser. 55.
16. M. N. Rychagov and S. A. Tereshchenko, RF Patent No. 2189014 (30 June 2000).

Translated by A. Svechnikov

Acoustical Physics, Vol. 50, No. 1, 2004, pp. 107–111. Translated from Akusticheskiĭ Zhurnal, Vol. 50, No. 1, 2004, pp. 123–128.
Original Russian Text Copyright © 2004 by Sharfarets.

Method for Calculating the Field of an Opaque Source and the Field Scattered by an Inhomogeneous Inclusion in a Planar Layered Waveguide

B. P. Sharfarets
Ul. Kubinskaya 14–70, St. Petersburg, 196128 Russia
e-mail: sharg@mail.rcom.ru

Received June 17, 2002

Abstract—A method for calculating the resulting field of an opaque radiator and the field scattered by an inhomogeneous inclusion in a planar layered waveguide is described. The inclusion is assumed to be located in the Fraunhofer zone of an external radiator, and the scattering amplitude of the inclusion is assumed to be known. *© 2004 MAIK "Nauka/Interperiodica".*

The literature concerning the problems of scattering by inhomogeneities in the presence of boundaries, including the case when the radiator itself represents a scatterer, is quite extensive. A number of recent publications are given in the list of references for illustration [1–16]. In this area of research, the problems of scattering by inhomogeneities in the presence of a surface and a bottom are of practical significance [1, 4, 5, 10–14]. Papers [1, 4, 5, 10] assume that the boundaries and the inhomogeneities of a medium have no effect on the scattering amplitude of an inclusion. Papers [13, 14], which extend the results of paper [12] and consider the problem of sound scattering by an inclusion located in a planar layered waveguide in the zero approximation, i.e., without allowance for multiple reflections between the inclusion and the waveguide boundaries and under the assumption that the inclusion is located in a locally homogeneous layer. Paper [14] formulates the conditions under which this solution is correct. Paper [16] takes into account the effect of the waveguide boundaries on the resulting scattering amplitude of an opaque radiator and the effect of multiple reflections between the radiator and the boundaries; however, it assumes that the medium is homogeneous.

The present paper describes a method that allows one to calculate the resulting field of an opaque radiator with allowance for the scattering of the primary field by this radiator. The method is shown to be applicable for calculating the field scattered by an inhomogeneous inclusion located in the Fraunhofer zone of an external radiator in a planar layered waveguide with allowance for multiple reflections of the scattered field from the waveguide boundaries. The only restriction used in the method is the assumption that the waveguide layer of minimum thickness enclosing the scatterer (either an opaque radiator or a passive scatterer) can be considered locally homogeneous in the sense of paper [14] (this paper also gives the conditions of applicability of this assumption); in other words, it is assumed that normal waves in this layer are quasi-plane waves.

Let us formulate the problem. Let an opaque radiator scattering its own waves or a scatterer scattering incident waves be located in a planar layered waveguide. Let the liquid layer of minimum thickness $\Delta z = 2h$ enclosing the scatterer be homogeneous. Along the whole of the waveguide thickness outside this layer, the properties of the liquid can arbitrarily vary with depth. We need to find the total field of radiation in the first case and the scattered field in the second case. We assume that the directional pattern (DP) of the radiator and the scattering amplitudes of the radiator and the inclusion are known.

To solve the first problem, we use expressions of paper [15] that relate the combined scattering amplitude to the DP of the source of primary waves. Remember the problem formulation used in that paper. An opaque radiator with the DP of the primary field $D_i^0(\boldsymbol{\xi})$, $i = 1, 2$, is located in a homogeneous half-space with the boundary $z = 0$ (the z axis is directed downwards) and a reflection coefficient $V_1(0, \boldsymbol{\xi})$ (the first argument equal to zero means that the function V_1 refers to $z = 0$). Here, $D_i^0(\boldsymbol{\xi})$ are the weighting factors of the integral expansions of the primary field in plane waves with the wave vectors $\mathbf{k}_i = (\boldsymbol{\xi}, (-1)^i\alpha)$, $k = |\mathbf{k}_i| = (|\boldsymbol{\xi}|^2 + \alpha^2)^{1/2}$, in the homogeneous boundless spaces lying above ($i = 1$) and below ($i = 2$) the horizontal layer of minimum thickness enclosing the scatterer (see, e.g., [17]). The radiator considered as a scatterer, in turn, is characterized by the scattering amplitude $T_m^l(\boldsymbol{\xi}_p, \boldsymbol{\xi}_s)$, where $l, m = 1, 2$. The physical meaning of this function is as follows. A scattered wave of amplitude $T_m^l(\boldsymbol{\xi}_p, \boldsymbol{\xi}_s)$ appears when a plane wave with a wave vector $\mathbf{k}_p = (\boldsymbol{\xi}_p, \alpha_m)$, a unit

1063-7710/04/5001-0107$26.00 © 2004 MAIK "Nauka/Interperiodica"

amplitude, and a zero-valued phase is incident from above ($m = 1$) or from below ($m = 2$) on a scatterer whose geometrical center is located at the point (x_0, y_0, z_0) in a boundless homogeneous space. The scattered field is considered above or below the scatterer for $l = 1$ and $l = 2$, respectively. Here, $\mathbf{k}_s = (\boldsymbol{\xi}_s, \alpha_l)$ is the wave vector of the scattered field; $|\mathbf{k}_p| = |\mathbf{k}_s| = k = \omega/c$ is the wave number; $a_{l(m)} = (-1)^{l(m)}(k^2 - \xi^2)^{1/2}$, where $l, m = 1, 2$; and $\xi = |\boldsymbol{\xi}| = (k_x^2 + k_y^2)^{1/2}$ are the vertical and horizontal components of the wave vectors of the incident and scattered fields, respectively. In this case, expressions (19) and (21) of paper [15] are applicable.

For a homogeneous half-space, the following obvious identity is valid:

$$V_1(z, \xi) = \exp(2j\alpha(\xi)z)V_1(0, \xi). \tag{1}$$

Here, $V_1(z, \xi)$ is the reflection coefficient at a depth z. By virtue of Eq. (1), expressions (19) and (21) of paper [15] can be rewritten in the form

$$\bar{T}_1(\boldsymbol{\xi}_s) - \int\limits_{R^2} T_2^1(\boldsymbol{\xi}_p, \boldsymbol{\xi}_s)V_1(z_0, \xi_p)\frac{\bar{T}_1(\boldsymbol{\xi}_p)}{\alpha(\xi_p)}d\xi_p = D_1^0(\boldsymbol{\xi}_s), \tag{2}$$

$$\bar{T}_2(\boldsymbol{\xi}_s) = \int\limits_{R^2} T_2^2(\boldsymbol{\xi}_p, \boldsymbol{\xi}_s)V_1(z_0, \xi_p)\frac{\bar{T}_1(\boldsymbol{\xi}_p)}{\alpha(\xi_p)}d\xi_p. \tag{3}$$

Here, z_0 is the z coordinate of the geometrical center of the radiator also serving as a scatterer. As it was shown in papers [15, 16], the effect of a boundary can be described by the following equivalent scheme: the initial opaque radiator is replaced with the sound-transparent radiator that generates the same primary field with DP $D_i^0(\boldsymbol{\xi})$, $i = 1, 2$, and the scattered field caused by the boundary is created by some secondary radiator. The DPs $\bar{D}_i^1(\boldsymbol{\xi})$ (here and below, the lower indices of all DPs have the same meaning as in the case of $D_i^0(\boldsymbol{\xi})$) of this radiator depend on the functions $\bar{T}_i(\boldsymbol{\xi})$ obtained as the solutions to the system of equations (2) and (3) and are related to them as follows:

$$\bar{D}_1^1(\boldsymbol{\xi}) = \bar{T}_1(\boldsymbol{\xi}) - D_1^0(\boldsymbol{\xi}), \quad \bar{D}_2^1(\boldsymbol{\xi}) = \bar{T}_2(\boldsymbol{\xi}). \tag{a}$$

The overbar in the functions $\bar{D}_i^1(\boldsymbol{\xi})$ and $\bar{T}_i(\boldsymbol{\xi})$ means that these quantities follow from the effect of the upper boundary; the upper index 1 of the functions $\bar{D}_i^1(\xi)$ means that the boundary takes part only once in the formation of these functions.

Expressions for the half-space $z \in (-\infty, H]$, $H > z_0 > 0$, in which case the boundary $z = H$ with a reflection coefficient $V_2(H, \xi)$ lies below the scatterer radiator, can be obtained in a manner similar to that used in [15]:

$$\underline{T}_2(\boldsymbol{\xi}_s) - \int\limits_{R^2} T_1^2(\boldsymbol{\xi}_p, \boldsymbol{\xi}_s)V_2(z_0, \xi_p)\frac{\underline{T}_2(\boldsymbol{\xi}_p)}{\alpha(\xi_p)}d\xi_p = D_2^0(\boldsymbol{\xi}_s), \tag{4}$$

$$\underline{T}_1(\boldsymbol{\xi}_s) = \int\limits_{R^2} T_1^1(\boldsymbol{\xi}_p, \boldsymbol{\xi}_s)V_2(z_0, \xi_p)\frac{\underline{T}_2(\boldsymbol{\xi}_p)}{\alpha(\xi_p)}d\xi_p. \tag{5}$$

The DPs $\underline{D}_i^1(\boldsymbol{\xi})$, $i = 1, 2$, of the secondary radiator whose action is governed by only the lower boundary are determined by the functions $\underline{T}_i(\boldsymbol{\xi})$ obtained as the solutions to the system of equations (4) and (5) and have the form similar to expressions (a):

$$\underline{D}_1^1(\boldsymbol{\xi}) = \underline{T}_1(\boldsymbol{\xi}), \quad \underline{D}_2^1(\boldsymbol{\xi}) = \underline{T}_2(\boldsymbol{\xi}) - D_2^0(\boldsymbol{\xi}). \tag{b}$$

The underline of these functions means that they depend on the lower boundary.

Thus, assuming that the DP of the radiator generating the primary field D^0, the scattering amplitude of the scatterer $T_m^l(\boldsymbol{\xi}_p, \boldsymbol{\xi}_s)$, and the geometry and reflection properties of the planar boundary are known, the DPs of the secondary radiator D^1 determining the field caused by the boundary can be found from integral equations (2)–(5) and expressions (a) and (b). We note that the domain of definition of the functions appearing in the integral equations (2)–(5) is $\boldsymbol{\xi} = (k_x, k_y) \in R^2$.

Consider now the situation in which the scatterer radiator is located in a planar layered waveguide of depth H and assume that the wave number varies with depth according to the formula

$$k(z) = \frac{\omega}{c(z)} = \begin{cases} k_1(z), & z \in [0, z_0 - h], \\ k_2(z), & z \in [z_0 + h, H], \\ k_0 = k_1(z_0 - h) = k_2(z_0 + h), \\ z \in (z_0 - h, z_0 + h). \end{cases} \tag{6}$$

Here, $2h$ is the parameter that exceeds or is equal to the vertical size of the scatterer radiator whose geometrical center is located at the point $(0, 0, z_0)$.

To solve the problem, we must consider two hypothetical half-spaces. The first of them has a boundary at $z = 0$, a reflection coefficient V_1, and a depth dependence of the wave number $k(z) = \begin{cases} k_1(z), & z \in [0, z_0 - h] \\ k_0, & z \in (z_0 - h, \infty) \end{cases}$. The second half-space has a boundary at $z = H$, a reflection coefficient V_2, and a depth dependence of the wave number $k(z) =$

$\begin{cases} k_0, & z \in (-\infty, z_0 + h) \\ k_2(z), & z \in [z_0 + h, H] \end{cases}$. In this case, Eqs. (2) and (3) remain valid for the first half-space and Eqs. (4) and (5) remain valid for the second half-space. It is known [18] that the reflection coefficients $V_1(z_0, \xi)$ and $V_2(z_0, \xi)$ appearing in these equations can be expressed in terms of the functions $Z_i(z, \xi)$, $i = 1, 2$, that are the solutions to the following problem:

$$(\partial^2/\partial\xi^2 + k^2(z) - \xi^2)Z_i(z, \xi) = 0, \quad i = 1, 2,$$

where $Z_1(z, \xi)$ satisfies the boundary condition at $z = 0$ and $Z_2(z, \xi)$ satisfies the boundary condition at $z = H$. The corresponding expressions have the form

$$V_i(z_0, \xi) = \frac{\alpha(z_0, \xi)Z_i(z_0, \xi) + (-1)^i j\partial Z_i(z_0, \xi)/\partial z}{\alpha(z_0, \xi)Z_i(z_0, \xi) + (-1)^{i-1} j\partial Z_i(z_0, \xi)/\partial z}, \quad i = 1, 2, \tag{7}$$

where $\alpha(z_0, \xi) = (k^2(z_0) - \xi^2)^{1/2}$.

Substituting V_1 and V_2 given by Eq. (7) into systems (2), (3) and (4), (5), respectively, one can obtain the DPs of secondary sources $\overline{D}_i^1$ and $\underline{D}_i^1$, $i = 1, 2$, determined by the single effects of the upper and lower boundaries of waveguide (6), respectively. Then, to obtain the combined directional pattern of the scatterer radiator, which is the sum of the initial DP of the radiator D_i^0 and the combined scattering amplitude of the opaque radiator D_i^s, $i = 1, 2$, formed due to a multiple action of inhomogeneities (boundaries and inclusions), we must use the procedure described in paper [16]. This procedure is as follows. The secondary radiator formed by a single action of the upper boundary with DP $\overline{D}^1$ (the lower index i is omitted for convenience) will cause the scattering by the real radiator; the scattered field will include the action of the lower boundary, which will create the secondary radiator with DP $\underline{D}^2$ (the index 2 means that boundaries acted two times in the formation of this secondary radiator, and the underline means that this secondary radiator was caused by the action of the lower boundary). The DP $\underline{D}^2$ can be obtained using Eqs. (4), (5), and (7). In this process, the right-hand side of integral equation (4) must be replaced with the function $\overline{D}_2^1$. In a similar way, the DP $\overline{D}^2$ of the secondary radiator accounting for the effect of the upper boundary and the presence of the secondary radiator with DP $\underline{D}^1$ can be calculated using Eqs. (2), (3), and (7) with the function $\underline{D}_1^1$ on the right-hand side of Eq. (2). The DPs of all secondary sources of higher orders can be found by a recurrent procedure. Schematically, the chains of successive secondary sources can be represented as follows:

$$D^0 \Rightarrow \begin{cases} \overline{D}^1 \Rightarrow \underline{D}^2 \Rightarrow \overline{D}^3 \Rightarrow \underline{D}^4 \Rightarrow \ldots \\ \underline{D}^1 \Rightarrow \overline{D}^2 \Rightarrow \underline{D}^3 \Rightarrow \overline{D}^4 \Rightarrow \ldots. \end{cases}$$

As was shown in paper [16], here, we deal with the formalism of accounting for all plane waves multiply reflected in the homogeneous layer Ω_0, including the waves generated by the primary field of the radiator and by all plane waves scattered by the source and multiply reflected from the boundaries of the layer Ω_0. Note that, geometrically, all secondary sources coincide with the initial radiator and generate the same field as the real radiator; the difference consists in the fact that they are transparent to sound.

Thus, the combined DP of the primary and scattered fields is given by the sum [16]

$$D = D^0 + D^1 + D^2 + \ldots \tag{8}$$

Here, the terms $D^1 = \overline{D}^1 + \underline{D}^1$, $D^2 = \overline{D}^2 + \underline{D}^2$, and so on can be found recursively from integral equations (2)–(5) and expressions (a) and (b). By physical considerations, series (8) always converges; however, one must estimate the error of replacing the series with a finite sum for each particular waveguide, scatterer radiator, frequency, and geometry of the problem. Paper [16] gives such estimators for the case of an ideal waveguide and a spherical scatterer.

In the case of a simple scatterer, i.e., when the primary wave is radiated by an external source, the problem is also reduced to the above scheme if the scatterer is located in the Fraunhofer zone of the source and normal waves existing in the layer where the scatterer resides can be represented as a set of quasi-plane waves. In this case, near the position of the scatterer, the primary field of homogeneous normal waves u_0 has the following asymptotic behavior

$$u_0 \approx (r)^{-1/2} \sum_{n=1}^{N} c_n \psi_n(z) \exp(j\xi_n r), \tag{9}$$

where $\psi_n(z)$ and ξ_n^2 are the eigenfunctions and eigenvalues of the problem $(\partial^2/\partial\xi^2 + k^2(z) - \xi^2)\psi(z, \xi) = 0$ with the corresponding boundary conditions at $z = 0$ and $z = H$, and c_n are the known coefficients depending on the depth and the DP of the source of primary waves. Let (r, φ, z_s) and $(0, z_0)$ be the coordinates of the geometrical centers of the scatterer and the source of primary field, respectively. By virtue of the assumption on the local homogeneity of the layer $\Omega_0 = \{x, y \in R^2, z \in [z_s - h, z_s + h]\}$, where $2h$ is the vertical size of the scatterer, we can write [14]

$$\psi_n(z) = a_n^+\exp(j\alpha_n(z_s)(z-z_s)) + a_n^-\exp(-j\alpha_n(z_s)(z-z_s)), \quad z\in[z_s-h, z_s+h], \tag{10}$$

where

$$a_n^{\pm} = \frac{1}{2j\alpha_n(z_s)}(j\alpha_n(z_s)\psi_n(z_s)\pm\psi'_{nz}(z_s)), \tag{11}$$

and $\alpha_n(z) = (k^2(z) - \xi_n^2)^{1/2}$. Assuming that the factor $\exp(j\xi_n r)$ adequately describes the horizontal component of the plane wave in the Fraunhofer zone near the scatterer and substituting Eqs. (10) and (11) into Eq. (9), we obtain

$$u_0 \approx \sum_{n=1}^{N}\frac{\exp(j\xi_n r)}{r^{1/2}}[b_n^+\exp(j(\mathbf{k}_n^+(\mathbf{R}-\mathbf{R}_s))) + b_n^-\exp(j(\mathbf{k}_n^-(\mathbf{R}-\mathbf{R}_s)))], \quad \mathbf{R}_s\in\Omega_0, \tag{12}$$

where $b_n^{\pm} = c_n a_n^{\pm}$; $\mathbf{k}_n^{\pm} = (\xi_n, \varphi, \pm\alpha(z_s))$ are the wave vectors of the field (9) incident on the scatterer, $\mathbf{R} = (x, y, z)$ is the position of the current point, $\mathbf{R}_s$ is the position of the geometrical center of the scatterer, and the coefficients c_n are determined in Eq. (9).

The sum of plane waves (12) causes a primarily scattered field with the scattering amplitude

$$D^0_{s^i}(\boldsymbol{\xi}_s) = \sum_{n=1}^{N}\frac{\exp(j\xi_n r)}{r^{1/2}} \times [b_n^+T_2^i(\boldsymbol{\xi}_n, \boldsymbol{\xi}_s, k_0) + b_n^-T_1^i(\boldsymbol{\xi}_n, \boldsymbol{\xi}_s, k_0)], \quad i = 1, 2. \tag{13}$$

Here, $\boldsymbol{\xi}_n = (\xi_n, \varphi)$ is the horizontal component of the wave vector of the incident wave, $\boldsymbol{\xi}_s = (\xi_s, \varphi_s)$ is the horizontal component of the wave vector of the scattered wave (the angle φ_s is measured relative to the geometrical center of the scatterer), the quantities with the index s are related to the scattered field, and the argument k_0 in the functions $T_m^i(\boldsymbol{\xi}_n, \boldsymbol{\xi}_s, k_0)$, $m = 1, 2$, means that these functions must be calculated for the homogeneous space with the wave vector k_0. We adhere to the notation used in the first problem for DPs in view of the fact that these problems are equivalent.

After determining the primary scattering amplitude (13), we can calculate the total scattering field by using the procedure described in the first part of the paper, in which the function $D^0_{s^i}(\boldsymbol{\xi}_s)$ given by Eq. (13) should replace the DP of the primary field D_i^0.

After we obtain either the resulting DP of the scatterer radiator D_i or the scattering amplitude of the passive scatterer D_{si}, we can calculate the field in the waveguide under consideration. For example, the field of normal waves has the form [17]

$$u'(r, \varphi, z) \approx \sqrt{\frac{2\pi}{r}}\sum_{n=1}^{N}\frac{D_1(\xi_n, \varphi)A^+(z', \xi_n) + D_2(\xi_n, \varphi)A^-(z', \xi_n)}{\alpha_n(z')N_n}\psi_n(z)\exp(j(\xi_n r - \pi/4))\xi_n^{1/2}, \tag{14}$$

where

$$A^{\pm}(z, \xi_n) = \psi_n(z)j\alpha_n(z)\pm\psi'_{nz}(z);$$

$$N_n = \psi_n(H)\frac{\partial}{\partial\xi}(\psi'_z(H, \xi) + g(\xi)\psi(H, \xi))_{\xi = \xi_n};$$

and $g(\xi)$ is the input admittance of the lower boundary. Expression (14) describes both the case of a scatterer radiator and the case of a passive scatterer. In the first case, the field u' in Eq. (14) is the primary field and D_i, $i = 1, 2$, is the combined DP, while in the second case, these quantities represent the scattered field and the combined scattering amplitude $D_i = D_{si}$, respectively. The parameter z' is the z coordinate of the geometrical center of the corresponding scatterer, and r is measured from this center. Note that the DP appearing in Eq. (14) is defined on a discrete set of points ξ_n, because this formula deals with the corresponding field of normal waves, and, consequently, the waveguide filtering properties manifest themselves.

It should be also noted that expression (14) is reduced to expressions derived earlier in papers [11, 13, 14] if we consider only the zero approximation for the scattering amplitude in the form of Eq. (13).

Remark. According to expressions (a) and (b), the calculation of the DPs for the secondary sources of scattered fields requires that the Fredholm integral equations of the second kind, i.e., Eqs. (2)–(5), be solved sequentially. The kernels of these integral equations remain the same for all iterations. As was shown in papers [15, 16], in the particular case of ideal boundaries and a spherical scatterer, these equations can be solved exactly, and the rate of convergence of series (8) can be estimated. However, in the general case of arbitrary waveguides and scatterers, these calculations require approximate methods, such as the methods described, for example, in paper [20]. For each particular waveguide, scatterer, and geometry of the scatterer location relative to the boundaries, this problem requires an independent study of possible assumptions to simplify the solution, the choice of an approximate method of solution, and the estimation of errors appearing in such a solution.

Thus, this paper suggests a method for estimating both the field of normal waves of an opaque radiator and the field scattered by an inhomogeneous inclusion located in the Fraunhofer zone of external sources on the basis of a unified approach. The decision about replacing series (8) by a finite sum requires estimating the residual sum of this series. An example of such an estimator was given earlier in paper [16]. Other examples of this type will be considered in the following papers.

REFERENCES

1. V. E. Belov, S. M. Gorskiĭ, A. Yu. Zinov’ev, and A. I. Khil’ko, Akust. Zh. **40**, 549 (1994) [Acoust. Phys. **40**, 485 (1994)].
2. J. C. Gaunaurd and H. Huang, J. Acoust. Soc. Am. **96**, 2526 (1994).
3. J. C. Gaunaurd and H. Haung, IEEE Trans. Ultrason. Ferroelectr. Freq. Control **43** (4), 690 (1996).
4. V. A. Eliseevnin and Yu. I. Tuzhilkin, Akust. Zh. **41**, 249 (1995) [Acoust. Phys. **41**, 214 (1995)].
5. A. Sarkissian, J. Acoust. Soc. Am. **102**, 825 (1997).
6. G. C. Bishop and J. Smith, J. Acoust. Soc. Am. **101**, 767 (1997).
7. G. C. Bishop and J. Smith, J. Acoust. Soc. Am. **105**, 130 (1999).
8. S. A. Yang, J. Acoust. Soc. Am. **105**, 93 (1999).
9. M. Ochmann, J. Acoust. Soc. Am. **105**, 2574 (1999).
10. G. Athanassoulis and A. Prospathopoulos, J. Acoust. Soc. Am. **107**, 2406 (2000).
11. V. M. Bel’kovich, V. A. Grigor’ev, B. G. Katsnel’son, and V. G. Petnikov, Akust. Zh. **48**, 162 (2002) [Acoust. Phys. **48**, 133 (2002)].
12. Yu. A. Kravtsov, V. M. Kuz’kin, and V. G. Petnikov, Akust. Zh. **30**, 339 (1984) [Sov. Phys. Acoust. **30**, 199 (1984)].
13. V. A. Grigor’ev, B. G. Kantsel’son, V. M. Kuz’kin, and V. G. Petnikov, Akust. Zh. **47**, 44 (2001) [Acoust. Phys. **47**, 35 (2001)].
14. V. M. Kuz’kin, Akust. Zh. **47**, 678 (2001) [Acoust. Phys. **47**, 591 (2001)].
15. A. V. Zatserkovnyĭ, V. A. Sergeev, and B. P. Sharfarets, Akust. Zh. **47**, 650 (2001) [Acoust. Phys. **47**, 565 (2001)].
16. B. P. Sharfarets, Akust. Zh. **48**, 547 (2002) [Acoust. Phys. **48**, 481 (2002)].
17. B. P. Sharfarets, Akust. Zh. **31**, 119 (1985) [Sov. Phys. Acoust. **31**, 68 (1985)].
18. L. M. Brekhovskikh, *Waves in Layered Media,* 2nd ed. (Nauka, Moscow, 1973; Academic, New York, 1980).
19. P. M. Morse and H. Feshbach, *Methods of Theoretical Physics* (McGraw-Hill, New York, 1953; Inostrannaya Literatura, Moscow, 1960), Vol. 2.
20. V. V. Ivanov, *Reference Book on Computer Methods of Calculations* (Naukova Dumka, Kiev, 1986).

Translated by A. Vinogradov

Acoustical Physics, Vol. 50, No. 1, 2004, pp. 112–113. Translated from Akusticheskiĭ Zhurnal, Vol. 50, No. 1, 2004, pp. 129–130.
Original Russian Text Copyright © 2004 by Konovalov, Kuz'menko.

SHORT COMMUNICATIONS

Effect of an Electric Load on the Duration of the Acoustic Pulse Radiated by a Piezoelectric Plate

S. I. Konovalov and A. G. Kuz'menko
St. Petersburg State Electrotechnical University, ul. Prof. Popova 5, St. Petersburg, 197376 Russia
e-mail: rot@post.etu.spb.ru

Received March 17, 2003

In a previous paper [1], we considered the possibility of producing a short electric pulse across a receiving piezoelectric plate through its excitation by a pulse of particle velocity when an electric *L*–*R* circuit is connected in parallel with the piezoelectric plate.

It is of interest to study the possibility of reducing the duration of an acoustic pulse radiated by a piezoelectric plate also by way of connecting an *L*–*R* circuit.

A schematic representation of the problem is shown in Fig. 1. An electric circuit consisting of *L* and *R* elements connected in series is, in its turn, connected in series with a piezoceramic plate. An electric pulse in the form of a half-period of a sinusoid at the antiresonant frequency of the piezoelectric plate is fed to the input of the circuit. The material of the plate is TsTSNV-1 ceramics. On one side, the plate borders air, and on the other side, it is loaded with a liquid (water).

This system can be characterized by the following parameters:

$\Omega = 1/\sqrt{LC_0}$; $n = \Omega/\omega_0$; and $Q = \omega_0 L/R$, where C_0 is the electric capacitance of the repressed piezoelectric plate and ω_0 is the angular antiresonant frequency of the piezoelectric plate. The problem consists in determining the optimum values of the parameters *Q* and *n* at which the duration of the resulting pulse of particle velocity is minimum. The pulse duration is taken as the time interval from the beginning of the pulse to the moment the signal level is reduced by 20 dB from the maximum amplitude, i.e., to 0.1 of the latter. For convenience, we measure the time in relative units $T = 2t/T_0$, where T_0 is the period of oscillations at the frequency ω_0. The procedure used for calculating the form of the particle velocity pulse is similar that used for a piezoelectric receiver. It is based on the use of an equivalent electric circuit and a Fourier transform. The calculation of the pulsed processes was carried out by a PC. The results of the calculations are as follows.

Figure 2 shows the dependences of the duration of the particle velocity pulse on the parameter *n* for different values of parameter *Q*: *Q* = (*1*) 3, (*2*) 2, (*3*) 1.5, and (*4*) 1. One can see that the optimum values are *Q* = 1.5 and *n* = 1.15, The corresponding pulse duration is $\tau_p = 5.5$.

Figure 3 presents the dependences of the maximum amplitude of the particle velocity pulse v_{max} (in relative

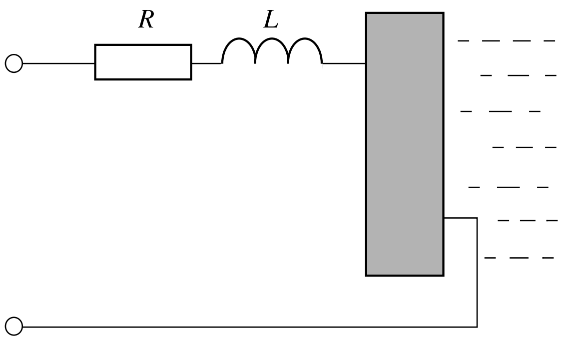

Fig. 1.

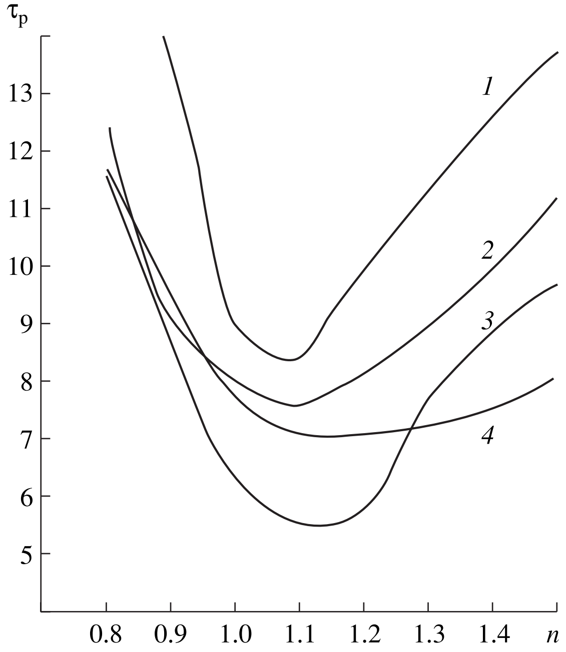

Fig. 2.

1063-7710/04/5001-0112$26.00 © 2004 MAIK "Nauka/Interperiodica"

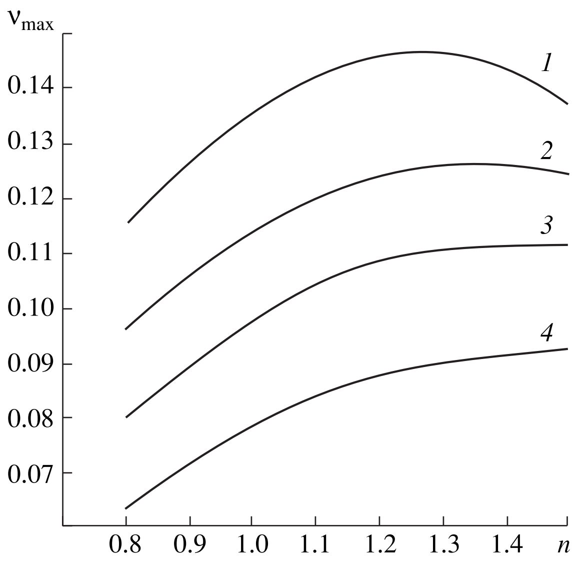

Fig. 3.

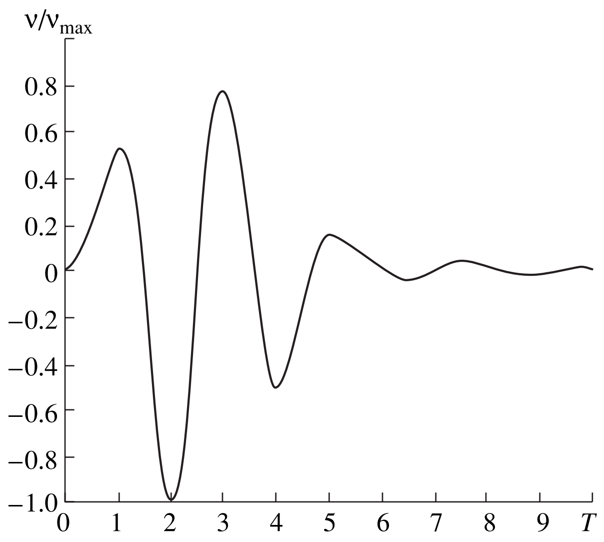

Fig. 4.

units) on the parameter *n*. The dependences correspond to the values of maximum amplitudes of particle velocity in the pulse within a constant factor. The numbering of curves is the same as in Fig. 2. From these data it follows that, for the optimal values of *Q* and *n*, the signal amplitude versus *n* practically reaches its maximum (curve *3*).

Figure 4 displays the form of the pulse of particle velocity normalized to unity, $v/v_{\max}$, for the optimal values of parameters *Q* and *n*.

For comparison, one should note that the duration of a pulse produced by a plate without electric load exceeds 20 half-periods with a maximum signal amplitude of $v_{\max} = 0.164$. In the presence of an optimal electric load, the pulse duration is 5.5 half-periods, which is about four times smaller. The corresponding pulse amplitude is $v_{\max} = 0.108$, i.e., it decreases by a factor of 1.5.

Thus, by means of calculation, the optimal values are determined for the parameters of the electric load, the use of which allows one to considerably reduce the duration of the acoustic pulse radiated by the piezoelectric plate.

REFERENCES

1. S. I. Konovalov and A. G. Kuz'menko, Akust. Zh. **47**, 856 (2001) [Acoust. Phys. **47**, 758 (2001)].

Translated by A. Svechnikov

Acoustical Physics, Vol. 50, No. 1, 2004, pp. 20–29. Translated from Akusticheskiĭ Zhurnal, Vol. 50, No. 1, 2004, pp. 26–36.
Original Russian Text Copyright © 2004 by Virovlyansky, Kazarova, Lyubavin.

Variations of Mode Amplitudes in a Range-Dependent Waveguide

A. L. Virovlyansky, A. Yu. Kazarova, and L. Ya. Lyubavin

Institute of Applied Physics, Russian Academy of Sciences,
ul. Ul'yanova 46, Nizhni Novgorod, 603600 Russia

e-mail: viro@hydro.sci-nnov.ru

Received November 25, 2002

Abstract—The ray method of calculating the mode amplitudes is used to analyze the sound fields in deep-water acoustic waveguides with two types of inhomogeneities of the refractive index: (i) weak inhomogeneities that cause small perturbations of ray trajectories and (ii) strong inhomogeneities with large spatial scales. Simple analytical relations are derived for describing the variations of the mode structure of the sound field in the presence of the aforementioned inhomogeneities. A new criterion defining the validity of the adiabatic approximation is formulated. To illustrate and test the results obtained, a numerical simulation of the sound fields is performed on the basis of the parabolic equation method. *© 2004 MAIK "Nauka/Interperiodica".*

1. INTRODUCTION

One of the factors that restricts the application of the normal-wave method to analyzing the sound fields in range-dependent waveguides is the complexity of the equations describing the dynamics of mode amplitudes [1–5]. In spite of the existence of high-accuracy and high-speed computer codes for sound field calculations by the coupled mode method (see, e.g., [6–8]), the development of approximate analytic approaches, which allow one to find the relation between the variations of the mode structure of a sound field and the changes in the parameters of the medium that cause such variations, is still topical. Earlier [9], we showed that, in the high-frequency approximation, the mode amplitudes can be surprisingly simply expressed in terms of the solutions of ray equations (similar results can be found in [10–14]). In other words, an analog of geometrical optics exists for the modes.

In this paper, the results of the previous study [9] are applied to the analysis of mode interaction, that is, to the energy redistribution between the modes in an inhomogeneous waveguide. Here, we consider two problems that often arise in practical applications. In both cases, to simplify the consideration, we restrict it to analyzing the waves in a range-dependent refractive waveguide. However, the results obtained can be extended to a waveguide with a rough boundary.

The first problem is concerned with the effect of weak inhomogeneities of the refractive index. In geometrical optics, this effect is taken into account by introducing corrections to the ray phases (eikonals) [1, 15, 16]. Thereby, the complex amplitude of a ray acquires an additional phase factor. Similar phase factors also appear in our "ray" equations for the mode amplitudes. It appears that even weak inhomogeneities can lead to a substantial redistribution of energy between the modes.

The second problem considered here is that of describing the field in a waveguide in terms of an approximation close to adiabatic. In such a waveguide, the longitudinal scale of the refractive index variations are comparable with the length of the ray cycle. The main result of considering this problem is a relatively simple formula expressing the validity criterion for the adiabatic approximation. The criterion obtained agrees with the well-known requirement of the smallness of variations in the parameters of the medium within the ray cycle and with the statement that the accuracy of the adiabatic approximation improves as the frequency becomes lower [2]. At the same time, our formula allows one to take into account the accumulation of errors with distance and to estimate the ultimate distances at which the adiabatic approximation is still valid.

All the results are obtained in the parabolic equation approximation, although they can be easily generalized to the case when the field is defined by the Helmholtz equation. The use of the parabolic equation is caused by the fact that, unlike the Helmholtz equation, it can be readily solved numerically, even for a range-dependent waveguide. A number of efficient computer codes exists to solve the parabolic equation. We uses one of these codes (called MMPE [17]) for a numerical simulation. The objective of the simulation was to illustrate the results obtained and to test the accuracy of our formulas.

1063-7710/04/5001-0020$26.00 © 2004 MAIK "Nauka/Interperiodica"

2. RAY AND MODE REPRESENTATIONS OF THE FIELD IN A RANGE-DEPENDENT WAVEGUIDE

Let us neglect the horizontal refraction and consider a model medium in which sound speed depends on nothing but depth z and distance r. In the small-angle approximation, the complex amplitude $u(r, z)$ of a monochromatic wave field is defined by the parabolic equation [1, 18]

$$2ik\frac{\partial u}{\partial r} + \frac{\partial^2 u}{\partial z^2} - 2k^2 U(r, z)u = 0, \tag{1}$$

$$U(r, z) = \frac{1}{2}(1 - n^2(r, z)), \tag{2}$$

where $n(r, z) = c_0/c(r, z)$ is the refractive index, c_0 is a constant, $k = 2\pi f/c_0$ is the wave number, and f is the carrier frequency.

2.1. Ray Representation of the Field

In the approximation of geometrical optics, the solution to Eq. (1) is represented in the form [1, 19, 20]

$$u = \sum_\nu A_\nu e^{ikS_\nu - i\mu_\nu \pi/2}, \tag{3}$$

where A and S are the amplitude and eikonal of the ray, respectively, and μ is the number of caustics touched by the ray. To describe the ray structure of the field, let us use the Hamiltonian formalism in which the ray trajectory is similar to the trajectory of a particle in classical mechanics and the longitudinal coordinate r is the analog of time. The analog of the mechanical momentum is the quantity $p = \mathrm{d}z/\mathrm{d}r = \tan\chi$, where χ is the grazing angle. The Hamiltonian is defined by the expression [20]

$$H = \frac{p^2}{2} + U(r, z). \tag{4}$$

The Hamilton equations

$$\frac{\mathrm{d}z}{\mathrm{d}r} = \frac{\partial H}{\partial p}, \quad \frac{\mathrm{d}p}{\mathrm{d}r} = -\frac{\partial H}{\partial z}, \tag{5}$$

that govern the motion of a mechanical particle [21] are ray equations in our case. The eikonal S, which is an analog of the mechanical action, is expressed as

$$S = \int(p\mathrm{d}z - H\mathrm{d}x), \tag{6}$$

where integration is performed along the ray trajectory (Eq. (6) expresses the solution to the system of equations (5)).

The analysis of the relation between rays and modes is considerably simplified if one uses canonical action–angle variables (I, θ), which can be defined in accordance with [21]. The action variable is expressed by the integral

$$I = \frac{1}{2\pi}\oint p\mathrm{d}z = \frac{1}{\pi}\int_{z_{\min}}^{z_{\max}} dz\sqrt{2(H - U(r, z))} \tag{7}$$

over the cycle of ray oscillations in the so-called reference waveguide, that is, in a conceptional range-independent waveguide whose cross section at the given distance r coincides with that of the actual waveguide (for each distance, there is an individual reference waveguide). The quantities $z_{\min}$ and $z_{\max}$ are the roots of the equation $U(r, z) = H$ that define the turning horizons of the ray trajectory in the reference waveguide. Actually, Eq. (7) defines H as a function of I and r. The canonical transformation that relates the momentum–coordinate (p, z) and action–angle (I, θ) variables are determined by the relation [21]

$$\mathrm{d}S = p\mathrm{d}z - H\mathrm{d}r = \mathrm{d}G - \theta\mathrm{d}I - H_1\mathrm{d}r \tag{8}$$

with a generating function $G(I, z, r)$ of the form

$$G(I, z, r) = \begin{cases} g(I, z, r), & p > 0 \\ 2\pi I - g(I, z, r), & p < 0, \end{cases} \tag{9}$$

where

$$g(I, z, r) = \int_{z_{\min}}^{z} \mathrm{d}z\sqrt{2[H(I, r) - U(z, r)]}. \tag{10}$$

Relation (8) yields two equations that define the relation between (p, z) and (I, θ),

$$p = \frac{\partial G}{\partial z}, \quad \theta = \frac{\partial G}{\partial I} \tag{11}$$

along with the expression for the Hamiltonian in action–angle coordinates

$$H_1(I, \theta, r) = H(I, r) + \Lambda(I, \theta, r), \tag{12}$$

where

$$\Lambda(I, \theta, r) = \left.\frac{\partial G(I, z, r)}{\partial r}\right|_{z = z(I, \theta, r)}. \tag{13}$$

Now, the Hamilton equations take the form

$$\frac{\mathrm{d}I}{\mathrm{d}r} = -\frac{\partial \Lambda}{\partial \theta}, \quad \frac{\mathrm{d}\theta}{\mathrm{d}r} = \omega(I, r) + \frac{\partial \Lambda}{\partial I}, \tag{14}$$

where

$$\omega(I, r) = \frac{\partial H(I, r)}{\partial I} \tag{15}$$

is the angular frequency of the spatial oscillations for the ray with the action variable I in the reference waveguide.

According to Eqs. (9)–(11), the angular variable θ falls into the interval from 0 to 2π. Performing the integration in Eq. (8), in view of the fact that the combination $G - I\theta$ goes to zero at the points where θ abruptly changes from 0 to 2π, we obtain

$$S = \int (I\mathrm{d}\theta - H\mathrm{d}r - \Lambda \mathrm{d}r) \\ - G(z_s, I_s, 0) + G(z_e, I_e, r) + \theta_s I_s - \theta_e I_e. \qquad (16)$$

Here and below, the subscripts s and e denote the ray parameters at the beginning and the end of the trajectory, respectively.

To make the quantity θ continuous, we, as usual, increase its value by 2π at the beginning of each new cycle. In accordance with the generating function accepted, each cycle of the trajectory joints its two sequential minima. Then, the quantities p, z, Λ, and G will become periodic functions of the continuous variable θ with a period of 2π. Expression (16) for the eikonal will still be valid, but θ_e will be equal to the residue of the division of θ by 2π at the end of the trajectory.

2.2. *Mode Representation for the Field*

Let us represent the field in the form of expansion [1, 2]

$$u(r, z) = \sum_m B_m(r)\varphi_m(r, z), \qquad (17)$$

where $\varphi_m(z, r)$ is the eigenfunction of the mth mode of the reference waveguide (the local mode) at a point r. In the WKB approximation, this function, between its turning points, is equal to

$$\varphi_m = \varphi_m^+ + \varphi_m^-, \qquad (18)$$

where

$$\varphi_m^{\pm}(z, r) = \sqrt{\frac{H_m}{p_m D_m}} e^{ik(\sigma g(I_m, z, r) - \pi/4)}, \qquad (19)$$

$$p_m = \sqrt{2(H(I_m, r) - U(r, z))}, \qquad (20)$$

$H_m = H(I_m, r)$, and $D_m = 2\pi/\omega(I_m, r)$. The quantity I_m denotes the action variable corresponding to the mth mode. Its value is determined by the quantization rule

$$kI_m = m + \frac{1}{2}. \qquad (21)$$

In [9] (see also [12–14]), it is shown that the mode amplitude can be approximately expressed through the so-called mode rays that obey the equation

$$I = I_m. \qquad (22)$$

Condition (22) defines the rays whose action variables are equal to the action variable I_m of the mode at a distance r. The contribution of a single mode ray is given by the expression

$$\delta B_m = \frac{1}{\sqrt{2\pi i \left|\frac{\partial I}{\partial p_s}\right|}} \exp[i\Phi], \qquad (23)$$

where

$$\Phi = k(S + \sigma g) + (\gamma - 2\mu - \sigma)\pi/4. \qquad (24)$$

Here, the functions S and g are defined by Eqs. (6) and (10) and calculated for the mode ray;

$$\sigma = -\mathrm{sgn}(p_e), \quad \gamma = -\sigma \,\mathrm{sgn}(I_{p_s})\,\mathrm{sgn}(z_{p_s}),$$

p_s and p_e are the initial and terminal values of the momentum of the mode ray, respectively; and μ is the number of points at which the mode ray touches the caustics. The function $\mathrm{sgn}(x)$ determines the sign of the corresponding argument. The calculation of the mode amplitude is completed by summing the contributions of all mode rays.

Note that the derivative appearing in the denominator of Eq. (23) can go to zero. At the corresponding points of the waveguide, the formula obtained fails. The set of such points is the analog of the ray caustic for modes (this fact was analyzed in [14] in more detail).

3. ANALYTICAL DESCRIPTION OF MODE INTERACTION

In a range-independent waveguide, the energy of each mode is conserved, and the mode amplitudes, to the accuracy of a phase factor, are independent of the distance. For a point source at the depth z_s, we have

$$B_m(r) = \varphi_m(z_s) e^{-ikH(I_m)r}. \qquad (25)$$

In an inhomogeneous waveguide, the modes interact, that is, the sound energy is transferred from one mode to another. Such an energy redistribution makes both phases and amplitudes of factors B_m functions of the distance.

3.1. *Weak Inhomogeneities*

Let the refractive index be equal to

$$n(z, r) = n_0(z) + \delta n(z, r), \qquad (26)$$

where $n_0(z)$ is the unperturbed profile and δn is the perturbation. The smallness of δn allows one to develop a very simple perturbation theory for rays. In the first approximation, the change in the ray trajectory can be neglected, and the eikonal variations are described by the well-known simple formula [1, 15, 16]:

$$\delta S = \int \delta n \mathrm{d}r, \qquad (27)$$

where the integration is performed along the unperturbed ray. By applying this formula to mode rays, we arrive at the following expression for the mode amplitude:

$$B_m(r) = (\varphi_m^-(z_s)e^{i\delta\Phi_m^+} + \varphi_m^+(z_s)e^{i\delta\Phi_m^-})e^{-ikH(I_m)r}, \quad (28)$$

where the additional term for the mode rays,

$$\delta\Phi_m^{\pm} = k\int\limits_{\Gamma_m^{\pm}} \delta n \mathrm{d}r \quad (29)$$

is calculated by integrating along the unperturbed ray trajectories Γ_m^+ and Γ_m^-. The superscripts "+" and "–" indicate the signs of the launch angles at the sound source. In [10, 11], Eq. (28) was obtained in another way. At $\delta n = 0$, this formula takes the form of Eq. (25).

The validity conditions for Eq. (28) actually coincide with those for the analogous ray formulas [9–11]. Therefore, here we only note that, in spite of the requirement of smallness of δn, Eq. (28) can describe the situation in which the value of $\delta\Phi_m^{\pm}$ is greater than π. With such phase shifts, the fluctuations of the mode amplitudes can be substantial (the example is presented in Section 4.1).

3.2. Adiabatic Approximation

In a so-called adiabatic waveguide, where the sound speed varies so smoothly that the action variable is conserved along each ray, no energy redistribution occurs between the modes [1, 2]. In such a waveguide, the mode amplitude can be described by Eq. (25) in a generalized form

$$B_m(r) = \varphi_m(z_s)\exp\left[-ik\int\limits_0^r H(I_m, r')\mathrm{d}r'\right]. \quad (30)$$

Of course, this well-known result can be also obtained from Eq. (23). Omitting simple but somewhat tedious calculations, we emphasize the only fact that, just as in the range-independent waveguide, a mode of the adiabatic waveguide is formed by the contributions of two mode rays with launch angles that are equal in their absolute values and opposite in their signs.

3.3. Perturbation Theory for the Eikonal of a Mode Ray

Let us consider a smoothly varying inhomogeneous waveguide in which the action variable does not remain strictly constant but weakly varies with distance. To estimate the effect of the nonadiabaticity on the mode amplitudes, let us compare the actual eikonal of the mode ray with the eikonal calculated in the adiabatic approximation, that is, with neglecting the summand Λ in Hamiltonian (12) and in all subsequent formulas. We consider an adiabatic mode ray (calculated in the adiabatic approximation) and an actual mode ray that correspond to the *m*th mode. The trajectories of these rays are assumed to be close to each other, and the values of integer constants σ, γ, and μ, which are determined by the topology of the trajectories, are supposed to be the same for both rays. According to Eq. (24), our problem is reduced to the comparison of the quantities $S + \sigma g$ for the adiabatic and actual rays. In view of Eqs. (14)–(24), for the nonadiabatic ray we obtain

$$S + \sigma g = S_1 + S_2 + S_3, \quad (31)$$

where

$$S_1 = \int(I\omega(I, r) - H(I, r))dr, \quad (32)$$

$$S_2 = \int(I\partial\Lambda/\partial I - \Lambda)dr, \quad (33)$$

$$\begin{aligned} S_3 = & -G(z_s, I_s, 0) + G(z_e, I_m, r) \\ & + \theta_s I_s - \theta_e I_m + \sigma g(z_e, I_m, r). \end{aligned} \quad (34)$$

In the latter expression, we used the fact that, in the nonadiabatic waveguide, the action variable of the mode ray is equal to I_m at the trajectory end in accordance with Eq. (22). The closeness to the adiabatic approximation is caused by the smallness of the perturbation of the quantity Λ. Formally, let us assume that this quantity is proportional to a small dimensionless parameter ε. In the adiabatic approximation, $\varepsilon = 0$ (and, hence, $S_2 = 0$), and I_s and I should be replaced by I_m in Eqs. (32) and (34).

By expressing I in the form of $I_m + \delta I$, where $\delta I = O(\varepsilon)$, to an accuracy of $O(\varepsilon^2)$, we obtain the following expression for the deviation S_1 from its adiabatic value:

$$\delta S_1 = \int\left[I_m\omega_m'\delta I + \frac{1}{2}(\omega_m' + I_m\omega_m'')\delta I^2\right]\mathrm{d}r. \quad (35)$$

The prime in ω denotes the derivative with respect to I, and the subscript m means that the corresponding derivative is taken at $I = I_m$. Let us use the relation

$$\int\mathrm{d}\theta = -\theta_s + \theta_e + 2\pi N, \quad (36)$$

where N is the number of cycles in the trajectory. In view of the second equation of Eqs. (14), we replace $\mathrm{d}\theta$ by $(\omega(I, r) + \partial\Lambda/\partial I)\mathrm{d}r$. Then, we obtain

$$-\delta\theta_s + \delta\theta_e = \int\left(\omega_m'\delta I + \frac{1}{2}\omega_m''\delta I^2 + \Lambda\right)\mathrm{d}r, \quad (37)$$

where $\delta\theta_s$ and $\delta\theta_e$ are the differences in the initial and terminal values of the angular variables for the rays being compared. Using Eq. (11), we estimate the difference in the values of S_3:

$$\delta S_3 = (\delta\theta_s - \delta\theta_e)I_m. \quad (38)$$

From Eqs. (31)–(38), it follows that

$$\delta(S + \sigma g) = \frac{\omega_m'}{2}\int\delta I^2 dr + \int(I\partial\Lambda/\partial I - \Lambda)dr. \quad (39)$$

By retaining only the terms of the order of O(ε), we arrive at the estimate for the difference in the eikonals of the adiabatic and actual mode rays:

$$\delta\Phi = -k\int \Lambda \mathrm{d}r. \tag{40}$$

3.4. Validity Criterion for the Adiabatic Approximation

We assume that the value of Λ is so small that $|\delta I| \ll I_m$. In this case, the dependence of the action variable on the initial instant of time must be nearly the same as in the adiabatic approximation. Therefore, the deviations from the adiabatic approximation manifest themselves primarily in “nonadiabatic” variations of the eikonals of mode rays. The validity condition for the adiabatic approximation is the inequality

$$|\delta\Phi| = \left|k\int \Lambda \mathrm{d}r\right| \ll \pi. \tag{41}$$

To simplify the use of this criterion, let us transform the integral appearing in Eqs. (40) and (41). In view of Eqs. (9) and (10), the derivative determining the quantity Λ (see Eq. (13)) can be represented in the form

$$\frac{\partial}{\partial r}G(I, z, r) = \int_{z_{\min}}^{z}\left(\frac{\partial H(I, r)}{\partial r} - \frac{\partial U(r, z)}{\partial r}\right) \times \frac{\mathrm{d}z}{\sqrt{2[H(I, r) - U(r, z)]}}. \tag{42}$$

By using Eq. (7), one can easily show that

$$\frac{\partial H(I, r)}{\partial r} = \frac{2}{D}\int_{z_{\min}}^{z}\frac{\partial U(r, z)}{\partial r}\frac{\mathrm{d}z}{\sqrt{2[H(I, r) - U(r, z)]}}. \tag{43}$$

Let us introduce the function

$$D(z, I, r) = \int_{z_{\min}}^{z}\frac{\mathrm{d}z}{\sqrt{2[H(I, r) - U(r, z)]}}. \tag{44}$$

It expresses the length of the trajectory fraction at which $p > 0$ in the reference waveguide; this trajectory connects the point of the minimum with the nearest point of the ray, which has the coordinate z. By combining Eqs. (42)–(44), we obtain

$$\frac{\partial}{\partial r}G(I, z, r) = \frac{2D(z, I)}{D}\int_{z_{\min}}^{z_{\max}}\frac{\partial U(r, z)}{\partial r} \times \frac{\mathrm{d}z}{\sqrt{2[H(I, r) - U(r, z)]}} - \int_{z_{\min}}^{z}\frac{\partial U(r, z)}{\partial r}\frac{\mathrm{d}z}{\sqrt{2[H(I, r) - U(r, z)]}}. \tag{45}$$

The right-hand side of this expression, which defines Λ, can be formally treated as a sum of two integrals along the ray with a given action variable I and with $p > 0$ in the reference waveguide. The factor $dz/\sqrt{2[H(I, r) - U(r, z)]}$ represents the element of distance in this conceptional waveguide. Because we consider a waveguide that is close to the adiabatic one, its parameters weakly vary within a single ray cycle, and the integration over the ray cycle in the reference waveguide can be approximately substituted by integration along the actual ray.

Let us consider the ith cycle of the trajectory that begins at the distance r_i. On the first half-cycle, where $p > 0$, Eq. (45) can be represented as

$$\left.\frac{\partial}{\partial r}G(I, z, r)\right|_{z = z(r)} = \frac{2\rho}{D}\int_0^{D/2} U_r(r_i + \rho)\mathrm{d}\rho - \int_0^{\rho} U_r(r_i + \rho)\mathrm{d}\rho, \tag{46}$$

where $z(r)$ is the trajectory of the mode ray and

$$U_r(r) \equiv \left.\frac{\partial}{\partial r}U(I, z, r)\right|_{z = z(r)}. \tag{47}$$

Expression (46) representing Λ at the corresponding point of the mode ray can be integrated over this half-cycle to yield

$$\int_0^{D/2}\mathrm{d}r\Lambda = \int_0^{D/2}\left(\rho - \frac{D}{4}\right)U_r(r_i + \rho)\mathrm{d}\rho. \tag{48}$$

This result can be obviously modified for the half-cycle with $p < 0$. As a result, we find that integral (40) over the ith ray cycle is approximately equal to

$$\delta\Phi_i = -k\int_0^{D/2}\left(\rho - \frac{D}{4}\right)\left.\frac{\partial U(r, z(r))}{\partial r}\right|_{r = r_i + \rho}\mathrm{d}\rho + k\int_{D/2}^{D}\left(\rho - \frac{3D}{4}\right)\left.\frac{\partial U(r, z(r))}{\partial r}\right|_{r = r_i + \rho}\mathrm{d}\rho. \tag{49}$$

In integrating over the incomplete first and last cycles of the trajectory, the integration limits in Eq. (49) should be changed in an evident way. To find the value of δΦ, one should combine the contributions of all cycles.

Formula (49) is useful to analyze the validity of the adiabatic approximation in specific applications. The integrals appearing in this formula can be easily calculated by using an ordinary ray computer code. In this case, it is unnecessary to find the rays exactly obeying condition (22). Actually, we speak of smoothly varying waveguides in which ray trajectories exhibit a regular behavior, and, if condition (41) is met for some ray, it will be also met for other rays with close launch angles at the sound source. Therefore, it is sufficient to consider a set of rays with the launch angles within the angular interval that is determined by the spread of launch angles of the mode rays. For the *m*th mode, the validity of the adiabatic approximation will be determined by the values of $\delta\Phi$ for the rays whose action variables are close to I_m at the end point of the trajectory.

3.5. Comparison with Other Criteria

The validity condition for the adiabatic approximation is usually formulated as the inequality [1]

$$D/L \ll 1, \tag{50}$$

which expresses the requirement of smallness of the cycle length D relative to the horizontal scale L of variations in the parameters of the medium. More accurate criteria are presented in monograph [5] (see also [24]) for waveguides of different types. In particular, in this monograph, the following inequality is given as a condition taking into account the frequency dependence:

$$kD^2/L \ll 1. \tag{51}$$

Conditions (50) and (51), along with similar ones, are obtained by estimating the terms of equations for mode amplitudes [1, 5], which are rejected when passing to the adiabatic approximation. Being necessary, these conditions, however, do not allow one to estimate the validity limits of the approximation in distance. It is obvious that, at very long ranges, the adiabatic approximation will sooner or later become invalid, even if conditions (50) and (51) are met.

Our method of estimating the validity limits for the adiabatic approximation is based on the available (though approximate) solution to the mode coupling equation. This allows one to look at the problem from a new point of view, and, particularly, to obtain an estimate that takes into account the accumulation of errors with distance. Our criterion is somewhat more complicated than conditions (50) and (51). However, the integrals in Eq. (49) can be easily calculated with a standard ray computer code. The action–angle variables used in the derivation of our formulas could require additional effort for their calculation, but they do not appear in the final expressions.

Note that conditions (50) and (51) agree well with our requirement $|\delta\Phi| \ll 1$, where $\delta\Phi$ is defined by Eq. (49). If we consider the increment $\delta\Phi$ in a single cycle of oscillations, we can see that, according to Eq. (49), this increment will be equal to zero if the quantity $\partial U/\partial r$ is constant, and, hence, it is determined by the variations of $\partial U/\partial r$ along the ray. For distances $0 \le \rho \le D/2$, we can roughly approximate the half-cycle of the ray trajectory by a straight-line segment: $z = 4\Delta z(\rho - D/4)/D$, where Δz is the amplitude of trajectory oscillations. The range-dependent part of the derivative $\partial U(r, z)/\partial r$ can be estimated as $U_1 z/(Lh)$, where U_1 and h are the characteristic value of U and the vertical scale of variations of this function, respectively. According to Eq. (49), we obtain $\delta\Phi \sim (U_1\Delta z/h)kD^2/L$. If the number of the trajectory cycles is not large, this relation leads to a less strict version of inequality (51): $U_1\Delta z/h \ll 1$ in practice.

4. NUMERICAL SIMULATION

To illustrate and test the results obtained, we performed the calculation of the sound field of a tone source in a miltimode waveguide. We used the MMPE computer code [17] developed to solve a wide-angle parabolic equation. For solving our standard parabolic equation (1), this code was slightly modified. The sound field was expanded into normal waves calculated with the use of the WAN code [22]. The sound speed field was represented by an unperturbed profile $c(z)$ to which a perturbation $\delta c(r, z)$ associated with the mode interaction was added. As $c(z)$, we chose Munk's profile [1, 16]

$$c(z) = c_0(1 + \varepsilon(e^{2(z-z_a)/B} - 2(z-z_a)/B - 1)), \tag{52}$$

where c_0 = 1.5 km/s, B = 1 km, z_a = –1 km, and ε = 0.0058. In the examples presented below, the sound source is at a point $(0, z_a)$, that is, on the axis of the unperturbed waveguide, and the frequency is 200 Hz. We restricted our simulation to studying the amplitudes of 100 initial propagating modes. Their turning points lie in the water bulk.

4.1. Mode Scattering by Small Inhomogeneities

Figure 1 shows the mode rays for every fifth mode of 100 initial ones. As was mentioned above, for each mode there are two rays whose launch angles are equal in their absolute values and opposite in sign. The absolute values of the launch angles are greater for modes of higher numbers.

Let us consider a small inhomogeneity of the sound speed field in the form

$$\delta c(r, z) = c_1 \exp\left(-\frac{(r-r_1)^2}{\delta r^2} - \frac{(z-z_1)^2}{\delta z^2}\right), \tag{53}$$

where c_1 = –0.001 km/s, δr = 2 km, and δz = 0.1 km. The isograms of $\delta c(r, z)$ are ellipses with centers at points (r_1, z_1). Let us consider two positions of the given inhomogeneity in the waveguide; they are indicated by numbers *1* (r_1 = 35 km, z_1 = –2.4 km) and *2* (r_1 = 22 km, z_1 = –0.6 km) in Fig. 1. In both cases, the area occupied by the inhomogeneity is shown as an ellipse corresponding to the value of δ that is e times smaller than c_1.

Let us begin with the situation when the inhomogeneity is in position *1*. According to Eqs. (28) and (29), the effect of the inhomogeneity on the mode amplitudes

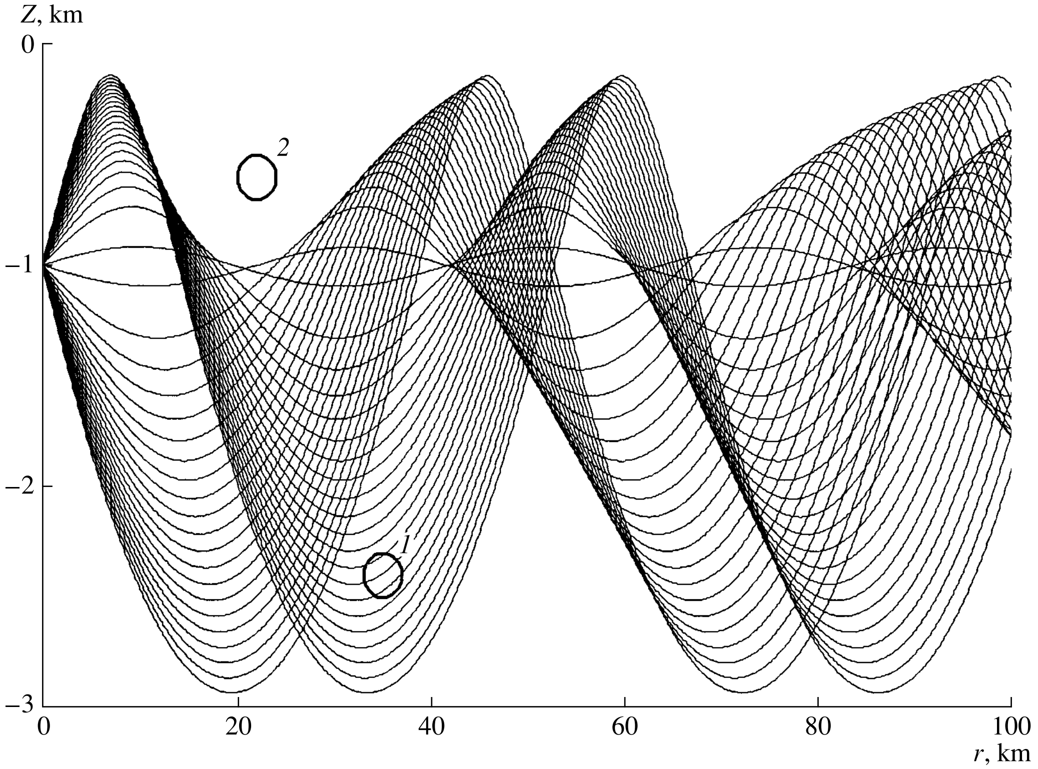

Fig. 1. Trajectories of the mode rays in a waveguide with the canonical sound speed profile (Munk's profile) for each fifth mode of the 100 initial ones. Ellipses *1* and *2* indicate the waveguide regions where the refractive index inhomogeneities were placed.

is determined by the additional phase shifts along the mode rays, $\delta\Phi_m^{\pm}$. In the example at hand, $|\delta\Phi_m^{\pm}| \ll \pi$ for most mode rays. The exceptions are the rays that either cross the aforementioned ellipse or pass in the vicinity of it. All these rays have negative launch angles at the source. Therefore, all $\delta\Phi_m^{\pm} = 0$, and the additional phase factor appearing in Eq. (28) can differ from unity for only one of the terms in parentheses. If $\delta\Phi_m^{-}$ is of the order of π, one can expect a considerable increase in the amplitude of the *m*th mode. At the top of Fig. 2, the variations in mode amplitudes are shown in the presence of the inhomogeneity (on average, the unperturbed values of $|B_m|$ are about 1 $\text{km}^{-1/2}$). At the bottom of Fig. 2, the dependence of $\delta\Phi_m^{-}$ on the mode number is shown. It can be seen that both the values of $\delta\Phi_m^{-}$ and the amplitude variations are especially high for the modes whose numbers fall in the interval $50 < m < 70$. The corresponding mode rays pass in the closest vicinity of the inhomogeneity center.

If the inhomogeneity is in position *2*, none of the mode rays shown in Fig. 2 crosses it. In this case, the inhomogeneity is in the shadow zone, and, according to Eqs. (28) and (29), it cannot influence the amplitudes of the 100 initial modes. This statement is confirmed by the results of calculations.

In the examples considered, an interesting effect can be observed: a mode can "ignore" the inhomogenety, even in the case if it is between the turning points. A qualitative explanation of this effect is offered in [11]. Here, we only note that the effect at hand can only

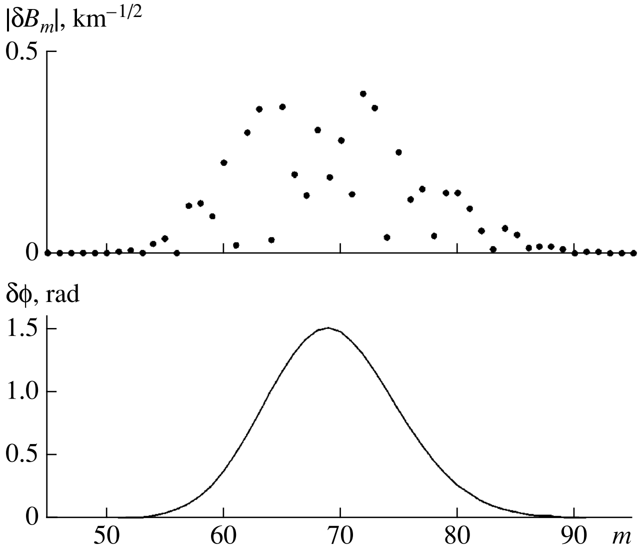

Fig. 2. Variations in the mode amplitudes due to the scattering by the inhomogeneity of the refractive index at point *1* (the upper plot) and the variations in the phase of a mode ray under the effect of the inhomogeneity (the lower plot).

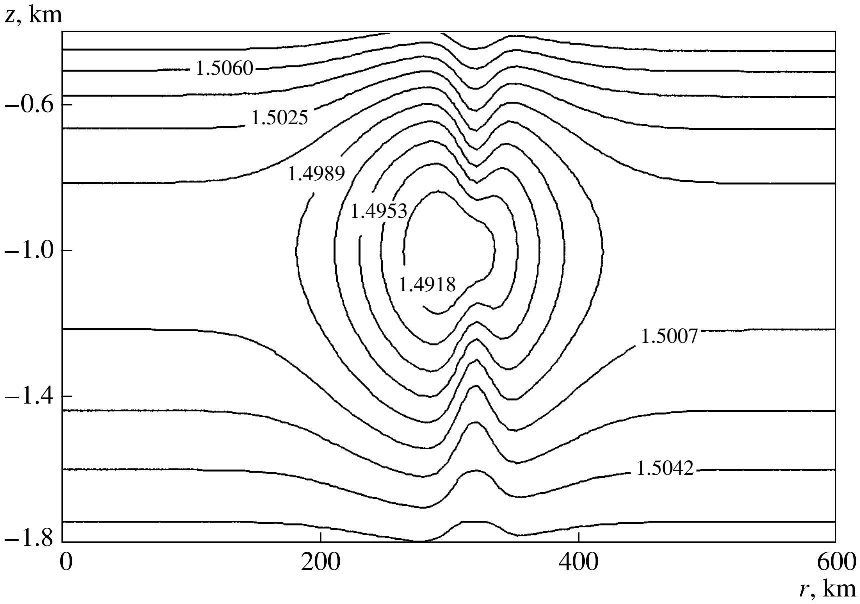

Fig. 3. Sound speed field modeling a synoptic eddy.

occur in the situation when a great number of modes propagate simultaneously. At the scattering by the inhomogeneity, a mode looses part of its energy through the energy transfer to other modes. However, in certain cases, which are defined by the requirement for the mode rays not to cross the inhomogeneity, the mode can regain its energy from other modes. In the situation when only one mode is incident on the inhomogeneity, its energy can only decrease due to scattering.

Note that the mode amplitudes obtained with the three calculation methods, namely, by Eqs. (23) and (28) and by the parabolic equation method, are close to each other.

4.2. Sound Propagation through a Synoptic Eddy

Let us consider a much stronger inhomogeneity of a large spatial scale, which models the effect of a synoptic eddy [23]:

$$\delta c(r, z) = c_2 \exp\left(-\frac{(r-r_2)^2}{\Delta r^2} - \frac{(z-z_2)^2}{\Delta z(r)^2}\right), \qquad (54)$$

where

$$\Delta z(r) = \Delta z_c - \Delta z_v \exp\left(-\frac{(r-r_v)^2}{\Delta r_v}\right). \qquad (55)$$

Let us specify the following values of the parameters: $c_2 = -0.01$ km/s, $r_2 = 300$ km, $z_2 = -1$ km, $\Delta r = 80$ km, $\Delta z_c = 0.5$ km, $\Delta z_v = 0.25$ km, $r_v = 320$ km, and $\Delta r_v = 20$ km. The isograms of the total sound speed field, $c(z) + \delta c(r, z)$, are shown in Fig. 3.

In Fig. 4, the squares indicate the mode amplitudes at a distance of 600 km. These amplitudes were calculated with the use of our main formula (23) (the value $|B_0| = 2.47$ km$^{-1/2}$ is outside the range of Fig. 4). The solid curve shows the deviations from the mode amplitudes found by numerically solving the parabolic equation. According to the data presented, the accuracy of Eq. (23) is rather high for the majority of the modes. However, the solid curve exhibits three high peaks, *A*, *B*, and *C*, with midpoints at the numbers $m = 27$, 32, and

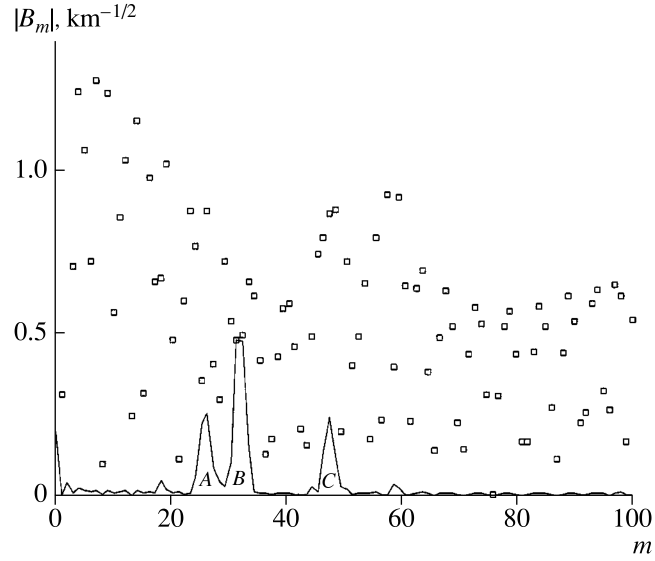

Fig. 4. Mode amplitudes predicted by Eq. (23) (squares) and their deviations from the corresponding amplitude values predicted by the parabolic equation method (solid curves).

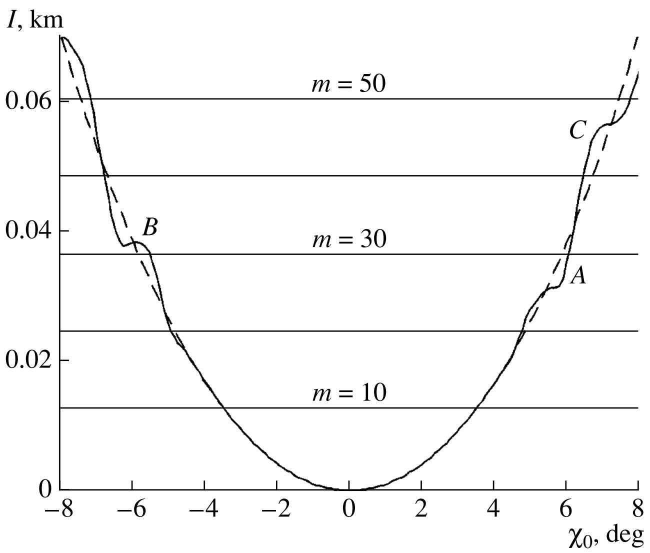

Fig. 5. Action variable at a distance of 600 km versus the launch angle in an unperturbed waveguide (dashed curve) and in the presence of a synoptic eddy (solid curve). The straight lines show the values of the action variables I_m for $m = 10$. 20, 30, 40, and 50. The symbols *A*, *B*, and *C* indicate the intervals where the derivative of the action with respect to the ray launch angle is small.

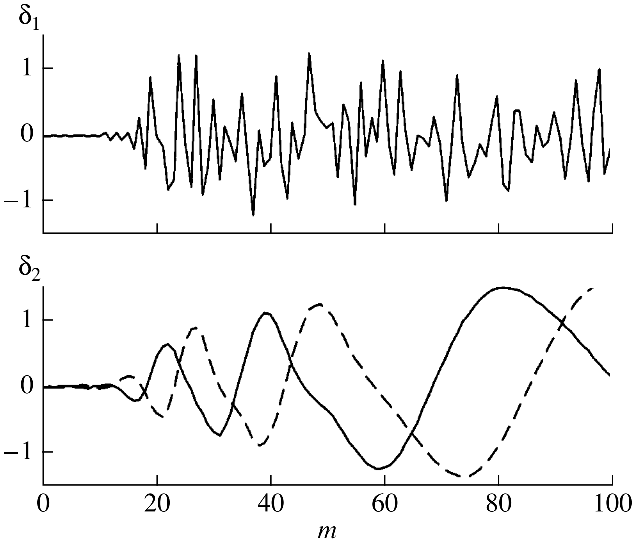

Fig. 6. Relative changes in the mode amplitudes in the presence of the eddy (the upper plot) and the deviations (normalized to π) of the phases of mode rays from their values calculated in the adiabatic approximation (the lower plot). The solid and dashed curves correspond to the rays with positive and negative launch angles, respectively.

48, respectively. For these and neighboring modes, Eq. (23) leads to a noticeable error.

The origin of this error can be understood from Fig. 5, which shows the action variable I of the ray as a function of the ray launch angle χ_0 for the disturbed (solid curve) and unperturbed (dashed curve) waveguides at a distance of 600 km. The launch angles of the mode rays can be found from the points at which the curves $I(\chi_0)$ cross the horizontal straight lines $I = I_m$. At the intervals *A*, *B*, and *C*, the solid curve has horizontal tangents at which the derivative $\partial I/\partial p_s$ appearing in the denominator of Eq. (23) goes to zero. Here, we face the analog of caustics for modes, i.e., the effect mentioned at the end of Section 2.2. For the modes whose action variables are close to the values of the function $I(\chi_0)$, Eq. (23) fails at the intervals *A*, *B*, and *C*. These are precisely the modes to which the peaks *A*, *B*, and *C* of Fig. 4 correspond. At $|\chi_0| > 8°$, both branches of the function $I(\chi_0)$ monotonically increase and no analogs of caustics occur for modes with $m > 50$.

The sound speed field shown in Fig. 3 varies rather smoothly, and one can expect that at least part of the modes can be described in an adiabatic approximation. For such modes, the value of $|B_m|$ is retained along the path. At the top of Fig. 6, the difference between the initial and terminal values of the mode amplitude is presented. The amplitudes were calculated by the parabolic equation. The difference shown is normalized to the average initial amplitude:

$$\delta_1 = \frac{|B_m(r)| - |B_m(0)|}{B}, \quad B = \frac{1}{100}\sum_{m=0}^{99}|B_m(0)|. \tag{56}$$

The lower plot of Fig. 6 shows the deviations of the eikonals of the mode rays from the values calculated in the adiabatic approximation (these deviations are divided by π):

$$\delta_2 = \frac{\delta\Phi}{\pi}. \tag{57}$$

The values of $\delta\Phi$ are calculated according to Eq. (49) for the mode rays that leave the source upwards (solid curve) and downwards (dashed curve). According to our criterion established in Section 3.4, the adiabatic approximation can be used for the mode at hand if the following condition is met for both its mode rays: $|\delta_2| \ll 1$. By comparing the upper and lower plots of Fig. 6, one can see that this condition is valid for the same 15–17 initial modes, for which $|\delta_1| \ll 1$. The smallness of δ_1 means that the mode amplitude remains nearly constant, just as one would expect in an adiabatic approximation.

5. CONCLUSIONS

The consideration described above is based on the ray approach proposed in [9] for describing mode amplitudes. This method is used here to analyze the field of a point source in two situations, which both often occur in applications and presume rather simple analytical representations.

It was shown that even very weak inhomogeneities of the refractive index may cause a noticeable redistribution of energy between modes. In the case of weak inhomogeneities, our main formula (23) can be simplified and reduced to Eq. (28). In another way, Eq. (23) was obtained in [10, 11]. The conclusion of [10, 11] about the selective nature of the scattering by the inhomogeneities that are small relative to the waveguide depth but large relative to the sound wavelength was confirmed (in particular, by direct numerical calculations): a mode amplitude is considerably influenced by only those inhomogenities that occur in the vicinities of the mode rays, i.e., the two geometric-optical rays leaving the source at the grazing angles equal to the angles of the Brillouin waves forming this mode. A qualitative explanation of this effect is given in [11].

Rather simple analytical relations were also obtained for another particular case when the longitudinal scale of fluctuations of the refractive index are comparable with the length of the ray cycle. The importance of these results is that they yield a new validity criterion for the adiabatic approximation. This criterion takes into account the accumulation of the approximation errors with distance. The generality of the criterion is limited by the fact that it is obtained by assuming the validity of geometrical optics.

An important part of this paper is the numerical simulation of the sound fields in inhomogeneous waveguides. This simulation confirmed the validity of both the initial formula (23) and its consequences.

ACKNOWLEDGMENTS

We are grateful to I.P. Smirnov who developed the computer code used in the ray calculations.

This work was supported by the Russian Foundation for Basic Research, project nos. 01-05-64394 and 00-02-17409.

REFERENCES

1. L. M. Brekhovskikh and Yu. P. Lysanov, *Fundamentals of Ocean Acoustics* (Gidrometeoizdat, Leningrad, 1982; Springer, New York, 1991).
2. L. M. Brekhovskikh and O. A. Godin, *Acoustics of Layered Media II: Point Sources and Bounded Beams*, 2nd ed. (Nauka, Moscow, 1989; Springer, Berlin, 1999).
3. A. T. Abawi, J. Acoust. Soc. Am. **111**, 160 (2002).
4. S. A. Stotts, J. Acoust. Soc. Am. **111**, 1623 (2002).
5. O. A. Godin, J. Acoust. Soc. Am. **111**, 1984 (2002).
6. F. B. Jensen, W. A. Kuperman, M. B. Porter, and H. Schmidt, *Computational Ocean Acoustics* (American Inst. of Physics, New York, 1994).
7. F. I. Kryazhev and V. M. Kudryashev, Akust. Zh. **43**, 203 (1997) [Acoust. Phys. **43**, 172 (1997)].
8. V. M. Kudryashev, Akust. Zh. **33**, 55 (1987) [Sov. Phys. Acoust. **33**, 32 (1987)].
9. A. L. Virovlyanskiĭ, L. Ya. Lyubavin, and A. A. Stromkov, Akust. Zh. **47**, 597 (2001) [Acoust. Phys. **47**, 517 (2001)].
10. A. L. Virovlyanskiĭ and A. G. Kosterin, Akust. Zh. **33**, 599 (1987) [Sov. Phys. Acoust. **33**, 351 (1987)].
11. A. L. Virovlyansky, V. V. Kurin, N. V. Pronchatov-Rubtsov, and S. I. Simdyankin, J. Acoust. Soc. Am. **101**, 163 (1997).
12. G. P. Berman and G. M. Zaslavsky, Physica A (Amsterdam) **97**, 367 (1979).
13. A. L. Virovlyansky and G. M. Zaslavsky, Phys. Rev. E **59**, 1656 (1999).
14. A. L. Virovlyansky, J. Acoust. Soc. Am. **108**, 84 (2000).
15. S. M. Rytov, Yu. A. Kravtsov, and V. I. Tatarskiĭ, *Introduction to Statistical Radiophysics*, Part 2: *Random Fields* (Nauka, Moscow, 1978).
16. *Sound Transmission through a Fluctuating Ocean*, Ed. by S. Flatte (Cambridge Univ. Press, Cambridge, 1979; Mir, Moscow, 1982).
17. K. B. Smith, J. Comput. Acoust. **9** (1), 243 (2001).
18. F. D. Tappert, in *Wave Propagation and Underwater Acoustics*, Ed. by J. B. Keller and J. S. Papadakis (Springer, New York, 1977; Mir, Moscow, 1980).
19. V. P. Maslov and M. V. Fedoryuk, *Semiclassical Approximation in Quantum Mechanics* (Nauka, Moscow, 1976; Reidel, Dordrecht, 1981).
20. J. Simmen, S. M. Flatte, and G.-Y. Wang, J. Acoust. Soc. Am. **102**, 239 (1997).
21. L. D. Landau and E. M. Lifshitz, *Course of Theoretical Physics*, Vol. 1: *Mechanics*, 3rd ed. (Nauka, Moscow, 1973; Pergamon Press, Oxford, 1976).
22. I. A. Okomel'kova and I. A. Shereshevskiĭ, Preprint No. 235, IPF AN SSSR (Inst. of Applied Physics, USSR Academy of Sciences, Gor'kii, 1989).
23. V. M. Kamenkovich, M. N. Koshlyakov, and A. S. Monin, *Synoptic Vortices in the Ocean* (Gidrometeoizdat, Leningrad, 1982).
24. D. M. Milder, J. Acoust. Soc. Am. **46**, 1259 (1969).
25. A. L. Virovlyanskiĭ and O. V. Lebedev, Akust. Zh. **44**, 451 (1998) [Acoust. Phys. **44**, 384 (1998)].

Translated by E. Kopyl

Acoustical Physics, Vol. 50, No. 1, 2004, pp. 30–36. Translated from Akusticheskiĭ Zhurnal, Vol. 50, No. 1, 2004, pp. 37–43.
Original Russian Text Copyright © 2004 by Galkin, Popov, Simakina.

Spatial Correlation of Sound Fields from Underwater Explosions in the Barents Sea

O. P. Galkin, R. Yu. Popov, and E. V. Simakina
Andreev Acoustics Institute, Russian Academy of Sciences, ul. Shvernika 4, Moscow, 117036 Russia
e-mail: bvp@akin.ru

Received December 25, 2002

Abstract—Results of an experimental study of the spatial correlation of signals from underwater explosions are presented for vertically and horizontally (across the path) separated reception points. The measurements were carried out on two propagation paths about 200 and 110 km long in the Barents Sea for frequencies below 500 Hz. The vertical correlation radius is found to increase with the distance to the source, which is primarily caused by the decrease in the sector of arrival angles of energy carrying signals. The transverse correlation radius weakly depends on the path length for frequencies below 300 Hz, while for higher frequencies, it decreases beginning from a distance of about 40 km, which can be attributed to the effect of short-period internal waves. *© 2004 MAIK “Nauka/Interperiodica”.*

The Barents Sea is a shallow ocean region whose characteristic feature is the signal propagation with multiple reflections from the boundaries of the water layer, which causes a strong attenuation of signals. For this reason, the habitual problem that arises in monitoring the water areas consisting of the detection of weak signals against the background of strong interference becomes critical in these regions. To overcome this difficulty, it is expedient to use large-aperture receiving antennas. However, the efficiency of this method is determined by the coherence ratio of sound signals (at least within the antenna aperture) and by the possible dependence of this ratio on the distance to the source of sound.

Note that the number of publications in this field of research is fairly large (see, e.g., [1–5]). Among them, we select the work by Urick and Lund [2] who studied the vertical coherence of shallow-water reverberation using explosive sources of sound. They found that the interval of arrival angles of reverberation signals narrows with time. The rays along which the signals travel become less steep. As a result, the vertical correlation radius of the sound field increases with time. We also should mention the paper [6] concerned with measuring the parameters of the vertical correlation of the reverberation field in the coastal slope conditions. They discovered a considerable anisotropy of the field in the azimuth plane. Our previous papers [7, 8] investigated the vertical and horizontal transverse (across the path of sound propagation) correlations of sound fields over the coastal slope of the Pacific shore of Kamchatka. It was found that the correlation parameters vary widely depending on the hydrophone positions, the relief and structure of the bottom, the source azimuth, the distance to the source, and the hydrographic conditions.

Below, we describe the results of experimental studies of the spatial correlation of sound fields produced by underwater explosions with receiving hydrophones spaced in the vertical and horizontal directions and placed at different distances from the points of explosion. The measurements were carried out in the Barents Sea for the hydrographic conditions characteristic of summer and autumn. Figure 1 shows the region of measurements and the two paths, one of which (path I) was used for studying the vertical correlation and the other (path II), for studying the transverse correlation.

The length of path I was equal to ~200 km. The receiving vessel lay to at point *a*. From its board, a vertical chain of six hydrophones was lowered into water. The length of the chain was 19 m. The distances between adjacent hydrophones were different. Starting from the deepest receiver and going in the upward direction, the successive distances between adjacent hydrophones were 5, 1, 2, 7, and 4 m. The chain center was located at a depth of ~100 m. The deviation of the center from this depth was traced with a depth gauge and was no greater then ±1 m. The vessel that produced the explosions of 2.5-kg trinitrotoluene charges at a depth of 100 ± 3 m moved away in a given direction with a velocity of 12 knots. The charges were dropped from the vessel in motion at preset time intervals. The distance between the vessels was determined approximately from the difference between the instant of explosion (transmitted via a radio channel) and the instant of the signal arrival at the hydrophones.

Figure 2a shows the sound velocity as a function of depth for eight points of the path (approximately, at every 30 km). Figure 2b shows the profile of the bottom along the path. The bottom relief was gradually hilly, the slopes were gentle and did not exceed 15'. The

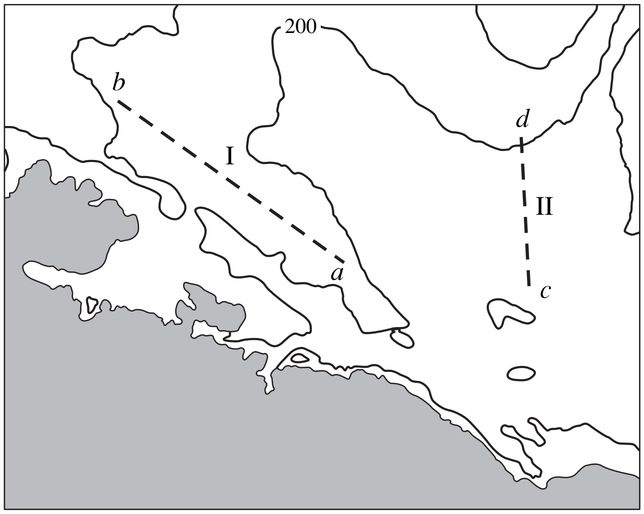

Fig. 1. Region of the experiment and the two paths used for studying the sound propagation.

depth along the path varied from 230 to 330 m. The bottom was formed of sediments consisting of coarsely grained sand, gravel, and pebble. During the measurements, the wind force and the sea state corresponded to Beaufort 3 and 2, respectively.

Analysis of signals that arrived at the hydrophones made it possible to study the vertical coherence of sound fields in shallow water and its dependence on the distance to the source.

It is common practice to use the correlation function (or, after normalization, the correlation coefficient) as a measure of the spatial coherence of the sound field of a broadband signal (including the case of receivers spaced in both the vertical and horizontal directions). However, actual measurements use the quantity

$$\Phi(\tau) = \frac{1}{T}\int_0^T x(t)y(t-\tau)dt, \tag{1}$$

where $x(t)$ and $y(t)$ are the signals received at two spatially separated points, T is the time of averaging (it usually coincides with the duration of the signal realization), and τ is the time shift. The function $\Phi(\tau)$ coincides with the correlation function only if the signals form a stationary ergodic process on the interval of averaging. The appropriateness of this assumption in the case under consideration is questionable. For this reason, we can deal here only with an estimate of the signal coherence.

In the measurements described in this paper, we used the concept of the short-term correlation function (the corresponding correlation coefficient is denoted as R_{sh}). In this case, the time of averaging is less than the lifetime of the multipath pulsed signal (or the so-called signal spread time T_{sp}) but greater than the period of the mean frequency of analysis T_m, which is required for the measurements of R_{sh} to be sufficiently precise [2]. In other words, the time T must satisfy the condition

$$T_m < T < T_{sp}. \tag{2}$$

Figure 3 shows the curves obtained from the measurements of vertical correlation. They illustrate variations of R_{sh} with time within the spread time T_{sp}, i.e., between the time of the first arrival (in a shallow sea this signal usually travels along the flattest ray) and the time of the last arrival of the signal (along the steepest ray). The curves are parameterized by the quantity Δz, which is the vertical spacing of hydrophones.

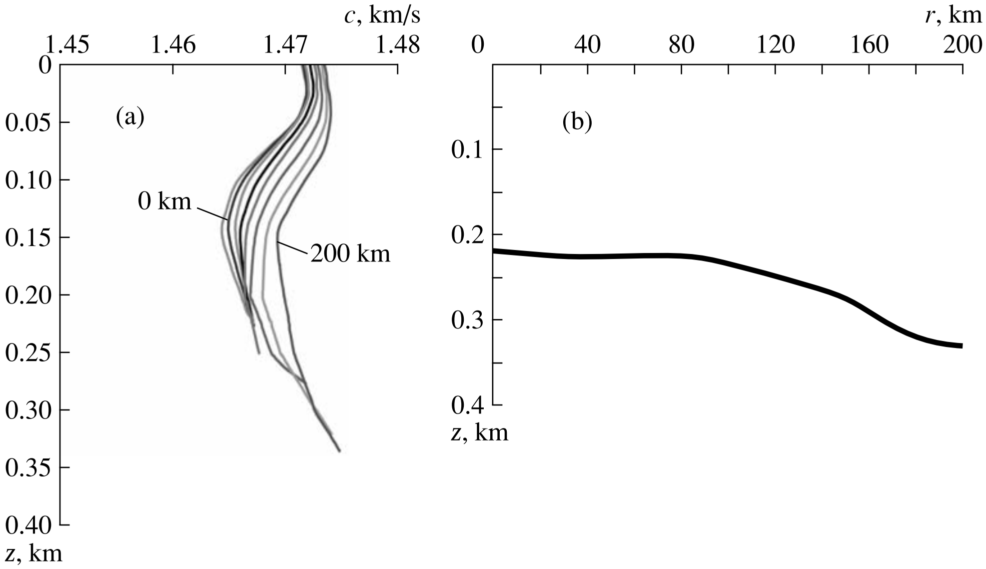

Fig. 2. Sound velocities as (a) functions of depth and (b) the bottom profile along path I.

Note that a rigorous analysis of the variation of R_{sh} with Δz requires the use of a single reference signal. Here, this condition is satisfied only for the curves corresponding to $\Delta z = 1$, 3, 5, 10, and 14 m; in these cases, we used the signal received by the second (from the lower end of the chain) hydrophone as the reference signal. For other values of Δz, the curves were obtained with the use of other reference signals. However, since the whole chain was located in the region of a small and slowly varying sound velocity gradient, we can neglect the variations of the field structure within the chain length of 19 m and assume that this (combined) pattern of variation of R_{sh} with Δz is sufficiently correct.

The signals were analyzed in a frequency band of 240–340 Hz for $T = 0.1$ s. Figure 3 shows three families of curves for distances to the sound source equal to ~20, ~100, and ~196 km.

To interpret the data obtained, we first note that simple geometrical considerations lead to the equality (with the wave front curvature being neglected)

$$\frac{\Delta t_i}{\Delta z} = \pm\frac{\sin\chi_i}{c},$$

where Δt_i is the difference in the times of signal propagation along the ith ray in the depth range Δz, χ_i is the angle of the signal arrival along this ray at the reception points (the sign depends on the direction of signal arrival in the vertical plane), and c is the sound velocity at these reception points. From this formula, it becomes clear that the signal segment formed by the reception of multipath signal components arriving along the flattest rays will have the temporal structure most stable to variations of the vertical coordinate. For shallow-water ocean regions, this segment adjoins the leading edge of the signal (as was mentioned earlier). The curves in Fig. 3 support this statement. An increase in Δz affects primarily the tails of arriving signals. As Δz increases, the correlation first decreases in the region of these tails and then changes its sign. With further increase in Δz, this region of negative correlation moves toward the signal's leading edge; in the tail region, the second positive correlation peak appears, and so on.

Comparing the curves $R_{\text{sh}}(t)$ for three distances r to the source and the same Δz, one can observe that the time-dependent variation of the function R_{sh} becomes slower as the distance r increases, i.e., the correlation coefficient changes its sign at a noticeably greater difference in the reception depths Δz. A similar result follows from the sound field characteristics calculated along the path. The behavior of the received explosion signals points to the fact that the spread time only slightly depends on the path length r and measures ~2 s (this time hardly can be determined with high accuracy, because the received signal has no apparent trailing edge exceeding the background of interference). Calculations show that the interval of the vertical arrival angles of energy carrying signals received within the first second of the multipath signal lifetime narrows with increasing distance. Earlier, we noted that the correlation of signals received along flat rays depends much less on the spacing between the reception points than the signals traveling along steep rays. This explains the behavior of the experimental curves in Fig. 3. Thus, the vertical correlation radius increases with the distance to the sound source.

This inference becomes more evident if we consider the case when the transmitted pulse duration δ noticeably exceeds the spread time T_{sp} (this case is of frequent occurrence in practice). Then, separate arrivals of the multipath signal are unresolved in time, and the spatial correlation of the sound field at the reception points is determined by the signal arrivals along the whole set of rays. If an underwater explosion is used as the sound source, the aforementioned case can be simulated by choosing the time of averaging in Eq. (1) to be somewhat greater (by the duration of the short sound pulse of the explosion) than the spread time of the arriving signal. Figure 4 shows the values of R obtained in this way for $\Delta z = 7$ m in the frequency range $\Delta f = 240$–340 Hz as a function of the distance to the sound source r (note that the values of R are calculated with the r-dependent correction for the signal-to-noise ratio). As seen from the curve, the vertical correlation radius of the sound field in a shallow sea increases with distance r (despite the decrease in the signal-to-noise ratio). Note that, when the sea roughness and the measured sound velocity profile are taken into account, the slope of the curve approximating the experimental points in Fig. 4 can be used as a path-averaged characteristic of acoustical and geological parameters of the bottom.

One can adequately interpret the above experimental results on the basis of two points supported by calculations. First, the parameters of the vertical correlation of sound fields in a shallow sea are mainly governed by the characteristics of the multipath sound propagation with multiple reflections of the signal from the waveguide boundaries. Second, the contribution of the signals multiply reflected from the waveguide boundaries to the total field steadily decreases with increasing distance; for this reason, in the region of the trailing edge, the signal level that must exceed the interference level is determined by the signals arriving along increasingly flatter rays.

Now, we consider the results obtained on path II used for investigating the transverse correlation of sound fields of underwater explosions. The path length slightly exceeded 100 km. Figure 5 shows the depth-dependent sound velocity for seven points of the path and the bottom profile along the path. The experiment duration was ~48 h, the sea state corresponded to Beaufort 3–4 during the experiment (the wind force was Beaufort 4–6). The sound signals were received at the southern end of the path using two hydrophones located at the bottom at a depth of ~110 m and spaced in the latitude direction (across the path) at a distance of ~2 km.

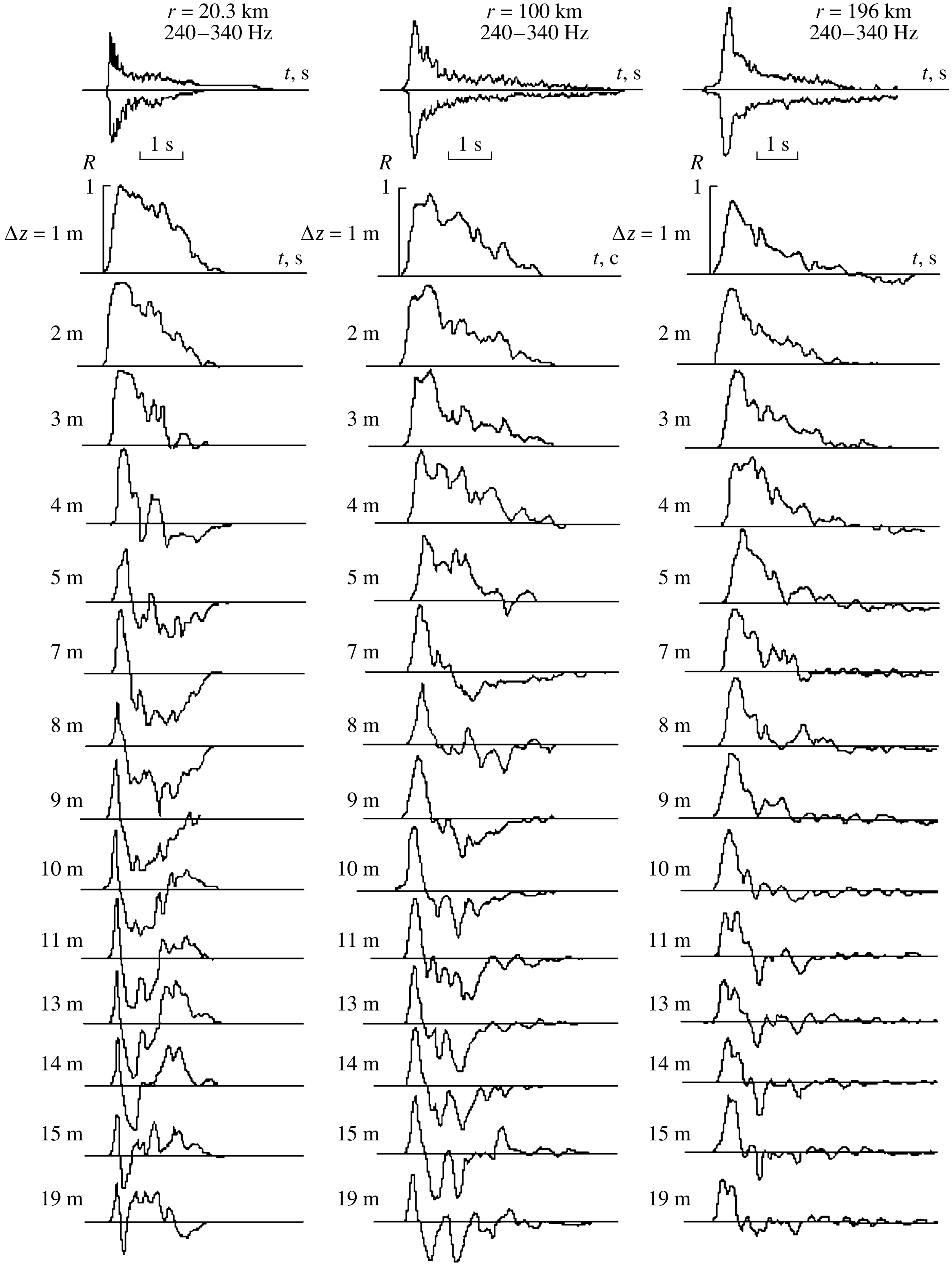

Fig. 3. Variation of the short-term correlation function with time within the spread time of the received signal for three distances to the source.

The signals received by the hydrophones were transmitted via radio channels to the vessel anchored at a distance of ~9 km from the hydrophones. Trinitrotoluene charges of 0.27 kg were used as explosive sound sources; they were blown up at a depth of 90 ± 3 m. Charges were dropped from the second vessel that

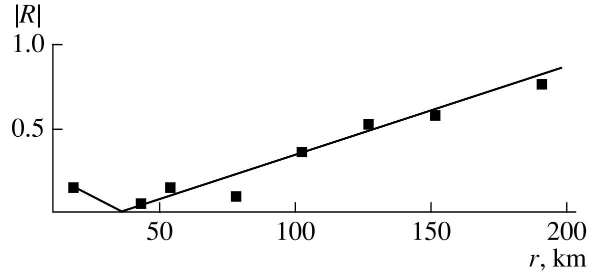

Fig. 4. Vertical correlation coefficient as a function of the distance to the source (the frequency band used in the analysis was 240–340 Hz).

moved away from the center of the reception base in the northern direction with a velocity of 12.5 knots. Charges were dropped at intervals of 1 min, so that the distance between the adjacent drop points were equal to ~375 m. The signals received were computer processed to calculate the cross correlation coefficient. The time of averaging always coincided with the spread time of the signal.

Figure 6 shows the correlation coefficient *R* of explosion signals received with two bottom-moored hydrophones in different frequency bands. It can be seen that, for frequencies below ~300 Hz, the correlation coefficient *R* only slightly varies as the distance to the signal source increases from 10 to ~110 km. However, for higher frequencies, the correlation coefficient *R* appreciably decreases. (Note that the reasons of scatter in the values of *R* for distances between 50 and 70 km are not yet completely understood.)

In most cases, the destruction of the spatial correlation of sound fields in oceanic waveguides is mainly caused by the variations in the temporal structure of the signal (related to the multipath nature of sound propagation) that occur when the reception or radiation points change their positions. This was precisely the case in the experimental study of the vertical correlation of sound field. However, when the reception base is oriented across the propagation path (i.e., when the path is normal to the base connecting the reception points and passed through the base center), the statistical processes in the water medium and the spatial variability of acoustical and geological characteristics of the sea bottom may significantly contribute to the destruction of the signal correlation in a shallow sea. Our approximate estimates showed that small-scale inhomogeneities of the sea medium contribute negligibly to the destruction of the spatial correlation of the sound field. Indeed, for small-scale inhomogeneities, the fluctuation of the travel time can be estimated by the formula $\tau = \left(\frac{\sqrt{\pi}}{2}\frac{\langle\mu^2\rangle}{c^2}ar\right)^{\frac{1}{2}}$ [10], where $\langle\mu^2\rangle$ is the average squared fluctuation of the refractive index of the medium, c is the sound velocity, a is the average size of random inhomogeneities in the medium, and r is the distance. For distances $r \sim 100$ km, the fluctuation of travel time τ does not exceed 0.01 ms ($a = 1.5$–1.9 m, $\langle\mu^2\rangle = (16–22) \times 10^{-10}$ [11]). On the other hand, even an approximate consideration of the effect of the short-period internal waves shows that their contribution to the formation of the sound field is considerable. According to [12] (with the remark that the conditions analyzed in [12] differ from the conditions of our experiment), the transverse correlation interval in the presence of the short-period internal waves can be approximately (with an error of about 30%) estimated by the relationship $d_{\text{h}} \approx \frac{\sqrt{6l}}{\Phi}$, where Φ is the parameter characterizing the inhomogeneities of the medium, which is equal to 15–17 for frequencies close to 400 Hz and distances of about 400–450 km, and $l \cong 3.7$ km is

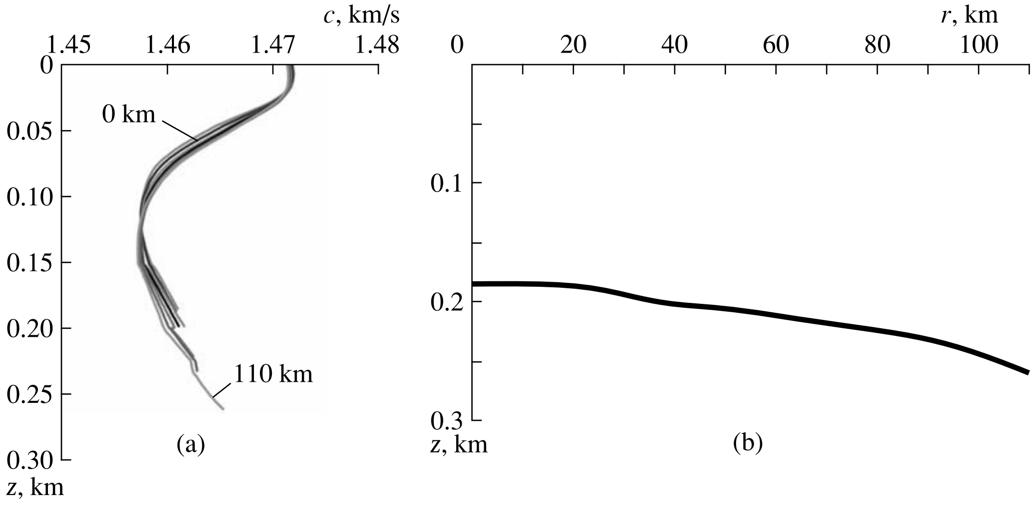

Fig. 5. Sound velocities as (a) functions of depth and (b) the bottom profile along path II.

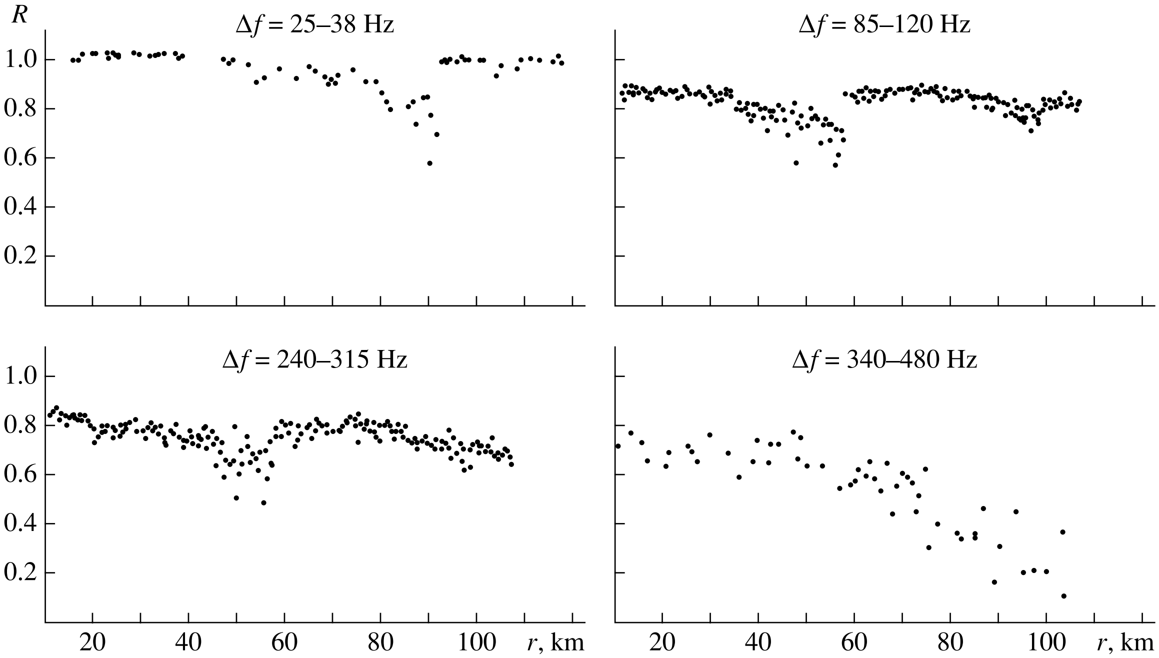

Fig. 6. Transverse correlation coefficient of explosion signals for different frequency bands used in the analysis.

the parameter obtained experimentally. With this rough (±30%) and simplified estimate, the spatial correlation radius determined from the decrease in the correlation coefficient by a factor of *e* appears, at a distance of 100 km, shorter than the 2-km distance between the hydrophones used in the experiment. With a decrease in the path length (the frequency of sound being intact), this radius increases and, for distances $r \cong 10$–15 km, it appears to be longer than the distance between the hydrophones. Taking into account the approximate nature of these theoretical estimates, one can see that they do not contradict the experimental data given in Fig. 6. Thus, the variations of the spatial correlation radius with distance in different frequency bands can be related to the effect of internal waves, whose characteristics are worthy of measuring during the experiments.

On the basis of the results described above and the analysis of the data obtained, we can make the following conclusions.

For frequencies below 500 Hz, the vertical correlation radius of sound fields in the Barents Sea increases with the distance to the sound source and, presumably, can be as large as 10 m. Such a behavior of the vertical correlation radius with distance is primarily related to a narrowing of the angular spectrum of arriving signals that make the major contribution to the total sound field intensity. This feature of the field structure is characteristic of a shallow sea and is caused by the bottom and surface reflections.

For frequencies below 300 Hz, the transverse (in the horizontal plane) correlation radius of sound fields in the region of experiment in the Barents Sea, under the condition that the source is located abeam of the receiving base, measures no less than 2 km and only slightly depends on the distance to the sound source. For higher frequencies (350–500 Hz), the correlation radius gradually decreases with increasing distance beginning from ~40 km. Such variations of the spatial correlation may be caused by the effect of short-period internal waves.

ACKNOWLEDGMENTS

We are grateful to S.V. Bogunets, L.I. Ezhov, and P.G. Tyurin for their assistance in the measurements and to A.E. Lenets and Yu.V. Semenov for performing the necessary calculations.

This work was supported by the Russian Foundation for Basic Research, project nos. 00-02-17694 and 02-02-17325.

REFERENCES

1. R. Urick, J. Acoust. Soc. Am. **54**, 115 (1973).
2. R. Urick and G. Lund, J. Acoust. Soc. Am. **47**, 343 (1970).
3. S. D. Pankova and Yu. I. Tuzhilkin, Akust. Zh. **45**, 388 (1999) [Acoust. Phys. **45**, 343 (1999)].
4. Q. Wang and R. Zhang, J. Acoust. Soc. Am. **92**, 932 (1992).
5. G. L. Spiesberger, J. Acoust. Soc. Am. **100**, 910 (1996).

6. R. Yu. Popov and E. V. Simakina, Akust. Zh. **40**, 655 (1994) [Acoust. Phys. **40**, 580 (1994)].
7. O. P. Galkin, A. V. Kulakov, and R. Yu. Popov, Akust. Zh. **48**, 614 (2002) [Acoust. Phys. **48**, 540 (2002)].
8. O. P. Galkin, R. Yu. Popov, Yu. V. Semenov, and E. V. Simakina, Akust. Zh. **47**, 616 (2001) [Acoust. Phys. **47**, 534 (2001)].
9. J. S. Bendat and A. G. Piersol, *Engineering Applications of Correlation and Spectral Analysis* (Wiley, New York, 1980; Mir, Moscow, 1983).
10. N. G. Kuznetsova and L. A. Chernov, Vopr. Sudostr., Ser. Akust., No. 15, 5 (1982).
11. S. D. Chuprov and R. F. Shvachko, in *Acoustics of the Ocean*, Ed. by L. M. Brekhovskikh (Nauka, Moscow, 1974), pp. 573–581.
12. *Sound Transmission through a Fluctuating Ocean*, Ed. by S. Flatte (Cambridge Univ. Press, Cambridge, UK, 1979; Mir, Moscow, 1982).

Translated by A. Vinogradov

Acoustical Physics, Vol. 50, No. 1, 2004, pp. 37–45. Translated from Akusticheskiĭ Zhurnal, Vol. 50, No. 1, 2004, pp. 44–54.
Original Russian Text Copyright © 2004 by Grigor'ev, Kuz'kin, Petnikov.

Low-Frequency Bottom Reverberation in Shallow-Water Ocean Regions

V. A. Grigor'ev[1], V. M. Kuz'kin[2], and B. G. Petnikov[2]

[1] *Voronezh State University, Universitetskaya pl. 1, Voronezh, 394693 Russia*
e-mail: grig@box.vsi.ru
[2] *Wave Research Center, General Physics Institute, Russian Academy of Sciences,*
ul. Vavilova 38, Moscow, 119991 Russia
e-mail: petnikov@kapella.gpi.ru

Received May 28, 2003

Abstract—A phenomenological model of long-range reverberation in a shallow sea is developed to describe the statistical characteristics and interference of the sound field scattered by bottom inhomogeneities. Experimental data on the scattering of low-frequency sound by the sea bottom are presented for a shallow-water region of the Barents Sea. The results of a numerical simulation of the low-frequency bottom reverberation in a multimode waveguide are described. The simulation is based on experimentally measured values of backscattering strength. © *2004 MAIK “Nauka/Interperiodica”.*

INTRODUCTION

The phenomenon of the backscattering of sound by the inhomogeneities of the ocean bottom had been the subject of intense theoretical and experimental studies for several decades. The urgency of these studies is caused by both basic problems of sound propagation in the ocean and the need to develop methods of remote sensing of oceanic waveguides. The theoretical fundamentals of the backscattering of sound by the ocean bottom (bottom reverberation) were initially developed in [1, 2]. The results of these studies refer to the case of relatively short waves and short paths, when ray considerations are valid for describing the sound field. For shallow-water waveguides at low frequencies, the ray theory fails, and the mode theory of bottom reverberation should be used (see, e.g., [3–6]). However, the authors of the cited papers restricted their considerations to the intensity approach, in which the average intensity of the scattered field is determined by the incoherent (intensity) summation of normal waves. With this approach, one actually neglects the stochastic nature of the scattered field and the interference phenomena caused by the propagation of both direct and scattered waves. The role of these effects is especially important in the comparative analysis of reverberation signals received with the use of single omnidirectional hydrophones (or sound sources) and with vertical antenna arrays that cover the majority of the waveguide and are tuned to receive (or to excite) individual normal waves.

Experimental data on the sound scattering by the bottom can be found, for example, in reviews [7–9]. They include the experimental dependences of the backscattering coefficient (backscattering strength) on the frequency (f) and the grazing angle (θ) of the incident and scattered sound beams, for both deep and shallow regions of the ocean. However, the data presented in the literature mainly apply to high frequencies ($f \geq 500$ Hz) and large grazing angles ($\theta \geq 15°$). This fact hampers the use of the corresponding backscattering strength values for estimating the intensity of long-range low-frequency reverberation, because, in a shallow sea, such a reverberation is formed by sound beams that are incident and reflected by the bottom at low grazing angles.

This paper extends the results of [3–6]. A simple phenomenological model of the bottom reverberation is developed with allowance for the interference structure of the random scattered sound field. The model is based on the representation of the scattering surface of the sea bottom in the form of a set of randomly distributed independent point sources with given statistical distributions of their strengths and sizes. An expression is obtained for the scattering diagram of a bounded bottom area. The scattered field is calculated by combining the sound fields of all point sources with a subsequent statistical averaging. The relation between the backscattering coefficient and the scattering diagram is determined. An experimental technique is proposed for estimating the backscattering coefficient at low frequencies and small grazing angles. The results of its application in a region of the Barents Sea are presented. The results of a numerical simulation of the low-frequency bottom reverberation in a multimode waveguide are described. The simulation is based on the experimental data on the backscattering strength. The calculations are performed for the cases when the transmission and reception are carried out with omnidirectional point source and receiver (multimode reverberation) and with linear vertical arrays matched to excite and receive a single mode (single-mode reverberation).

MODEL OF THE BOTTOM REVERBERATION

Suppose that, at the carrier frequency f_0, a narrowband pulsed signal is transmitted with acoustic power W_0, duration τ, and spectral bandwidth $\Delta f \ll f_0$, the modulus of the signal spectrum being approximately constant within this bandwidth. Let us introduce a cylindrical coordinate system (r, z, φ) and consider an ocean waveguide whose water layer is bounded by a free surface from above, $z \geq z_{sur}$, and by the bottom from below, $z \leq z_b$. We restrict our consideration to the cylindrically symmetric problem with density $\rho(r, z)$ and speed of sound $c(r, z)$ being independent of the azimuth angle φ.

As to the waveguide boundaries, we admit the following assumptions. The upper boundary is assumed to be perfectly flat and smooth, $z_{sur}(r, \varphi) = 0$, with no scattering from it. Such an assumption is justified by the fact that, in a shallow sea, the bottom reverberation is often an order of magnitude higher than the surface one. The lower boundary, $z_b(r, \varphi)$, is represented by a multiscale relief, $h(r, \varphi)$, superimposed on a large-scale bottom roughness $H(r)$: $z_b(r, \varphi) = H(r) + h(r, \varphi)$. We assume that the characteristic length r_c of spatial correlation of the random field $h(r, \varphi)$ is much smaller than the characteristic scale of spatial variations of $H(r)$ and does not exceed 10 m. We also assume that the value of $h(r, \varphi)$ is small enough, so that the factor $V_{m\mu} = \int_0^\infty \psi_\mu(r, z)\frac{\partial \psi_m(r, z)}{\partial r}dz$ that governs the interaction of normal waves due to the roughness $h(r, \varphi)$ obeys relation [10]

$$\frac{|V_{m\mu}|}{|\xi_m - \xi_\mu|} \ll 1. \tag{1}$$

Here, $\psi_m(r, z)$ and $\xi_m(r)$ are the eigenfunctions and eigenvalues of the transverse Sturm–Liouville problem with the boundary conditions at the bottom and surface ($\xi_m = q_m + i\gamma_m/2$). The aforementioned assumption means that we neglect the transformation of modes in the course of the sound propagation over the randomly rough bottom; i.e., the forward-scattered sound field is assumed to be negligibly small in comparison with the coherent field propagating in the waveguide.

On the other hand, we assume that this random roughness $h(r, \varphi)$ is precisely the factor responsible for the sound backscattering that determines the bottom reverberation. However, low-frequency bottom backscattering is governed not only by the aforementioned roughness but also by random inhomogeneities of the upper sediment layer (see, e.g., [9]). For such inhomogeneities, the assumption of their weak influence on the sound propagation is also valid. Let us combine the random roughness of the relief and the inhomogeneities of the upper sediment layer by accepting the general term: "sea-floor inhomogeneities." These inhomogeneities are assumed to be uniform and isotropic. Actually, the backscattering of sound by such inhomogeneities is accompanied by intermode transformations.

The scattering area is in the far-field zone relative to the transmitting–receiving system [11]. The size of this area is assumed to be sufficiently small for the changes in attenuation of the incident waves to be neglected within the area. At the same time, the area size must be large enough to take into account the statistical properties of the scattering bottom. In particular, the accepted assumptions mean that the approximation of single backscattering is valid and this process has little effect on the intensity of the forward-propagating sound field.

To simplify the subsequent calculations, we also assume that the density $\rho(r, z)$ of the water layer, the sound speed $c(r, z)$ in it, and the general bottom relief $H(r)$ smoothly vary with distance r, so that inequality (1) is valid. Thus, we neglect the transformation of modes in the sound propagation through the waveguide.[1]

To begin, let us consider long-range reverberation with a point source and a point receiver of sound. In this case, the signals transmitted and received correspond to all normal waves of the waveguide at hand (multimode reverberation). Then, on the basis of the model developed, we will consider the situation when vertical transmitting and receiving antenna arrays are tuned to excite and receive a single normal wave (single-mode reverberation). In the latter case, the transmitting–receiving system is supposed to lie on a single vertical line at the origin of coordinates, $r = 0$.

A. Multimode Reverberation Regime

Assume that the sound source and the receiver are at depths z_s and z_r, respectively. Neglecting the frequency dispersion of modes within the band Δf, represent the complex amplitude of the sound field at a long horizontal range r from the source as a sum of the discrete-spectrum noninteracting modes at the carrier frequency [10]:

$$w_s(r, z) = \sum_{m=1}^{M} w_m(r, z), \tag{2}$$

---

[1] The latter assumption is not crucial, and the theory presented here can be developed for a waveguide with a mode interaction caused by variations in the density, sound speed, and bottom relief.

where

$$w_m(r, z) = \sqrt{\rho_s c_s W_0}\frac{\psi_m(0, z_s)\psi_m(r, z)}{\sqrt{\xi_m(r)r}} \times \exp(i\pi/4)\exp\left[i\int_0^r \xi_m(r')dr'\right]. \tag{3}$$

Here, $\rho_s = \rho(0, z_s)$ and $c_s = c(0, z_s)$ are the water density and sound speed at the depth z_s and M is the number of efficiently interacting propagating modes.

Let us consider an elementary scattering bottom area located in the far-field zone at depth z_b and distance r from the source and assume that this area represents a localized inhomogeneity with some directivity pattern. Then, in the approximation of single backscattering, the field scattered by this inhomogeneity has the following form [12] at the reception horizon z_r:

$$w_r(0, z_r) = \sum_{\mu = 1}^{M} w_\mu(0, z_r), \tag{4}$$

where

$$w_\mu(0, z_r) = \sqrt{\frac{1}{8\pi}}\exp(i\pi/4)\frac{b_\mu(r, z_b)\psi_\mu(0, z_r)}{\sqrt{\xi_\mu(0)r}} \times \exp\left[i\int_0^r \xi_\mu(r')dr'\right]. \tag{5}$$

Here,

$$b_\mu(r, z_b) = \psi_\mu(r, z_b)\sum_{m = 1}^{M} T_{\mu m}(r, z_b)w_m(r, z_b) \tag{6}$$

is the excitation factor of the μth scattered mode and $T_{\mu m}(r, z_b)$ is an element of the matrix of mode transformation (the scattering diagram of the bottom area); this matrix describes the transformation of the forward-propagating mth normal wave into the backward-traveling μth normal wave. As a result, the problem consists in determining the scattering diagram, which has the dimensionality of length. Here and below, we use Greek subscripts (μ, ν, …) to indicate normal waves of the scattered field and Latin subscripts (m, n, …) to indicate the modes of the initial (incident) field. In the most general case, the scattering diagram $T_{\mu m}$ can be written as

$$T_{\mu m}(r, z_b) = \zeta_{\mu m}(r)F(\theta_\mu, \theta_m)\sqrt{dS_{\mu m}}. \tag{7}$$

Here, $\zeta_{\mu m}(r)$ is a stochastic process that describes the relative fluctuations of the field scattered from mth to μth modes, $F(\theta_\mu, \theta_m)$ is a deterministic function characterizing the angular redistribution of the scattered field, $dS_{\mu m}$ is the area of the elementary insonified surface portion, θ_m is the grazing angle of the mode-producing (Brillouin) ray corresponding to the mth mode, and $\cos\theta_m = \xi_m(r)c(r, z_b)/2\pi f_0$. The statistical properties of the scattering diagram are symmetric with respect to the mode number interchange: $T_{\mu m} = T_{m\mu}$ [13].

According to the assumption on the uniformity and isotropy of the bottom roughness, the field $\zeta_{\mu m}(r)$ is also uniform and isotropic. Because this field independently characterizes the scattering of the sound wave by different bottom areas, it can be represented as

$$\zeta_{\mu m}(r) = \vartheta_{\mu m}(r)\exp\left\lfloor i\phi_{\mu m}(r)\right\rfloor, \tag{8}$$

where $\vartheta_{\mu m}$ and $\phi_{\mu m}$ are statistically independent, the phase $\phi_{\mu m}$ is uniformly distributed in the interval $(0, 2\pi)$ (with the probability density function $\eta(\phi_{\mu m}) = 1/2\pi$), and the amplitude $\vartheta_{\mu m}$ obeys the Rayleigh distribution

$$\eta(\vartheta_{\mu m}) = \frac{\vartheta_{\mu m}}{\sigma_{\mu m}^2}\exp\left(-\frac{\vartheta_{\mu m}^2}{2\sigma_{\mu m}^2}\right). \tag{9}$$

Here, $\overline{\vartheta_{\mu m}} = \sqrt{\pi/2}\,\sigma_{\mu m}$, $\overline{\vartheta_{\mu m}^2} = 2\sigma_{\mu m}^2$, and the overbar denotes averaging over the statistical ensemble of scatterers.

There is great variety [6] of the experimental angular dependences $F(\theta_\mu, \theta_m)$ of the backscattering strength in shallow-water ocean regions, and this variety is determined by the wave size of the bottom scatterers and by the physical properties of the sediments. The dependences that fit the majority of experimental data are those of Lambert and Lommel–Zeeliger [7–9]. In further considerations, we use the Lambert scattering diagram corresponding to equal scattering strengths in all directions, i.e., to the isotropy of scattering in the vertical plane. The angular distribution of the scattered field is given by the expression

$$F(\theta_\mu, \theta_m) = \sqrt{\sin\theta_\mu \sin\theta_m}. \tag{10}$$

In this case, the stochastic field of Eq. (8) does not depend on the mode number: $\zeta_{\mu m}(r) = \vartheta(r)\exp[i\phi(r)]$ and $\sigma_{\mu m} = \sigma = \text{const}$. The first theoretical explanation of this simple angular dependence of bottom scattering was given in [14].

The insonified surface is an annular element with area[2]

$$\Delta S_{\mu m} \approx \Delta S = 2\pi r\Delta r_{ac}, \tag{11}$$

where Δr_{ac} is the effective width of the ring, $\Delta r_{ac} = c_{ac}\tau/2 \ll r$, c_{ac} is some effective value of the sound speed, and τ is the duration of the received pulse (or, for complex signals, the duration of the correlation response after its matched processing, which is applied in the reception channel). Note that, because of the intermode dispersion, the duration of the correlation

---

[2] Strictly speaking, the area of the ring depends on the group velocities of normal waves [4, 5], but here we neglect this dependence.

response is several seconds in the case of multimode transmission and reception and can be much longer than the duration of the emitted signal. It is essential that this duration weakly depends on the distance r between the sound source (receiver) and the scattering area. This weak dependence is the consequence of two concurrent effects that influence the response duration in different ways [10]. First, as the distance grows, the intermode dispersion causes an increase in the interval between the pulses corresponding to individual normal waves, which leads to an increase in the total effective duration. Second, the highest modes decay because of attenuation, and the number of the pulses corresponding to intense normal waves decreases. To illustrate this effect, the envelopes of the correlation responses are presented in Fig. 1 for different distances. The signals were recorded by one of the authors of this paper in a shallow-water region of the Barents Sea. This experiment was carried out to study the propagation of the direct (without scattering) narrowband frequency-modulated pulses on a path between a spaced point source and point receiver. The carrier frequency was 240 Hz. Thus, in the low-frequency sensing of the ocean with omnidirectional sources and receivers, the width Δr_{ac} of the ring was about 1 km. This value is comparable with the period of interference-caused beats of the sound field in the waveguide, $D = 2\pi/|\xi_{m,\mu} - \xi_{n,\nu}|$, and, in accordance with our assumption, is much greater than the length r_c of spatial correlation: $r_c \ll \Delta r_{ac} \sim D$. Hence, in modeling the reverberation signals, one should break down the insonified surface into individual rings (elementary areas) of small width r_c, within which incident and scattered sound fields are constant. Let us denote the radius of such a ring as r_β and the number of rings as B ($B = \Delta r_{ac}/r_c$, $\beta = 1, 2, \ldots, B$, $r - \Delta r_{ac}/2 \le r_\beta \le r + \Delta r_{ac}/2$).

Using Eqs. (7)–(11), one can express the excitation factor (6) of the mode scattered by the βth ring as

$$b_\mu(r_\beta, z_b) = \sqrt{2\pi r_\beta r_c}\,\vartheta(r_\beta)\exp[i\phi(r_\beta)] \times \psi_\mu(r_\beta, z_b)\sqrt{\sin\theta_\mu}\sum_{m=1}^{M}\sqrt{\sin\theta_m}\,w_m(r_\beta, z_b). \quad (12)$$

Then, according to Eqs. (4) and (5), the complex amplitude of the scattered field at the reception point takes the form

$$P(r) = \sqrt{\frac{1}{8\pi}}\exp(i\pi/4) \times \sum_{\beta=1}^{B}\sum_{\mu=1}^{M}\frac{b_\mu(r_\beta, z_b)\psi_\mu(0, z_r)}{\sqrt{\xi_\mu(0)r_\beta}}\exp\left[i\int_0^{r_\beta}\xi_\mu(r')dr'\right]. \quad (13)$$

Thus, Eq. (13) explicitly describes the total sound field scattered by the bottom inhomogeneities. With this expression, one can easily obtain the well-known formula [4, 5] for the averaged intensity $I_{sc} = |P(r)|^2/\rho_r c_r$ of the sound field at the reception point:

$$\langle I_{sc}\rangle = \frac{\sigma^2\rho_s c_s W_0 \tau c_{ac}}{4r\rho_r c_r}\sum_{\mu=1}^{M}\sum_{m=1}^{M}\sin\theta_\mu\sin\theta_m \times \frac{|\psi_\mu(0, z_r)|^2|\psi_\mu(r, z_b)|^2}{|\xi_\mu(0)||\xi_m(r)|}|\psi_m(0, z_s)|^2 \times |\psi_m(r, z_b)|^2\exp\left\{-\int_0^r[\gamma_\mu(r') + \gamma_m(r')]dr'\right\}. \quad (14)$$

Here and below, the angular brackets mean averaging over a spatial interval that is greater than the period D of the interference beats and, consequently, much greater than the length r_c of spatial correlation. In Eq. (14), $\rho_r = \rho(0, z_r)$ and $c_r = c(0, z_r)$ are the water density and the sound speed at depth z_r.

B. Single-Mode Reverberation Regime

Let us now consider the reverberation in the case of linear vertical arrays with signal transmission and reception matched to a single normal wave, for instance, the first one. This situation is especially interesting in connection with the development of the mode tomography in oceanic waveguides [15]. The technique of tuning the arrays to emit (receive) individual normal waves can be found in [16].

Suppose that the sources are at depths z_j, $j = 1, 2, \ldots, J$, where J is the number of individual sound sources. According to [16], we specify the particle velocity at the surface of the jth source to be proportional to the complex-conjugate eigenfunction $\psi_1^*(0, z_j)$ of the first mode. The associated emitted power is

$$W_j = \kappa_j|\psi_1(0, z_j)|^2 W_0, \quad (15)$$

where W_0 is the total power emitted by the vertical array with noninteracting array elements. From the normalization condition $\sum_{j=1}^{J} W_j = W_0$, in view of Eq. (15), the following expression for the proportionality factor κ_j can be obtained:

$$\kappa_j = \kappa_0 = \left[\sum_{j=1}^{J}|\psi_1(0, z_j)|^2\right]^{-1}. \quad (16)$$

Let us summarize the fields of the point sources. Then, in view of Eqs. (15) and (16), the field $p_{ar}(r, z)$ of the array at a large horizontal distance r can be expressed as

$$p_{ar}(r, z) = \sum_{m=1}^{M} p_m(r, z), \quad (17)$$

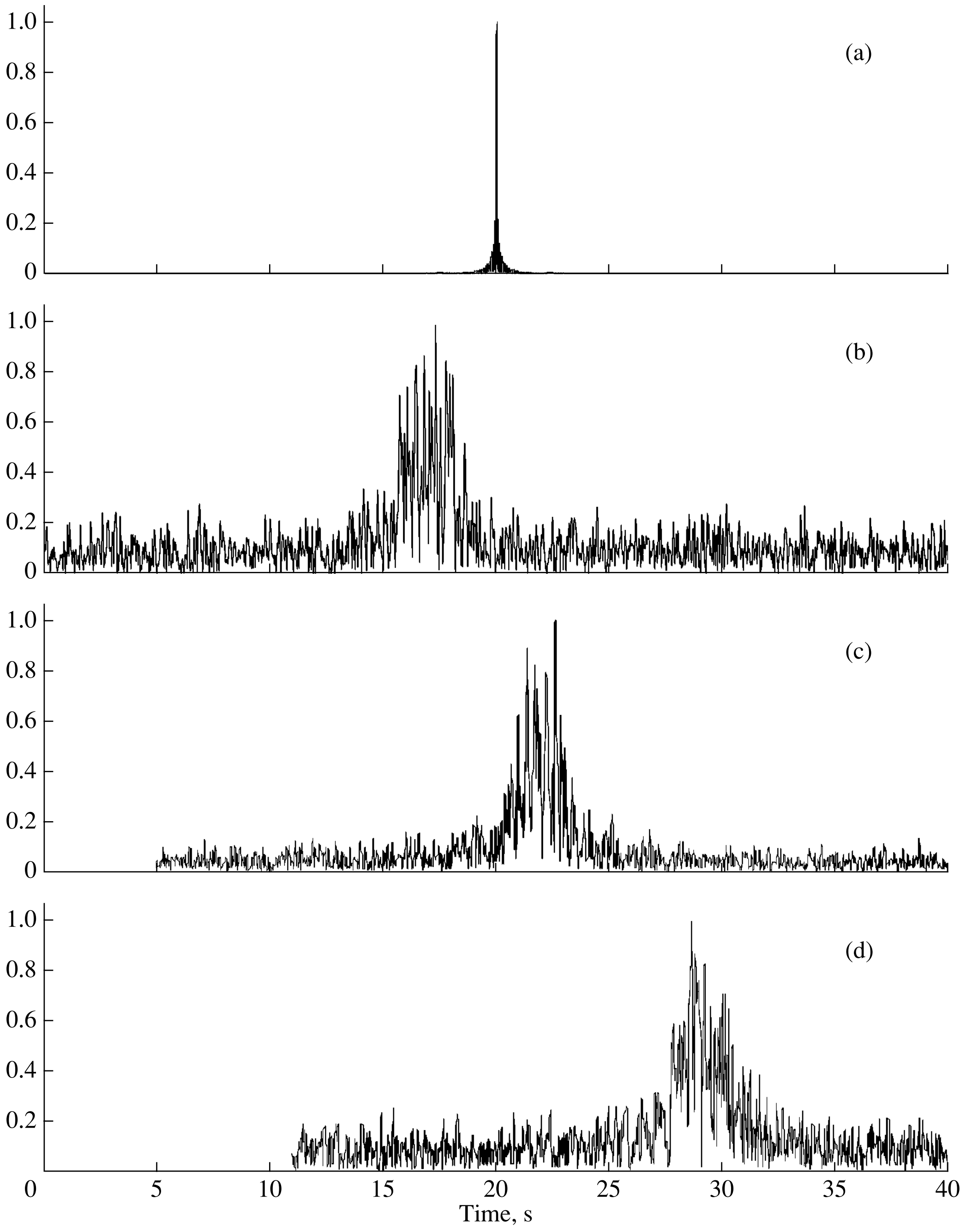

Fig. 1. Signal envelope at the output of the correlation receiver: the distance from the source is (a) 1 m, (b) 23.5 km, (c) 31.1 km, and (d) 39.6 km.

where

$$p_m(r, z) = a_m \frac{\psi_m(r, z)}{\sqrt{\xi_m(r) r}} \exp\left[i \int_0^r \xi_m(r') dr' \right]. \quad (18)$$

Here,

$$a_m = \sqrt{\kappa_0 W_0} \exp(i\pi/4)$$
$$\times \sum_{j=1}^{J} \sqrt{\rho_j c_j} \psi_1^*(0, z_j) \psi_m(0, z_j) \quad (19)$$

is the excitation factor of the *m*th mode.

Suppose that the elements of the receiving array are at depths z_i, $i = 1, 2, \ldots, I$, where I is the number of reception channels. Let the transfer ratio of the *i*th channel be $q_i = \upsilon_i \psi_1^*(0, z_i)$. The quantity υ_i can be found from the condition that the sum of the transfer ratios over all channels equals unity:

$$\upsilon_i = \upsilon_0 = \left[\sum_{i=1}^{I} |\psi_1(0, z_i)| \right]^{-1}. \quad (20)$$

With the approach accepted above, let us find the scattered field at the output of each receiver of the array. By combining these fields with the weighting factors q_i and using Eq. (20), the array response $u_{ar}(r, z_b)$ (the signal at the array output) can be written as

$$u_{ar}(r, z_b) = \sum_{\beta=1}^{B}\sum_{\mu=1}^{M}\sum_{m=1}^{M}\frac{a_\mu\psi_\mu(r_\beta, z_b)}{\sqrt{\xi_\mu(0)r_\beta}} \times \exp\left[i\int_0^{r_\beta}\xi_\mu(r')dr'\right]T_{\mu m}(r_\beta, z_b)p_m(r_\beta, z_b), \quad (21)$$

where

$$a_\mu = \sqrt{\frac{1}{8\pi}}\exp(i\pi/4)\upsilon_0\sum_{i=1}^{I}\psi_1^*(0, z_i)\psi_\mu(0, z_i). \quad (22)$$

Note that, because of the orthogonality of the eigenfunctions [10], the weighting factor a_1, Eq. (22), is much greater than the factors of other modes if the transmitting and receiving arrays are large enough to cover the most part of the waveguide. Thus, the transmission and reception of a single mode (the first one in our case) take place. Accordingly, there is nearly no increase in the duration of the sound pulse under the effect of the intermode dispersion. In practice, the pulse duration is limited by the frequency band of the sound sources ($\tau \cong 1/\Delta f$) used in the acoustic sensing of the medium. Usually, at low frequencies, the value of τ is 0.025–0.1 s, and the effective width of the ring is $\Delta r_{ac} \cong$ 20–70 m.

With the appropriate spatial averaging, one can obtain the following expression for the mean intensity of the scattered sound field received by the vertical array: $I_{sc}^{ar} = |u_{ar}(r, z_b)|^2/\tilde{\rho}\tilde{c}$. As a result, we have

$$\langle I_{sc}^{ar}\rangle = \frac{2\sigma^2\pi c_{ac}\tau}{r\tilde{\rho}\tilde{c}}\sum_{\mu=1}^{M}\sum_{m=1}^{M}\sin\theta_\mu\sin\theta_m \times \frac{|a_\mu|^2|a_m|^2|\psi_\mu(r, z_b)|^2|\psi_m(r, z_b)|^2}{|\xi_\mu(0)||\xi_m(r)|} \times \exp\left\{-\int_0^r[\gamma_\mu(r') + \gamma_m(r')]dr'\right\}. \quad (23)$$

Here, $\tilde{\rho}$ and $\tilde{c}$ are the density and sound speed averaged over the array aperture.

C. Random Field $\zeta_{\mu m}(r)$ and the Bottom Backscattering Coefficient

To model the bottom reverberation determined by Eqs. (13), (14), (21), and (23), one should establish the relation between the statistical characteristics of the field $\zeta_{\mu m}(r)$ and the backscattering coefficient g, which is a common and measurable parameter characterizing the sound scattering by the ocean bottom. Let us assume that the transmission–reception regime corresponds to the aforementioned multimode reverberation. The average backscattering coefficient g is defined [7] as follows:

$$\langle g\rangle = \frac{\langle W_{sc}\rangle}{\langle I_i\rangle\Delta S} = \frac{\bar{P}_{sc}^2 r_0^2}{\bar{P}_i^2\Delta S}, \quad (24)$$

where W_{sc} is the power scattered by the bottom area ΔS (11) given by Eq. (11) into a unit solid angle, I_i is the intensity of the incident wave in the vicinity of the scattering bottom area, $\bar{P}_{sc}$ is the rms sound pressure of the scattered field near the scattering area, $\bar{P}_i$ is the rms sound pressure of the acoustic field incident on this area, and r_0 = 1 m. In the waveguide conditions of sound propagation, we have $\bar{P}_i = \sqrt{\langle|w_s(r, z_b)|^2\rangle}$, and, according to Eq. (2), the mean value of the intensity $I_i = |w_s(r, z_b)|^2/\rho_b c_b$ has the form

$$\langle I_i\rangle = \frac{\rho_s c_s W_0}{\rho_b c_b r}\sum_{m=1}^{M}\frac{|\psi_m(0, z_s)|^2|\psi_m(r, z_b)|^2}{|\xi_m(r)|} \times \exp\left[-\int_0^r\gamma_m(r')dr'\right], \quad (25)$$

where $\rho_b = \rho(r, z_b)$ and $c_b = c(r, z_b)$. Considering the insonified bottom area as the sound source, we can represent the average intensity of the scattered field at the reception point as

$$\langle I_{sc}\rangle = \frac{\rho_b c_b\langle W_{sc}\rangle}{\rho_r c_r r}\sum_{\mu=1}^{M}\frac{|\psi_\mu(0, z_r)|^2|\psi_\mu(r, z_b)|^2}{|\xi_\mu(0)|} \times \exp\left[-\int_0^r\gamma_\mu(r')dr'\right]. \quad (26)$$

By comparing Eqs. (14) and (26), we obtain

$$\langle W_{sc}\rangle = \frac{\sigma^2\rho_s c_s W_0\tau c_{ac}}{4\rho_b c_b} \times \frac{\displaystyle\sum_{\mu=1}^{M}\sum_{m=1}^{M}\sin\theta_\mu\sin\theta_m\frac{|\psi_\mu(0, z_r)|^2|\psi_\mu(r, z_b)|^2|\psi_m(0, z_s)|^2|\psi_m(r, z_b)|^2}{|\xi_\mu(0)||\xi_m(r)|}\exp\left\{-\int_0^r[\gamma_\mu(r') + \gamma_m(r')]dr'\right\}}{\displaystyle\sum_{\mu=1}^{M}\frac{|\psi_\mu(0, z_r)|^2|\psi_\mu(r, z_b)|^2}{|\xi_\mu(0)|}\exp\left\{-\int_0^r\gamma_\mu(r')dr'\right\}}. \quad (27)$$

The substitution of Eqs. (11), (25), and (27) into Eq. (24) leads to the desired relation between the quantities σ and $\langle g\rangle$:

$$\sigma^2 = 4\pi\langle g\rangle \frac{\sum\limits_{\mu=1}^{M}\frac{|\psi_\mu(0,z_r)|^2|\psi_\mu(r,z_b)|^2}{|\xi_\mu(0)|}\exp\left\{-\int_0^r\gamma_\mu(r')dr'\right\}\sum\limits_{m=1}^{M}\frac{|\psi_m(0,z_s)|^2|\psi_m(r,z_b)|^2}{|\xi_m(r)|}\exp\left\{-\int_0^r\gamma_m(r')dr'\right\}}{\sum\limits_{\mu=1}^{M}\sum\limits_{m=1}^{M}\sin\theta_\mu\sin\theta_m\frac{|\psi_\mu(0,z_r)|^2|\psi_\mu(r,z_b)|^2|\psi_m(0,z_s)|^2|\psi_m(r,z_b)|^2}{|\xi_\mu(0)||\xi_m(r)|}\exp\left\{-\int_0^r[\gamma_\mu(r')+\gamma_m(r')]dr'\right\}}. \quad (28)$$

To obtain the backscattering coefficient at low frequencies ($f \cong 200$ Hz), several experiments were performed in a shallow-water region of the Barents Sea. With the omnidirectional sound source and receiver positioned on a drifting vessel, the bottom-scattered signals that arrived from distances of about $r \cong 10$ km were recorded ($r \cong c_{ac}t/2$, where t is the time elapsed from the beginning of transmission to the moment of reception of the scattered signals). The duration of the pulses was $\tau = 3$ s. The average backscattering coefficient was estimated as

$$\tilde{S} \equiv 10\log\langle g\rangle = 20\log\frac{\bar{P}_{sc0}}{\bar{P}_0} - 40\log\frac{\bar{P}_i}{\bar{P}_0} - 10\log\frac{\Delta S}{r_0^2}, \quad (29)$$

where $\tilde{S}$ is the backscattering strength, $\bar{P}_{sc0}$ is the rms pressure of the scattered sound field at the reception point, and $\bar{P}_0$ is the rms pressure of the emitted field at a distance of 1 m from the source. The second summand on the right-hand side of Eq. (29) is the doubled propagation loss in the waveguide at a distance r. The loss was measured separately, with the use of two vessels. From one of them, a pilot hydrophone was deployed to a depth close to the depth of the waveguide. The second vessel, which went off the first one, towed a calibrated sound source. The measurements of the propagation loss were repeated several times along different directions. The data obtained were subsequently averaged.

The experimental data on the backscattering strength $\tilde{S}(r)$, Eq. (29), are presented in Fig. 2 for three pulsed transmissions. In spite of averaging over a distance exceeding the period of interference beats, a small difference can be seen in the curves corresponding to different pulses. This difference is caused by the vessel drift. The scattering bottom areas changed from pulse to pulse, and averaging incompletely smoothed out the variations of the reverberation signals. Averaging over all pulses and directions showed that the scattering strength was $\tilde{S}$ = 37–47 dB for the regions of experiments in the Barents Sea. The confidence interval was no higher than 4 dB for a given sea region.

The estimate obtained the backscattering coefficient is a mean value corresponding to small grazing angles of the incident and scattered sound waves. In the shallow-water regions at hand, for the first ten most intense modes, the calculations yielded values of 3°–16° for the grazing angles θ_m of the mode-forming rays. It is worth mentioning that the backscattering coefficient determined by the aforementioned technique in a waveguide proves to depend on the distance r. In fact, as the distance increases, the number of most intense modes decreases, and, hence, the effective grazing angle also decreases. At the same time, it is well known [9] that the backscattering coefficient does depend on this angle. For typical propagation conditions of shallow seas, the numerical calculations based on Eq. (28) show that the value of $\langle g\rangle$ noticeably changes at distances of about several tens of kilometers.

NUMERICAL SIMULATION OF BOTTOM SCATTERING

Figure 3 shows the reverberation signals calculated according to Eqs. (13) (multimode regime) and (21) (single-mode regime). The letters in the plots denote different realizations of the scattered field, that is, different scattering areas with different values of $\zeta_{\mu m}(r)$. The smooth curves indicate the levels $P_{sc} = \sqrt{\rho_r c_r\langle I_{sc}\rangle}$ and $P_{sc}^{ar} = \sqrt{\bar{\rho}\bar{c}\langle I_{sc}^{ar}\rangle}$ of the reverberation signals calculated by Eqs. (14) and (23). In the simulation, we chose a regular waveguide with depth z_b = 120 m and the sound speed profile $c(z)$ presented in Fig. 4. The follow-

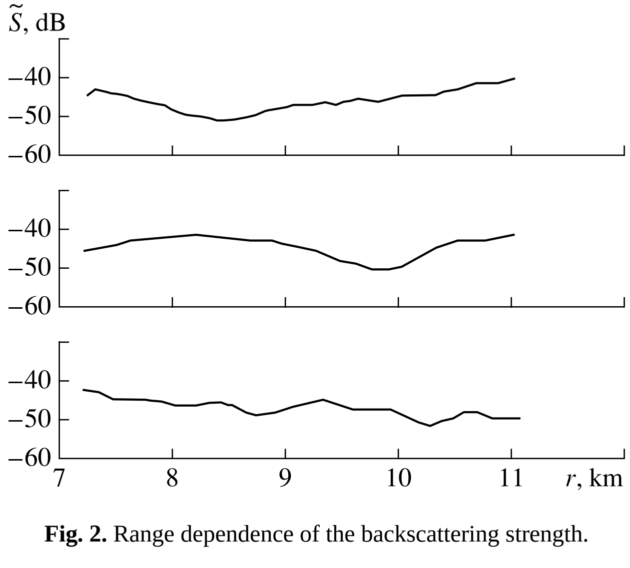

Fig. 2. Range dependence of the backscattering strength.

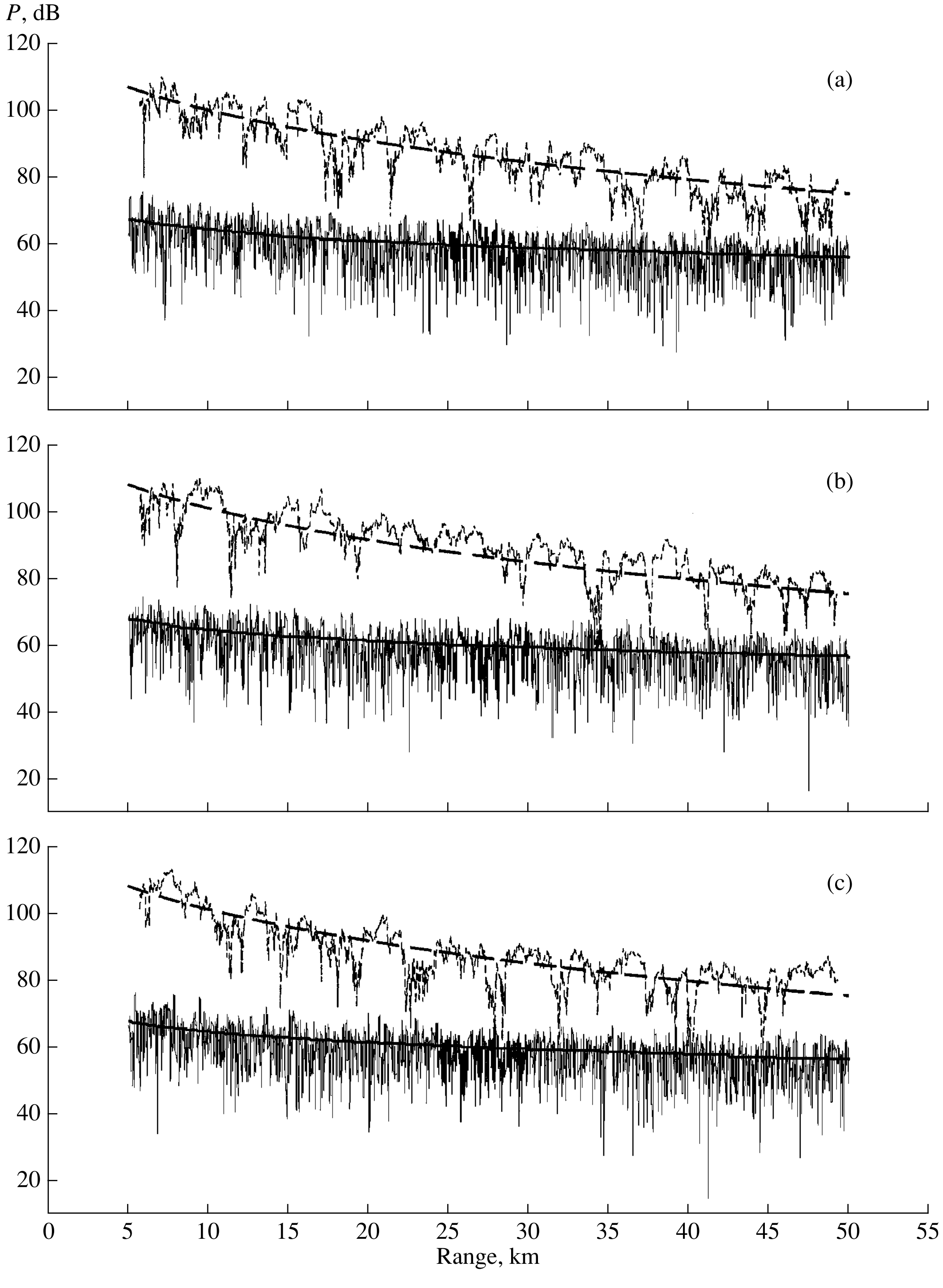

Fig. 3. Model reverberation signals (broken lines) and the mean levels of the reverberation signals (smooth lines). The dashed lines correspond to a point sound source and a point receiver, and the solid lines to vertical transmitting and receiving arrays. The abscissa represents the distance from the source (receiver) to the scattering area.

ing parameters of the homogeneous fluid bottom were specified: the sound speed c_1 = 1750 m/s, the density ρ_1 = 1.9 g/cm^3, and the absorption coefficient α = 0.01 [11]. The correlation length of the bottom inhomogeneities was r_c = 10 m. The carrier frequency of the signals was f_0 = 230 Hz, with the bandwidth Δf = 10 Hz. The power of emitted signals was W_0 = 2 kW, and the backscattering strength was $\tilde{S}$ = 37 dB (for the distance 10 km from the scattering area). In miltimode calculations, the point sound source and the point receiver

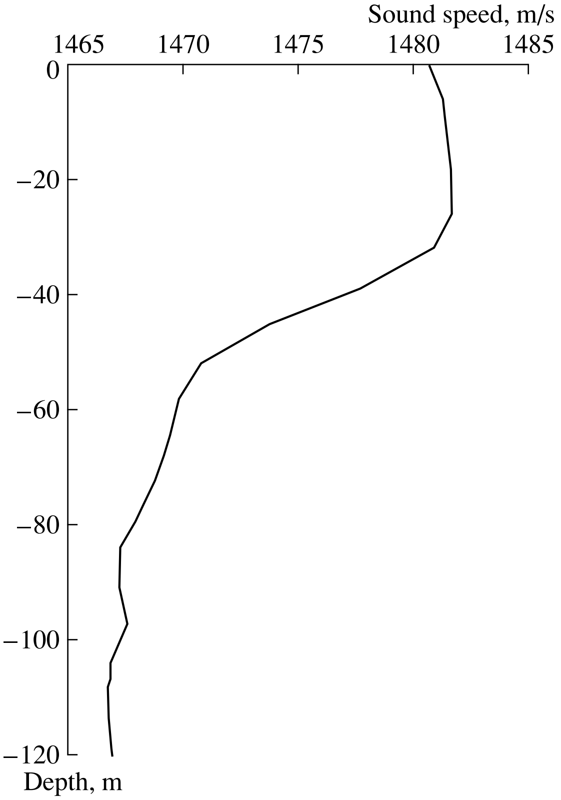

Fig. 4. Vertical sound speed profile.

were placed at the bottom with $z_s = z_r = 120$ m. In single-mode calculations, the transmitting and receiving arrays were assumed to coincide in space. The array length was 87 m. The arrays consisted of 30 equidistant elements each, with the lowest elements positioned at the bottom.

The data presented show that the reverberation signals change considerably when the pulsed transmissions vary. However, in general, the single-mode array response to the scattered signals is much lower that to the signal received by a single receiver in the multimode regime. It is worth mentioning that the difference in the mean levels decreases as the distance to the scattering area increases. This fact can be attributed to the decrease in the number of the intense normal waves that govern the multimode reverberation.

CONCLUSION

Thus, a model of the bottom reverberation in shallow-water ocean regions is developed in the adiabatic approximation. The model describes the statistical characteristics and the interference of the scattered sound field on the basis of the measured values of the bottom backscattering coefficient. The experimental data on the backscattering strength in the waveguide propagation conditions are presented. A numerical simulation of the low-frequency bottom reverberation is carried out for the case of a monostatic monitoring layout. The difference in the long-range reverberation signals is estimated for the cases of transmission and reception by omnidirectional sources and receivers and by long vertical arrays matched to excitation and reception of the first normal wave.

ACKNOWLEDGMENTS

This work was supported by the Russian Foundation for Basic Research, project no. 02-02-16509, and the Federal Objective Program “Integration of Science and Higher Education in Russia for 2002–2006,” project no. I04-10.

REFERENCES

1. Yu. M. Sukharevskiĭ, Dokl. Akad. Nauk SSSR **55** (9), 823 (1947).
2. Yu. M. Sukharevskiĭ, Dokl. Akad. Nauk SSSR **58** (2), 229 (1947).
3. R. Zhang and G. Jin, J. Sound Vibr. **119**, 215 (1987).
4. D. D. Ellis, J. Acoust. Soc. Am. **97**, 2804 (1995).
5. V. M. Kudryashov, Akust. Zh. **45**, 363 (1999) [Acoust. Phys. **45**, 320 (1999)].
6. F. Li, J. Lin, and R. Zhang, in *Proceedings of 8th Western Pacific Acoustics Conference, Melbourne, Australia* (2003).
7. V. I. Volovov and Yu. Yu. Zhitkovskiĭ, in *Acoustics of the Ocean*, Ed. by L. M. Brekhovskikh (Nauka, Moscow, 1974), pp. 395–490.
8. V. I. Volovov and Yu. Yu. Zhitkovskiĭ, Vopr. Sudostr., Ser. Akust., No. 8, 126 (1977).
9. A. V. Bunchuk and Yu. Yu. Zhitkovskiĭ, Akust. Zh. **26**, 641 (1980) [Sov. Phys. Acoust. **26**, 363 (1980)].
10. B. G. Katsnel’son and V. G. Petnikov, *Acoustics of a Shallow Sea* (Nauka, Moscow, 1997).
11. Yu. P. Lysanov, Akust. Zh. **17**, 93 (1971) [Sov. Phys. Acoust. **17**, 74 (1971)].
12. V. A. Grigor’ev, B. G. Katsnel’son, V. M. Kuz’kin, and V. G. Petnikov, Akust. Zh. **47**, 44 (2001) [Acoust. Phys. **47**, 35 (2001)].
13. Young-Chung Cho, J. Acoust. Soc. Am. **67**, 1421 (1980).
14. N. P. Chotiros, in *Proceedings of 5th European Conference on Underwater Acoustics, Lyon, France* (2000), Vol. 2, p. 1271.
15. V. Yu. Zaĭtsev, A. G. Nechaev, and L. A. Ostrovskiĭ, in *Acoustics of the Oceanic Medium*, Ed. by L. M. Brekhovskikh and I. B. Andreeva (Nauka, Moscow, 1989), pp. 98–107.
16. J. H. Miller, Ching-Sang Chiu, and J. F. Lynch, in *Proceedings of the International Conference on Theoretical and Computational Acoustics, Mystik* (1993).

Translated by E. Kopyl

Acoustical Physics, Vol. 50, No. 1, 2004, pp. 46–51. Translated from Akusticheskiĭ Zhurnal, Vol. 50, No. 1, 2004, pp. 55–61.
Original Russian Text Copyright © 2004 by Zaslavskiĭ.

Parametric Scattering of High-Frequency Elastic Waves by a Small Spherical Cavity Oscillating under the Action of a Rayleigh Wave

Yu. M. Zaslavskiĭ

Institute of Applied Physics, Russian Academy of Sciences,
ul. Ul'yanova 46, Nizhni Novgorod, 603950 Russia
e-mail: zaslav@hydro.appl.sci-nnov.ru

Received January 14, 2003

Abstract—Scattering of high-frequency transverse and longitudinal plane waves incident on a spherical cavity located at a small depth under the surface of a half-space is considered. The cavity oscillates as a whole in the field of a low-frequency Rayleigh surface wave, the oscillation vectors of the longitudinal, transverse, and surface waves being coplanar. The cavity radius is assumed to be small compared to the wavelengths of the sounding wave and the pumping surface wave. The scattered compression and shear waves at the combination frequencies $\omega \pm \Omega$ are calculated in the dipole approximation. Expressions obtained describe the qualitative behavior of the combination-frequency signal levels produced at the outputs of horizontally and vertically oriented geophones moving over the free surface of the elastic half-space. *© 2004 MAIK "Nauka/Interperiodica".*

INTRODUCTION

This paper presents the results of calculating the characteristics of elastic waves generated at combination frequencies due to the parametric scattering of longitudinal (first version) or transverse (second version) waves (*P* or *SV* waves) incident on a hollow spherical cavity at a certain depth under the free surface of an elastic half-space (Fig. 1). The elastic half-space, in its turn, is excited by an intense low-frequency vibrator, which generates a pumping Rayleigh surface wave at a low frequency Ω. The latter wave travels near the surface and causes the cavity to oscillate as a whole. In addition, a high-frequency vibrator positioned on the surface of the half-space produces a directional beam of plane longitudinal waves at frequency ω. The beam is incident on the spherical cavity, which represents a small inhomogeneity for the bulk waves; i.e., its linear dimension is noticeably smaller than the shortest wavelength of the high-frequency transverse wave, so that the inequalities $2\pi c_R/\Omega \gg 2\pi c_{l,\,t}/\omega \gg a$ are valid under the conditions of the problem. Another configuration considered in this paper is with a high-frequency vibrator placed at a certain depth under the surface, such that it produces a directional sounding beam of plane transverse waves at a frequency ω, which covers the depth of the inhomogeneity. Both the above statements of the problem are of interest for estimating the parameters of the desired signals when they are received in the presence of signals caused by the linear scattering from inhomogeneities located, for example, at a small depth under the earth's surface. The desired signals are the signals at combination frequencies associated with the parametric scattering from the oscillating inhomogeneity. On the whole, this analysis is performed to predict the possibility of solving various problems of nondestructive testing and monitoring of media and structural units, nondestructive testing of machines, and medical diagnostics [1]. Note, for example, a similar effect of combination scattering of high-frequency acoustic waves, which produces Doppler shifted frequency components that can be used to check a liquid jet for the presence of gas bubbles and to estimate their properties [2]. This class of problems also includes such applied geophysical problems as sounding of shallow engineering structures, which is the main area of application of the approach developed in this paper. At present, experiments on the seismic sounding of inhomogeneities in the ground are performed in a variety of configurations [3, 4]. However, the application of the parametric scat-

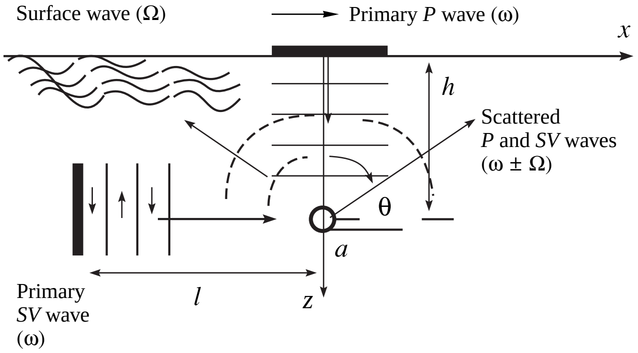

Fig. 1. Schematic diagram of the parametric scattering of high-frequency elastic waves from an inhomogeneity.

1063-7710/04/5001-0046$26.00 © 2004 MAIK "Nauka/Interperiodica"

tering of plane waves for these purposes requires special consideration.

THEORY AND ESTIMATES

Let a low-frequency Rayleigh surface wave travel in the positive x direction along the boundary $z = 0$. The wave is described by two displacement components (the $\exp(-i\Omega t)$ factor is omitted) [5]:

$$U_x = \frac{A_0 e^{ik_R x}}{\sqrt{1-\left(\frac{c_R}{c_l}\right)^2}} = \left\{ \exp\left[-\frac{\Omega z}{c_R}\sqrt{1-\left(\frac{c_R}{c_l}\right)^2}\right] - \frac{2\sqrt{1-\left(\frac{c_R}{c_l}\right)^2}\sqrt{1-\left(\frac{c_R}{c_t}\right)^2}}{2-\left(\frac{c_R}{c_t}\right)^2}\exp\left[-\frac{\Omega z}{c_R}\sqrt{1-\left(\frac{c_R}{c_t}\right)^2}\right]\right\}, \tag{1}$$

$$U_z = -iA_0 \mathrm{e}^{ik_R x}\left\{ \exp\left[-\frac{\Omega z}{c_R}\sqrt{1-\left(\frac{c_R}{c_l}\right)^2}\right] - \frac{2}{2-\left(\frac{c_R}{c_t}\right)^2}\exp\left[-\frac{\Omega z}{c_R}\sqrt{1-\left(\frac{c_R}{c_t}\right)^2}\right]\right\}, \tag{2}$$

where c_R, c_l, and c_t are the velocities of the Rayleigh wave, the longitudinal bulk wave, and the transverse bulk wave, respectively, and $k_R = \Omega/c_R$.

We assume that the hollow cavity oscillates exactly as does its center corresponding to a certain point of the medium, which in turn oscillates in the Rayleigh wave unperturbed by the inhomogeneity. The main condition for this situation to take place is the inequality $a \ll h \approx \lambda_R$; i.e., the wavelength of the surface wave must be approximately equal to the depth of the inhomogeneity and much greater than the radius of the cavity [5].

Consider the first version of the problem. It assumes that the inhomogeneity oscillates in the field of the primary high-frequency longitudinal wave produced by a piston vibrating at the surface. The oscillating inhomogeneity creates an alternating dipole moment, which is equivalent to the alternating force that acts on the medium at the high frequency ω [6], these oscillations being phase modulated by the oscillations at the low frequency Ω. The vertical Rayleigh wave component creates an alternating phase delay, so that the dipole strength can be written as

$$\mathbf{F} \cong \mathbf{z}^0 4\pi\rho c_t^2 a u_z^{P(\omega)} \times \exp\left(-i\omega t - i\frac{\omega}{c_l}U_z^{R(\Omega)}(h)\cos(\Omega t)\right), \tag{3}$$

where $\mathbf{z}^0$ is the unit vector of the vertical axis, $u_z^{P(\omega)}$ is the z component of the high-frequency plane compression wave in the region occupied by the inhomogeneity and covered by the directional beam, and $U_z^{R(\Omega)}(h)$ is the z component of the low-frequency surface Rayleigh wave given by formula (2) at $z = h$.

The expression for $\mathbf{F}$ assumes that the inequality $c_l^2 \gg c_t^2$ holds and the cavity is hollow, which allows us to write it in form (3) without any significant loss of generality. This formula with the periodic function in the exponent can be expanded in the series in terms of harmonics of frequency Ω [7]:

$$\begin{aligned}\exp(-i(\omega/c_l)U_z^{R(\Omega)}\cos(\Omega t)) &= J_0((\omega/c_l)U_z^{R(\Omega)}) \\ &+ 2\sum_1^\infty(-1)^n J_{2n}((\omega/c_l)U_z^{R(\Omega)})\cos 2n\Omega t \\ &- 2i\sum_0^\infty(-1)^n J_{2n+1}((\omega/c_l)U_z^{R(\Omega)})\cos(2n+1)\Omega t,\end{aligned}$$

with the Bessel functions as the coefficients. Truncating the series beyond its first term under the condition $(\omega/c_l)U_z^{R(\Omega)} \ll 1$ and replacing the function $2J_1((\omega/c_l)U_z^{R(\Omega)})$ with its argument yields the formula for the first Stokes and anti-Stokes harmonics of the dipole moment:

$$F_{1z} = 2\pi\rho c_t^2 a\frac{\omega}{c_l}u_z^{P(\omega)}U_z^{R(\Omega)}(h) \times(\exp-i(\omega+\Omega)t + \exp-i(\omega-\Omega)t). \tag{4}$$

For all subsequent terms F_{nz}, $n = 2, 3\ldots$, a similar formula is valid. The combination-frequency waves, $P(\omega \pm \Omega)$ and $S(\omega \pm \Omega)$, scattered by the oscillating inhomogeneity can easily be calculated using expression (4) for the dipole strength as secondary fields produced by the dipole moment.

Finally, the vertical and horizontal components of the seismic signals received by geophones on the earth's surface can be calculated, which is of practical interest. For simplicity, the field is calculated below only on the x axis, which lies in the same vertical plane as the inhomogeneity (Fig. 1). To reflect the real situation, it will be necessary to allow for the attenuation of the primary sounding wave incident on the inhomogeneity and the attenuation of the scattered waves at the combination frequencies within the distance from the scatterer to the geophones on the earth's surface. In addition, the scattered longitudinal and transverse waves will be transformed into one another at the reflection from the free surface. This effect should also be taken into account in the estimates of the resultant seismic response recorded by the geophones.

The longitudinal r component of the compression wave received at an arbitrary distance r from the source is given by the expression

$$u_r^P = \frac{F_{1z}\cos\theta}{4\pi\rho c_l^2 r}\exp\left\{i\frac{(\omega\pm\Omega)r}{c_l} - \frac{\Theta_l(\omega\pm\Omega)r}{2c_l}\right\}, \quad (5)$$

where θ is the polar angle measured relative to the dipole axis (z axis) and Θ_l is the damping decrement of the longitudinal waves in the ground [8].

A similar formula describes the transverse θ component of the shear wave excited by this source at the same distance:

$$u_\theta^S = -\frac{F_{1z}\sin\theta}{4\pi\rho c_t^2 r}\exp\left\{i\frac{(\omega\pm\Omega)r}{c_t} - \frac{\Theta_t(\omega\pm\Omega)r}{2c_t}\right\}, \quad (6)$$

where Θ_t is the damping decrement of the transverse wave in the ground.

In formulas (5) and (6), we should use Eq. (4) for the dipole strength with an allowance for the loss due to the attenuation of the sounding wave on its path from the high-frequency source placed at the surface to the inhomogeneity located at depth h. The mutual $P \longleftrightarrow S$ wave transformation on the free surface can be taken into account by the assumption that the waves are locally planed, so that the well-know formulas [9] for acoustic waves scattered by a planar solid body–free space interface can be used.

The longitudinal and transverse waves scattered from the oscillating sphere at the combination frequencies can be represented as

$$\begin{aligned} u_r^P(\omega\pm\Omega) &= \frac{c_t^2 a\omega u_{z0}^{P(\omega)} U_z^{R(\Omega)}(h)\cos\theta}{2c_l^3 r} \\ &\times \exp\left\{-i(\omega\pm\Omega)\left(t-\frac{r}{c_l}\right) - \frac{\Theta_l}{2c_l}(\omega h + (\omega\pm\Omega)r)\right\}, \end{aligned} \quad (7)$$

$$\begin{aligned} u_\theta^S(\omega\pm\Omega) &= -\frac{a\omega u_{z0}^{P(\omega)} U_z^{R(\Omega)}(h)\sin\theta}{2c_l r} \\ &\times \exp\left\{-i(\omega\pm\Omega)\left(t-\frac{r}{c_t}\right) - \frac{\Theta_l\omega h}{2c_t} - \frac{\Theta_t(\omega\pm\Omega)r}{2c_t}\right\}, \end{aligned} \quad (8)$$

where $u_{z0}^{P(\omega)}$ is the amplitude of the sounding wave in the immediate vicinity of the vibrating piston. Below, we use the relationship $r = h/\cos\theta$.

The responses of the horizontally and vertically (x, z) oriented geophones, which are placed on the earth's surface along the line extending above the inhomogeneity from the high-frequency signal source to the low-frequency Rayleigh wave source, to the total seismic signal can be expressed in terms of the amplitudes of the scattered waves:

$$\begin{aligned} U_x &= \sin\theta\lfloor(1+V_{ll})e^{-i\Delta\phi}u_r^P(\omega\pm\Omega) + V_{tl}u_\theta^S(\omega\pm\Omega)\rfloor \\ &+ \cos\theta[(1+V_{tt})u_\theta^S(\omega\pm\Omega) + V_{lt}e^{-i\Delta\phi}u_r^P(\omega\pm\Omega)], \end{aligned} \quad (9)$$

$$\begin{aligned} U_z &= \cos\theta\lfloor(1+V_{ll})e^{-i\Delta\phi}u_r^P(\omega\pm\Omega) + V_{tl}u_\theta^S(\omega\pm\Omega)\rfloor \\ &- \sin\theta[(1+V_{tt})u_\theta^S(\omega\pm\Omega) + V_{lt}e^{-i\Delta\phi}u_r^P(\omega\pm\Omega)], \end{aligned} \quad (10)$$

where the spectral components of responses at combination frequencies are determined with allowance for the phase difference $\Delta\phi$ due to the difference in the times of arrival of the longitudinal and transverse waves at the geophone and for the reflection and transformation effects at the solid body–free space interface. The output signals of the x and y geophones are determined by the elastic displacements in both waves calculated by Eqs. (7) and (8). The reflection and transformation coefficients V_{ll}, V_{lt}, V_{tl}, and V_{tt}, which enter into Eqs. (9) and (10), and the phase difference $\Delta\phi$ are given by the expressions [9]

$$V_{ll} = \frac{\dfrac{2c_t^3\sin\theta\sin2\theta}{c_1^3}\sqrt{1-\dfrac{c_t^2\sin^2\theta}{c_l^2}} - 1 + \dfrac{4c_t^2\sin^2\theta}{c_l^2}\left(1-\dfrac{c_t^2\sin^2\theta}{c_l^2}\right)}{\dfrac{2c_t^3\sin\theta\sin2\theta}{c_l^3}\sqrt{1-\dfrac{c_t^2\sin^2\theta}{c_l^2}} + 1 - \dfrac{4c_t^2\sin^2\theta}{c_l^2}\left(1-\dfrac{c_t^2\sin^2\theta}{c_l^2}\right)}, \quad (11)$$

$$V_{tl} = \frac{\sin4\theta}{\cos^2 2\theta + 2\sin\theta\sin2\theta\sqrt{\dfrac{c_t^2}{c_l^2} - \sin^2\theta}}, \quad (12)$$

$$V_{lt} = -\frac{2\frac{c_t^2}{c_l^2}\sin 2\theta\left(1-2\frac{c_t^2}{c_l^2}\sin^2\theta\right)}{\left(1-2\frac{c_t^2}{c_l^2}\sin^2\theta\right)^2+2\frac{c_t^2}{c_l^2}\sin 2\theta\sin\theta\sqrt{1-\frac{c_t^2}{c_l^2}\sin^2\theta}}, \quad (13)$$

$$V_{tt} = -\frac{\cos^2 2\theta - 2\sin 2\theta\sin\theta\sqrt{\frac{c_t^2}{c_l^2}-\sin^2\theta}}{\cos^2 2\theta + 2\sin 2\theta\sin\theta\sqrt{\frac{c_t^2}{c_l^2}-\sin^2\theta}}, \quad (14)$$

$$\Delta\phi = \frac{\omega h}{\cos\theta}\left(\frac{1}{c_t}-\frac{1}{c_l}\right). \quad (15)$$

Figure 2 shows the amplitudes of the $\omega \pm \Omega$ spectral components at the outputs of both geophones versus their position on a $10\lambda_R$-long portion of the axis for different inhomogeneity depths $\omega h/c_t$ = (a) 4, (b) 8, (c) 12, (d) 16, and (e) 20. The curves were calculated with the parameters $c_l/c_t = 1.73$, $\Theta_l = 0.03$, $\Theta_t = 0.06$, and $\omega/\Omega = 10$ using the Mathcad 2001 software package. It can easily be seen that the typical maximum of the curves representing the level of the seismic response versus the distance to the inhomogeneity epicenter moves rightwards with increasing inhomogeneity depth, the behavior being somewhat different for the x and z geophones, which should be taken into account in realizing the nondestructive testing technique or in monitoring real media. When the parameters, such as both frequencies ω and Ω and both propagation velocities c_l and c_t, are known, the inhomogeneity depth h can be determined from the position of the maximum and from other typical features of the plots.

In the second version of the problem, the sounding field is a high-frequency beam of transverse plane waves launched along the free earth's surface (see Fig. 1). This situation is analyzed in a similar way with the natural assumption that the source has the form of a vertically oriented piston inserted into the medium, it vibrates tangentially to the working surface and is at a certain distance l from the center of the hollow spherical cavity, which lies at depth h under the free boundary. Unlike the first version, this configuration uses the z component of the high-frequency shear wave and the x component of the low-frequency Rayleigh wave to produce a phase modulation of the sounding shear wave. Here, the dipole strength is given by a similar formula:

$$\mathbf{F} \equiv \mathbf{z}^0 4\pi\rho c_t^2 a u_z^{S(\omega)} \times \exp\left(-i\omega t - i\frac{\omega}{c_t}U_x^{R(\Omega)}(h)\cos\Omega t\right), \quad (16)$$

where $U_x^{R(\Omega)}(h)$ is the x component of the Rayleigh wave at $z = h$ (see Eq. (1)), and the amplitudes of the first combination (Stokes's and anti-Stokes's) harmonics are

$$F_{1z} = 2\pi\rho c_t a\omega u_z^{S(\omega)}U_x^{R(\Omega)}(h) \times (\exp - i(\omega+\Omega)t + \exp - i(\omega-\Omega)t). \quad (17)$$

In this case, the scattered longitudinal and transverse combination waves are represented by expressions similar to Eqs. (7) and (8):

$$u_r^P(\omega\pm\Omega) = \frac{c_t a\omega u_{z0}^{S(\omega)}U_x^{R(\Omega)}(h)\cos\theta}{2c_l^2 r} \times \exp\left\{-i(\omega\pm\Omega)\left(t-\frac{r}{c_l}\right)-\frac{\Theta_t\omega l}{2c_t}-\frac{\Theta_l(\omega\pm\Omega)r}{2c_l}\right\}, \quad (18)$$

$$u_\theta^S(\omega\pm\Omega) = -\frac{a\omega u_{z0}^{S(\omega)}U_x^{R(\Omega)}(h)\sin\theta}{2c_t r} \times \exp\left\{-i(\omega\pm\Omega)\left(t-\frac{r}{c_t}\right)-\frac{\Theta_t(\omega l+(\omega\pm\Omega)r)}{2c_t}\right\}. \quad (19)$$

Now, we use the same relationships (9) and (10) with expressions (18) and (19) for $u_r^P(\omega \pm \Omega)$ and $u_\theta^S(\omega \pm \Omega)$ substituted into them to evaluate the response to the total seismic signal at the outputs of the horizontally and vertically (x, z) oriented geophones, i.e., U_x and U_z. Similar calculations of the $\omega \pm \Omega$ spectral component at the outputs of both geophones at $l = h$ for the same parameters as in the previous case have shown that, as the inhomogeneity goes deeper under the surface, a minimum of the signal level is observed at depth $h\Omega/c_R = 1.2$, because the x component of the low-frequency surface wave passes through zero at this depth ($h \approx 0.2\lambda_R$). This minimum is illustrated in Fig. 3. In the previous sounding configuration, the signal level decreased with increasing inhomogeneity depth in a more monotonic manner. This behavior can serve as an additional indication of the presence of the inhomogeneity and as a measure of its depth. However, the signal amplitudes observed in this sounding scheme are an order of magnitude lower than those in the first sounding configuration. Therefore, the second scheme may apparently be regarded as an additional refining option.

Finally, note that the estimates of the signals scattered by the inhomogeneity in a linear way and of those scattered parametrically show that the first ones are $\omega U^{R(\Omega)}/c_{l,t}$ times greater, which amounts to 70–80 dB for soft ground ($c_l \sim 300$ m/s, $c_t \sim 170$ m/s, $U^{R(\Omega)} \sim 10$ μm, $\omega \sim 2\pi 300$ s^{-1}, and $\Omega \sim 2\pi(20$ to $30)$ s^{-1}), and is even greater for rigid ground, because the surface wave amplitude in it is much lower under the action of the

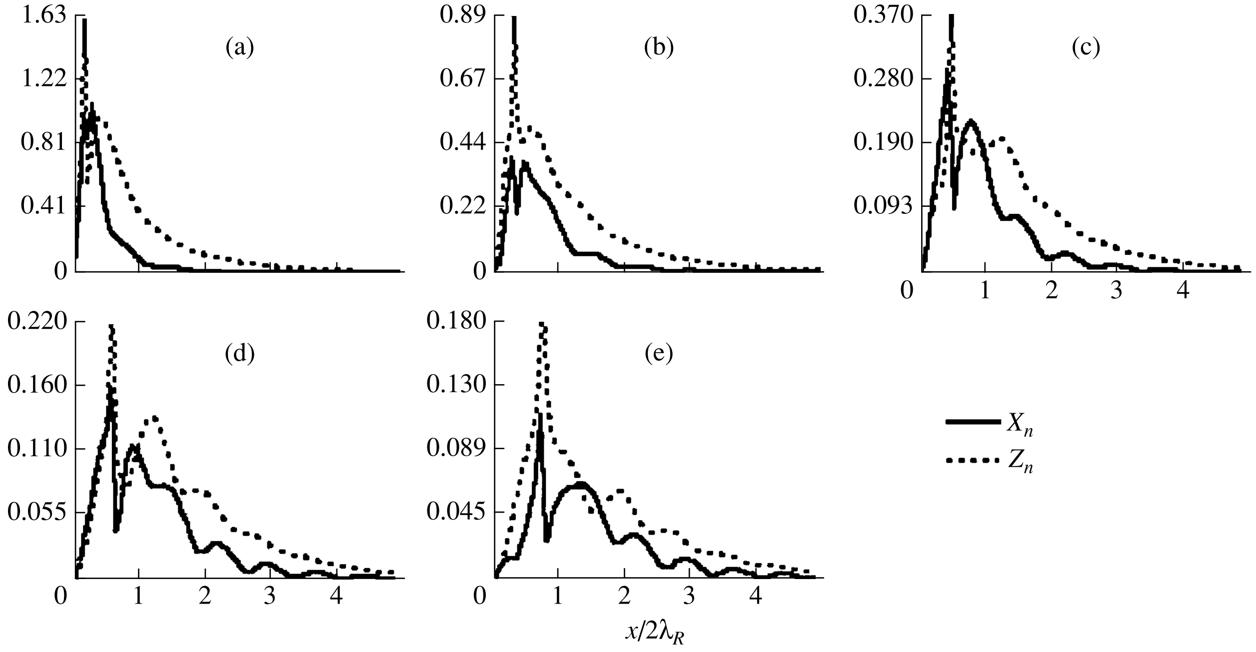

Fig. 2. Signal amplitude (in arbitrary dimensionless units) at the outputs of the (solid lines) x- and (dotted lines) z-polarized geophones versus the distance along the x axis for the first sounding scheme at h = (a) $0.2\lambda_R/\pi$, (b) $0.4\lambda_R/\pi$, (c) $0.6\lambda_R/\pi$, (d) $0.8\lambda_R/\pi$, and (e) λ_R/π.

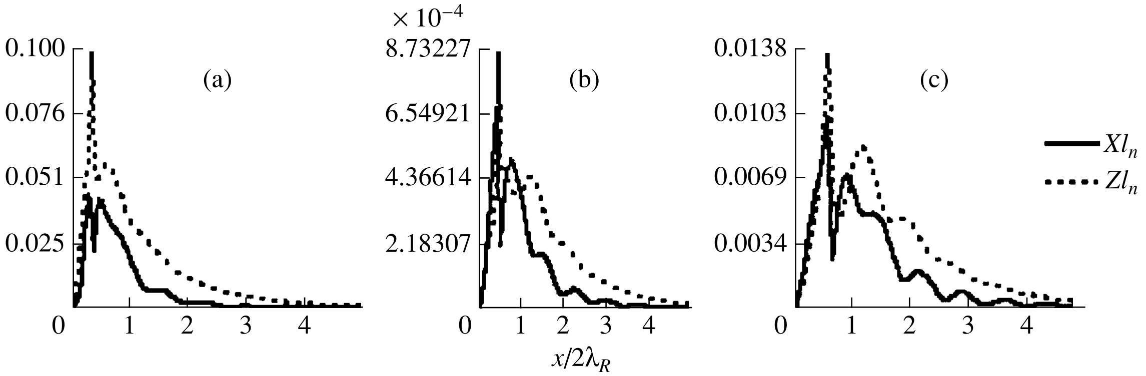

Fig. 3. Signal amplitude (in arbitrary dimensionless units) at the outputs of the (solid lines) x- and (dotted lines) z-polarized geophones versus the distance along the x axis for the second sounding scheme at h = (a) $0.4\lambda_R/\pi$ (b) $0.6\lambda_R/\pi$, and (c) $0.8\lambda_R/\pi$.

same pumping source. This estimate shows how high should be the sensitivity of a system to provide the reception of parametrically scattered elastic waves under even the most favorable geophysical conditions. It is also important to note that the case considered, in which the inhomogeneity has the form of a small hollow spherical cavity, is the most simple for calculations and analysis from the viewpoint of the method used. It can however be assumed that, if the experimental conditions only slightly go beyond the above limitations or the cavity is filled with a material that slightly differs in its density and rigidity from the surrounding medium, the expected level of the parametrically scattered signal will only slightly deviate quantitatively from the above result towards, presumably, lower values. This observation shows that the possibilities and the area of application of the approach used in this study are fairly wide. As for the practical side of the problem, it should be noted that it is the parametric scattering that can be regarded as an efficient countermeasure against sounding interferences due to the backscatter of the primary wave from numerous interfaces in the subsurface layered structure in the upper part of the section, because the oscillations of interfaces in the field of the surface wave noticeably differ from the oscillations of local inhomogeneities.

CONCLUSIONS

A qualitative analysis of the parametric scattering of high-frequency longitudinal and transverse waves from a spherical cavity of small wave dimensions, which lies at a small depth under the earth's surface and oscillates under the action of a low-frequency Rayleigh surface wave, is performed. Formulas for estimating the level and the angular distribution of the parametrically scattered compression and shear waves at combination frequencies are obtained. Theoretical results are presented in the form of plots for a number of depths at a given pumping frequency. They can however be referred to a number of pumping frequencies at a given inhomogeneity depth. In applications, the second representation is more important. Note that variations in the pumping frequency can be incorporated into particular techniques and algorithms implemented in the reconnaissance systems. It is shown that the extraction and analysis of seismic signals at the combination frequencies produced by the parametric scattering of waves can basically be used to detect small cavities in the ground and to determine their depth. A practical system must use the data collected by vertically and horizontally oriented geophones changing their positions on the surface in a discrete manner. The recording equipment must be sensitive enough to extract signals 70 to 80 dB lower than the signals produced by the linear acoustic scattering from small inhomogeneities.

ACKNOWLEDGMENTS

This work was supported by the Russian Foundation for Basic Research, project no. 02-02-17089.

REFERENCES

1. Y. Yamakoshi, J. Sato, and T. Sato, IEEE Trans. Ultrason. Ferroelectr. Freq. Control **37** (2), 45 (1990).
2. I. N. Didenkulov, L. M. Kustov, A. I. Mart'yanov, and N. V. Pronchatov-Rubtsov, in *Proceedings of the Nizhni Novgorod Acoustic Scientific Session* (Nizhni Novgorod, 2002), p. 300.
3. V. S. Averbakh, V. V. Artel'nyĭ, B. N. Bogolyubov, *et al.*, Akust. Zh. **47**, 437 (2001) [Acoust. Phys. **47**, 371 (2001)].
4. V. S. Averbakh, B. N. Bogolyubov, D. V. Dolinin, *et al.*, Akust. Zh. **47**, 732 (2001) [Acoust. Phys. **47**, 640 (2001)].
5. I. A. Viktorov, *Acoustic Surface Waves in Solids* (Nauka, Moscow, 1981).
6. M. A. Isakovich, *General Acoustics* (Nauka, Moscow, 1973).
7. *Handbook of Mathematical Functions*, 2nd ed., Ed. by M. Abramowitz and I. A. Stegun (Dover, New York, 1971; Nauka, Moscow, 1979).
8. *Seismic Survey: A Handbook of a Geophysicist*, Ed. by I. I. Gurvich and V. P. Nomokonov (Nedra, Moscow, 1981).
9. L. M. Brekhovskikh and O. A. Godin, *Acoustics of Layered Media* (Nauka, Moscow, 1989; Springer, New York, 1990).

Translated by A. Khzmalyan

Acoustical Physics, Vol. 50, No. 1, 2004, pp. 52–56. Translated from Akusticheskiĭ Zhurnal, Vol. 50, No. 1, 2004, pp. 62–67.
Original Russian Text Copyright © 2004 by Zverev.

Imaging through an Inhomogeneous Layer with an Acoustic Antenna Array

V. A. Zverev
Institute of Applied Physics, Russian Academy of Sciences,
ul. Ul'yanova 46, Nizhni Novgorod, 603600 Russia
e-mail: zverev@hydro.appl.sci-nnov.ru

Received June 17, 2002

Abstract—A method is proposed for obtaining images through a layer of an inhomogeneous medium by using an antenna array scanning in angle or space. The method is based on the wave front inversion, which allows one to form an undisturbed sound field on the object of location in an inhomogeneous medium. This property makes it possible to suppress the effect of the thin inhomogeneous layer on the signals observed at the array output. The technique consists in a mutual processing of two received signals, one of which is obtained by locating the objects through the inhomogeneous medium and the other is obtained by locating the same objects, in the same medium, by the front-inverted wave. The mutual processing procedure consists in using the first received signal to form a filter for the second signal. The method is tested by a numerical simulation. *© 2004 MAIK "Nauka/Interperiodica".*

Many media in which electromagnetic waves do not propagate at all or produce no reflections from the objects to be detected prove to be transparent for sound waves. However, a drawback of the latter consists in that, when propagating in these media, they are often subject to strong disturbances, which cause considerable problems in obtaining high-quality images. Methods for obtaining images of scattering objects in the presence of inhomogeneities considerably distorting the wave fields were proposed in a number of recent publications [1–3]. Method considered in [1] is based on the separation of the fluctuations of radiation (instead of their usual suppression) for the visualization of acoustic objects moving under a layer of inhomogeneities. Method considered in [2] determines the coordinates of point scatterers by means of analyzing the radiation produced by a chain of sources and received by a chain of receivers. To eliminate the effect of inhomogeneities on the result of observation, a time reversal of waves is used. The latter technique is described in detail in a review [3]. As shown in this review by many examples, the method of wave front inversion provides good images of acoustic objects in bad media. However, in all the numerous cases considered in [3], good images are obtained by scanning the sound field in close vicinity of the object of interest. Such a technique can serve to illustrate the advantages of applying the WFI method in acoustics but cannot be used to obtain an image in practice without inserting the probe into the medium to be studied.

The objective of the present study is to show that it is possible to obtain a good WFI image through a thin layer of strong inhomogeneities by appropriately processing the disturbed signals. The proposed method of imaging is based on the following idea. The distortions produced by the inhomogeneities of the medium in the signal propagating through it are precisely the same when one observes the array response through the given inhomogeneous layer by sending an ordinary probing signal and by sending a WFI signal from the same array. However, the signals received after sending the ordinary probing signal and the WFI signal will have different intensity distributions. The difference is caused by the fact that, in advance (before being reflected by the object), the WFI signal reproduces the spatial intensity distribution which the ordinary signal acquires after its reflection by the object. As a result, we have two relations. The first relates the distorted signal to that of interest in the ordinary location process. The second relates the distorted signal obtained in the WFI process to the corresponding image. There is one more relation between these images. One of them, which corresponds to a thin inhomogeneous layer close to the array, is the square of the other. The aforementioned relations are independent and, in principle, can serve to find both unknown quantities, one of which is the undisturbed signal of interest in the vicinity of the object to be detected.

Below, the problem stated is solved in application to a linear antenna array with scanning in angle and space. The array can be placed both in the far-field zone relative to the object of interest and in the near-field zone (a focused array). The problem is not solved completely. The solution found yields the distribution of the objects in the coordinates of scanning; these coordinates are measured with respect to their values corresponding to the strongest object. The coordinates of this object remain unknown. The solution consists in that, based on the first disturbed signal, a filter is formed for the second signal.

The sound field received by the array in an inhomogeneous medium is modulated by a certain function $E(x)$ and can be represented as

$$K(x) = E(x)A(x), \tag{1}$$

where x is the coordinate along the linear array and $A(x)$ is the sound field along the same line in the absence of inhomogeneities. The inhomogeneous layer is assumed to be sufficiently thin and to be located so close to the array that the quantity $E(x)$ does not depend on the angle at which the wave arrives at the array. Suppose that there is only one strong signal at the array input, while other signals are much weaker. Then, we can write

$$A(x) = A_0(x) + m(x), \tag{2}$$

where $A_0(x)$ is the strong signal and $m(x)$ is the weak one (it is sufficient to consider one such signal). Let us normalize Eq. (2) by factoring out the quantity $A_0(x)$:

$$A(x) = A_0(x)\left(1 + \frac{m(x)}{A_0(x)}\right). \tag{3}$$

Relations (1), (2), and (3) are also valid for the signal received by the array in response to the probing WFI signal. In the corresponding relations for the reception of the WFI wave, the function $E(x)$ will be the same as in Eq. (1) but the function $A(x)$ will be different. This occurs because the WFI wave insonifies the objects with amplitudes proportional to those of the scattered signals. As a result, the amplitudes of the inverse wave will be multiplied by themselves. The relations between the signals will change: the strong signal will become stronger and the weak signal will become weaker. To make considerations simpler, let us assume that, in the inverted wave, all signals but the strongest one can be neglected. In fact, for this assumption to be true, a number of sendings and receptions of the iterations of the inverted signals can be required [3]. In view of these considerations, one can write the following relation for the received WFI signal:

$$KO(x) = E(x)A_0(x). \tag{4}$$

From the comparison of Eqs. (4) and (3), the following algorithm of signal processing can be proposed to suppress the effect of the inhomogeneous layer: Eq. (3) should be divided by Eq. (4). The result is as follows:

$$P(x) = \frac{K(x)}{KO(x)} = 1 + \frac{m(x)}{A_0(x)}. \tag{5}$$

To obtain the images of the objects, it is sufficient to process the function $P(x)$ determined by Eq. (5) by applying the same algorithm as for the "pure" signal taken from the array aperture [4]. According to Eq. (5), the signal images will be normalized to the strong signal as a reference one. The information on the position of the signal $A_0(x)$ itself will be lost. The advantage of the proposed procedure (and the reason for accepting it) is that, by processing the signals in this way, one can fully eliminate the mutiplicative noise $E(x)$.

Thus, the mutual processing procedure for the signals received by the array hydrophones is reduced to obtaining their ratios. One can guess that here we deal with a nonlinear signal processing. To establish what kind of signal processing is actually used, let us apply the spectral approach to solving the same problem.

It is known (see, for example, [4]) that the signals at the input and output of the array with scanning in angle are related to each other by the convolution procedure:

$$W(k\alpha) = \frac{\exp(ikr)}{\sqrt{i\lambda r}}\int_{-\infty}^{\infty} p(\xi)H\left(k\alpha - \frac{k\xi}{r}\right)d\xi. \tag{6}$$

Here, $p(\xi)$ is the signal at the array input, $k = \frac{2\pi}{\lambda}$, λ is the wavelength, r is the distance, α is the angle of scanning, and $H(\xi, \alpha)$ is the array directivity pattern [4].

In a spectral form, Eq. (6) can be represented as

$$G_w\left(u\frac{r}{k}\right) = G_p\left(u\frac{r}{k}\right)G_H\left(u\frac{r}{k}\right), \tag{7}$$

where G_z is the Fourier spectrum of the function z (z is an arbitrary function) and $u = \frac{kx}{r}$ is the spatial frequency.

The function $G_H(u)$ coincides with the function $E(x)$ introduced by Eq. (1); it describes the distortions of the sound field at the array (see, e.g., [4]). This function characterizes the effect of the inhomogeneous layer through which the wave propagates.

Both aforementioned relations between the input and output signals have the form of Eq. (7) for the specific case of angle-scanning arrays. In these relations, the same functions $G_H(u)$ appear that describe the medium of wave propagation. The distortions will vanish if the functions $G_W(u)$, one of which is obtained by a simple location procedure and the other by the WFI, are divided by each other. This division yields the following ratio of the spectra $G_k(u)$:

$$G_k(u) = \frac{G_p(u)}{G_0(u)}, \tag{8}$$

where $G_0(u)$ is the spatial spectrum of the signal observed at the array output when locating the object with the WFI wave.

To clear up the result of applying Eq. (8), let us follow the approach described in [5]. The spectra $G_p(u)$ and $G_0(u)$ take the forms

$$G_p(u) = A_0\exp(ix_0u) + m\exp(ix_1u), \tag{9}$$

$$G_0(u) = A_0^2\exp(ix_0u) + m^2\exp(ix_1u). \tag{10}$$

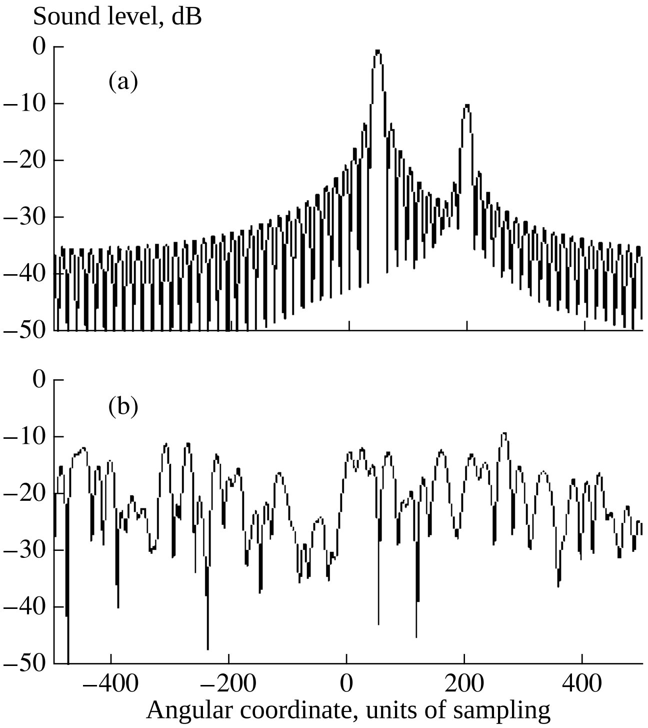

Fig. 1. Images obtained with the array in the (a) absence and (b) presence of the inhomogeneous layer.

By neglecting the term with $\frac{m^2}{A_0^2}$ in comparison with unity, from Eq. (8) in view of Eqs. (9) and (10), we obtain the same result as that given by Eq. (5).

The aforementioned procedure of dividing the spectra can be treated as a linear filtration, in which the first signal is used to form the linear filter for the second one. The examples of such a filtration are presented in [6–9].

The solution of the problem can be illustrated by numerical modeling according to [4]. Suppose that two reflectors exist in the medium and their reflectivities differ by 10 dB from each other. By insonifying these reflectors with a wave produced by a relatively distant sound source, we obtain two spherical waves. Let us assume that the insonification is monochromatic.

With an array located in the far-field zone relative to the reflectors [4], we obtain the array response in the homogeneous medium. Figure 1 shows the absolute value of such a response. In the same figure, the absolute value of the response of the same array is presented for the medium in which a layer with random inhomogeneities of the refractive index exists. With such inhomogeneities, no traces of the initial response can be noticed. The inhomogeneities of the refractive index were modeled by using a generator of random sequences. Such a pseudorandom sequence was introduced into the exponent of the imaginary argument [10].

Now, let us perform the inversion of the wave front. This is done by sending the complex-conjugated array response disturbed by the layer into the medium. In the medium, the undisturbed wave field will exist. The magnitude of this field is shown in Fig. 2 (fortunately, the numerical methods allow one to obtain such information).

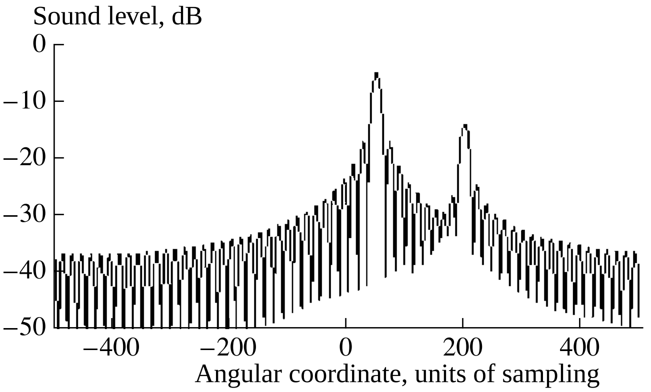

Fig. 2. The WFI result in the medium.

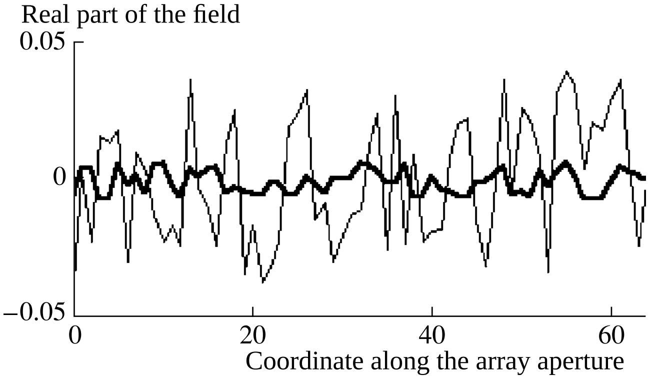

Fig. 3. Real part of the sound field at the array aperture with the ordinary location method (thin curve) and the difference in the real parts of the fields at the aperture with the ordinary and WFI location (thick curve).

As results of the ordinary location and the location with the WFI wave, we obtain the medium-disturbed wave fields at the array receivers. The real part of one of these fields and their difference are shown in Fig. 3. The non-zero difference of the fields is caused by the aforementioned nonuniformity of the angular intensity distribution in the inverted probing wave.

The result of mutual processing of the two reflected signals (ordinary and WFI ones) is illustrated by Fig. 4. The image obtained is actually free from the effect of inhomogeneities, yields the true ratio of the amplitudes corresponding to the objects, and correctly characterizes their relative positions. The response to the strongest object corresponds to the initial angle.

In the numerical modeling, Eqs. (4), (5) and (8) were not simplified. In the wave field received by the array with the WFI probing signal, all terms were retained. This fact does not manifest itself in Fig. 4,

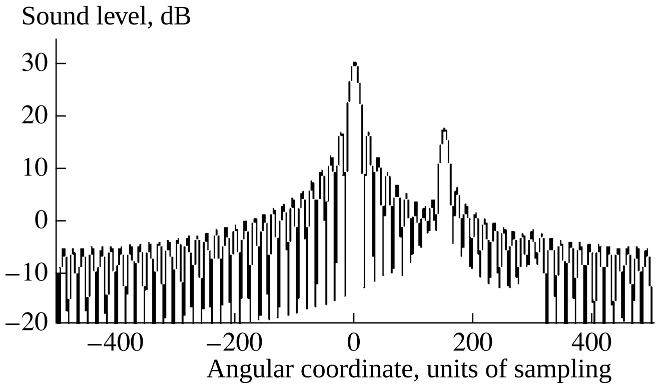

Fig. 4. Result of mutual processing of the signals of ordinary and WFI location.

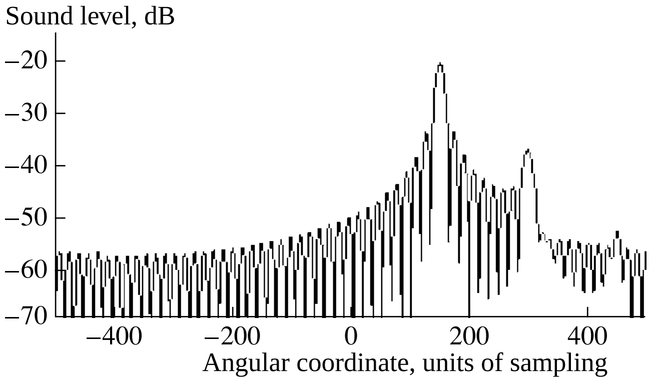

Fig. 5. Result of mutual processing of the signals of ordinary and WFI location with the strongest signal filtered out.

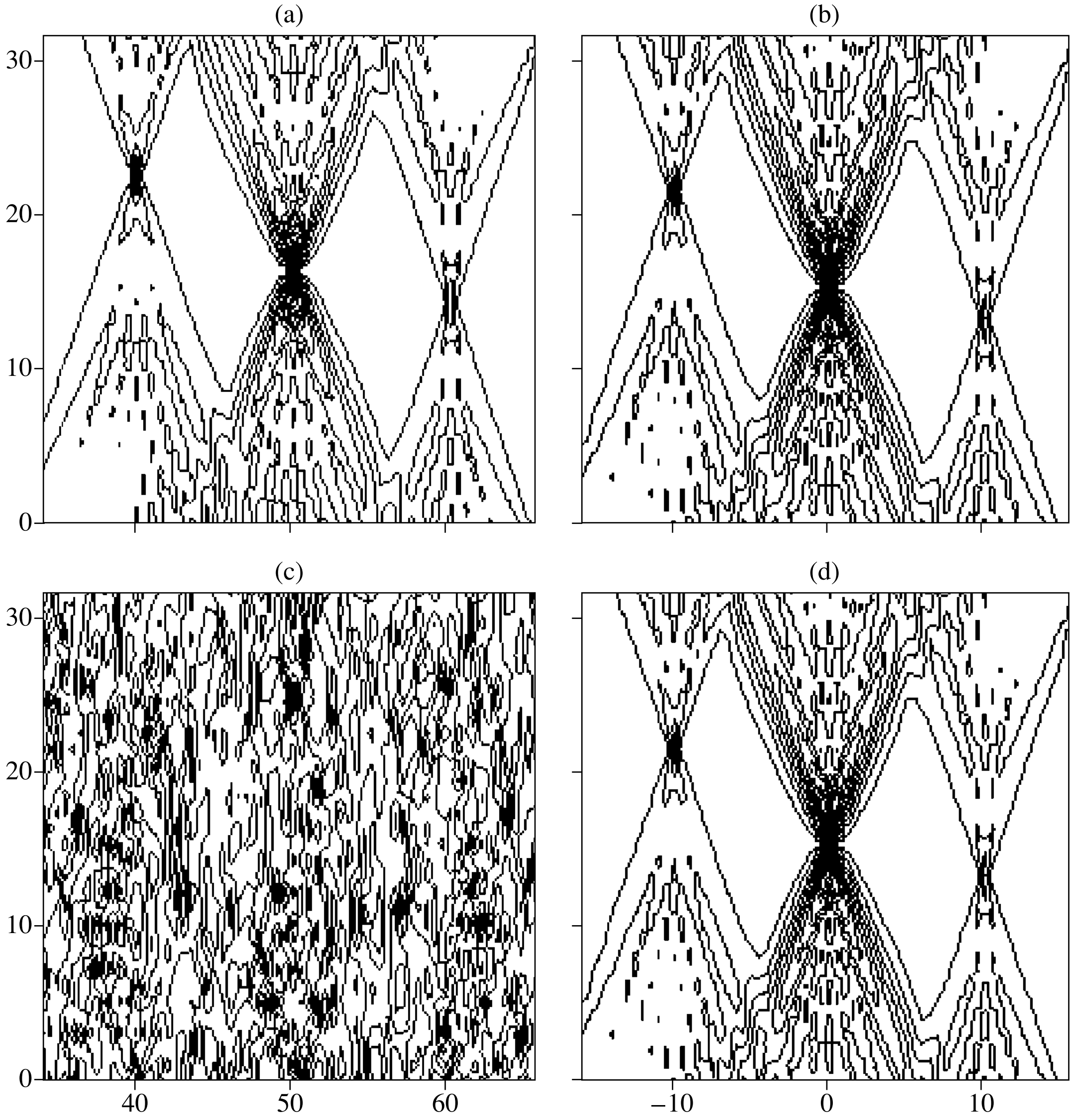

Fig. 6. Results of the location with a focused array. The vertical and horizontal coordinates are the distance and the azimuth, respectively. Images (a) and (b) correspond to the homogeneous medium. Images (c) and (d) correspond to locating through the inhomogeneous layer. Images (a) and (c) are obtained by the ordinary location method. Images (b) and (d) are obtained by mutual processing of the signals of ordinary and WFI location.

because the side lobes of the strong signal mask the additional signals obtained from the processing procedure. To make visible all additional terms of the image, the signal shown in Fig. 4 was additionally processed. The processing procedure consisted in eliminating the strongest signal with the use of the dark-field method [6, 11]. This method of filtering allows one to filter out a narrowband signal along with its side lobes. The result is shown in Fig. 5. Here, additional low-level images can be noticed at some distance from the main image. The additional images occur because the WFI result does not include just the strongest signal. Further iterations with the WFI signal can lead to smaller distortions of this kind. Thus, in our case, the additional signals of Fig. 5 will not manifest themselves, if one uses the signal of the next iteration rather than that of the initial one in the processing procedure. To make the additional signals noticeable, one should filter out the strongest signal remaining in Fig. 5 with the use of the dark-field method. The presence of additional signals as a result of filtering indicates that the procedure used is not purely linear and can be treated as approximately linear, to an accuracy within the additional signals.

A focused array can be considered in the same way. Equations (1)–(5) are also valid for such an array. The only difference is that the final processing procedure for the function $P(x)$ of Eq. (5) should include the Fourier–Fresnel transform with a parameter that depends on the distance to the object. Figure 6 shows the results of numerical modeling for the focused array. The sum of three signals was modeled:

$$S = S_1(1;\,50;\,16) + S_2(0.3;\,70;\,22) + S_3(0.25;\,30;\,14), \tag{11}$$

where the numbers enclosed in parentheses and separated by semicolons denote the amplitude, azimuth, and range, respectively. The amplitude is presented in arbitrary units, and the coordinates are measured in the units of sampling. Two upper images of Fig. 6 are obtained in the absence of the inhomogeneous layer. Figure 6a corresponds to the ordinary location procedure. Figure 6b illustrates the mutual processing procedure according to Eq. (5), with the subsequent Fourier–Fresnel transformation. The lower images of Fig. 6 are obtained with the inhomogeneous layer.

The figures show that the images obtained by using the proposed technique of processing two received signals are the same for the cases of free space and an inhomogeneous layer. At the same time, this layer strongly distorts the signals obtained in ordinary location.

The illustration presented is obtained by using computer code similar to that proposed in [6], which, in turn, is based on [10]. The code used for obtaining the results of Fig. 6 differs from its original version in that our random signal modulating the sound field at the array has an extremely broad band of spatial frequencies. Therefore, the filtering algorithm used in [10] cannot suppress the noise, and the WFI method should be used to extract the signal from the noise background.

In conclusion, let us consider some conditions for the proposed method of imaging through the inhomogeneous layer to be feasible. The layer should be stationary and should not change its properties within the time of location and all subsequent iterations with the WFI sendings. Also, the layer should be sufficiently thin for Eq. (1) to adequately describe all distortions produced by it. The objects of location should be point objects for the frequencies and scattering angles used in the location procedure. The latter condition should be met for the object to reradiate a spherical wave independently of the form of the insonifying field. Otherwise, the consideration significantly thickens. For the first probing signal, it is advantageous to use the field emitted by a single array element rather than by the entire array [3] for the maximal smoothing of the spatial structure of the insonifying field.

ACKNOWLEDGMENTS

I am grateful to V.I. Talanov for his interest in this work and useful comments.

This work was supported by the Russian Foundation for Basic Research, project nos. 00-15-96741 and 02-02-17056.

REFERENCES

1. N. V. Zuikova, T. V. Kondrat'eva, and V. D. Svet, Akust. Zh. **49**, 183 (2003) [Acoust. Phys. **49**, 148 (2003)].
2. S. K. Lehman and A. J. Devaney, J. Acoust. Soc. Am. **113**, 2742 (2003).
3. M. Fink, D. Cassereau, A. Derode, *et al.*, Rep. Prog. Phys. **63**, 1933 (2000).
4. V. A. Zverev, *Physical Fundamentals of Image Formation by Wave Fields* (Inst. Prikl. Fiz., Ross. Akad. Nauk, Nizhni Novgorod, 1998).
5. V. A. Zverev and A. A. Stromkov, Akust. Zh. **47**, 657 (2001) [Acoust. Phys. **47**, 572 (2001)].
6. V. A. Zverev and A. A. Stromkov, *Extraction of Signals from Noise by Numerical Methods* (Inst. Prikl. Fiz., Ross. Akad. Nauk, Nizhni Novgorod, 2001).
7. V. A. Zverev, Izv. Vyssh. Uchebn. Zaved., Radiofiz. **43** (5), 406 (2000) [Radiophys. Quantum Electron. **43** (5), 366 (2000)].
8. V. A. Zverev, Izv. Vyssh. Uchebn. Zaved., Radiofiz. **44** (7), 636 (2001).
9. V. A. Zverev, P. I. Korotin, and A. V. Tsiberev, Akust. Zh. **47**, 468 (2001) [Acoust. Phys. **47**, 419 (2001)].
10. V. A. Zverev and A. A. Pavlenko, Akust. Zh. **47**, 355 (2001) [Acoust. Phys. **47**, 297 (2001)].
11. V. A. Zverev, Akust. Zh. **40**, 401 (1994) [Acoust. Phys. **40**, 360 (1994)].

Translated by E. Kopyl

Acoustical Physics, Vol. 50, No. 1, 2004, pp. 57–65. Translated from Akusticheskiĭ Zhurnal, Vol. 50, No. 1, 2004, pp. 68–76.
Original Russian Text Copyright © 2004 by Ivanov.

Suppression of the Sound Field Produced behind an Aperture in a Screen by an Extraneous Source

V. P. Ivanov

Institute of Mechanical Engineering, Russian Academy of Sciences,
ul. Bardina 4, Moscow, 117334 Russia
e-mail: airapetov@imach.ac.ru

Received October 23, 2002

Abstract—The three-dimensional problem of the active suppression of sound behind an aperture in a perfectly rigid screen is formulated and solved. *© 2004 MAIK "Nauka/Interperiodica".*

INTRODUCTION

This paper extends the results reported in [1] to the three-dimensional case and contributes to the development of the active noise control technique [2–6]. At first, it is necessary to formulate the conditions that must be satisfied by a transmitting–receiving device to realize the solution of the active noise control problem. The device must be an antenna array with small but not zero-size elements of the simplest type: the auxiliary sources must be monopoles or dipoles. Consider the following problem. Let an external field U_F characterized by the wave number k and the volume velocity density f be incident on a perfectly rigid screen Γ from the half-space $z > 0$. Let the screen be in the plane $z = 0$ and have a circular aperture S_0 of radius a_0 centered at the origin of coordinates. We study the case when the wave dimension ka_0 is about unity. Centers of spherical receivers of radius a are located in the half-space $z > 0$ on half-spheres of radii R_j ($j = 1, 2$; $R_1 < R_2$), each of the half-spheres accommodating N_j receivers, which average the field over their surfaces. Centers of hemispherical auxilliary radiators F_{jm} ($j = 0, 1, \ldots, J$; $m = 1, 2, \ldots, M_j$) of radius a_1 reside in the plane $z = 0$ on circles of radii r_j ($R_0 < r_i < r_j < R_1$ for $i < j$). Consider a bounded region F lying outside the sphere of radius $R_2 + a$. Assume that the function f is unknown, but the integral $Q_F = \iint_F |f|\, dx$ and the distance r_F^* between the origin and the region F are known. The total field U in the half-spaces $z > 0$ and $z < 0$ outside the receivers and auxilliary radiators satisfies the inhomogeneous Helmholtz equation

$$(\Delta + k^2)U = -4\pi f, \qquad (1)$$

where $k = \omega/c$ and $\operatorname{supp} f \subset F$, and the boundary conditions: (i) $\partial U/\partial n = 0$ at $z = 0$ outside the aperture S_0 and hemispheres F_{jm}; (ii) $\partial U/\partial n = f_{jm}$ on the hemispheres F_{jm} ($j = 0, 1, \ldots, J$; $m = 1, 2, \ldots, M_j$); (iii) $\partial U/\partial n = 0$ on the receivers S_{jn} ($j = 1, 2$; $n = 1, 2, \ldots, N_j$); (iv) the edge condition; and (v) the ultimate attenuation condition at infinity, $\sup|U| < \infty$ at $\operatorname{Im} k > 0$. Let us require that only the zeroth and first spherical harmonics of the function f_{jm} are nonzero on the hemispheres F_{jm}. The aim is to determine the numbers N_j of the auxilliary radiators, the positions of their centers, the wave dimension ka_1, and the functions f_{jm} such that the condition

$$\sup|U| < \varepsilon\, Q_F/r_F^* \qquad (2)$$

be met for the field U in the half-space $z < 0$ behind the screen outside a hemisphere of a given radius R. Here, ε is a small positive number. Since the wave dimensions of the receivers and auxilliary radiators are small in terms of wavelength, we can assume that k is nonresonant for the regions bounded by the surfaces S_{jn} and F_{jm}.

1. SOLUTION OF THE PROBLEM OF THE FIELD MEASUREMENT AND SEPARATION

Since the field cannot be measured at a point in the process of the field measurement and separation in the region and only a finite number of measurements can be performed, the measured field must be represented as a finite Fourier series in a complete set of functions, where the Fourier amplitudes are functionals of the field distributions over the receiver surfaces. Let U_F be the incident field produced by extraneous sources. To solve the problem defined by expressions (1) and (2), it is necessary to formulate an auxilliary problem of field measurement and separation [7]. Specifically, it is necessary to find the numbers M_j ($j = 1, 2$), the wave dimension ka, and the positions of the receivers S_{jn} so that the field U_F inside the sphere of radius R_1 and the field diffracted by the aperture plus the field U_d produced by the auxilliary radiators outside the sphere of radius R_2 can be retrieved to a given accuracy from the measured amplitude of the average density of the velocity potential induced on the receiver surfaces by the total field. We additionally assume that, on the surface of the auxilliary radiator F_{jn}, the density of the potential associated with the field produced by the radiator itself and with the fields of the first and second diffraction is constant. Earlier [6], it was shown that this choice of the density of the potential solves the sound suppression problem with the minimum power of the auxilliary radiators.

Since the wave number is nonresonant, we represent the unknown total field U as

$$U = \int_F f G_F dF + \sum_{j=1}^{2} \sum_{n=1}^{N_j} \int_{S_{jn}} \mu_{jn} G_{jn} ds_{jn} + \sum_{j=1}^{J} \sum_{m=1}^{M_j} \int_{F_{jm}} \nu_{jm} G_{jm} dF_{jm} - \int_{S_0} \mu_0 \frac{\exp(ikR_0)}{R_0} ds_0, \tag{3}$$

for $z > 0$ and

$$U = \int_{S_0} \mu_0 \frac{\exp(ikR_0)}{R_0} ds_0,$$

for $z < 0$, where

$$G_\alpha = \frac{\exp(ikR_\alpha)}{R_\alpha} + \frac{\exp(ikR_\alpha^*)}{R_\alpha^*}.$$

Here, α is one of the indices of integrands on the right side of Eq. (3); R_0, R_F, R_{jn}, and R_{jm} are the distances from the observation point to a point on the aperture S_0, in the region F, and on the surfaces S_{jm} and F_{jn}, respectively; the asterisk indicates the distances from the observation point to the corresponding points of mirror reflections of the region F and surfaces S_{jn} and F_{jm} with respect to the plane $z = 0$; ν_{jm} is the density of the potential of radiation produced by the body F_{jn} and by diffraction from its surface; μ_{jn} is the density of the potential induced on the surfaces S_{jm}; and μ_0 is the normal velocity of the medium in the aperture S_0. Let us substitute the representation of the field U for $z > 0$ into the boundary condition on the surface S_{qp} and take into account the fact that the receiver averages the field over its surface. Next, we integrate the relationship obtained with the above procedure over the surface S_{qp}. As a result, we obtain a finite system of algebraic equations for an infinite number of amplitudes of the spherical harmonics of the field diffracted from the aperture, the field of the auxilliary radiators F_{jn}, and the incident field of the extraneous sources. The right-hand side of the system is proportional to the zeroth harmonic of the velocity potential on the receiver surfaces S_{qp} ($q = 1, 2$; $p = 1, 2, \dots, N_q$):

$$\sum_{n=0}^{\infty} \sum_{m=-n}^{n} [g_{1nm} h_n^{(1)}(kR_q) + g_{2nm} \psi_n(kR_q)] P_n^m(\cos\vartheta_{qp}^0) \exp(im\varphi_{qp}^0) = -\frac{\psi_0(ka) h_0^{(1)\prime}(ka)}{\psi_0'(ka)} b_{qp}(1 + \delta_{qp}) = c_{qp}, \tag{4}$$

$$q = 1, 2, \quad p = 1, 2, \dots, N_q.$$

In Eq. (4),

$$g_{1nm} = l_{1nm} + l_{2nm}, \quad b_{qp} = \int_{S_{qp}} \mu_{qp} ds_{qp},$$

b_{qp} are the quantities measured directly,

$$l_{1nm} = (-1)^{n+m}(2n+1)\frac{(n-m)!}{(n+m)!} \int_{S_0} \mu_0 \psi_n(k\rho_0) P_n^m(0) \times \exp(-im\varphi_0) ds_0,$$

$$l_{2nm}(J, M_j) = (-1)^{n+m}(2n+1)\frac{(n-m)!}{(n+m)!} \times \sum_{j=0}^{J} \sum_{p=1}^{M_j} d_{jp} \psi_n(kr_j) P_n^m(0) \exp(-im\varphi_{jp}^0),$$

$$d_{jp} = 4\pi a_1^2 \psi_0(ka_1) v_{jp} = \text{const},$$

$$g_{2nm} = [1 + (-1)^{n+m}](2n+1)\frac{(n-m)!}{(n+m)!} \times \iint_F f h_n^{(1)}(kr_F) P_n^m(\cos\vartheta_F) \exp(-in\varphi_F) dF.$$

Here, δ_{qp} is the error of the measurement method due to the discrete structure of the receiving antenna and due to the field measurement technique, (ρ_0, φ_0) are the coordinates of the integration point on the surface S_0, (r_F, ϑ_F, φ_F) are the spherical coordinates of the integration point in the region F, (r_j, φ_{jp}^0) are the coordinates of the center of the F_{jp} auxilliary radiator, (R_q, ϑ_{qp}^0, φ_{qp}^0) are the coordinates of the center of the qpth receiver in the main coordinate system connected with the center of the aperture S_0, $\psi_n(x)$ and $h_n^{(1)}(x)$ are the Bessel and Hankel spherical functions, and $P_n^m(x)$ are the associated Legendre polynomials. If the incident field is a plane wave $A\exp(-ikr\cos\Omega)$, the coefficients

g_{2nm} are obtained from the formulas

$$g_{2nm} = (-i)^{n+1}\frac{A}{k}[1$$

$$+ (-1)^{n+m}(2n+1)\frac{(n-m)!}{(n+m)!}P_n^m(\cos\vartheta_F)\exp(-im\varphi_F),$$

where $\cos\Omega = \cos\vartheta\cos\vartheta_F + \sin\vartheta\sin\vartheta_F\cos(\varphi - \varphi_F)$. When $ka \ll 1$ and the centers of the receivers are uniformly distributed on the hemisphere of radius R_q, the error δ_{qp} can be estimated as

$$|\delta_{qp}| \le \frac{b^*}{|b_{qp}|}\left|\frac{\psi_0'(ka)3\sqrt{2}}{\psi_0(ka)h_0^{(1)\prime}(ka)}\right|$$
$$\times N(N+3)[\ln(N+2)]\left(1 - \frac{aN}{R_1}\right), \tag{5}$$
$$b^* = \max|b_{qp}|,$$

where $N = \max(N_1, N_2)$, and $aN < R_1$. Note that the numbers N_1 and N_2 are unknown and will be determined in the process of solving the problem. If the numbers N_1 and N_2 are known and the measurement error $\delta = \max\delta_{qp}$ is specified, condition (5) readily yields the estimate

$$ka \le \left[\frac{\delta}{\sqrt{2}N(N+3)\ln(N+2)(1 - aN/R_1)}\right]^{1/3} \tag{6}$$

for the admissible wave dimension of the receivers uniformly distributed over the hemispheres of radii R_q (q = 1, 2) to obtain the specified small measurement error.

The field measurement process will be physically feasible if the inequality

$$ka \ge ka^* \tag{7}$$

is satisfied, where ka^* is a fixed number characterizing the sensitivity of the receivers employed. If the parameter ka satisfies condition (6) and the inequality $ka \ge ka^*$ holds, the measurement problem is physically feasible. Thus the wave dimension of the receivers must not be too large, so that the field diffracted from the antenna introduces no considerable error into the measurement process.

Let us rewrite system (4) by omitting the terms equal to zero:

$$\sum_{n=0}^{\infty}\sum_{m=0}^{n}[g_{1n,2n-m}h_n^{(1)}(kR_q) + g_{2n,2m-n}\psi_n(kR_q)]$$
$$\times P_n^{2m-n}(\cos\vartheta_{qp}^0)\exp[(2m-n)\varphi_{qp}^0] = c_{qp}, \tag{8}$$
$$q = 1, 2, \quad p = 1, 2, \dots, N_q.$$

The solution of system (8) can be reduced to solving two systems for q = 1 and 2. Both systems have an infinite numbers of solutions. At low frequencies, the field is primarily determined by the first spatial harmonics. Therefore, we set $N_1 = N_2 = (M+1)(2M+3)$ and construct a reduced system for the first $(M+1)(2M+3)$ spatial harmonics:

$$\sum_{n=0}^{2M+1}\sum_{m=0}^{n}[g_{1n,2m-n}^*h_n^{(1)}(kR_q) + g_{2nm2m-n}^*\psi_n(kR_q)]$$
$$\times P_n^{2m-n}(\cos\vartheta_{qp}^0)\exp[i(2m-n)\varphi_{qp}^0] = c_{qp}, \tag{9}$$
$$q = 1, 2, \quad p = 1, 2, \dots, (M+1)(2M+3).$$

Let us introduce new unknown variables

$$X_{1n,2m-n}^* = g_{1n,2m-n}^*h_n^{(1)}(kR_1) + g_{2n,2m-n}^*\psi_n(kR_1),$$
$$X_{2n,2m-n}^* = g_{1n,2m-n}^*h_n^{(1)}(kR_2) + g_{2n,2m-n}^*\psi_n(kR_2),$$

and let $W_n = \psi_n(kR_1)h_n^{(1)}(kR_2) - h_n^{(1)}(kR_1)\psi_n(kR_2)$. If $W_n \ne 0$, which means that k is not a resonant wave number for the layer $R_1 < r < R_2$ with perfectly soft boundaries, the amplitudes $g_{2n,2m-n}^*$ of the incident field are given by the expression

$$g_{2n,2m-n}^* = W_n^{-1}[h_n^{(1)}(kR_2)X_{1n,2m-n}^*$$
$$- h_n^{(1)}(kR_1)X_{2n,2m-n}^*]. \tag{10}$$

Let us place the centers of the receivers S_{qp} on the hemisphere of radius R_q as follows. We select the latitudes ϑ_{qj}^0 ($j = 0, 1, \dots, M$) and place 4/+ 3 receiver centers at the longitudes $\varphi_{jl}^0 = 2\pi l/(4j+3)$ ($l = 0, 1, \dots, 4j+2$). Let us renumber the right-hand side of system (9), i.e., we set $c_{qp} = c_{qjl}$ if $j(2j+1) \le p \le (j+1)(2j+3)$ and $p = j(2j+1)$+/+1. Consider the elements

$$A_{0,n}^{2m-n}(\gamma_j) = P_n^{2m-n}(\gamma_j), \quad \gamma_j = \cos(\vartheta_{qj}^0),$$
$$0 \le n \le 2M+1, \quad 0 \le m \le n, \quad 0 \le j \le M,$$

$$A_{s,n}^{2m-n}(\gamma_j) = A_{s-1,n}^{2m-n}(\gamma_j)$$
$$- A_{s-1,L_n}^{2m-n}(\gamma_j)A_{s-1,n}^{2m-n}(\gamma_{M-j+1})/A_{s-1,L_n}^{2m-n}(\gamma_{M-j+1}),$$

where $L_n = 2(M-n)$ for even n and $L_n = 2(M-n)+1$ for odd n and $\hat{\imath} \le M - s$, $1 \le j \le M$, $n \le 2(m-s)+1$.

When the conditions

$$A_{s,2m-s}^{2j}(\gamma_{M-s}) \ne 0 \quad \text{for} \quad -s \le j \le s,$$
$$A_{s,2(m-s)+1}^{2j}(\gamma_{M-s}) \ne 0 \quad \text{for} \quad -(s+1) \le j \le s, \tag{11}$$
$$s = 0, 1, \dots, M$$

are met, the determinant of system (9) is nonzero. The physical meaning of conditions (11) can easily be seen at $s = 0$: the receiver centers must not lie at the points where the field vanishes. Let Δ_{M-s} be the Vandermonde determinant of the dimension $4(M-s)+3$:

$$\Delta_{M-s} = \left\{ \exp\left(\chi \frac{2\pi i m}{4(M-s)+3}\right), \quad \begin{matrix} -2(M-s)-1 \le \chi \le 2(M-s)+1 \\ 0 \le m \le 4(M-s)+2 \end{matrix} \right\}. \tag{12}$$

Then, the solution to system (9) can be written for an arbitrary M in the explicit form

$$X^*_{qn,\,2m-n} = \sum_{i=g}^{M} \sum_{j=\nu_1(i)}^{\nu_2(i)} \frac{(-1)^{\sigma_j} \Delta_{M-i}(\rho_j) D^{\rho_j}_{M-g-1,\,S(g-1)}(\gamma_g)}{\Delta_{M-i,\,S(m-i)}(\gamma_i) B^{2m-n}_{M-g,\,S(g)}(\gamma_g)}, \tag{13}$$

where $q = E\left(\left|\frac{2m-n}{2}\right|\right)$, $q = 1, 2$, $n = 0, 1, \ldots, 2M+1$, $m = 0, 1, \ldots, n$, $\sigma_j = M - i - g + j + 2m - n$, and $S(g) = 2g$ for even $2m - n$ and $\sigma_j = M - i - g + j + 2m - n + 1$ and $S(g) = 2g + 1$ for odd $2m - n$;

$$\rho_j = 2m - n + j(4i + 3),$$

$$\nu_1 = E\left(\frac{2i + 1 + 2m - n}{4i + 1}\right), \quad \nu_2 = E\left(\frac{2i + 1 - 2m + n}{4i + 1}\right),$$

and $E(x)$ is the integral part of x. In Eqs. (13), $\Delta_{M-i}(\rho_j)$ is the determinant of the matrix, in which the column number $\chi = \rho_j$ is replaced with part of the column of free terms c_{qil} that belong to rows of number i. The coefficients B^j_{kl} and D^j_{kl} are defined by recurrent formulas given in the Appendix. Thus, approximate values of the amplitudes of spherical harmonics of the incident field, g^*_{2nm}, are calculated from the total field measured on the receiver surfaces.

2. SOLUTION OF THE SOUND SUPPRESSION PROBLEM

Using representation (3) at $z > 0$ and the summation theorem for spherical functions [8], let us write the field U inside the hemisphere of radius R^*, $R^* < r_0 - a_1$, $z > 0$, in the form

$$U = ik \sum_{n=0}^{\infty} \sum_{m=0}^{\infty} \Bigg[g_{2n2m-n} + \sum_{j=0}^{J} \sum_{p=0}^{M_j} h_n^{(1)}(kr_j) P_n^{2m-n}(0) \exp[-i(2m-n)\varphi^0_{qp}] d_{jp} \Bigg] \times \psi_n(kr) P_n^{2m-n}(\cos\vartheta) \exp[i(2m-n)\varphi] + V, \tag{14}$$

$$V = -\int_{S_0} \frac{\exp(ikR_0)}{R_0} ds_0, \quad + \sum_{j=1}^{2} \sum_{n=1}^{N_j} \int_{S_{jn}} \mu_{jn} G_{jn} ds_{jn}.$$

To make the following calculations more clear, let us consider the physical basis of solving the sound suppression problem. The constants d_{jp}, which characterize the field produced by the auxilliary radiators, are chosen from the condition that the first $(M + 1)(2M + 3)$ spatial harmonics in the sum on the right-hand side of Eq. (14) be zero; i.e., the field produced by the auxilliary radiators is in antiphase with the first $(M + 1)(2M + 3)$ harmonics of the incident field of the primary source. Therefore, as a result of the superposition of the fields produced by the primary source and by the auxilliary radiators, the field incident on the aperture in the screen will be small. The field diffracted by the receivers, which is a component of V, can be made small by choosing a sufficiently small wave dimension ka^*, i.e., by choosing receivers of an appropriate class. Then, the diffracted field behind the aperture will be small, because the magnitude of the field incident on the aperture is small. Let us place centers of the auxilliary hemispherical radiators on $M + 1$ circles of radius r_j at the points $\vartheta^0_{jp} = \pi/2$, $\varphi^0_{jp} = 2\pi p/(4j + 3)$ ($p = 0, 1, \ldots, 4j + 2$), i.e., we set $J = M$ and $M_j = 4j + 2$. Let us require that the equalities

$$\sum_{j=0}^{M} \sum_{p=0}^{4j+2} d_{jp} h_n^{(1)}(kr_j) \exp[i(n-2m)\varphi^0_{jp}] = -g^*_{2n,\,2m-n}/(2n+1)P_n^{n-2m}(0) = \beta_{nm}, \tag{15}$$

$n = 0, 1, \ldots, 2M + 1$, $m = 0, 1, \ldots, n$ be met, where β_{nm} are the constants calculated from the measurements. Owing to the special choice of the radiator coordinates, the solution to the system can be written in the explicit form for an arbitrary M:

$$\begin{aligned} d_{jp} = {} & \sum_{k=0}^{j} \sum_{m=0}^{2k} \beta_{2km} \Delta_{jp2km}/\Delta + \sum_{k=j+1}^{M} \sum_{m=k-j}^{k+j} \beta_{2km} \Delta_{jp2km}/\Delta \\ & + \sum_{k=0}^{j-1} \sum_{m=0}^{2k+1} \beta_{2k+1,\,m} \Delta_{jp2k+1,\,m}/\Delta + \sum_{k=j}^{M} \sum_{m=k-j}^{k+j} \beta_{2k+1,\,m} \Delta_{jp2k+1,\,m}/\Delta, \end{aligned} \tag{16}$$

where

$$\frac{\Delta_{jpnm}}{\Delta} = \sum_{l=-\nu_1(j)}^{\nu_2(j)} (-1)^{j+g+L+Q(j,L)} \frac{\Delta_{M-j}}{\Delta} \times \frac{K^{n-2m}_{M-g,\,Q(n-2m)}(kr_g)}{F^{n-2m}_{M-g,\,Q(n-2m)}(kr_g) F^{L}_{M-j,\,Q(jL)}},$$

$Q_{n-2m} = 2g$ for even n; $Q_{n-2m} = 2g + 1$ for odd n; $Q(j, L) = 2j$ for even L; $Q(j, L) = 2j + 1$ for odd L; $g = E(|(2m - n)/2|)$; $L = n - 2m + l(4g + 3)$; Δ_{M-j}, $\nu_1(j)$, and $\nu_2(j)$ are defined by formulas (11) and (12); and $\Delta_{M-j}(L)$ is the determinant Δ_{M-j} with the column of number $\chi = L$ replaced by a column containing zeros except for unity in the pth row. The coefficients K^j_{kl} and F^j_{kl} are defined by recurrent formulas given in the Appendix. Formulas (10), (13), and (16) and the right-hand side of Eq. (15) analytically relate the measured quantities c_{qjl} to the amplitudes of the potentials at the auxilliary radiators, d_{jp}. The explicit dependence of the solution on M allows us to find M from relation (2). The field continuity condition on the aperture readily gives an integral equation for the normal velocity μ_0. The right-hand side of this equation, f_0, is an uncompensated portion of the total field incident on the aperture. Let us estimate the function f_0:

$$|f_0| \le \frac{Q_F}{2M+2} \frac{a_0}{r^*_{F-a_0}} \left[\frac{r_0^2}{(r_M - r_0)^2} \left(\frac{a_0}{r_0}\right)^{2M+2} + \frac{1}{M}\left(\frac{a_0}{r_0}\right)^2 \left(\frac{a_0}{r_M}\right)^{2M+1} + \frac{3r_0}{2(r_M - r_0)}\left(\frac{r_0}{r_M}\right)^{2M+1} \right] + \frac{\pi^2}{4(M+2)A_1}\left(\frac{a_0}{R_q}\right)^{2M+1} \frac{1}{|\ln(a_0/R_q)|} = f_0^*, \quad Q_F = \int_F |f| dF, \tag{17}$$

where

$$A_1 = \left[k \sum_{n=0}^{\infty} n(n+1) \left| \psi_n(kR_q) h_n^{(1)}(kr_F^*) \right| 2Q_F + \frac{Q_F(r_0 - a_0)}{r_F^* - a_0} \frac{4r_0^2 M^2}{(r_M - r_0)^2} \times \left[\frac{(r_M/R_1)^n}{n+2}\left(\frac{r_M}{r_0}\right)^2 + \frac{(r_n/R_1)^n}{n+1}\left(\frac{r_M}{r_0}\right) \right] \right]^{-1}.$$

In formula (17), r_F^* is the distance from the origin of coordinates to region F. By estimating the solution to the integral equation, we obtain the expression

$$|\mu_0| \le \frac{f_0^*(M)\mu_0^*}{a_0\eta}, \quad \mu_0^* = \max_q \sum_{n=0}^{\infty} \sum_{m=-n}^{n} \frac{\int_{-1}^{1} \left| S^{(1)}_{mn}(-ika_0, \eta) \right| d\eta \left| \eta S^{(1)}_{mn}(-ika_0, \eta) \right|}{8\pi k a_0 \left| N_{mn}(-ika_0) R^{(1)}_{|m|,n}(-ika_0, 0) R^{(3)}_{|m|,n}(-ika_0, 0) \right|}.$$

The functions $S^{(1)}_{mn}(-ika_0, \eta)$, $R^{(i)}_{|m|,n}(-ika_0, i\xi)$, and $N_{mn}(-ika_0)$ are defined in [8]. For small ka_0, $|\mu_0| \le \frac{f_0^*(M)}{\pi^2(a_0^2 - \rho_0^2)^{1/2}}$. For the field diffracted by the aperture S_0, the following estimate is valid in the lower half-space outside the sphere of radius R at an arbitrary ka_0:

$$|U| \le 2\pi f_0^*(M)\mu_0^* \frac{a_0}{R - a_0}. \tag{18}$$

For small ka_0, we have

$$ka_0|U| \le \frac{2 f_0^*}{\pi} \frac{a_0}{R_3 - a_0}. \tag{19}$$

To find the number M, let us use condition (2), in which the field U is given by Eq. (3). As follows from expressions (2), (18), and (19), for an arbitrary ka_0, the following relationships hold:

$$|U| \le 2\pi\mu_0^* f_0^*(M) \frac{a_0}{R - a_0} = \varepsilon_1 Q_F / r_F^*, \quad 0 < \varepsilon_1 < \varepsilon. \tag{20}$$

For small ka_0, we obtain

$$|U| \le \frac{2 f_0^*}{\pi} \frac{a_0}{R - a_0} = \varepsilon_1 Q_F / r_F^*. \tag{21}$$

The right-hand side of relationships (20) and (21) have the form of a nonlinear equation for M. A solution to this equation exists, because the left-hand side of the equalities in formulas (20) and (21) tends to zero with increasing M, and ε_1 is a sufficiently small positive number. After M is determined, we calculate the densities d_{jp} of the velocity potentials from Eqs. (16) and use formula (6) to find the wave dimension ka of the receiver and refine the number M by taking into account the field diffracted by the receivers' antenna, which is a small quantity compared to the field of extraneous sources and auxilliary radiators.

Because the type of the radiator is determined by the distribution of the normal velocity of the surface F_{jp} rather than by the distribution of the potential, to calculate the amplitudes of monopoles and dipoles, we substitute the field U given by formula (3) into the boundary condition at the surface of the radiator F_{jp}. Our calculations show that the function f_{qp} contains harmonics of an arbitrary order; i.e., the suppression problem is solved with radiators of a complex structure containing arbitrary K-poles. This could be expected, because the radiators themselves are bodies, which diffract the acoustic field, and the normal velocity of their surface will therefore contain arbitrary harmonics. Let us require that the radiator's wave dimension be sufficiently small. In this case, the function f_{qp} can be represented as its principal part f^*_{qp} and a residual whose magnitude is no greater than ε_2. The wave dimension of the radiator can be determined from ε_2 by a procedure similar to the one used for the receiver. If we require that $\varepsilon = \varepsilon_1 + \varepsilon_2$, the suppression problem will be solved completely. The functions f^*_{qp} ($q = 0, 1, \ldots, M$, $p = 0, 1, \ldots, 4q + 2$) that solve the suppression problem are given by the formulas

$$\begin{aligned}
f^*_{qp} = {} & \frac{d_{qp}}{a_1^2\psi_0(ka_1)}[1 + i(ka_1)^2\psi'_0(ka_1)h^1_0(ka_1)] \\
& + \sum_{\substack{j=1\\ j=q}}^{q}\sum_{\substack{m=0\\ m\neq p}}^{4j+2} ik^2 d_{jm}\sum_{n=0}^{\infty}(2n+1) \\
& \times \sum_{l=0}^{n}(-1)^{21-n}Q^{(0)}_{00,\,n-21,\,n}(r_j, \vartheta^0_{jm} = \pi/2, \varphi^0_{jm}) \\
& \times \sum_{s=-1}^{1} Q^{(1)}_{s1,\,n-21,\,n}\left(r_q, \theta^0_{qp} = \frac{\pi}{2}, \varphi^0_{qp}\right)\frac{\psi_0(ka_1)}{3} \\
& \times P^s_1(\cos\theta_{qp})\exp(is\varphi_{qp}) \\
& + \sum_{j=q+1}^{M}\sum_{m=0}^{4j+2} ik^2 d_{jm}\sum_{n=0}^{\infty}(2n+1) \\
& \times \sum_{l=0}^{n}(-1)^{21-n}Q^{(0)}_{00,\,n-21,\,n}(r_j, \vartheta^0_{jm} = \pi/2, \varphi^0_{jm}) \\
& \times \sum_{s=-1}^{1} Q^{(1)}_{s1,\,n-21,\,n}\left(r_q, \theta^0_{qp} = \frac{\pi}{2}, \varphi^0_{qp}\right)\frac{\psi_0(ka_1)}{3} \qquad (22) \\
& \times P^s_1(\cos\theta_{qp})\exp(is\varphi_{qp}) \\
& + \sum_{j=1}^{2}\sum_{n=1}^{(M+1)(2M+3)} ik^2\sum_{l=0}^{\infty}\sum_{m=0}^{l}(-1)^l(2l+1) \\
& \times \sum_{u=-1}^{1} Q^{(0)}_{u1,\,l-2m,\,l}(r_q, \vartheta^0_{qp} = \pi/2, \varphi^0_{qp}) \\
& \times \frac{\psi_0(ka_1)}{3}P^u_1(\cos\vartheta_{qp})\exp(iu\varphi_{qp})b_{jn}\psi_0(ka) \\
& \times h^{(1)}_l(kR_j)P^{j-2m}_l(\cos\vartheta_{jn})\exp[i(l-2m)\varphi_{jn}] \\
& + ik^2\sum_{n=0}^{2M+1}\sum_{m=0}^{n} g^*_{2n,\,2m-n}\sum_{t=-1}^{1} Q^{(0)}_{t1,\,2m-n,\,n} \\
& \times (r_q, \vartheta^0_{qp} = \pi/2, \varphi^0_{qp})\frac{\psi_0(ka_1)}{3}P^t_1(\cos\vartheta_{qp})e^{it\varphi_{qp}};
\end{aligned}$$

where $Q^{(0,\,1)}_{tsln}$ are the conversion factors between different coordinate systems defined in [8]. The physical meaning of formula (22) is as follows. The field produced by the auxilliary radiators consists of their own radiation generated by the zeroth and first harmonics of the normal velocity f_{qp} plus the field due to diffraction of the uncompensated portion of the extraneous field by the elements of the transmitting antenna and the secondary diffraction components from the receiver antennas, the aperture, and the adjacent radiators. This allows us to relax the limitation imposed on the radiator's wave dimension from above. For the auxilliary radiators, we can introduce the physical feasibility condition in the form $\max|f_{qp}| \leq f^*(ka_1)$. The constant f^* characterizes the maximum power density admissible for the chosen class of radiators at a particular ka_1. Thus, the radiator must be small enough for the suppression to be accomplished by monopoles and dipoles and large enough to suppress the field of a given intensity.

As an example, consider the suppression of the plane wave

$$\begin{aligned}
& A\exp\{-ikr(\cos\vartheta\cos\vartheta_F \\
& + \sin\vartheta\sin\vartheta_F\cos(\varphi-\varphi_F)]\},
\end{aligned}$$

incident on the aperture S_0 of radius $a_0 = 1$ m in the direction (θ_F, φ_F). For a sound pressure of 100 dB at 20 Hz, the amplitude is $A = 0.013$ m^2/s. Let us set $c = 340$ m/s, $r_j = (2.7 + 0.2j)$ m, and $a_1 = 0.1$ m. If we choose $M = 1$, the suppression level is 10 dB within 1 m behind the screen. Assume that the amplitudes of the plane wave harmonics near the aperture S_0 are measured exactly and are expressed as

$$\begin{aligned}
g_{2n,\,2m-n} = {} & g^*_{2n,\,2m-n} = (-i)^{n+1}2A(2n+1) \\
& \times \frac{(2n-2m)!}{k(2n)!}P^{2m-n}_n(\cos\vartheta_F)\exp(i(2m-n)\varphi_F).
\end{aligned}$$

The amplitudes (in meters per second) of the velocity potential density at the radiators that solve the field suppression problem at $\theta_F = \pi/3$ and $\varphi_F = 0$ are shown in the table:

$\nu_{00} = -0.324 + i0.911$, $\nu_{01} = -0.058 - i0.28$,
$\nu_{02} = -0.437 + i0.683$, $\nu_{10} = 0.015 - i0.015$,
$\nu_{11} = -0.026 - i0.022$, $\nu_{12} = -0.02 + i0.037$,
$\nu_{13} = -0.0002 + i0.02$, $\nu_{14} = -0.027 + i0.046$,
$\nu_{15} = -0.008 + i0.008$, $\nu_{16} = 0.05 + i0.04$.

To improve the degree of suppression, the number of auxilliary radiators must be increased and a greater number of spatial harmonics must be canceled. For example, to suppress the field by 30 dB, the first 36 spatial modes ($M = 3$) must be canceled.

APPENDIX

The coefficients B^j_{kl} are determined by the recurrent formulas

$$B^j_{N-s,s}(\gamma_s) = A^j_{N-s,s}(\gamma_s), \quad \gamma_s = \cos\vartheta^0_{qs},$$
$$0 \le s \le N, \quad -s \le j \le s, \quad j \ne m,$$

$$B^m_{N-s,s}(\gamma_s) = A^m_{N-s,s}(\gamma_s), \quad 0 \le s \le m-1,$$
$$m+1 \le s \le N;$$

$$B^m_{1,n}(\gamma_s) = A^m_{0,m}(\gamma_s) - A^m_{0,m}(\gamma_N)A^m_{0,N}(\gamma_s)/A^m_{0,N}(\gamma_N),$$
$$0 \le s \le N-1;$$

$$B^m_{N-j,n}(\gamma_s) = B^m_{N-j-1,n}(\gamma_s)$$
$$-\frac{B^m_{N-j-1,n}(\gamma_{j+1})B^m_{N-j-1,j+1}(\gamma_s)}{B^m_{N-j-1,j+1}(\gamma_{j+1})},$$
$$n \le j \le N-2, \quad s \le j;$$

$$B^m_{N-n+1,p}(\gamma_i) = A^m_{N-n,p}(\gamma_i) - \frac{A^m_{N-n,p}(\gamma_n)B^m_{N-n,n}(\gamma_i)}{B^m_{N-n,n}(\gamma_n)},$$
$$m+1 \le p \le n-1, \quad i \le n-1;$$

$$B^m_{N-n+j,p}(\gamma_i) = B^m_{N-n+j-1,p}(\gamma_i)$$
$$-\frac{B^m_{N-n+j-1,p}(\gamma_{n-j+1})B^m_{N-n+j-1,n-j+1}(\gamma_i)}{B^m_{N-n+j-1,n+j-1}(\gamma_{n-j+1})},$$
$$m+1 \le p \le n-j, \quad i \le n-j, \quad 2 \le j \le n-m-1;$$

$$B^m_{N-j,m}(\gamma_j) = B^m_{N-j-1,m}(\gamma_i)$$
$$-\frac{B^m_{N-j-1,j+1}(\gamma_j)B^m_{N-j-1,Mj+1}(\gamma_i)}{B^m_{N-j-1,j+1}(\gamma_{j+1})},$$

$i \le j$; s and p are integers,

$$B^m_{N-M,M}(\gamma_M) = B^m_{N-M-1,M}(\gamma_M)$$
$$-\frac{B^m_{N-M-1,M+1}(\gamma_M)B^m_{N-M-1,M+1}(\gamma_M)}{B^m_{N-M-1,M+1}(\gamma_{M+1})}, \quad |m| = M.$$

The coefficients D^j_{kl} are calculated by the recurrent formulas

$$D^j_{N-M-s+2,M+s-2}(\gamma_{M+s-2})$$
$$= B^j_{N-M-s+2,M+s-2}(\gamma_{M+s-2})$$
$$-\frac{B^j_{N-M-s,M+s}(\gamma_{M+s-1})B^j_{N-m-s+1,M+s-1}(\gamma_{M+s-2})}{B^j_{N-M-s+1,M+s-1}(\gamma_{M+s-1})},$$
$$|j| = M;$$

s and q are integers,

$$D^j_{N-q,q}(\gamma_i) = D^j_{N-q-1,q+1}(\gamma_i)$$
$$-\frac{D^j_{N-q-1,q+1}(\gamma_{q+1})B^j_{N-q-1,q+1}(\gamma_i)}{B^j_{N-q-1,q+1}(\gamma_{q+1})},$$
$$|j|-1 \le q \le |m|+s-3, \; i \le q.$$

In the system of rows $(|j| - s)$:

$$E\left(\frac{(2|j|+1)(k-1)}{2(k-1)+1}\right) + 1 \le s \le E\left(\frac{(2|j|+1)k}{2k+1}\right),$$
$$1 \le k \le E\left(\frac{(j-m)\operatorname{sgn} j}{2|m|+1}\right),$$

where $E(x)$ is the integral part of x and

$$D^j_{N-J+s+1,J-s-1}(\gamma_{J-s-1}) = D^j_{N-J+s,J-s}(\gamma_{J-s-1})$$
$$-\frac{B^{(2ks-(2k-1)J-k)\operatorname{sgn} j}_{N-J+s,J-s}(\gamma_{J-s-1})D^j_{N-J+s,J-s}(\gamma_{J-s})}{B^{(2ks-(2k-1)J-k)\operatorname{sgn} j}_{N-J+s,J-s}(\gamma_{J-s})},$$
$$|j| = J.$$

The coefficients B^{2m-n}_{kl} and D^{2m-n}_{kl} are determined by the recurrent formulas

$$B^{2m-n}_{0,n}(\gamma_i) = A^{2m-n}_{0,|2m-n|}(\gamma_i), \quad 0 \le n \le 2N+1,$$
$$0 \le m \le n, \quad 0 \le i \le n;$$

$$B^{2m-n}_{N-t+1,n-2l}(\gamma_i) = A^{2m-n}_{N-t,n-2l}(\gamma_i),$$
$$0 \le i \le t = E(n/2);$$

$$B^{2m-n}_{N-t+1,n-2l}(\gamma_i) = A^{2m-n}_{N-t,n-2l}(\gamma_i)$$
$$-B^{2m-n}_{N-t,n}(\gamma_i)A^{2m-n}_{N-t,n-2l}(\gamma_t)/B^{2m-n}_{N-t,n}(\gamma_t),$$

$$0 \le l \le (n-|2m-n|-2)/2, \quad 0 \le i \le t-1;$$

$$B^{2m-n}_{N-t+s,\, n-2l}(\gamma_i) = B^{2m-n}_{N-t+s-1,\, n-2l}(\gamma_i) - \frac{B^{2m-n}_{N-t+s-1,\, Q(n-2l)}(\gamma_i) B^{2m-n}_{N-t+s-1,\, n-2l}(\gamma_{t-s+1})}{B^{2m-n}_{N-t+s-1,\, Q(n-2l)}(\gamma_{t-s+1})},$$

$$t+1 \le n-2l \le 2(t-s+1);$$

$Q(n-2l) = 2(t-s+1)$ for even n; $Q(n-2l) = 2(t-s+1)+1$ for odd n;

$$D^{\beta_j}_{N-k,\, S(k-1)}(\gamma_{k-1}) = D^{\beta_j}_{N-k+1,\, S(k-1)}(\gamma_{k-1}) - \frac{B^{(|\beta_j|-4q-3)\operatorname{sgn}\beta_j}_{N-k,\, S(k)}(\gamma_{k-1}) D^{\beta_j}_{N-k,\, S(k)}(\gamma_k)}{B^{(|\beta_j|-4q-3)\operatorname{sgn}\beta_j}_{N-k,\, S(k)}(\gamma_k)},$$

$$\beta_j = 2m-n+j(4i+3), \quad q = E(\beta_j/2),$$

$S(k) = 2q$ for even β_j; $S(k) = 2q+1$ for odd β_j,

$$-E\left(\frac{2t-n+2m+1}{4i+3}\right) \le j \le E\left(\frac{2t+1+n-2m}{4i+3}\right),$$

$$i \le t \le N,$$

$$E\left(E(|\beta_j|/2) - \frac{1}{4}\left(\frac{2|\beta_j|}{2l-1} - 3\right)\right)$$

$$\le k \le E\left(E(|\beta_j|/2) - \frac{1}{4}\left(\frac{2|\beta_j|}{2l+1} - 3\right)\right) \text{ for}$$

$$l = 1, 2, \ldots, |j|.$$

The coefficients F^j_{kl} and K^j_{kl} are determined by the recurrent formulas given below.

Consider the auxilliary coefficients $H^{2j}_{s,\, 2p}(kr_i)$ and $H^{2j+1}_{s,\, 2p+1}(kr_i)$

$$H^{2j}_{0,\, 2p}(kr_i) = h^{(1)}_{2p}(kr_i), \quad p = 0, 1, \ldots, M,$$

$$-p \le j \le p, \quad i = 0, 1, \ldots, M,$$

$$H^{2j+1}_{0,\, 2p+1}(kr_i) = h^{(1)}_{2p+1}(kr_i), \quad p = 0, 1, \ldots, M,$$

$$-(p+1) \le j \le p, \quad i = 0, 1, \ldots, M,$$

where j is an integer, $h^1_n(x)$ is the Hankel spherical function,

$$H^{2j}_{s,\, 2p}(kr_i) = H^{2j}_{s-1,\, 2p}(kr_i) - \frac{H^{2j}_{s-1,\, 2p}(kr_{M-s-1}) H^{2j}_{s-1,\, 2(M-s+1)}(kr_j)}{H^{2j}_{s-1,\, 2(M-s+1)}(kr_{M-s+1})},$$

$$H^{2j+1}_{s,\, 2p+1}(kr_i) = H^{2j+1}_{s-1,\, 2p+1}(kr_i) - \frac{H^{2j+1}_{s-1,\, 2p+1}(kr_{M-s+1}) H^{2j+1}_{s-1,\, 2(M-s+1)+1}(kr_i)}{H^{2j+1}_{s-1,\, 2(M-s+1)+1}(kr_{M-s+1})},$$

$1 \le s \le M$, $0 \le i \le M-s$, $0 \le p \le M-s$, s is the iteration number.

Let us define the F^j_{kl} coefficients by the formulas

$$F^{n-2m}_{M-t+1,\, 2p}(kr_i) = H^{n-2m}_{M-t,\, 2p}(kr_i) - \frac{H^{n-2m}_{M-t,\, 2p}(kr_t) H^{n-2m}_{M-t,\, 2g}(kr_i)}{H^{n-2m}_{M-t,\, 2g}(kr_t)},$$

for even n,

$$g = E\left(\left|\frac{n-2m}{2}\right|\right), \quad t = E\left(\frac{n}{2}\right),$$

$$F^{n-2m}_{M-t+1,\, 2p+1}(kr_i) = H^{n-2m}_{M-t,\, 2p+1}(kr_i) - \frac{H^{n-2m}_{M-t,\, 2p+1}(kr_t) H^{n-2m}_{M-t,\, 2g+1}(kr_i)}{H^{n-2m}_{M-t,\, 2g+1}(kr_t)},$$

for odd n, $g \le p \le 2t-1$, $0 \le i \le 2t-1$;

$$F^{n-2m}_{M-t+l,\, 2p}(kr_i) = F^{n-2m}_{M-t+l-1,\, 2p}(kr_i) - \frac{F^{n-2m}_{M-t+l-1,\, 2p}(kr_{t-l+1}) F^{n-2m}_{M-t+l-1,\, 2(t-1)}(kr_i)}{F^{n-2m}_{M-t+l-1,\, 2(t-l+1)}(kr_{t-l+1})},$$

for even n,

$$F^{n-2m}_{M-t+l,\, 2p+1}(kr_i) = F^{n-2m}_{M-t+l-1,\, 2p+1}(kr_i) - \frac{F^{n-2m}_{M-t+l-1,\, 2p+1}(kr_{t-l+1}) F^{n-2m}_{M-t+l-1,\, 2(t-l+1)}(kr_i)}{F^{n-2m}_{M-t+l-1,\, 2(t-l+1)}(kr_{t-l+1})},$$

$$2 \le l \le t-g, \quad 0 \le i \le 2t-l, \quad p \le 2t-l,$$

for odd n, where l is an integer.

The coefficients K^j_{kl} are calculated as follows:

$$K^{2k-2m}_{M-j+2,\, 2(j-2)}(kr_i) = F^{2k-2m}_{M-j,\, 2(j-1)}(kr_i) - \frac{F^{2k-2m}_{M-j,\, 2(j-1)}(kr_{j-1}) F^{2k-2m}_{M-j+1,\, 2(j-1)}(kr_i)}{F^{2k-2m}_{M-j+1,\, 2(j-1)}(kr_{j-1})},$$

$$n = 2k, \quad i \le j-2,$$

$$K^{2k+1-2m}_{M-j+2,\, 2(j-2)+1}(kr_i) = F^{2k+1-2m}_{M-j,\, 2(j-1)+1}(kr_i) - \frac{F^{2k+1-2m}_{M-j+1,\, 2(j-1)+1}(kr_{j-1}) F^{2k+1-2m}_{M-j+1,\, 2(j-1)+1}(kr_i)}{F^{2k+1-2m}_{M-j+1,\, 2(j-1)+1}},$$

$$n = 2k+1,$$

$$K^{2k-2m}_{M-j+1,\, 2(j-q)}(kr_i) = K^{2k-2m}_{M-j+q-1,\, 2(j-q+1)}(kr_i) - \frac{K^{2k-2m}_{M-j+q-1,\, 2(j-q+1)}(kr_{j-q+1}) F^{2k-2m}_{M-j+q-1,\, 2(j-q+1)}(kr_i)}{F^{2k-2m}_{M-j+q-1,\, 2(j-q+1)}(kr_{j-q+1})},$$

$n = 2k$, $3 \le q \le j-g$, $i \le j-q$, q is an integer,

$$K^{2k+1-2m}_{M-j+q,\,2(j-q)+1}(kr_i) = F^{2k+1-2m}_{M-j+q-1,\,2(j-q+1)+1}(kr_i)$$

$$-\frac{K^{2k+1-2m}_{M-j+q-1,\,2(j-q+1)+1}(kr_{j-q+1})F^{2k+1-2m}_{M-j+q-1,\,2(j-q+1)+1}(kr_i)}{F^{2k+1-2m}_{M-j+q-1,\,2(j-q+1)+1}(kr_{j-q+1})}, \quad n = 2k+1.$$

REFERENCES

1. V. P. Ivanov, Akust. Zh. **33**, 946 (1987) [Sov. Phys. Acoust. **33**, 551 (1987)].
2. G. V. Alekseev and F. S. Panasyuk, Akust. Zh. **45**, 723 (1999) [Acoust. Phys. **45**, 649 (1999)].
3. A. I. Boĭko and V. V. Tyutekin, Akust. Zh. **45**, 454 (1999) [Acoust. Phys. **45**, 402 (1999)].
4. S. Vosukainen, Acust. Acta Acust. **83**, 103 (1997).
5. S. J. Elliott, in *Proceedings of ISVR, Active 99* (Proceedings Univ. of Southampton, 1999), p. 3.
6. V. P. Ivanov, Akust. Zh. **47**, 83 (2001) [Acoust. Phys. **47**, 68 (2001)].
7. V. P. Ivanov, Akust. Zh. **36**, 872 (1990) [Sov. Phys. Acoust. **36**, 487 (1990)].
8. E. A. Ivanov, *Electromagnetic Wave Diffraction by Two Bodies* (Nauka i Tekhnika, Minsk, 1968).

Translated by A. Khzmalyan

Acoustical Physics, Vol. 50, No. 1, 2004, pp. 66–73. Translated from Akusticheskiĭ Zhurnal, Vol. 50, No. 1, 2004, pp. 77–85.
Original Russian Text Copyright © 2004 by Kapustina, Kolesnikova, Romanova.

A Vortex Mechanism for the Formation of Two-Dimensional Domains in Cholesteric Liquid Crystals under the Effect of Ultrasound

O. A. Kapustina, N. A. Kolesnikova, and O. V. Romanova
Andreev Acoustics Institute, Russian Academy of Sciences, ul. Shvernika 4, Moscow, 117036 Russia
e-mail: bvp@akin.ru

Received October 15, 2002

Abstract—An experimental verification is presented for the new theoretical model of a vortex mechanism that explains the formation of two-dimensional domains in planar layers of cholesteric liquid crystals under the effect of ultrasound in the range of frequencies not exceeding the inverse relaxation time of the orientational order parameter. The limits of applicability of this model are determined. *© 2004 MAIK “Nauka/Interperiodica”.*

One of the most remarkable physical phenomena proper to liquid crystals is the formation of ordered one- and two-dimensional spatially modulated structures (domains) under external actions of different kinds (acoustic, electrical, magnetic, etc.). The condition for the existence of such structures is of a threshold character and depends on the equilibrium of volumetric and dissipative forces proper to a specific kind of action [1–3].

This paper presents the results of an experimental study of the conditions for the formation of two-dimensional domains in planar layers of cholesteric liquid crystals, with a cholesteric helical pitch P_0 much smaller than the layer thickness d, under the effect of ultrasound when the viscous and elastic wavelengths λ_v and λ satisfy the inequalities

$$\lambda_v \ll d, \quad \lambda \gg d.$$

Analysis of experimental data on the threshold characteristics of domains (the amplitude of the particle velocity V_0^{th} in the wave incident upon a layer, which corresponds to the domain formation, and the spatial period of domains at the threshold of the effect Λ^{th}) is performed in the framework of the model of a vortex mechanism for the destabilization of the planar macrostructure of the mesophase layer, which was proposed in [4] and postulates a new approach to describing this phenomenon.

It is well known that cholesteric liquid crystals have a layered structure and helical ordering: in passing from one cholesteric plane to another, the director **n** characterizing the local orientation of molecules rotates uniformly in space with respect to the helix axis h (the z axis in Fig. 1a). The nominal “free” helical pitch P_0 of this structure is equal to $2\pi/q_0$ (q_0 is the helical wave number). However, since the states n and $-n$ are indistinguishable, the interval of periodicity along the z axis is equal to $P_0/2 = \pi/q_0$. Creating tangential boundary conditions on both sides of a thin mesophase layer, it is possible to obtain a single crystal of a cholesteric liquid crystal with a so-called planar texture [2]. If the layer thickness satisfies the condition $d = 0.5mP_0$ ($m = 1, 2, 3, \ldots$), the spectral conformation preserves the equilibrium state and has a free helical pitch of P_0 (Fig. 1b). In the case when d is smaller or greater than $0.5mP_0$, the helix is forced to slightly change its pitch to be completely consistent with these boundary conditions. In this case, a nonequilibrium conformation arises with a forced helical pitch P, which is smaller or greater than P_0 depending on the compression or extension of the helix.

Experiments on observation of domain formation in planar layers of cholesteric liquid crystals and determination of their threshold characteristics were carried out in the conditions schematically represented in Fig. 1c. Here, (*1*) a liquid crystal fills a plane capillary formed by (*2*) a thin glass plate and (*3*) a substrate. The inner surfaces of the plate and the substrate are treated according to a technique conventional for the formation of tangential boundary conditions and production of a planar texture.[1] The thickness of the layer of a cholesteric liquid crystal in the cell was set either with the help of thoriated mylar spacers (10, 40, 80, and 100 μm) or by changing the distance between plates *2* and *3* within the range 5–240 μm by shifting plate *2*. Utilization of a cell with a variable layer thickness provided an opportunity in the process of observation not only to

---

[1] To form a planar arrangement of molecules of a cholesteric liquid crystal, a coating of polyvinyl alcohol was applied to the cell surfaces bounding the crystal. After that, the surfaces were polished in one of the directions determining the orientation of the director **n**.

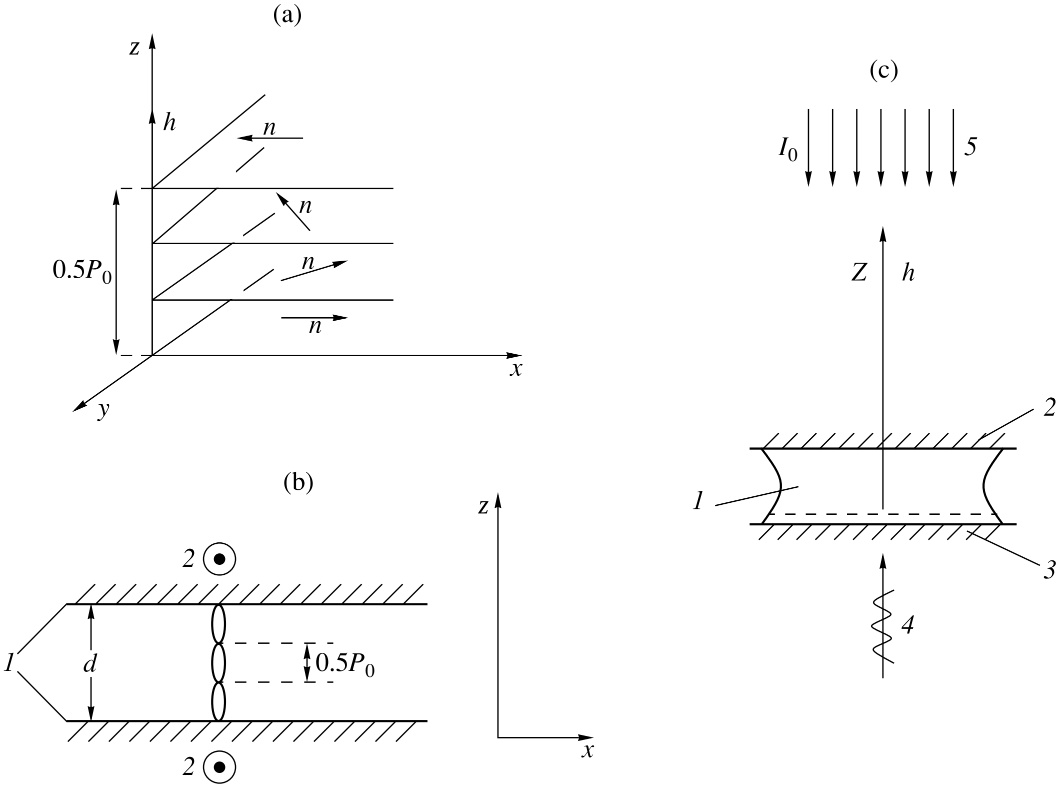

Fig. 1. Analysis of ultrasonic action on the planar texture of a cholesteric liquid crystal. Molecule arrangement in the cholesteric mesophase. (a) Sequential cholesteric planes. (b) A schematic diagram of the planar structure of a cholesteric liquid crystal between two (*1*) surfaces with tangential boundary conditions formed by (*2*) polishing these surfaces in a preset direction; the helix is directed along the *z* axis and the director lies in the horizontal plane everywhere. (c) Geometry of the problem and a simplified experimental setup: (*1*) a cholesteric liquid crystal, (*2*) an optically transparent plate (glass), (*3*) a substrate with a light-reflecting coating, (*4*) a longitudinal ultrasonic wave, and (*5*) a light beam of intensity I_0 incident upon the liquid crystal layer.

evaluate the degree of extension or compression of a cholesteric structure with a forced helical pitch P but also to realize the equilibrium states of this structure, which correspond to the condition $d = 0.5mP_0$. A longitudinal ultrasonic wave was incident upon a layer of a cholesteric liquid crystal in the direction of the helix axis. The ultrasonic frequency was measured within the range 0.35–15 MHz. To control the level of the effect, the voltage fed to the ultrasonic transducers was measured by a voltmeter. The voltage was recalculated either to the oscillation amplitude at the transducer–liquid crystal boundary according to the method of analyzing multilayer oscillatory systems [6] or to the acoustic intensity of the wave incident upon the layer according to the data (initial) of transducer calibration performed by the method of acoustic radiometer. Observation on the orientation state of liquid crystals in cells with constant and variable layer thickness was conducted using the polarization-optical technique in reflected light according to the known schemes described earlier [2, 5, 7].

Diluted solutions of cholesteric liquid crystals (cholesteryl chloride, cholesteryl nonanoate, and cholesteryl propienate) in a nematic liquid crystal (ZhK404), whose helical pitch P_0 was large in comparison with the light wavelength λ_0 and equal to 2, 4, 10, and 30 μm, were studied.[2] The pitch value was measured by the Cano–Grandjean method [8].

Experiments were set up as follows: the voltage across the transducer was increased and changes in the orientation state of three planar layers of liquid crystals in three solutions under study were observed by a polarization microscope in the conditions of homogeneous (frequencies of 0.9–15 MHz) and quasi-homogeneous (frequencies of 0.35–3.65 MHz) wave fields. These observations show that when the threshold voltage U^{th} is reached, an inhomogeneous distribution of orientation of the director **n** is formed, which manifests itself optically as a two-dimensional system of equidistant bright fringes parallel and perpendicular to the director position in the initial unperturbed orientation state of the layer. This is a so-called square grid with spatial periods Λ_x and Λ_y and with the sides parallel and perpendicular to the direction of polishing of the boundary surfaces of the cell (Figs. 2a, 2a').

---

[2] It is known that, when the light wavelength is comparable with the helical pitch, the optical properties of cholesteric liquid crystals change radically [8].

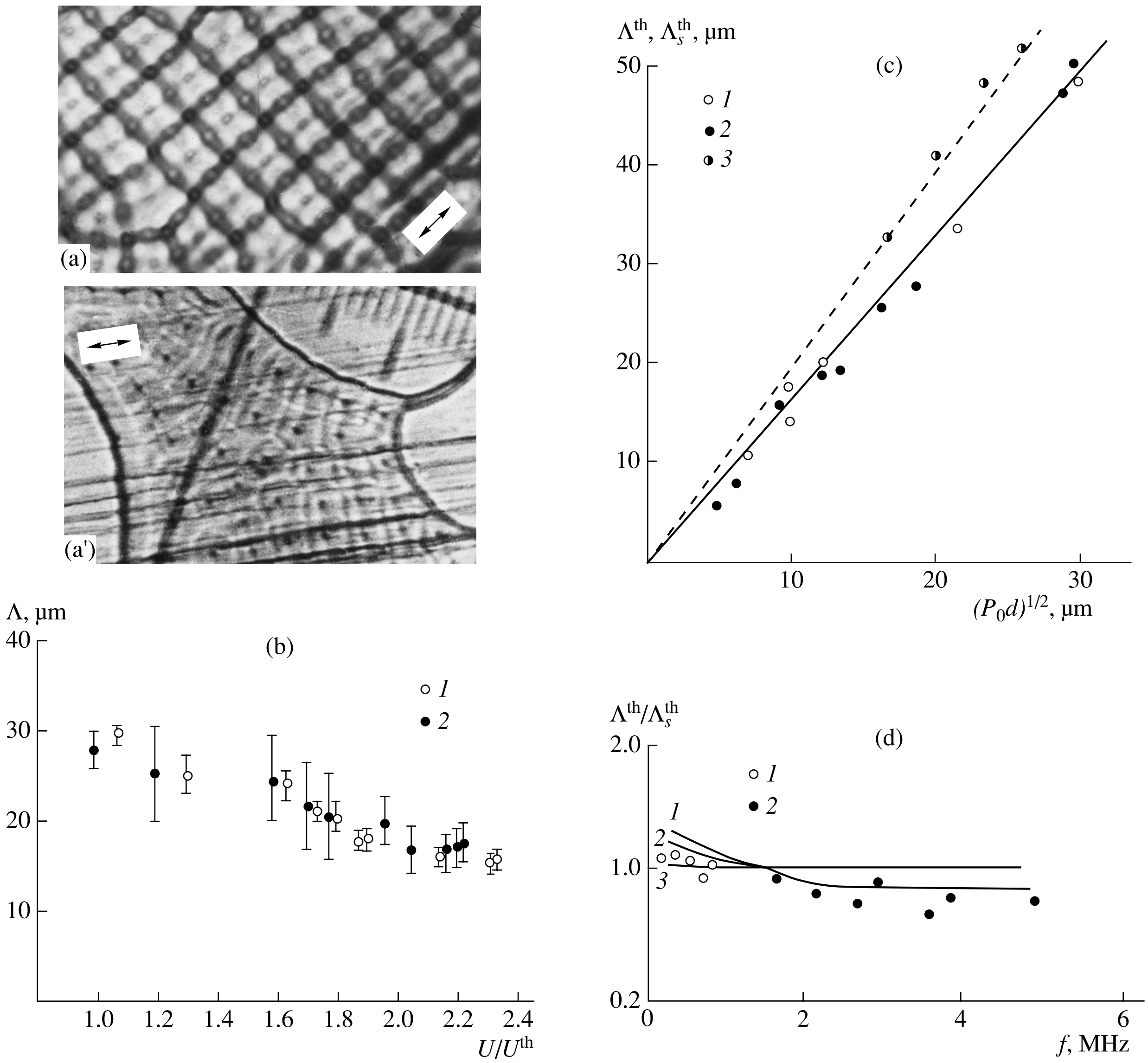

Fig. 2. Analysis of relationships determining the spatial period of domains. (a, a') Optical patterns of planar texture distortions in an ultrasonic field in samples without and with disclinations, which force the square grid to slightly change its orientation with respect to the direction (shown by the symbol ⟷) of the substrate polishing lines (top view; microscope magnification is different in two images); the layer thickness is 40 μm, the helical pitch is 4 μm, the ultrasonic frequency is 0.375 MHz, and the spatial period of the grid is ~19.5 × 19.5 μm. (b) Dependence of domain period on the level of action for a layer with a thickness of 80 μm in (*1*) homogeneous and (*2*) quasi-homogeneous wave fields; the helical pitch is 4 μm and the frequency is 2.95 MHz. (c) Relation of the domain period at the threshold of the effect to the layer thickness and the helical pitch in (*1*) cholesteryl chloride–ZhK404 and (*2*) cholesteryl nonanoate–ZhK404 solutions under ultrasonic action (a frequency of 2.95 MHz) and in a (*3*) cholesteryl chloride–MBBA solution under static extension. (d) Influence of ultrasonic frequency on the relative domain period at a layer thickness of 22 μm and a helical pitch of 4 μm; curves *1–3* correspond to the theoretical dependences of the period for the values of the extension parameter δ equal to 0.01, 0.5, and 0.9; experimental values of the period in the cholesteryl chloride–ZhK404 solution for layers (*1*) with and (*2*) without disclinations.

To describe this effect quantitatively, we conducted experimental studies of the dynamics of the development of structures, determination of their period and threshold level of external action in the conditions of varying parameters of the wave field, and determination of the layer thickness of liquid crystals and the cholesteric helical pitch.

Figure 2b presents a typical dependence of the current values of the spatial period $\Lambda = \Lambda_x \cong \Lambda_y$ on the action level for a sample with a thickness of 80 μm of the cholesteryl chloride–ZhK404 solution with a helical pitch of 4 μm. Here, U and U^{th} are the current and threshold values of the voltage at the ultrasonic transducer, respectively. Notations *1* and *2* refer to the values of Λ observed in homogeneous and inhomogeneous wave fields at a frequency ~2.95 MHz, respectively. One can see that, near the threshold, the structure period has the value greater than that in the over-threshold mode, and at $U \cong 2U^{\mathrm{th}}$ it reaches a constant value. It is essential that the degree of homogeneity of the wave field does not influence the dynamics of the process.

The behavior described above takes place within the whole frequency range considered, in samples with a thickness of 10–240 μm. The results of these observations are generalized in Fig. 2c. Here, we give the threshold values obtained in these experiments for the spatial period Λ^{th} of the two-dimensional domains that are formed in the cholesteryl chloride–ZhK404 and cholesteryl nonanoate–ZhK404 solutions (notations *1* and *2*, respectively) with the equilibrium values of the helical pitch P_0 equal to 2, 4, 10, and 30 μm at a frequency of ~2.95 MHz. Analysis of these data provides an opportunity to draw a conclusion that, at a constant ultrasonic frequency at the threshold of the effect, the relation of the spatial period to the thickness of the liquid crystal layer and the helical pitch is approximated by a functional dependence of the form $\Lambda^{\mathrm{th}} \sim (P_0 d)^{1/2}$. The threshold values of the period Λ_s^{th} of domains formed in planar layers of a cholesteryl nonanoate–MBBA solution with a helical pitch of 12 μm in the conditions of static extension (notation *3*), which were obtained in [9], are given in the same figure for comparison. One can see that the dependence characteristic of the ultrasonic field persists, but in these conditions the angular coefficient of the plot approximating it is higher. These values of Λ_s^{th} will be used below as a normalizing parameter for representing the experimental values of Λ^{th}, which will allow us to simplify the comparison of experimental and theoretical data. It is necessary to note that the values of Λ_s^{th} given above are obtained for the solution containing a classical nematic liquid crystal, *N*–(*n*-methoxybenzylidene)–*n*-butylaniline (MBBA), which is one of the components of the nematic mixture of ZhK404 used in our experiments.

The connection of the spatial period of domains with ultrasonic frequency is represented by the family of experimental values of $\Lambda^{\mathrm{th}}/\Lambda_s^{\mathrm{th}}$ given in Fig. 2d. They are obtained for a layer with a thickness of 22 μm of the cholesteryl chloride–ZhK404 solution with a helical pitch of 4 μm. Notations *1* and *2* refer to the systems of domains formed in the layer regions bounded by paired disclinations (see Fig. 2a), where the cholesteric structure is extended [2], and in the conditions of the absence of these disclinations (an equilibrium cholesteric structure).[3] According to these data, the ultrasonic frequency almost does not influence the spatial period of domains.

Let us examine the basic rules characterizing the magnitude of action at the threshold of the effect. The results of experiments on the influence of the thickness of a liquid crystal layer and the helical pitch on the threshold Mach number $M^{\mathrm{th}} = V^{\mathrm{th}}/c$ for cholesteryl chloride–ZhK404 solutions at a frequency of 2.95 MHz are generalized by the plot given in Fig. 3a. A description of the adopted notations is given in the figure caption. It follows from these data that, in the region of values $P_0/d \ll 1$, the connection of the threshold Mach number with the layer thickness and helical pitch is determined by a relation of the form $M^{\mathrm{th}} \sim (P_0/d)^{1/2}$.

Experimental data illustrating the connection of the threshold Mach number with the ultrasonic frequency at fixed values of P_0 and d are given in Fig. 3b. They belong to a cholesteryl chloride–ZhK404 layer with a thickness of 22 μm and a helical pitch of 4 μm. It is necessary to note the difference of the values of M^{th} obtained in experiments with the samples containing disclinations (frequencies of 0.3, 0.5, 0.6, 0.8, and 0.9 MHz) from those corresponding to the samples without disclinations (frequencies of 1.2–14.5 MHz) (notations *1* and *2*). This fact needs to be analyzed. It is essential that, in each of these regions, a change in ultrasonic frequency almost does not influence the threshold Mach number.

Let us discuss the experimental data given above for the behavior of the threshold characteristics of two-dimensional domains in cholesteric liquid crystals from the point of view of the theoretical model described in [4]. Traditionally, a theoretical analysis of structural transformations in liquid crystals is performed within the framework of a macroscopic approach [1–3], which was formulated as far back as the 1870s by Leslie and Ericksen and is based on the classical linear hydrodynamics, that takes into account only the anisotropy of viscous properties of liquid crystals. This concept is still valid. However, certain difficulties arose in analyzing acoustically induced domains. It turned out that a common approach provides a description adequate to experimental data only in the sonic frequency range [10, 11]. Experiments by Gurov and Kapustina [5] with cholesteric liquid crystals proved that, in the ultrasonic range, the theoretical model [12, 13] based on the equations of linear hydrodynamics fails even if one takes into account the existence of regions with an extended cholesteric structure in a planar layer. Later, it was found [14] that, for nematic liquid crystals only the inclusion of nonequilibrium thermodynamics with allowance for relaxation phenomena in the mesophase, which lead to anisotropy of dynamic elasticity, provide an opportunity to match the results of calculating the threshold characteristics of domains in the framework of classical hydrodynamics and the experimental data for this type of liquid crystals in the frequency range 1–10 MHz. Extension of this approach to the analysis of structural transformations in planar layers of cholesteric liquid crystals in an ultrasonic field led to the development of a theoretical model of a "vortex" mech-

---

[3] It was impossible to obtain homogeneous liquid crystal layers free of disclinations in these experiments because of the design peculiarities of the cells used in the lowest frequency range of 0.3–0.9 MHz.

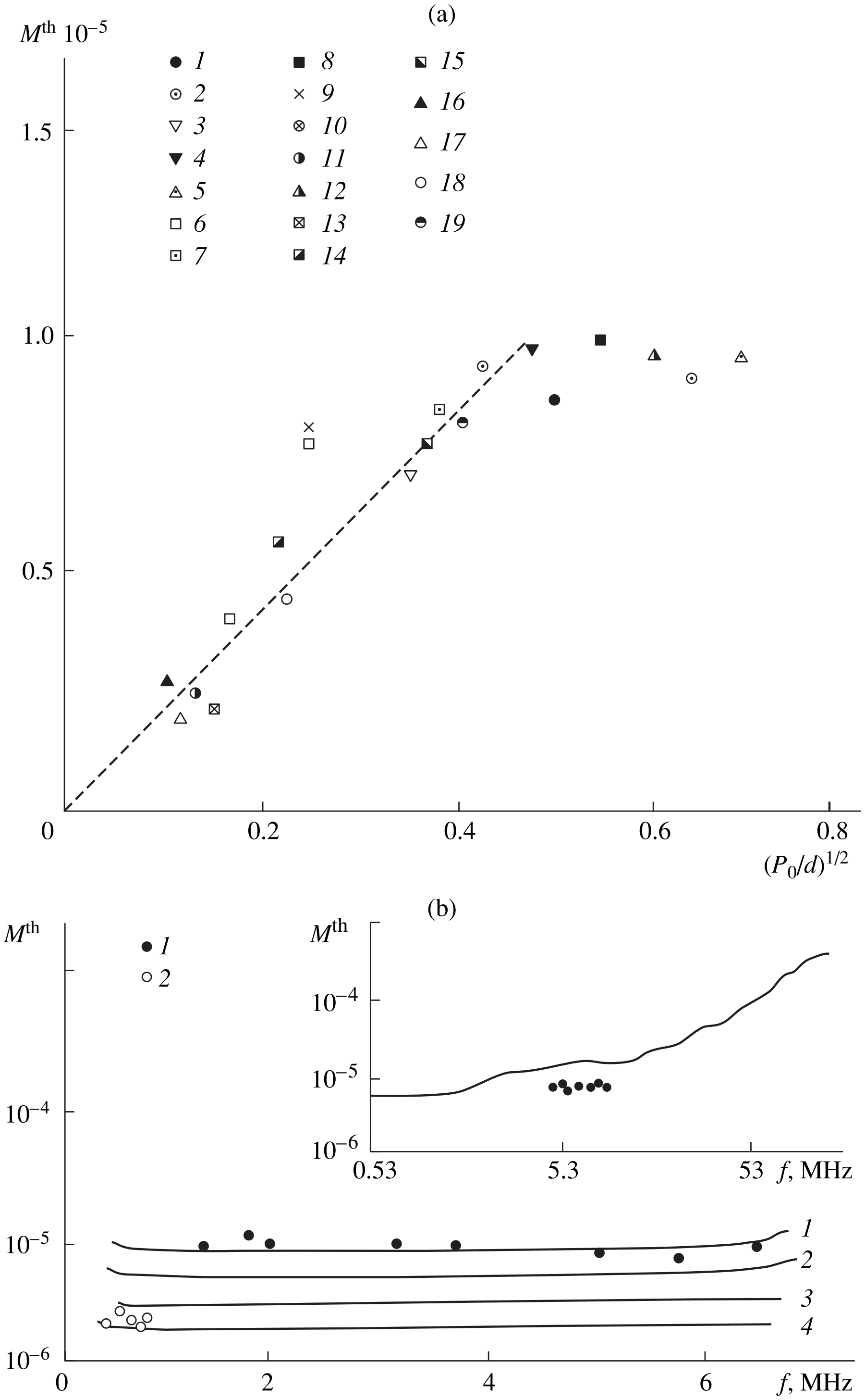

Fig. 3. Basic relationships determining the behavior of the threshold of the effect. (a) Influence of the layer thickness and helical pitch on the threshold Mach number in the cholesteryl chloride–ZhK404 solution at a frequency of 2.95 MHz. The values of P_0 and d are given using the following notations: (*1*) 2 and 10 μm; (*2*) 4 and 10 μm; (*3*) 2 and 22 μm; (*4*) 4 and 22 μm; (*5*) 10 and 22 μm; (*6*) 2 and 40 μm; (*7*) 4 and 40 μm; (*8*) 10 and 40 μm; (*9*) 4 and 80 μm; (*10*) 10 and 80 μm; (*11*) 2 and 90 μm; (*12*) 30 and 90 μm; (*13*) 2 and 100 μm; (*14*) 4 and 100 μm; (*15*) 10 and 100 μm; (*16*) 2 and 240 μm; (*17*) 4 and 240 μm; (*18*) 10 and 240 μm; and (*19*) 30 and 240 μm. (b) Relation of the threshold Mach number to ultrasonic frequency for a layer thickness of 22 μm and a helical pitch of 4 μm. Curves *1*–*4* correspond to theoretical frequency dependences for the values of the extension parameter equal to 0, 0.5, 0.7, and 0.9. Experimental threshold values in the frequency range of 0.3–6 MHz are presented for layers (*1*) with and (*2*) without disclinations. The inset shows theoretical and experimental threshold values in the high-frequency range for layers without disclinations.

anism of domain formation [4], which we discuss below.

The vortex model is based on the solutions of classical equations of hydrodynamics, where the universal property of a medium, i.e., a capability to restore thermodynamic equilibrium perturbed by compression and expansion in an ultrasonic wave, is taken into account. According to [4], relaxation processes change the character of motion of a cholesteric liquid and lead to anisotropy of the dynamic modulus of elasticity $\Delta E = DE(\omega\tau)^2/[1 + (\omega\tau)^2]$. Here, $\omega = 2\pi f$, f is the ultrasonic frequency, τ is the relaxation time of the orientational order parameter, and $2DE = (E_{\parallel} - E_{\perp})\big|_{\omega = 0}^{\omega = \infty}$ is the dispersion jump of anisotropy of the elastic modulus of the medium under compression in an ultrasonic wave along the crystal axis ($E_{\parallel}$) and in the direction perpendicular to it ($E_{\perp}$). A general scheme of formation of two-dimensional domains that is based on the vortex model is as follows: a random, periodic along a cholesteric layer, deviation of the director from the equilibrium orientation causes shear stress and moments, which give rise to oscillating vortex flows of the cholesteric liquid with the same periodicity. Displacement of particles in these flows lags in phase with respect to the compression ε of the medium in an ultrasonic wave, which causes nonlinear stationary moments of the form $\overline{\gamma\theta\dot{\varepsilon}}$, and these moments increase the initial random rotation of the director. At the threshold of the effect, the action of these rotational moments is compensated by Frank's elastic moments, which tend to retain the initial arrangement of cholesteric layers. However, as ultrasonic intensity increases, this balance is violated and, as a compromise, a distortion periodic in the x and y axes is formed in the director field, which can be described by two angular variables [4] θ, $\varphi \sim \exp(iq_x x + iq_y y)\sin q_z z$. Here and above, θ and φ are the angles determining the deviation of molecules from the unperturbed cholesteric plane and from the initial orientation in this plane, respectively; q_x, q_y, and q_z are the wave numbers of distortion along the x, y, and z axes; $q_z = 2\pi/d$; and γ is the rotational viscosity of the liquid crystal. According to [4], for the physical situation adequate to the conditions of the experiments described above and the cholesteric structure extended along the helix axis (the z axis),[4] the threshold Mach number in the wave incident on the layer is represented in the most general form by the relation

$$M^{\text{th}}(\omega, q_i) = [\eta K_{33}(3+\beta)q_s^4/32\gamma q_0^2 DE]^{1/2}F(\omega, q_i), \tag{1}$$

where $K = K_{11} = K_{33}$ and K_{22} are the Frank's elastic constants, $\beta = K_{22}/K$, $q_s = 2\pi[2\beta/(3+\beta)]^{1/4}/(P_0 d)^{1/2}$, $\eta = 0.5(\alpha_4 + 0.5\alpha_6)$, and α_4 and α_6 are the Leslie coefficients of viscosity. The wave number of domains at the threshold of the effect is determined from the condition for the minimum of the function $F(\omega, q_i)$ with respect to the quantities q_i. The expression for $F(\omega, q_i)$ is omitted here because of its awkwardness. For qualitative estimation, we use analytical representations of threshold characteristics at low and high frequencies, which follow from Eq. (1). According to [4], we have

for $\omega \gg \omega_1$, $M^{\text{th}} \sim \omega^{1/2}$

$$\Lambda^{\text{th}} = \Lambda_s^{\text{th}}\{(a+2\delta)/[1+(1+a^2+2a\delta)^{1/2}]\}^{1/2} \sim (P_0 d)^{1/2} \tag{2}$$

and for $\omega \ll \omega_1$, $M^{\text{th}} \sim \omega^{-1/2}$

$$\Lambda^{\text{th}} \approx \Lambda_s^{\text{th}}/\sqrt{2}a\omega\tau \sim (P_0 d)^{1/2}\omega^{-1}. \tag{3}$$

Here, $\Lambda_s^{\text{th}} = \dfrac{\pi\sqrt{2}}{q_s} = (P_0 d)^{1/2}[(3+\beta)/8\beta]^{1/4}$ is the threshold value of the period of two-dimensional domains arising according to the theory [14] in a planar layer of a cholesteric liquid crystal under the conditions of static extension of cholesteric layers along the helix axis, if the value of this extension δ_z reaches the critical value equal to

$$\delta_c = P_0[2\beta(3+\beta)]^{1/2}/2d, \quad \delta = \delta_z/\delta_c,$$

$$a = (\rho P_0 d/4\pi^2\eta\tau)[(3+\beta)/2\beta]^{1/2},$$

$$\omega_1 = (2\pi\eta/\rho P_0 d)[2\beta/(3+\beta)]^{1/2}.$$

In a range of frequencies determined by the inequality $\omega_1 < \omega < \omega_2$, the effect of the vortex mechanism is most efficient, and the relation of the threshold characteristics to the layer thickness, helical pitch, and ultrasonic frequency is described by the following expressions:

$$\Lambda^{\text{th}} = \Lambda_s^{\text{th}} = \sqrt{2}\pi/q_s \sim (P_0 d)^{1/2}, \tag{4}$$

$$M^{\text{th}} \approx (q_s/q_0)\{\rho K_3(3+\beta)(1-\delta)/16\gamma\tau DE\}^{1/2} \sim (P_0 d)^{1/2}, \quad \omega_2 = 1/\tau. \tag{5}$$

The estimates following from Eqs. (2)–(4) demonstrate that the relation of the domain spatial period to the layer thickness and helical pitch is determined as $\Lambda^{\text{th}} \sim (P_0 d)^{1/2}$, and the influence of ultrasonic frequency can manifest itself only within the range $\omega \ll \omega_1$.[5] These theoretical predictions correlate with the experimental data presented in Figs. 2c and 2d. The relation of the threshold Mach number to the helical pitch and

---

[4] It is known that such an extension of a cholesteric structure along the helix axis can be caused by a lack of parallelism of the layer boundaries near the Grandjean lines or by the presence of paired disclinations, at which the number of cholesteric layers changes in a layer with parallel boundaries [2].

[5] Estimates demonstrate that, in the range of the values of P_0 and d considered above, the frequency $f_1 = \omega_1/2\pi$ does not exceed 0.5 MHz.

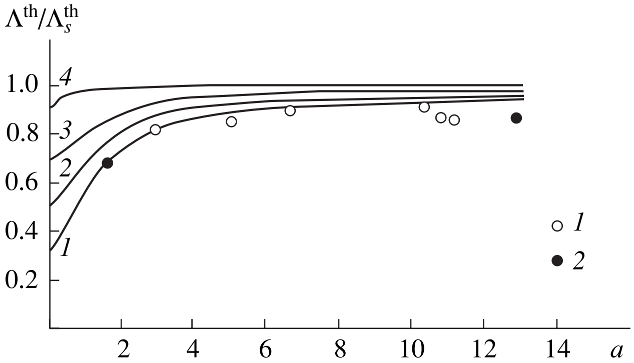

Fig. 4. Comparison of experimental and theoretical dependences of the relative period of domains at the threshold of the effect on the parameter *a*. The ultrasonic frequency is 2.95 MHz. The calculation is conducted for the relative extension of the layer equal to 0.01, 0.2, 0.5, and 0.9 (plots *1*–*4*). The experimental threshold values refer to cholesteryl chloride–ZhK404 solutions with a helical pitch of (*1*) 2 and (*2*) 4 μm.

layer thickness within the range $P_0/d \ll 1$ also coincides with the experimental dependence of the form $M^{th} \sim (P_0/d)^{1/2}$ (see Fig. 3a). The theoretical conclusion that the frequency dependence of the threshold of domain formation in the region $\omega_1 < \omega < \omega_2$ is weak agrees qualitatively with the results of measurements (see Fig. 3b). The peculiarities of the threshold behavior at the frequencies $\omega < \omega_1$ and $\omega > \omega_2$ and the behavior of the anomaly observed in the values of M^{th} in samples with disclinations can be explained by comparing quantitatively the experimental and theoretical values of the threshold characteristics of domains.

Figure 4 presents the theoretical dependence of the relative period of domains, $\Lambda^{th}/\Lambda_s^{th}$, on the theoretical parameter *a* characterizing the influence of the layer thickness and helical pitch. The dependence is given for several values of relative extension of cholesteric structure, namely, 0.01, 0.2, 0.5, and 0.9 (curves *1*–*4*), in the frequency range of $\omega \gg \omega_1$. In the calculation, the following values of the material constants of liquid crystals were adopted: $\eta = 0.05$ Pa, $\rho = 10^3$ kg/m^3, $\tau = 3 \times 10^{-8}$ s, and $\beta = 2.8 \times 10^{-2}$. The experimental values of $\Lambda^{th}/\Lambda_s^{th}$ given in the figure belong to cholesteryl chloride–ZhK404 solutions with a helical pitch of 2 and 4 μm (notations *1* and *2*) for the values of layer thickness equal to 10, 40, 80, 100, and 240 μm and 10, 22, 40, 80, and 100 μm, respectively, at a frequency of 2.95 MHz. They were obtained by processing the data given in Fig. 2c. One can see that the experimental values of the relative period lie near theoretical curve *1* corresponding to the relative extension $\delta = 0.01$, which corresponds to the conditions of this series of experiments: observations were conducted using samples with the values of P_0 and *d* satisfying the condition $d = mP_0/2$, so that the cholesteric helix could "fit" into the capillary formed by the cell plates almost without changing the equilibrium value of the pitch. One should note the following fact that follows from the theory and is confirmed by experimental data: in the range of P_0 and *d* corresponding to the condition $a \gg 1$ the relative domain period almost does not depend on the extension of the cholesteric structure.

The family of plots in Fig. 2d presents the dependence of the relative domain period on ultrasonic frequency that was calculated by Eq. (3) in the range of 0.3–4.5 MHz at constant values of layer thickness and helical pitch ($d = 22$ μm, $P_0 = 4$ μm, and $a \approx 10$) [4]. The relative extension of the helical structure is a parameter, which takes the values of 0.01, 0.5, and 0.9 (curves *1*–*3*, respectively). One can see that the experimental values of the relative period of the domains that were observed in the samples without disclinations at the frequencies not exceeding f_1 lie near curve *1*. Oppositely, the values of the relative period of domains formed in liquid crystal layers with disclinations in the frequency range close to f_1 correlate with curves *2* and *3*, which correspond to higher values of δ. The experimental setup provides an opportunity to evaluate the relative extension δ only in order of magnitude. Therefore, it is possible to note only the quantitative coincidence of experimental and theoretical data, which confirms the fact of influence of the local extension of a cholesteric structure on the domain period and its relation to ultrasonic frequency. According to Eq. (5), which represents the behavior of the threshold Mach number in the frequency range satisfying the condition $\omega_1 < \omega < \omega_2$, the connection of M^{th} with the layer thickness and helical pitch is approximated by a relation of the form $M^{th} \sim (P_0/d)^{1/2}$, which is confirmed by experimental data (Fig. 3a). The deviation from this relation at the values of P_0 close to *d* is connected with the violation of the restriction $P_0 \ll d$ introduced in constructing the model [4].

We can judge on the frequency dependence of the threshold Mach number from analyzing the family of curves for a cholesteric liquid crystal with a helical pitch of 4 μm at a layer thickness of 22 μm (see Fig. 3b). The value of the extension δ of the cholesteric structure is a parameter of the curves, and it is equal to 0, 0.5, 0.7, and 0.9 (curves *1*–*4*). One can see that, in the frequency range of 0.3–6 MHz, at all values of δ, the theoretical threshold demonstrates a weak dependence on ultrasonic frequency. As the experiment showed, only the values of M^{th} obtained for samples without disclinations lie near theoretical curve *1*, which corresponds to the equilibrium state of the helix ($\delta = 0$), while the values of M^{th} for samples with disclinations are grouped near theoretical curves *3* and *4*, which determine the frequency dependence of the thresholds for liquid crystal layers with an extended cholesteric structure. These data allowed us to reveal the origin of the anomaly in the behavior of the threshold Mach number as a function of ultrasonic frequency, which was observed in experiments, and to confirm the hypothesis postulated in the model [4] concerning the role of local changes of the cholesteric pitch in the mechanism of domain formation. According to the theory, Eq. (5), which is represented graphically by the family of curves *1–4* in Fig. 3b, describes the change in the domain threshold within the range $\omega_1 < \omega < \omega_2$, where the values of M^{th} do not depend on frequency. According to theoretical concepts, outside this frequency interval the threshold must grow with both decreasing and increasing frequency. Such a behavior of the threshold at the frequencies exceeding $f_2 = \omega_2/2\pi = 5.2$ MHz is confirmed by the plot in the inset in Fig. 3b (courtesy of E.N. Kozhevnikov; the calculation is performed for $d = 100$ μm, $P_0 = 10$ μm, and $\delta = 0.8$).[6] However, according to the experimental data given in the inset, which were obtained at frequencies greater than f_2, the threshold M^{th} does not depend on frequency and has almost the same value as at the frequencies smaller than f_2. This suggests that the ultrasonically initiated structural transition in liquid crystals is a complex phenomenon determined apparently by the influence of various competing mechanisms [16], and, therefore, it cannot be explained within the framework of a single universal model of a vortex mechanism. At the same time, the comparative analysis of experimental and theoretical data characterizing the behavior of the threshold characteristics of domains in liquid crystals as a function of varying layer thickness, helical pitch, and ultrasonic frequency confirms good prospects for the new approach to form an explanation of orientation phenomena on the basis of the traditional equations of linear dynamics with allowance for not only the anisotropy of the viscous properties of cholesteric liquid crystals but also the connection of the elastic properties of mesophase with the relaxation of the orientational order parameter.

In conclusion, it is necessary to note that the model of the vortex mechanism underlying the formation of two-dimensional domains under the effect of ultrasound in a planar layer of a liquid crystal with a helical pitch much smaller than the layer thickness provides an adequate description of the phenomenon observed in the experiment in the frequency range satisfying the condition $f < f_2$. The aforementioned deviation of experimental data obtained for the influence of ultrasonic frequency on the threshold of the effect from the predictions of the model [4], which occurs at frequencies exceeding the inverse relaxation time, points to the necessity for considering additional factors that may lead to orientational instability of a planar structure of a cholesteric liquid crystal in an ultrasonic field in the indicated frequency range. It should be noted that the results reported in this paper are important from the point of view of substantiation of the necessity to involve new ideas and approaches in the analysis of orientation phenomena at ultrasonic frequencies and their verification using different types of liquid crystals, as well as the development of the applied aspects of the problem that are connected with designing new active acoustooptic elements based on liquid crystals, which provide an opportunity to control the parameters of a light beam [17].

ACKNOWLEDGMENTS

This work was supported by the Russian Foundation for Basic Research, project no. 00-02-17732.

REFERENCES

1. *Handbook of Liquid Crystals*, Ed. by D. Demus, J. Goodby, G. W. Gray, H. W. Spiess, and V. Vill (Wiley–VCH, Weinheim, 1998), Vol. 1, pp. 549–568.
2. P. de Gennes, *The Physics of Liquid Crystals* (Clarendon Press, Oxford, 1974; Mir, Moscow, 1977).
3. S. A. Pikin, *Structural Transformations in Liquid Crystals* (Nauka, Moscow, 1981).
4. E. N. Kozhevnikov, Akust. Zh. **47**, 501 (2001) [Acoust. Phys. **47**, 430 (2001)].
5. I. N. Gurova and O. A. Kapustina, Akust. Zh. **43**, 338 (1997) [Acoust. Phys. **43**, 290 (1997)].
6. V. I. Domarkas and R. Yu. Kazhis, *Control and Measurement Piezoelectric Transducers* (MINTIS, Vilnius, 1975).
7. M. Born and E. Wolf, *Principles of Optics*, 6th ed. (Pergamon Press, Oxford, 1980; Nauka, Moscow, 1986).
8. V. A. Belyakov and A. S. Sonin, *Optics of Cholesteric Liquid Crystals* (Nauka, Moscow, 1982).
9. N. Scaramuzza, R. Bartolino, and G. Berbero, J. Appl. Phys. **53**, 8593 (1982).
10. E. Guyon and P. Pieranski, Phys. Rev. A **9**, 404 (1974).
11. D. I. Anikeev and O. A. Kapustina, Zh. Éksp. Teor. Fiz. **110**, 1328 (1996) [JETP **83**, 731 (1996)].
12. E. N. Kozhevnikov, in *Abstracts of VI All-Union Conference on Liquid Crystals, Chernigov* (1988), Vol. 1, p. 121.
13. E. N. Kozhevnikov, Zh. Éksp. Teor. Fiz. **92**, 1306 (1987) [Sov. Phys. JETP **65**, 731 (1987)].
14. D. I. Anikeev, O. A. Kapustina, and V. N. Lupanov, Zh. Éksp. Teor. Fiz. **100**, 197 (1991) [Sov. Phys. JETP **73**, 109 (1991)].
15. C. A. Castro, A. Hikata, and C. Elbaum, Phys. Rev. A **17**, 353 (1978).
16. *Physical Properties of Liquid Crystals*, Ed. by D. Demus *et al.* (Wiley, Weinheim, 1999), pp. 447–466.
17. A. P. Kapustin and O. A. Kapustina, *Acoustics of Liquid Crystals* (Nauka, Moscow, 1985), p. 247.

Translated by M. Lyamshev

---

[6] The frequency f_2 by definition is the quantity inverse of the relaxation time τ of the orientational order parameter. Adopting as τ the value of 3×10^{-8} s typical of nematic liquid crystals [15], we arrive at $f_2 = \omega_2/2\pi = 5.2$ MHz.

Acoustical Physics, Vol. 50, No. 1, 2004, pp. 74–76. Translated from Akusticheskiĭ Zhurnal, Vol. 50, No. 1, 2004, pp. 86–89.
Original Russian Text Copyright © 2004 by Kleshchev.

Diffraction of Point-Source-Generated Sound by an Elastic Cylindrical Shell

A. A. Kleshchev
St. Petersburg State Naval Technical University, ul. Lotsmanskaya 3, St. Petersburg, 190008 Russia
e-mail: gakusei@VG2068.spb.Edu

Received October 23, 2002

Abstract—The three-dimensional problem of the scattering of a harmonic sound wave by an elastic cylindrical shell is solved using Debye potentials. All potentials are represented in the form of integrals depending on the axial component of the wave vector. *© 2004 MAIK "Nauka/Interperiodica".*

Let a harmonic wave of angular frequency ω be produced by a point source Q and assume that this wave is incident on an infinite elastic cylindrical shell whose axis (the Z axis) lies at a distance r_0 from the source. The shell is immersed in an external fluid medium with density ρ_0 and sound velocity c_0.

The potential Φ_i of the harmonic point source is determined by the series [1–3]

$$\Phi_i(r, \varphi, z) = \frac{i}{2}\sum_{n=0}^{\infty}\cos(n\varphi)\varepsilon_n\int_{-\infty}^{+\infty}\exp(i\gamma z) \times H_n^{(1)}(k_\gamma r_0)J_n(k_\gamma r)d\gamma, \quad r < r_0, \tag{1}$$

where $k_\gamma = (k^2 - \gamma^2)^{1/2}$; $k = \omega/c_0$; γ and k_γ are the axial and radial components of the wave vector, respectively; $\varphi_0 = 0$; $z_0 = 0$ (see Fig. 1); and

$$\varepsilon_n = \begin{cases} 1, & n = 0 \\ 2, & n \neq 0. \end{cases}$$

Potential $\Phi_s(r, \varphi, z)$ of the wave scattered by the shell, can be represented by analogy with $\Phi_i(r, \varphi, z)$:

$$\Phi_s(r, \varphi, z) = \sum_{n=0}^{\infty}a_n\cos(n\varphi) \times \int_{-\infty}^{+\infty}A(\gamma)\exp(i\gamma z)H_n^{(1)}(k_\gamma r)d\gamma, \tag{2}$$

where a_n and $A(\gamma)$ are unknown coefficients and functions of γ, which are determined from boundary conditions.

The cylindrical components of the displacement vector $\mathbf{U}(U_r, U_\varphi, U_z)$ can be expressed in terms of the potential Φ and the cylindrical components of the function $\mathbf{A}(A_r, A_\varphi, A_z)$ [4–6]:

$$\left.\begin{aligned} U_r &= \frac{\partial\Phi}{\partial r} + \frac{1}{r}\frac{\partial A_z}{\partial\varphi} - \frac{\partial A_\varphi}{\partial z}, \\ U_\varphi &= \frac{1}{r}\frac{\partial\Phi}{\partial\varphi} + \frac{\partial A_r}{\partial z} - \frac{\partial A_z}{\partial r}, \\ U_z &= \frac{\partial\Phi}{\partial z} + \frac{1}{r}A_\varphi + \frac{\partial A_\varphi}{\partial r} - \frac{1}{r}\frac{\partial A_r}{\partial\varphi}. \end{aligned}\right\} \tag{3}$$

In their turn, the cylindrical components A_r, A_φ, and A_z of the function $\mathbf{A}$ can be expressed in terms of the Debye potentials U and V [4–9]:

$$A_r = k_2^2 rU + r\frac{\partial^2 U}{\partial r^2} + z\frac{\partial^2 U}{\partial r\partial z} + 2\frac{\partial U}{\partial r} + i\frac{1}{r}k_2 z\frac{\partial V}{\partial\varphi}, \tag{4}$$

$$A_\varphi = -ik_2\left[z\frac{\partial V}{\partial r} - r\frac{\partial V}{\partial z}\right] + \frac{1}{r}\frac{\partial U}{\partial\varphi} + \frac{\partial^2 U}{\partial r\partial\varphi} + \frac{1}{r}z\frac{\partial^2 U}{\partial z\partial\varphi}, \tag{5}$$

$$A_z = k_2^2 zU + z\frac{\partial^2 U}{\partial z^2} - ik_2^2\frac{\partial V}{\partial\varphi} + r\frac{\partial^2 U}{\partial r\partial z} + 2\frac{\partial U}{\partial z}, \tag{6}$$

where k_2 is the wave number of the transverse wave in the shell material.

The vector function $\mathbf{A}$ is expressed in terms of the Debye potentials U and V as [5, 6]

$$\mathbf{A} = \operatorname{curl}\operatorname{curl}(\mathbf{R}U) + ik_2\operatorname{curl}(\mathbf{R}V), \tag{7}$$

where $\mathbf{R}$ is the radius vector of a point belonging to the shell.

The efficiency of this representation becomes apparent if one takes into account that the functions U and V obey the scalar Helmholtz equation, which is separable in circular cylindrical coordinates:

$$(\Delta + k_2^2)U = 0, \tag{8}$$

$$(\Delta + k_2^2)V = 0. \tag{9}$$

1063-7710/04/5001-0074$26.00 © 2004 MAIK "Nauka/Interperiodica"

Representations of the vector function **A** in Cartesian and circular cylindrical coordinate systems are given in [10–12], and its representation in a spherical coordinate system is given in [9].

The potentials Φ, U, and V can also be expanded in series in eigenfunctions of the Helmholtz equation [6, 8, 9]:

$$\begin{aligned}\Phi(r,\varphi,z) = \sum_{n=0}^{\infty}\cos(n\varphi)\Bigg[b_n\int_{-\infty}^{+\infty}B(\gamma)\exp(i\gamma z)J_n(h_\gamma r)d\gamma \\ + b'_n\int_{-\infty}^{+\infty}B'(\gamma)\exp(i\gamma z)N_n(h_\gamma r)d\gamma\Bigg],\end{aligned} \tag{10}$$

$$\begin{aligned}U(r,\varphi,z) = \sum_{n=1}^{\infty}\sin(n\varphi)\Bigg[c_n\int_{-\infty}^{+\infty}C(\gamma)\exp(i\gamma z)J_n(\kappa_\gamma r)d\gamma \\ + c'_n\int_{-\infty}^{+\infty}C'(\gamma)\exp(i\gamma z)N_n(\kappa_\gamma r)d\gamma\Bigg],\end{aligned} \tag{11}$$

$$\begin{aligned}V(r,\varphi,z) = \sum_{n=0}^{\infty}\cos(n\varphi)\Bigg[d_n\int_{-\infty}^{+\infty}D(\gamma)\exp(i\gamma z)J_n(\kappa_\gamma r)d\gamma \\ + d'_n\int_{-\infty}^{+\infty}D'(\gamma)\exp(i\gamma z)N_n(\kappa_\gamma r)d\gamma\Bigg],\end{aligned} \tag{12}$$

where $h_\gamma = (k_1^2 - \gamma^2)^{1/2}$; $k_1 = \omega/c_1$ is the wave number of the longitudinal wave in the shell material; c_1 is the longitudinal wave velocity in the material; $N_n(\kappa_\gamma r)$ is the Neumann cylindrical function; $\kappa_\gamma = (k_2^2 - \gamma^2)^{1/2}$; b_n, b'_n, c_n, c'_n, d_n, d'_n and $B(\gamma)$, $B'(\gamma)$, $C(\gamma)$, $C'(\gamma)$, $D(\gamma)$, $D'(\gamma)$ are unknown coefficients and functions, which are determined from the following boundary conditions at the outer and inner surfaces of the elastic shell:

(i) the normal component of the displacement vector, U_r, is continuous at the outer boundary of the shell;

(ii) the sound pressure in the liquid is equal to the normal stress at the outer boundary of the shell;

(iii) the normal stress at the inner boundary of the shell is equal to zero; and

(iv) the tangential stresses at the shell boundaries are equal to zero.

In an analytical form, these boundary conditions are written as

$$\frac{\partial\Phi}{\partial r} + \frac{1}{r}\frac{\partial A_z}{\partial\varphi} - \frac{\partial A_\varphi}{\partial z} = -\frac{\partial}{\partial r}(\Phi_i + \Phi_s)\Big|_{r=a}, \tag{13}$$

$$\begin{aligned}(\lambda+2\mu)\frac{\partial U_r}{\partial r} + \lambda\left(\frac{1}{r}\frac{\partial U_\varphi}{\partial\varphi} + \frac{1}{r}U_r + \frac{\partial U_z}{\partial z}\right) \\ = -\rho_0\omega^2(\Phi_i + \Phi_s)\big|_{r=a},\end{aligned} \tag{14}$$

$$(\lambda+2\mu)\frac{\partial U_r}{\partial r} + \lambda\left(\frac{1}{r}\frac{\partial U_\varphi}{\partial\varphi} + \frac{1}{r}U_r + \frac{\partial U_z}{\partial z}\right) = 0\big|_{r=b}, \tag{15}$$

$$\frac{\partial U_\varphi}{\partial r} - \frac{1}{r}U_\varphi + \frac{1}{r}\frac{\partial U_r}{\partial\varphi} = 0\big|_{\substack{r=a\\ r=b}}, \tag{16}$$

$$\frac{\partial U_r}{\partial z} + \frac{\partial U_z}{\partial r} = 0\big|_{\substack{r=a\\ r=b}}. \tag{17}$$

The substitution of series (1), (2), and (10)–(12) into boundary conditions (13)–(17) gives an infinite set of equations for the unknown coefficients and functions $a_nA(\gamma)$, $b_nB(\gamma)$, $b'_nB'(\gamma)$, $c_nC(\gamma)$, $c'_nC'(\gamma)$, $d_nD(\gamma)$, and $d'_nD'(\gamma)$. Because of orthogonality of trigonometrical functions $\cos(n\varphi)$ and $\sin(n\varphi)$, the infinite set of equations falls into seven equations with a fixed index n for determining seven combinations of unknown coefficients and functions.

The product $a_nA(\gamma)$ for the potential Φ_s of the scattered wave is calculated by Cramer's rule from the ratio of two determinants of the seventh order:

$$a_nA(\gamma) = \Delta'/\Delta, \tag{18}$$

where Δ and Δ' are the determinant of the set of equations and the minor, which have the form

$$\Delta = \begin{vmatrix} a_{11} & a_{12} & a_{13} & a_{14} & a_{15} & a_{16} & a_{17} \\ a_{21} & a_{22} & a_{23} & a_{24} & a_{25} & a_{26} & a_{27} \\ a_{31} & a_{32} & a_{33} & a_{34} & a_{35} & a_{36} & a_{37} \\ a_{41} & a_{42} & a_{43} & a_{44} & a_{45} & a_{46} & a_{47} \\ a_{51} & a_{52} & a_{53} & a_{54} & a_{55} & a_{56} & a_{57} \\ a_{61} & a_{62} & a_{63} & a_{64} & a_{65} & a_{66} & a_{67} \\ a_{71} & a_{72} & a_{73} & a_{74} & a_{75} & a_{76} & a_{77} \end{vmatrix},$$

$$\Delta' = \begin{vmatrix} b_{11} & a_{12} & a_{13} & a_{14} & a_{15} & a_{16} & a_{17} \\ b_{21} & a_{22} & a_{23} & a_{24} & a_{25} & a_{26} & a_{27} \\ 0 & a_{32} & a_{33} & a_{34} & a_{35} & a_{36} & a_{37} \\ 0 & a_{42} & a_{43} & a_{44} & a_{45} & a_{46} & a_{47} \\ 0 & a_{52} & a_{53} & a_{54} & a_{55} & a_{56} & a_{57} \\ 0 & a_{62} & a_{63} & a_{64} & a_{65} & a_{66} & a_{67} \\ 0 & a_{72} & a_{73} & a_{74} & a_{75} & a_{76} & a_{77} \end{vmatrix}.$$

The values of the elements of both determinant and minor can be found in [9]. In the presence of a liquid

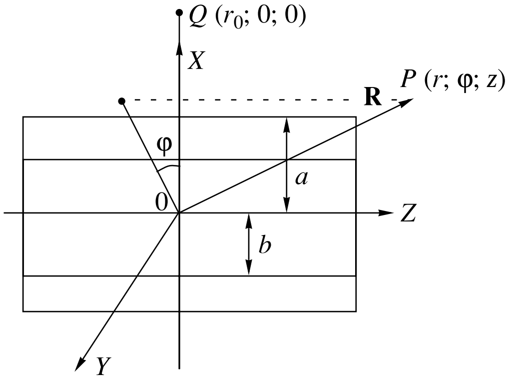

Fig. 1. Cylindrical shell insonified by a wave produced by a point source.

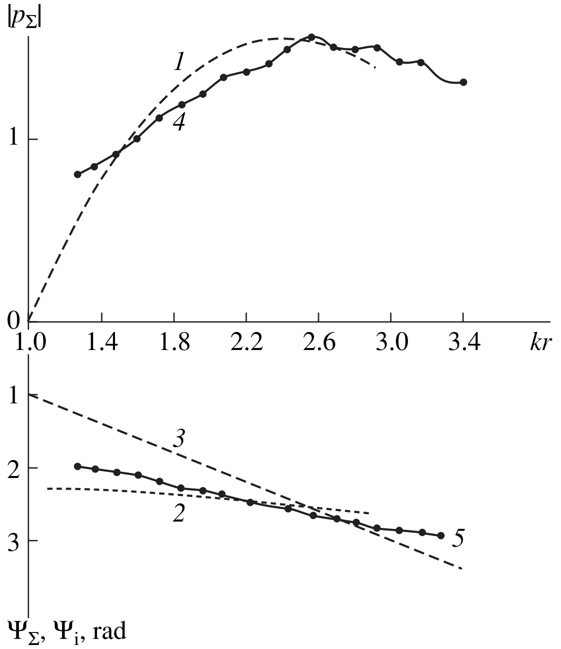

Fig. 2. Calculated and experimental distributions of $|p_\Sigma|$ and ψ_Σ along the OQ direction near a hollow cylindrical shell.

filler in the shell, the rank of the determinant and the minor increases by unity.

Let us find the asymptotics of the field scattered by the elastic shell according to formula (2) with the use of relationship (18). Let us assume that the radial coordinate r_0 of the source Q tends to infinity and the amplitude of the spherical wave radiated by this source is equal to unity at a point O. Then, the near scattered field of the shell at a distance of several radii a from its surface will coincide with the scattered field from a source of a plane harmonic wave of unit amplitude. The solution to this problem is well understood [13].

On the other hand, for evaluating the correctness and accuracy of the proposed method, it is possible to compare the results of calculation with an experiment performed with a steel (hollow) cylindrical shell insonified by a near-point sound source. The experimental procedure allowing one to measure the amplitudes and phases of the scattered p_s or diffracted p_Σ ($p_\Sigma = p_i + p_s$, where p_i is the pressure in the incident wave) sound fields is described in [14–16]. Figure 2 shows the results of the experiment for a steel cylindrical shell 8.0 cm in diameter and 0.4 mm in thickness. The source Q was located at a distance of 4.5 m from the shell axis Z (Fig. 1). The amplitude $|p_\Sigma|$ and phase ψ_Σ of diffracted pressure p_Σ were measured along the OQ direction (Fig. 1). The distance from the shell surface was measured in kr units, where k is the wave number in the liquid and r is the distance from the shell surface. The wave dimension of the shell ka was chosen to be equal to 1.0. The experimental values of $|p_\Sigma|$ and ψ_Σ were compared with the computed values of $|p_\Sigma|$ and ψ_Σ for an ideal acoustically soft cylinder (curve *1* and line *2* in Fig. 2, respectively). Curve *3* shows the phase ψ_i of the incident wave; $|p_i|$ was taken equal to 1. Curve *4* characterizes $|p_\Sigma|$, and line *5* characterizes ψ_Σ for the shell. These experimental and numerical results serve as a test for calculations by the proposed method.

REFERENCES

1. E. L. Shenderov, *Wave Problems in Hydroacoustics* (Sudostroenie, Leningrad, 1972), p. 350.
2. L. M. Brekhovskikh, *Waves in Layered Media*, 1st ed. (Nauka, Moscow, 1957; Academic, New York, 1960), p. 502.
3. L. B. Felsen and N. Marcuvitz, *Radiation and Scattering of Waves* (Prentice Hall, Englewood Cliffs, N.J., 1973; Mir, Moscow, 1978), Vols. 1, 2.
4. P. Debye, Ann. Phys. (Leipzig) **30** (4), 755 (1909).
5. V. A. Fok, *Problems of Diffraction and Propagation of Electromagnetic Waves* (Sovetskoe Radio, Moscow, 1970).
6. A. A. Kleshchev and I. I. Klyukin, Tr. Leningr. Korablestroit. Inst., No. 109, 3 (1976).
7. A. A. Kleshchev, J. Tech. Acoust. **3** (4), 16 (1997).
8. A. A. Kleshchev, J. Tech. Acoust. **3** (4), 20 (1997).
9. A. A. Kleshchev, *Wave Diffraction and Propagation in Elastic Media and Solids* (Vlas, St. Petersburg, 2002).
10. V. T. Buchwald, Q. J. Mech. Appl. Math. **14**, 293 (1961).
11. F. Ahmad, J. Acoust. Soc. Am. **109**, 886 (2001).
12. Y. Fan, A. N. Sinclair, and F. Honarvar, J. Acoust. Soc. Am. **106**, 1229 (1999).
13. H. Überall, Akust. Zh. **47**, 149 (2001) [Acoust. Phys. **47**, 115 (2001)].
14. A. A. Kleshchev and I. I. Klyukin, in *Proceedings of VII All-Union Acoustical Conference, Leningrad* (1973), pp. 123–125.
15. A. A. Kleshchev, in *Proceedings of VII All-Union Acoustical Conference, Leningrad* (1973), pp. 143–146.
16. A. A. Kleshchev, *Underwater Acoustic Scatterers* (Sudostroenie, St. Petersburg, 1992).

Translated by A. Svechnikov

Acoustical Physics, Vol. 50, No. 1, 2004, pp. 77–80. Translated from Akusticheskiĭ Zhurnal, Vol. 50, No. 1, 2004, pp. 90–93.
Original Russian Text Copyright © 2004 by Lapin.

A Monopole–Dipole Resonator for Flexural Waves in a Rod

A. D. Lapin
Andreev Acoustics Institute, Russian Academy of Sciences, ul. Shvernika 4, Moscow, 117036 Russia
e-mail: mironov@akin.ru

Received March 17, 2003

Abstract—For flexural waves in a rod, a simplest resonator responding not only displacements but also to the inclination (the derivative of the displacement) of the rod axis is studied. The resonator consists of two spring–mass systems attached through a rigid (nonbending) bar to the elastic rod in which a flexural wave propagates. One of the springs is oriented perpendicularly to the rod, and the other is parallel to it. It is shown that, at a certain friction, the single monopole–dipole resonator under consideration completely absorbs the incident resonance-frequency flexural wave, which propagates in the elastic rod. *© 2004 MAIK “Nauka/Interperiodica”.*

In practice, the absorption of flexural waves in rods and plates is achieved with the use of resonators [1–4]. A simplest resonator is a spring–mass system [5–7]. Such a resonator oriented in the direction perpendicular to the rod and attached to it through a spring represents a monopole-type resonator, which responds to the displacements of the rod axis. At the resonance frequency, the incident flexural wave is totally reflected from a lossless monopole resonator, and no traveling wave is observed behind it. The presence of friction in the resonator reduces its efficiency as a wave reflector. A resonator with friction absorbs flexural waves. Previous studies show that a single monopole resonator with optimal friction absorbs no more than half the energy of the incident wave. A complete absorption of the resonance-frequency flexural wave can be achieved by using a combination of a lossless resonator and a resonator with a certain loss when the distance between the resonators is equal to an odd number of quarter-wavelengths [8].

This paper considers a single resonator of the monopole–dipole type. The simplest version of this resonator is a structure consisting of two spring–mass systems, which are attached through a common rigid (nonbending) bar to an elastic rod with flexural waves propagating in it. One of the spring–mass systems is perpendicular to the rod and represents a monopole resonator responding to the rod displacements. The other spring–mass system is parallel to the rod and represents a dipole resonator responding to the inclination (the derivative of the displacement) of the rod axis. Figure 1a shows the monopole–dipole resonator under study. It contains (*1*) a spring with an elastic coefficient $\kappa_1(1 - i\varepsilon_1)$, (*2*) a spring with an elastic coefficient $\kappa_2(1 - i\varepsilon_2)$, (*3*) a rigid connecting bar of length L, and (*4*) an elastic rod with a flexural wave propagating in it. One can expect that, at a certain friction, such a resonator will completely absorb the resonance-frequency flexural wave propagating in a thin elastic rod.

Consider a Cartesian coordinate system with the x axis directed along the axis of the unperturbed rod and assume that the rod vibrates in the xy plane. Let the monopole–dipole resonator be attached to the rod at the point $x = 0$. Assume that a harmonic flexural wave is incident on the resonator from the left, so that the particle displacement in this wave is described by the expression

$$w_0(x, t) = \exp[i(kx - \omega t)], \tag{1}$$

where k is the wave number of the flexural wave. Under the effect of this wave, the resonator vibrates and produces a normal point force $F(t)$ and a bending moment $M(t)$ acting on the rod. For the rod connected with the resonator, the equation of motion can be represented in the form

$$\rho\frac{\partial^2 w}{\partial t^2} + D\frac{\partial^4 w}{\partial x^4} = F(t)\delta(x) - M(t)\delta'(x), \tag{2}$$

where ρ is the linear density of the rod, D is its flexural rigidity, and $\delta(x)$ and $\delta'(x)$ are the delta-function and its derivative.

Let us introduce the following notations: $\xi_1(t)$ is the displacement of the mass m_1 from its equilibrium position along the y axis and $\xi_2(t)$ is the displacement of the mass m_2 from its equilibrium position along the x axis. Then, the equations of motion of the resonator can be represented in the form

$$m_1\ddot{\xi}_1(t) = -F(t), \quad m_2\ddot{\xi}_2(t) = -f(t), \tag{3}$$

where the forces $F(t)$ and $f(t)$ are determined by the expressions

$$F(t) = \kappa_1(1 - i\varepsilon_1)[\xi_1(t) - w(0, t)], \tag{4}$$

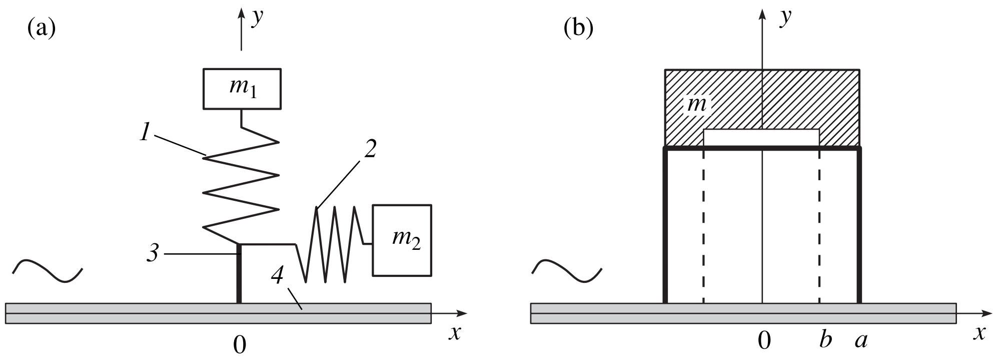

Fig. 1. A monopole–dipole resonator.

$$f(t) = \kappa_2(1-i\varepsilon_2)\left[\xi_2(t) + L\left(\frac{\partial w}{\partial x}\right)_{x=0}\right] = -M(t)/L. \qquad (5)$$

Here, $w(x, t)$ is the total field in the rod, i.e., the sum of the incident and scattered fields, and ε_1 and ε_2 are the dissipation factors.

In the case of the harmonic incident wave given by Eq. (1), the normal force and the bending moment can be represented as $F(t) = F_0\exp(-i\omega t)$ and $M(t) = M_0\exp(-i\omega t)$, where F_0 and M_0 are the complex amplitudes of the force and the moment, respectively. According to Eq. (2), the scattered field in the rod is equal to the sum of the monopole and dipole fields determined by the formulas

$$w_1(x, t) = \frac{iF_0}{4k^3D}\{\exp(ik|x|) + i\exp(-k|x|)\}\exp(-i\omega t), \qquad (6)$$

$$w_2(x, t) \ \mathrm{sgn}x\frac{M_0}{4k^2D}\{\exp(ik|x|) - \exp(-k|x|)\}\exp(-i\omega t), \qquad (7)$$

where $k^4 = \rho\omega^2/D$, $\mathrm{sgn}x = +1$ for $x > 0$, and $\mathrm{sgn}x = -1$ for $x < 0$. At $x = 0$, the following relationships are valid:

$$w_1 = \frac{iF_0}{4k^3D}(1+i)\exp(-i\omega t), \quad \frac{\partial w_1}{\partial x} = 0,$$

$$w_2 = 0, \quad \frac{\partial w_2}{dx} = \frac{M_0}{4kD}(1+i)\exp(-i\omega t).$$

Let us choose the amplitudes F_0 and M_0 so as to satisfy Eqs. (4) and (5). According to Eqs. (3), the displacements of the masses can be expressed as

$$\xi_1(t) = \frac{F_0}{m_1\omega^2}\exp(-i\omega t),$$
$$\xi_2(t) = -\frac{M_0}{Lm_2\omega^2}\exp(-i\omega t). \qquad (8)$$

Substituting Eqs. (1) and (6)–(8) into Eqs. (4) and (5), we obtain the desired force and moment amplitudes:

$$F_0 = i\omega\left\{\left[\mathrm{Re}Y + \frac{\varepsilon_1\omega}{\kappa_1}\right] + i\left[\frac{1}{m_1\omega} - \frac{\omega}{\kappa_1} + \mathrm{Im}Y\right]\right\}^{-1} \qquad (9)$$

$$M_0 = -k\omega L^2\left\{\left[\frac{\omega L^2}{4kD} + \frac{\varepsilon_2\omega}{\kappa_2}\right] + i\left[\frac{1}{\omega m_2} - \frac{\omega}{\kappa_2} - \frac{\omega L^2}{4kD}\right]\right\}^{-1}, \qquad (10)$$

where $Y = \frac{-i\omega w_1(0, t)}{F(t)} = \frac{\omega(1+i)}{4k^3D}$ is the compliance of an infinite rod under a point force.

The scattered fields of the monopole and dipole types can be obtained from Eqs. (6) and (7), respectively, by substituting the amplitudes F_0 and M_0 into them. The monopole scattering resonance occurs at frequency ω_1, determined as the solution to the equation

$$\frac{1}{m_1\omega} - \frac{\omega}{\kappa_1} + \mathrm{Im}Y = 0. \qquad (11)$$

The dipole scattering resonance occurs at frequency ω_2, satisfying the equation

$$\frac{1}{\omega m_2} - \frac{\omega}{\kappa_2} - \frac{\omega L^2}{4kD} = 0. \qquad (12)$$

The total field in the rod is expressed as

$$w(x, t) = \left\{\exp(ikx) + \frac{iF_0}{4k^3D}[\exp(ik|x|) + i\exp(-k|x|)] + \mathrm{sgn}x\frac{M_0}{4k^2D}[\exp(ik|x| - \exp(-k|x|))]\right\}\exp(-i\omega t), \qquad (13)$$

where the force and moment amplitudes are determined by Eqs. (9) and (10).

Let us consider the structure of the total field given by Eq. (13) for certain values of the parameters. Let $m_2 = 0$ and $\varepsilon_1 = 0$. In this case, the vibratory system is a monopole resonator without friction. Then, at the frequency ω_1, the incident wave is totally reflected from the resonator:

$$w(x<0,t) = \{2i\sin(kx) - i\exp(kx)\}\exp(-i\omega t),$$
$$w(x>0,t) = -i\exp(-kx - i\omega t).$$

Now, let $m_1 = 0$ and $\varepsilon_2 = 0$. In this case, the vibratory system is a dipole resonator without friction, and, at frequency ω_2, the incident wave is also totally reflected from the resonator:

$$w(x<0,t) = \{2\cos(kx) - \exp(kx)\}\exp(-i\omega t),$$
$$w(x>0,t) = \exp(-kx - i\omega t).$$

Let $\varepsilon_1 = \varepsilon_2 = 0$ and $\omega_1 = \omega_2$. This means that the friction in the vibratory system is absent and the natural frequencies ω_1 and ω_2 coincide. Then, at $\omega = \omega_1 = \omega_2$, the incident wave is not reflected from the resonator but only changes its phase as it passes the resonator:

$$w(x<0,t) = \{\exp(ikx)$$
$$-(1+i)\exp(kx)\}\exp(-i\omega t),$$
$$w(x>0,t) = \{-\exp(ikx)$$
$$+(1-i)\exp(-kx)\}\exp(-i\omega t).$$

Let $\varepsilon_1 = \dfrac{\kappa_1}{4k^3D}$, $\varepsilon_2 = \dfrac{\kappa_2 L^2}{4kD}$, and $\omega_1 = \omega_2$. In this case, in both the monopole and dipole resonators, the dissipative loss is equal to the radiation loss, and the natural frequencies ω_1 and ω_2 coincide. Then, at $\omega = \omega_1 = \omega_2$, we have the field

$$w(x<0,t)$$
$$= \left\{\exp(ikx) - \frac{1}{2}(1+i)\exp(kx)\right\}\exp(-i\omega t),$$

$$w(x>0,t) = \frac{1}{2}(1-i)\exp(-kx - i\omega t).$$

Hence, with these values of the parameters, a single monopole–dipole resonator completely absorbs the incident homogeneous wave propagating in the thin rod, and only an inhomogeneous (exponentially decaying) wave remains behind the resonator. Note that by using two identical, symmetrically positioned ($y > 0$ and $y < 0$) monopole–dipole resonators, it is possible to absorb a flexural wave in a relatively thick rod as well. When the incident wave has the form of Eq. (1), no scattered longitudinal wave is generated in a rod with symmetric resonators.

Now, let us consider a more complicated resonator model (Fig. 1b). A cylindrical elastic bar of radius a and length L (e.g., a rubber bar) is loaded from above with a mass m uniformly distributed over a ring $b < r < a$, while no load is applied from above within the circle $r < b$. The linear dimensions of the bar are small compared to the longitudinal and flexural wavelengths in it. Denote the Young modulus and the dissipation factor of the elastic material as E_1 and ε. The flexural rigidity of the bar is equal to $D_1 = E_1 S r_0^2$, where $r_0 = a/2$ and $S = \pi a^2$ are the radius of inertia and the area of the circle of radius a, respectively. The bar is cut through along the cylindrical surface $r = b$, so that the elastic medium within the region $r < b$ does not affect the vibrations of the mass m along the bar axis. Let the resonator (the bar with the mass) be attached to an elastic rod at the point $x = 0$ and let flexural wave (1) be incident on this resonator. Under the effect of the wave, the resonator vibrates and produces a normal point force $F(t) = F_0\exp(-i\omega t)$ and a bending moment $M(t) = M_0\exp(-i\omega t)$, which act on the rod. The scattered field in the rod is equal to the sum of the monopole and dipole fields determined by Eqs. (6) and (7), respectively. The amplitudes F_0 and M_0 are obtained from the relations that express the equality of the displacements and inclinations of the rod and bar axes at the point of their junction. Denoting the displacements in the bar along the y and $(-x)$ axes as $u(y, t)$ and $v(y, t)$, we represent the boundary conditions in the form

$$w_0(0,t) + w_1(0,t) + w_2(0,t) = u(0,t),$$
$$\left[\frac{\partial}{\partial x}(w_0 + w_1 + w_2)\right]_{x=0} = \left(\frac{\partial v}{\partial y}\right)_{y=0}. \quad (14)$$

The displacements u and v are produced in the bar by the force $-F(t)$ and the bending moment $-M(t)$, respectively, and can be calculated by the standard method [9]. If the length of the bar is small compared to the longitudinal and flexural wavelengths, we obtain the expressions

$$u(0,t) = \frac{1}{\omega}\left[\frac{1}{m\omega} - (1+i\varepsilon)\frac{\omega}{\kappa_1}\right]F(t),$$
$$\left(\frac{\partial v}{\partial y}\right)_{y=0} = \frac{1}{\omega L^2}\left[\frac{1}{m\omega} - (1+i\varepsilon)\frac{\omega}{\kappa_2}\right]M(t), \quad (15)$$

where $\kappa_1 = \dfrac{E_1 S_1}{L}$, $\kappa_2 = \dfrac{3D_1}{L^3}$, and $S_1 = \pi(a^2 - b^2)$. The quantities κ_1 and κ_2 are the effective elastic coefficients of the "perpendicular" and "parallel" springs. Substituting Eqs. (1), (6), (7), and (15) into Eqs. (14), we obtain the desired force and moment amplitudes. They are determined from Eqs. (9) and (10), where $m_1 = m_2 = m$ and $\varepsilon_1 = \varepsilon_2 = \varepsilon$. The total field in the rod is obtained from Eq. (13) by substituting the amplitudes F_0 and M_0 into it. The resonance frequencies of the monopole and dipole scattering are determined from the dispersion relations (11) and (12), respectively, with the use of the relations $m_1 = m_2 = m$, $\kappa_1 = E_1S_1/L$, and $\kappa_2 = 3D_1/L^3$.

When the conditions $\omega = \omega_1 = \omega_2$ and $\varepsilon = \dfrac{\kappa_1}{4k^3D} = \dfrac{\kappa_2 L^2}{4kD}$ are satisfied, the resonator completely absorbs the incident flexural wave of frequency ω. The second of these two conditions, which expresses the equality of the dissipative loss and the radiation loss, is reduced to the form $(ka)^2 = \dfrac{4}{3}\dfrac{S_1}{S}$. For a thin (compared to the flexural wavelength) bar, this condition can be satisfied only when $S_1 \ll S$.

REFERENCES

1. I. I. Klyukin, Akust. Zh. **6**, 213 (1960) [Sov. Phys. Acoust. **6**, 209 (1960)].
2. I. I. Klyukin and Yu. D. Sergeev, Akust. Zh. **10**, 60 (1964) [Sov. Phys. Acoust. **10**, 49 (1964)].
3. V. V. Tyutekin and A. P. Shkvarnikov, Akust. Zh. **18**, 441 (1972) [Sov. Phys. Acoust. **18**, 369 (1972)].
4. M. A. Isakovich, V. I. Kashina, and V. V. Tyutekin, Akust. Zh. **23**, 384 (1977) [Sov. Phys. Acoust. **23**, 214 (1977)].
5. *Handbook of Acoustics*, Ed. by M. J. Crocker (Wiley, New York, 1997).
6. M. Gurgoze and H. Batan, J. Sound Vibr. **195** (1), 164 (1996).
7. M. Gurgoze, J. Sound Vibr. **223** (4), 667 (1999).
8. A. D. Lapin, Akust. Zh. **49**, 427 (2003) [Acoust. Phys. **49**, 363 (2003)].
9. I. M. Babakov, *The Theory of Oscillations* (Nauka, Moscow, 1965).

Translated by E. Golyamina

Acoustical Physics, Vol. 50, No. 1, 2004, pp. 81–85. Translated from Akusticheskiĭ Zhurnal, Vol. 50, No. 1, 2004, pp. 94–99.
Original Russian Text Copyright © 2004 by Luk'yanov.

Relation for the Amplitudes of Acoustic Waves Excited by Thin Elastic Plates

V. D. Luk'yanov
Military Engineering and Technical University, ul. Zakhar'evskaya 22, St. Petersburg, 191185 Russia
e-mail: LVV@VL2771.SPB.edu

Received April 16, 2002

Abstract—Relations between the amplitudes of acoustic waves excited by a thin elastic plate under the effect of external forces and the amplitudes of waves scattered by this plate are obtained. Two cases are considered: when the plate separates acoustic media filling two half-spaces and when it separates acoustic media filling an acoustic waveguide. The energy conservation law is used to derive the identities that determine the relations between the amplitudes of acoustic waves radiated by a thin elastic plate under the action of forces. *© 2004 MAIK "Nauka/Interperiodica".*

When solving diffraction problems for different kinds of waves, it is expedient to have some relations that allow one to test (at least indirectly) the final analytical and, especially, numerical results. In quantum mechanics, results obtained in the framework of the scattering theory are tested by the so-called optical theorem, which states that, in the case of scattering by a certain potential, the total effective scattering cross section is proportional to the imaginary part of the scattering amplitude at zero angle [1]. In solving scattering problems for waves of different nature, the corresponding relations, for which the term "optical theorem" is retained, are derived from the energy conservation law. As applied to the problems of scattering by passive objects, this law reads that, in the absence of absorption, the energy supplied to a scatterer is equal to the energy scattered by it. Different forms and generalizations of the optical theorem in acoustics can be found in [2–11].

In acoustics, along with the scattering problems, it is often necessary to solve the problems of acoustic wave excitation. The latter deal with the situation when a body vibrating under the action of forces excites pressure waves in the surrounding medium. For these problems, it is useful to have a formula that relates the parameters of the excited acoustic field as a consequence of the energy conservation law, by analogy with the optical theorem in the scattering problems.

This paper presents such formulas for two-dimensional problems of acoustic wave excitation by a thin elastic plate: the formulas relate the parameters of the force acting on the plate and exciting its vibrations to the parameters of the acoustic field generated by the plate. The theoretical consideration is performed for the case of a flexurally vibrating plate which separates different acoustic media (ideal compressible liquids or gases) filling an acoustic waveguide. To obtain identities, the problem of wave radiation is replaced by an equivalent problem of reflection and transmission of specially selected waves. The incident, reflected, and transmitted waves are chosen so as to obtain identical vibrations of the plate in the excitation and reflection problems. In addition, relations between the wave amplitudes in these two problems are derived, i.e., formulas that relate the sound radiation from the plate to its acoustic transparency.

It is necessary to note a certain relation of the problems under consideration to the reciprocity principle established for linear equations of acoustics in the case of sound scattering by elastic bodies [12]. In particular (for example, in [13]), the reciprocity principle serves as the basis for determining the symmetry properties of the scattering matrix. According to the reciprocity principle, it is possible to relate the sound field scattered by an elastic body to the acoustic field produced by this body under the action of some forces. This approach was used in [14] to derive the formulas for the sound fields generated by elastic plates and shells. Based on the reciprocity principle, the relation between the sound radiation and the acoustic transparency of an infinite plate separating different media was investigated in [15, 16]. In the cited publications, asymptotic methods were used to study the sound radiation from a plate under the effect of a point force with the observation point positioned at a distance far exceeding the wavelength. However, it should be noted that the application of the reciprocity principle requires a complete solution of a certain auxiliary problem of wave excitation, while the solution to another problem is expressed through the auxiliary one. Below, only the energy relations are determined, and, therefore, no complete solution of the auxiliary problem is necessary.

Let us consider a planar acoustic waveguide of constant width H, which occupies the region ($-\infty < x < +\infty$,

$0 \le y \le H$). A thin elastic plate separating two ideal compressible liquids is positioned in the waveguide cross section ($x = 0$, $0 \le y \le H$). Consider the problem of a stationary wave radiation from this plate under the action of some forces. The dependence of the force and the wave processes on time t is assumed to be harmonic with a circular frequency ω and is determined by the factor $\exp(-i\omega t)$, which is omitted in the following calculations.

The acoustic pressures that occur in the right-hand ($x > 0$) and left-hand ($x < 0$) parts of the waveguide are denoted as $P_1(x, y)$ and $P_2(x, y)$, respectively. These pressures satisfy the homogeneous Helmholtz equations

$$\frac{\partial^2 P_s(x,y)}{\partial x^2} + \frac{\partial^2 P_s(x,y)}{\partial y^2} + k_s^2 P_s(x,y) = 0,$$

where k_s is the wave number in liquid, $k_s = \omega/c_s$, c_s is the speed of sound in the medium, and the index s takes the values $s = 1$ or 2 depending on which half-space is characterized by the given quantity.

At the waveguide walls, the acoustic pressure obeys some boundary conditions describing the mechanical behavior of the walls. Without specifying these conditions, we assume that the spectrum of normal modes of the waveguide is known and the boundary conditions are such that, for the normal modes of number n to the right and to the left of the plate, the pressure distributions throughout the waveguide cross section are identical and have the form $\varphi_n(y)$, where $n = 1, 2, \ldots$. These functions are normalized according to the relation

$$\int_0^H \varphi_n^2(y)dy = \Phi, \qquad (1)$$

where Φ is a constant.

The pressure $p_{sn}^{\pm}(x, y)$ corresponding to the normal mode of number n is given by the expression

$$p_{sn}^{\pm}(x,y) = \varphi_n(y)\exp(\pm i\lambda_{sn}x), \qquad (2)$$

where $s = 1$ for the waves to the right of the plate and $s = 2$ for the waves to the left of the plate, and λ_{sn} is the wave number of the nth normal mode. In the absence of absorption in the acoustic medium, the normal modes of the waveguide are separated into propagating ones, whose wave numbers λ_{sn} are real, and inhomogeneous ones, whose wave numbers λ_{sn} are purely imaginary. The waves $p_{sn}^{+}(x, y)$ propagate ($\mathrm{Re}\lambda_{sn} > 0$, $\mathrm{Im}\lambda_{sn} = 0$) and attenuate ($\mathrm{Re}\lambda_{sn} = 0$, $\mathrm{Im}\lambda_{sn} > 0$) in the positive direction of the Ox axis, and the waves $p_{sn}^{-}(x, y)$, in the negative direction.

The flexural displacement of the plate $U = U(y)$ obeys the inhomogeneous Kirchhoff equation, which, with allowance for the contact with the acoustic medium, has the following form for $0 < y < H$:

$$gU^{(4)}(y) - m\omega^2 U(y) = f(y) + P_2(0,y) - P_1(0,y). \qquad (3)$$

Here, g is the flexural rigidity of the plate and m is its surface density; the density of forces acting on the plate is chosen in the form

$$f_j(y) = f_j\varphi_j(y), \qquad (4)$$

where f_j is the force amplitude and $j = 1, 2, \ldots$.

The condition that the plate displacement be equal to the normal displacement of the liquid on the plate is expressed as

$$U(y) = \frac{1}{\rho_1\omega^2}\frac{\partial P_1(0,y)}{\partial x} = \frac{1}{\rho_2\omega^2}\frac{\partial P_2(0,y)}{\partial x}, \qquad (5)$$

where ρ_1 and ρ_2 are the densities of the acoustic media to the right and to the left of the plate, respectively.

The ends of the plate are restrained in some way at the waveguide walls. In the general case, the plate performs complex vibrations with all plate modes being excited, which leads to the excitation of the whole spectrum of normal modes in the waveguide.

In certain particular cases of the plate end restraint, the plate only performs the vibrations described by $\varphi_j(y)$. Then, only the normal modes $p_{1j}^{+}(x, y)$ are exited in the waveguide part corresponding to $x > 0$ and $p_{2j}^{-}(x, y)$, in the waveguide part $x < 0$. Such a situation occurs, e.g., when the waveguide walls are fixed and the sliding restraint conditions are satisfied at the plate ends.

Let the plate vibrations excite all normal modes in the waveguide. The pressure field excited in the waveguide can be expanded in the normal modes as

$$P_1(x,y) = \sum_{n=1}^{\infty} A_n p_{1n}^{+}(x,y), \qquad (6)$$

$$P_2(x,y) = \sum_{n=1}^{\infty} B_n p_{2n}^{-}(x,y), \qquad (7)$$

where the expansion coefficients A_n and B_n are the desired amplitudes of normal modes excited in the waveguide.

In addition, let us also consider the reflection problem for normal modes that are incident on the plate from the right-hand part of the waveguide:

$$P_1^{-}(x,y) = \sum_{n=1}^{\infty} a_n p_{1n}^{-}(x,y). \qquad (8)$$

When reflected from the plate, these waves excite the field

$$P_1^+(x, y) = \sum_{n=1}^{\infty} b_n p_{1n}^+(x, y), \tag{9}$$

and when transmitted through the plate, they excite the field

$$P_2^-(x, y) = \sum_{n=1}^{\infty} c_n p_{1n}^-(x, y). \tag{10}$$

Let us choose the wave amplitudes a_n, b_n, and c_n in Eqs. (8)–(10) so as to satisfy the following conditions: the pressure produced on the plate by the waves should be equal to the pressure produced by the external force given by Eq. (4) together with the pressure of liquids in the problem of wave radiation by the plate, i.e.,

$$\begin{aligned} &P_2^-(0, y) - P_1^+(0, y) - P_1^-(0, y) \\ &= f_j(y) + P_2(0, y) - P_1(0, y), \end{aligned} \tag{11}$$

and the displacement of the liquid near the plate along the plate normal should be equal to the displacement in the case of the wave excitation under the action of the external force, i.e.,

$$\frac{1}{\rho_1\omega^2}\left(\frac{\partial P_1^+(0, y)}{\partial x} + \frac{\partial P_1^-(0, y)}{\partial x}\right) = \frac{1}{\rho_1\omega^2}\frac{\partial P_1(0, y)}{\partial x}, \tag{12}$$

$$\frac{1}{\rho_2\omega^2}\frac{\partial P_2^-(0, y)}{\partial x} = \frac{1}{\rho_2\omega^2}\frac{\partial P_2(0, y)}{\partial x}. \tag{13}$$

When Eqs. (11)–(13) are satisfied, the plate vibrates in the same way in the problem of radiation under the action of a force and in the problem of reflection of a plane wave.

From Eqs. (11)–(13) and condition (5) with allowance for representations (6)–(10), we obtain a system of linear algebraic equations in the desired quantities:

$$\begin{cases} c_n - b_n - a_n = f_j\delta_{jn} + B_n - A_n, \\ -a_n + b_n = A_n, \\ c_n = B_n, \\ \dfrac{1}{Z_{1n}}A_n = -\dfrac{1}{Z_{2n}}B_n. \end{cases} \tag{14}$$

Here, δ_{jn} is the Kronecker delta: $\delta_{jj} = 1$ and $\delta_{jn} = 0$ for $n \neq j$; Z_{sn} is the radiation impedance for the nth normal mode of the waveguide to the right ($s = 1$) and to the left ($s = 2$) of the plate: $Z_{sn} = \rho_s c_s\, k_s/\lambda_{sn}$.

Solving the system of equations (14) for the quantities a_n, b_n, and c_n, we obtain relations between the normal mode amplitudes in the problem of scattering by the plate and in the problem of radiation from the plate under the action of forces:

$$\begin{aligned} a_n &= -f_j\delta_{jn}/2, \quad b_n = A_n - (f_j\delta_{jn}/2), \\ c_n &= -(Z_{2n}/Z_{1n})A_n. \end{aligned} \tag{15}$$

Let us assume that, in the waveguide under consideration, at some frequency ω, we have N_1 propagating first normal modes to the right of the plate and N_2 propagating first normal modes to the left of the plate. First, we consider the case when a normal wave $w_j(x, y) = a_j p_j^-(x, y)$ that is incident on the end of the waveguide is a propagating one ($j \le N_1$). This wave carries a power flux

$$\Pi_j = \frac{1}{2\rho_1\omega}\operatorname{Im}\int_0^H \overline{w_j(x, y)}\frac{\partial w_j(x, y)}{\partial x}dy = \frac{\Phi}{2\omega Z_{1j}}|a_j|^2.$$

The normal waves reflected from the plate carry away the power flux $\Pi_1 = \frac{\Phi}{2\omega}\sum_{n=1}^{N_1}\frac{|b_n|^2}{Z_{1n}}$, and the waves transmitted through the plate transfer the power flux $\Pi_2 = \frac{\Phi}{2\omega}\sum_{n=1}^{N_2}\frac{|c_n|^2}{Z_{2n}}$, where the constant Φ is determined by normalization (1). From the power conservation law expressed as

$$\Pi_j = \Pi_1 + \Pi_2 \tag{16}$$

we obtain the equality

$$\frac{|a_j|^2}{Z_{1j}} = \sum_{n=1}^{N_1}\frac{|b_n|^2}{Z_{1n}} + \sum_{n=1}^{N_2}\frac{|c_n|^2}{Z_{2n}}.$$

From this equality with allowance for expressions (15), we derive the desired relation between the amplitudes of normal modes excited in the waveguide, this relation being valid for any $j \le N_1$:

$$\frac{1}{Z_{1j}}\operatorname{Re}(f_j\bar{A}_j) = \sum_{n=1}^{N_1}\frac{|A_n|^2}{Z_{1n}} + \sum_{n=1}^{N_2}\frac{|B_n|^2}{Z_{2n}} \tag{17}$$

(the overbar above A_j means complex conjugation).

Correct to the dimensional factors on both sides of identity (17), the latter expresses the equality of the work of the forces acting on the plate and the vibration energy carried by plane waves propagating away from the plate. In the particular case when, owing to the special choice of restraint conditions for the plate ends at the waveguide walls, the plate excites only one propagating normal mode of number j, and only one term of the same number remains on the right-hand side of identity (17).

Taking into account the third equation in system (14), identity (17) can be represented in the form

$$\frac{1}{Z_{1j}}\mathrm{Re}(f_j\bar{A}_j) = \sum_{n=1}^{N_1}\frac{|A_n|^2}{Z_{1n}} + \sum_{n=1}^{N_2}\frac{Z_{2n}|A_n|^2}{Z_{1n}^2}. \qquad (18)$$

In the particular case, when the acoustic medium is present on only one side of the plate, namely, at $x > 0$, we can formally set $Z_{2n} = 0$ in Eq. (18). As a result, we obtain the identity

$$\frac{1}{Z_{1j}}\mathrm{Re}(f_j\bar{A}_j) = \sum_{n=1}^{N_1}\frac{|A_n|^2}{Z_{1n}}. \qquad (19)$$

Now, let the density of forces in Eq. (19) contain the pressure distribution of an inhomogeneous normal mode ($j > N_1$). It is well known that an inhomogeneous wave $a_j p_j^-(x, y)$ alone causes no energy transfer. However, according to [17, 18], in the presence of an inhomogeneous normal mode $b_j p_j^+(x, y)$ reflected from an obstacle, i.e., from the plate in our case, a nonzero power flux Π_j carried toward the plate by the acoustic pressure is present:

$$w_j(x, y) = a_j p_j^-(x, y) + b_j p_j^+(x, y).$$

With allowance for Eqs. (15), we have

$$\begin{aligned}\Pi_j &= \frac{1}{2\rho_1\omega}\mathrm{Im}\int_0^H \overline{w_j(x, y)}\frac{\partial w_j(x, y)}{\partial x}dy \\ &= \frac{\Phi}{2\omega|Z_{1j}|}\mathrm{Re}(f_j\bar{A}_j).\end{aligned} \qquad (20)$$

Using expression (20), from equality (16) of the power fluxes for $j > N_1$, we derive an identity similar to identity (17), in which the impedance Z_{1j} appearing on its left-hand side is replaced by $|Z_{1j}|$.

In the special case when a single inhomogeneous normal mode of number $s > N$ is excited in the waveguide, the right-hand side of identity (17) is equal to zero, and, hence, the quantity $f_j\bar{A}_j$ is purely imaginary.

Changing to normalized normal modes in Eq. (2),

$$p_{sn}^{+}(x, y) = |Z_{sn}|^{-1/2}\varphi_n(y)\exp(\pm i\lambda_{sn}x)$$

and replacing the force in representation (4) by $f_j(y) = |Z_{1j}|^{-1/2} f_j\varphi_j(y)$, we reduce identity (17) to the form

$$\mathrm{Re}(f_j\bar{A}_j) = \sum_{n=1}^{N_1}|A_n|^2 + \sum_{n=1}^{N_2}|B_n|^2.$$

A similar consideration can be performed for the excitation of plane waves by an infinite plate extending along the straight line ($x = 0$, $-\infty < y < +\infty$) and separating two acoustic media that fill the half-spaces $x < 0$ and $x > 0$ with $-\infty < y < +\infty$. Under the action of forces with density $f(y) = f_0\exp(ik_y y)$, where f_0 is the force amplitude and the inequalities $k_y < k_1$ and $k_y < k_2$ are assumed to be satisfied, the plate excites plane pressure waves in the two half-spaces:

$$P_1(x, y) = A\exp(ik_{1x}x + ik_y y) \quad \text{for } x > 0, \qquad (21)$$

$$P_2(x, y) = B\exp(ik_{2x}x - ik_y y) \quad \text{for } x < 0. \qquad (22)$$

Here, A and B are the amplitudes of plane waves and $k_{sx} = \sqrt{k_s^2 - k_y^2}$.

As in the case of the waveguide, let us now consider the problem of reflection from the plate for a plane wave. When a plane wave $P_1^-(x, y) = a\exp(ik_{1x}x - ik_y y)$ is incident on the plate at $x > 0$, it gives rise to a reflected wave $P_1^+(x, y) = b\exp(ik_{1x}x + k_y y)$ at $x > 0$ and a transmitted wave $P_2^-(x, y) = c\exp(ik_{2x}x + ik_y y)$ at $x < 0$. For the amplitudes of plane waves, we obtain a system of linear equations, which differs from system (14) only by the absence of subscripts in the amplitude notations and by the substitution of f_0 for f_j. Therefore, the desired identity, which follows from the comparison of the power fluxes, has the form

$$\frac{1}{Z_1}\mathrm{Re}(f_0\bar{A}) = \frac{1}{Z_1}|A|^2 + \frac{1}{Z_2}|B|^2, \qquad (23)$$

where Z_s represents the impedances of the acoustic media: $Z_s = \rho_s c_s\frac{k_s}{k_{sx}}$, $s = 1, 2$.

As in the derivation of identity (18), with allowance for the relation between the amplitudes of waves generated by the plate, from Eq. (23) we obtain

$$\mathrm{Re}(f_0\bar{A}) = \left(1 + \frac{Z_2}{Z_1}\right)|A|^2. \qquad (24)$$

For the case of a plate separating identical liquids, identity (24) takes the form $\mathrm{Re}(f_0\bar{A}) = 2|A|^2$.

If in the lower half-plane the medium is absent, this case can be formally described by setting the density of the acoustic medium in it equal to zero. Then, we have $Z_2 = 0$ and, from identity (24), we obtain $\mathrm{Re}(f_0\bar{A}) = |A|^2$ for the problem of the plane wave reflection from a plate whose one side is in contact with an acoustic medium.

When passing to normalized plane waves, we replace the factor $\exp(ik_{sx}x \pm ik_y y)$ involved in the expression for the waves by $Z_s^{-1/2}\exp(ik_{sx}x \pm ik_y y)$, and the factor $\exp(ik_y x)$ in the expression for the density of external forces by $Z_1^{-1/2}\exp(ik_yx)$. In terms of this normalization, the waves $P_s(x, y)$ and $P_s^{\pm}(x, y)$ transfer equal powers through a unit area in the direction normal to the plate. Identity (23) takes the form $\mathrm{Re}(f_0\bar{A}) = |A|^2 + |B|^2$.

Identities (23) and (17), which were obtained without determining the plate displacement and the amplitude of the waves radiated by the plate, can be directly verified. For this purpose, we determine the complete solution to the radiation problem. We seek the displacement of the plate in the form

$$U = U(y) = u\exp(ik_yy), \tag{25}$$

where u is the desired amplitude of the plate displacement.

For the quantities A, B, and u, from conditions (3) and (5) with allowance for representations (21), (22), and (25), we obtain a system of linear algebraic equations

$$u = \frac{f_0 + B - A}{-i\omega Z_p} = \frac{i}{\omega Z_1}A = -\frac{i}{\omega Z_2}B. \tag{26}$$

Here, Z_p is the impedance of flexural vibrations of the plate, which is equal to the ratio of the total pressure onto the plate, $f(y) + P_2(0, y) - P_1(0, y)$, to the vibration velocity of the plate $v = -i\omega u$, $Z_p = -im\omega\left(1 - \frac{gk^4\sin^4\varphi}{m\omega^2}\right)$.

From system (26), we determine the expression for the quantity A:

$$A = \frac{Z_1 f_0}{Z_p + Z_1 + Z_2}. \tag{27}$$

To verify identity (23), we substitute expression (27) for the amplitude A into this identity. As a result, on both right-hand and left-hand sides of the identity, we obtain the same quantity $\frac{(Z_1 + Z_2)^2|f_0|^2}{(\mathrm{Im}Z_p)^2 + (Z_1 + Z_2)^2}$.

REFERENCES

1. L. D. Landau and E. M. Lifshitz, *Course of Theoretical Physics*, Vol. 3: *Quantum Mechanics: Non-Relativistic Theory*, 4th ed. (Nauka, Moscow, 1989; Pergamon, New York, 1977).
2. H. Hönl, A. W. Maue, and K. Westpfahl, *Theorie der Beugung* (Springer, Berlin, 1961; Mir, Moscow, 1964).
3. B. P. Belinskiĭ and D. P. Kouzov, Akust. Zh. **26**, 13 (1980) [Sov. Phys. Acoust. **26**, 8 (1980)].
4. B. P. Belinskiĭ, Akust. Zh. **30**, 154 (1984) [Sov. Phys. Acoust. **30**, 90 (1984)].
5. G. A. Kriegsmann, A. N. Norris, and E. L. Reiss, J. Sound Vibr. **99**, 301 (1985).
6. E. L. Shenderov, *Sound Radiation and Scattering* (Sudostroenie, Leningrad, 1989).
7. B. P. Belinskiy, J. Sound Vibr. **139**, 522 (1990).
8. I. V. Andronov, Akust. Zh. **39**, 13 (1993) [Acoust. Phys. **39**, 5 (1993)].
9. Y. P. Guo, Proc. R. Soc. London, Ser. A **451**, 543 (1995).
10. I. V. Andronov and B. P. Belinskiy, J. Acoust. Soc. Am. **103**, 673 (1998).
11. G. A. Kriegsmann, J. Acoust. Soc. Am. **107**, 1121 (2000).
12. L. M. Lyamshev, Dokl. Akad. Nauk SSSR **125**, 1231 (1959) [Sov. Phys. Dokl. **4**, 406 (1959)].
13. Yu. I. Bobrovnitskiĭ, Akust. Zh. **49**, 14 (2003) [Acoust. Phys. **49**, 10 (2003)].
14. L. M. Lyamshev, Akust. Zh. **5**, 501 (1959) [Sov. Phys. Acoust. **5**, 518 (1959)].
15. E. L. Shenderov, Akust. Zh. **12**, 387 (1966) [Sov. Phys. Acoust. **12**, 336 (1966)].
16. E. L. Shenderov, *Wave Problems in Hydroacoustics* (Sudostroenie, Leningrad, 1972).
17. Yu. I. Bobrovnitskii, J. Sound Vibr. **152** (1), 175 (1992).
18. D. P. Kouzov, G. L. Nikitin, O. B. Agranova, and V. G. Yakovleva, in *Proceedings of XXIII School–Seminar on Analysis and Synthesis in Nonlinear Mechanical Vibratory Systems* (Inst. Probl. Mashinoved. Ross. Akad. Nauk, St. Petersburg, 1996), p. 63.

Translated by E. Golyamina

Acoustical Physics, Vol. 50, No. 1, 2004, pp. 86–90. Translated from Akusticheskiĭ Zhurnal, Vol. 50, No. 1, 2004, pp. 100–105.
Original Russian Text Copyright © 2004 by Perov, Rinkevich.

Wavelet-Transform Analysis and Filtering of Signals Produced by an Ultrasonic Laser Interferometer

D. V. Perov and A. B. Rinkevich

Institute of Metal Physics, Ural Division, Russian Academy of Sciences,
ul. S. Kovalevskoi 18, Yekaterinburg, 620219 Russia
e-mail: peroff@imp.uran.ru; rin@imp.uran.ru

Received March 5, 2003

Abstract—Methods based on the discrete wavelet transform are used to study ultrasonic pulses in aluminum single crystals. Longitudinal elastic waves propagating in the [111] crystallographic direction were generated at 5 MHz. Methods for filtering images of an acoustic field on the basis of wavelet transform are developed. Recommendations on the choice of filtering parameters are given. *© 2004 MAIK "Nauka/Interperiodica".*

INTRODUCTION

The wavelet transform has presently become one of the most reliable, convenient, and mathematically rigorous methods for analyzing functional dependences. This method can be used to determine instantaneous dominating periods of oscillations and reveal the modulation type, latent periodicity, and correlation between oscillations of different periods. The method shows a great promise for the analysis of pulsed and noise-like signals. There are two main types of wavelet transform: continuous and discrete ones [1, 2]. The continuous transform is mostly used to analyze functions. The discrete transform is the basic means in interference compression algorithms and filtering procedures. The results of the wavelet transform are the wavelet spectrum and the scalogram, which serve as a source of both local and general information on the properties of the function analyzed. A wavelet spectrum is a diagram, which uses colors or shades of grey to map the values of the wavelet transform coefficients. The abscissa axis represents the time, and the ordinate axis represents the period of signal oscillations. A scalogram is a generalized characteristic of the time function under analysis. It shows the distribution of oscillation power in oscillation period. The maxima of the scalogram show which periods predominate.

The processing algorithms do not as yet fully take into account specific features of acoustic signals. Therefore, advantages of the wavelet analysis in this field have not been realized in full measure.

Ultrasonic laser interferometry is one of the modern techniques for detecting acoustic signals and visualizing the wave fields. It provides high-selectivity broadband local measurements. The Doppler interferometry, which is widely used at present, provides calibrated measurements. Existing software is capable of representing the information on acoustic fields in various forms, including visualization of wave fronts and elastic energy distribution over the beam at a particular time. The broadband character of the technique and the effect of surface roughness are the sources of noise and interference. Therefore, it is worthwhile to develop general-purpose algorithms for filtering signals produced by ultrasonic laser interferometers. It has been shown in [3, 4] that the wavelet transform is a promising means for solving this problem. However, the goal of these studies was to apply the wavelet transform in a limited field of ultrasonic nondestructive testing. It is therefore necessary to examine the signals produced by ultrasonic interferometers in detail by the wavelet transform method.

In this paper, we use the discrete wavelet transform to analyze longitudinal acoustic waves in aluminum single crystals. We consider an algorithm developed for filtering two-dimensional images of acoustic fields on the basis of the discrete wavelet transform.

EXPERIMENTAL TECHNIQUE

The experimental portion of this work was conducted with the use of an OFV-3001 ultrasonic laser interferometer belonging to Fraunhofer Institute of Nondestructive Testing (Dresden, Germany). A coherent optical beam produced by a helium–neon laser was split into two parts. One part was passed through an acoustooptical modulator (Bragg cell); the second was guided to the object under study through a system of optical lenses. The beam reflected from the object was applied to a photodetector, where interference with the reference beam, which had passed through the Bragg cell, was observed.

If the reflecting surface of the object is illuminated by an ultrasonic wave, components shifted in frequency due to the Doppler effect appear in the spectrum of the reflected signal. A 1-m/s velocity of the object produces a 3.17-MHz Doppler shift. In a harmonic elastic wave,

1063-7710/04/5001-0086$26.00 © 2004 MAIK "Nauka/Interperiodica"

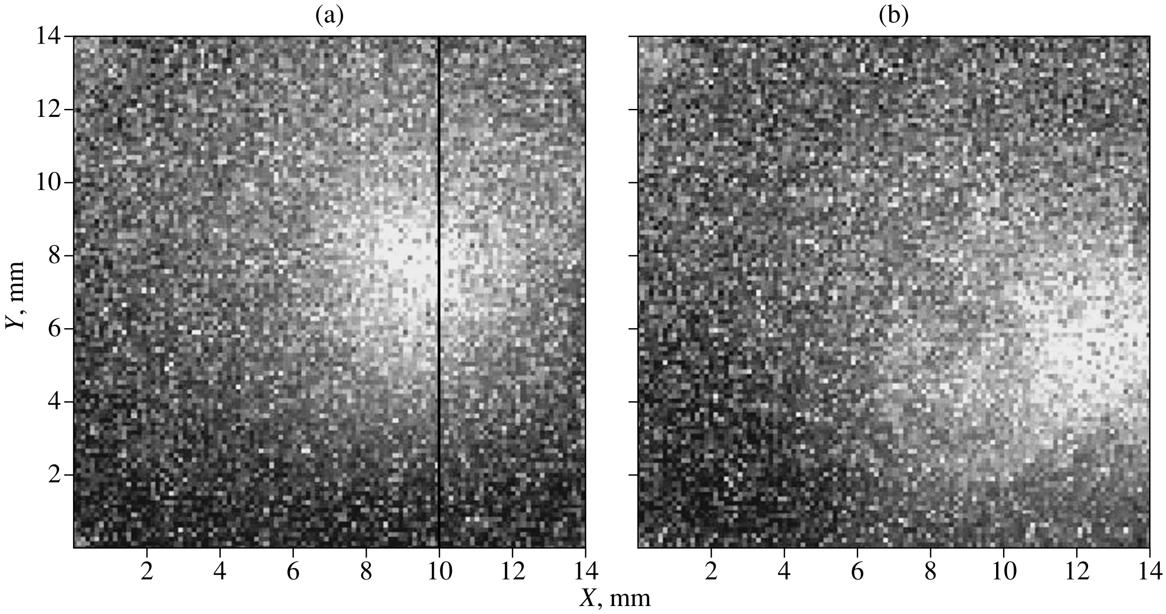

Fig. 1. Amplitude distribution of elastic displacements in a beam of longitudinal waves that has traveled through the aluminium single crystal in the [111] direction for an unpolished reflecting surface at 5 MHz: (a) first and (b) second pulses.

the particle velocity is proportional to the amplitude of the displacement. Therefore, the amplitude distribution of the elastic displacement can be obtained by scanning the object's surface and measuring the particle velocity.

The output signal of the interferometer was recorded and converted into a code by a digital oscilloscope. A personal computer was used to analyze and store the information. A scanner moved the sample in the vertical and horizontal directions. The typical scanner increment was 0.125 or 0.25 mm. The equipment was capable of accumulating the signal in order to improve the signal-to-noise ratio. At each point, the signal was averaged over 50 to 300 measurements. Longitudinal elastic waves were excited by a piezoelectric transducer with a resonance frequency of 5 MHz. The transducer plate was 13 mm in diameter. The pattern of damped ultrasonic echo-signals was observed by a USIP12 flaw detector. Each sample had two flat surfaces. On one of them, the piezoelectric transducer was placed; on the other, the laser beam was incident, and the elastic field was detected at this surface.

Results of measurements were stored by a computer program based on the LabView 5.0 software. The time dependence of the response amplitude at each point of the scanned field, i.e., the type A scan, contained 1000 discrete signal samples. The scanned area was 14 × 14 mm. After the scanning, the following characteristics of the elastic displacement field can be visualized: (i) a type A scan at each point of scanning; (ii) a type B scan, i.e., a diagram that combines type A scans along a particular direction; and (iii) a type C scan, i.e., the very elastic displacement amplitude distribution over the scanned area. To construct a type C scan, it is necessary to choose a time interval on the type A scan over which the maximum (or minimum) amplitude value distribution will be analyzed. This feature provides a separate observation of the acoustic fields produced by pulsed excitation due to, for example, pulses that have passed through the sample different numbers of times.

An aluminum single crystal in the form of a 16- to 20-mm long cylinder was used as a sample. It had two parallel faces, one of which was perpendicular to the [111] axis and polished so that the roughness height was no greater than 8 μm. The second face was not polished, and its roughness height was 30 to 40 μm and roughness width was about 100 μm.

RECORDING OF THE ACOUSTIC FIELD: IMAGE FILTERING

Acoustic fields in aluminum single crystals detected by the laser interferometry technique were studied in [5], where the analysis was mostly focused on the response of the interferometer to elastic displacements in transverse waves. Below, we examine the efficiency of the wavelet filtering procedure and address the question of how to choose the filtering parameters. Figure 1 shows the type C scans of an unpolished [111] surface of the sample. The maximum amplitude of the interferometer's response is shown in white. The *X* and *Y* axes represent the distances from the scan origin (0, 0) in millimeters. The longitudinal acoustic waves were excited by a piezoelectric transducer at 5 MHz in the pulsed mode. The amplitude was measured for a 1-μs-long interval, which corresponded to the length of the ultrasonic pulse. The delay was chosen such that Fig. 1a shows the amplitude distribution of elastic displace-

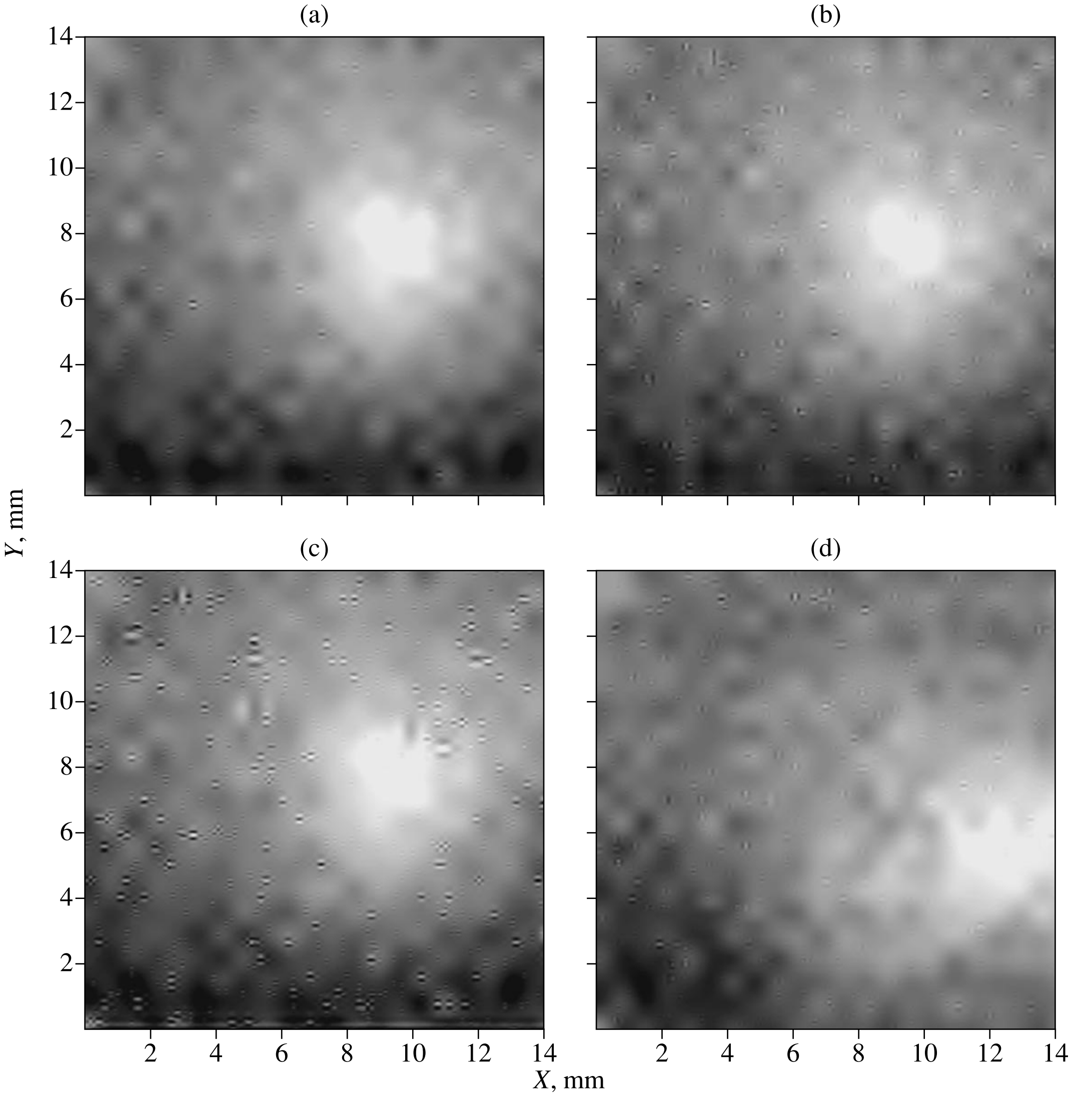

Fig. 2. Amplitude distribution of elastic displacements in the pulse shown in Fig. 1a after filtering with four expansion levels and a fixed threshold using (a, c) Sym8 and (b) Sym4 wavelet functions and (a, b) soft and (c) hard thresholdings. Figure 2d refers to the second pulse in Fig. 1b filtered with the Sym8 function, four expansion levels, and soft thresholding.

ments in the pulse that has traveled through the sample once in the forward direction. Figure 1b shows the distribution for the second pulse, which has traveled three times through the sample length. At each point of the scanned area, the measurements used a 200-fold accumulation. Both these distributions obtained from a rough surface contain an intense noise component.

A result of the wavelet transform of these distributions is shown in Fig. 2. A detailed description of the filtering algorithm can be found in [4]. Here, we only describe it briefly.

The wavelet filtering procedure relies on the recurrent fast wavelet transform (FWT) algorithm proposed by Mallat [2]. The FWT principle consists in separating the frequency domain, on which the analyzed signal is defined, into two equal parts with a pair of low-pass and high-pass filters referred to as quadrature mirror filters (QMFs). As a result, at the first level of the expansion, the original vector of length N generates two new vectors, each of which consists of $N/2$ elements. One of them is the low-frequency portion of the original signal, it is referred to as the set of approximation coefficients or as the approximation of the signal. The other vector is the high-frequency portion of the original signal, it is referred to as the set of detailing coefficients or as signal details. Further, this separation procedure can again be applied to the approximation of the original signal. The number of times this procedure is applied is called the number of expansion levels of the FVT algorithm. Note that the procedure is completely reversible; i.e., with the approximation and detail vectors being known, the original signal can be reconstructed exactly with the help of the inverse fast wavelet transform (IFWT).

Two-dimensional images can be processed in a similar manner with the help of the two-dimensional FWT, which is performed in two stages. At first, the QMFs are applied to rows of the analyzed matrix and the columns at the filter outputs are decimated by a factor of two. Then, all columns of each of the two new matrices are processed by the QMFs once more and the rows of the four arrays obtained are decimated by a factor of two. As a result, at the first level of the expansion, the original $M \times N$ matrix generates four $M/2 \times N/2$ matrices: the approximation and horizontal, vertical, and diagonal details. Note that, as in the one-dimensional case, the two-dimensional IFWT exists.

The wavelet filtering procedure itself is as follows. For all vectors or matrices of the detailing coefficients obtained at all expansion levels of the FWT algorithm, thresholds symmetric about the zero level are adjusted, their values being chosen in accordance with a certain strategy. The elements of the vectors or matrices that are above the thresholds are kept unchanged, while the others are zeroed. This procedure is called the hard thresholding. When the array elements that remain nonzero after the threshold limiting are additionally shifted towards zero by the corresponding threshold levels, the procedure is called the soft thresholding [6].

Figures 2a–2c show images obtained by filtering the image presented in Fig. 1a. As the basis functions, the procedure used wavelets of the Sym family, or symlets. Wavelets belonging to this family are denoted as SymM, where M is the wavelet order. It is known that [2], among other features, parameter M characterizes locality of the wavelet. In particular, the SymM wavelet consists of $2M - 1$ nonzero samples. Detailed information about symlets and other compactly supported wavelets used with the FWT algorithm can be found in [2]. Figure 2a is obtained with the Sym8 function and four expansion levels; Fig. 2b, with the Sym4 function and the same number of levels. Both cases employ the strategy with a fixed threshold and soft thresholding. The threshold levels are determined as [6]

$$T_i = \pm s_i \sqrt{2 \ln NM}, \tag{1}$$

where i is the index of the expansion level, $s_i = \text{med}(|w_i|)/0.6745$, and $\text{med}(\cdot)$ stands for median of the matrix. Thresholds for the one-dimensional case can also be specified by formula (1) with the product of row and column numbers replaced with the length of the corresponding vector.

The same image was filtered with the use of the hard thresholding. The result obtained with the Sym8 function and four expansion levels is illustrated in Fig. 2c. The image shown in Fig. 2d is the amplitude distribution of the second pulse from Fig. 1b after filtering with the use of the Sym8 function, four expansion levels, and the soft thresholding strategy. By comparing these results, we can conclude that the soft thresholding strategy is preferable, because the hard thresholding produces a large number of clearly outlined local artefacts (Fig. 2c), which affect the visual perception of the filtered image. It is also reasonable to employ a higher order wavelet function, say Sym8. It has been shown that, to efficiently filter pulsed ultrasonic signals, it is sufficient to use four expansion levels [7].

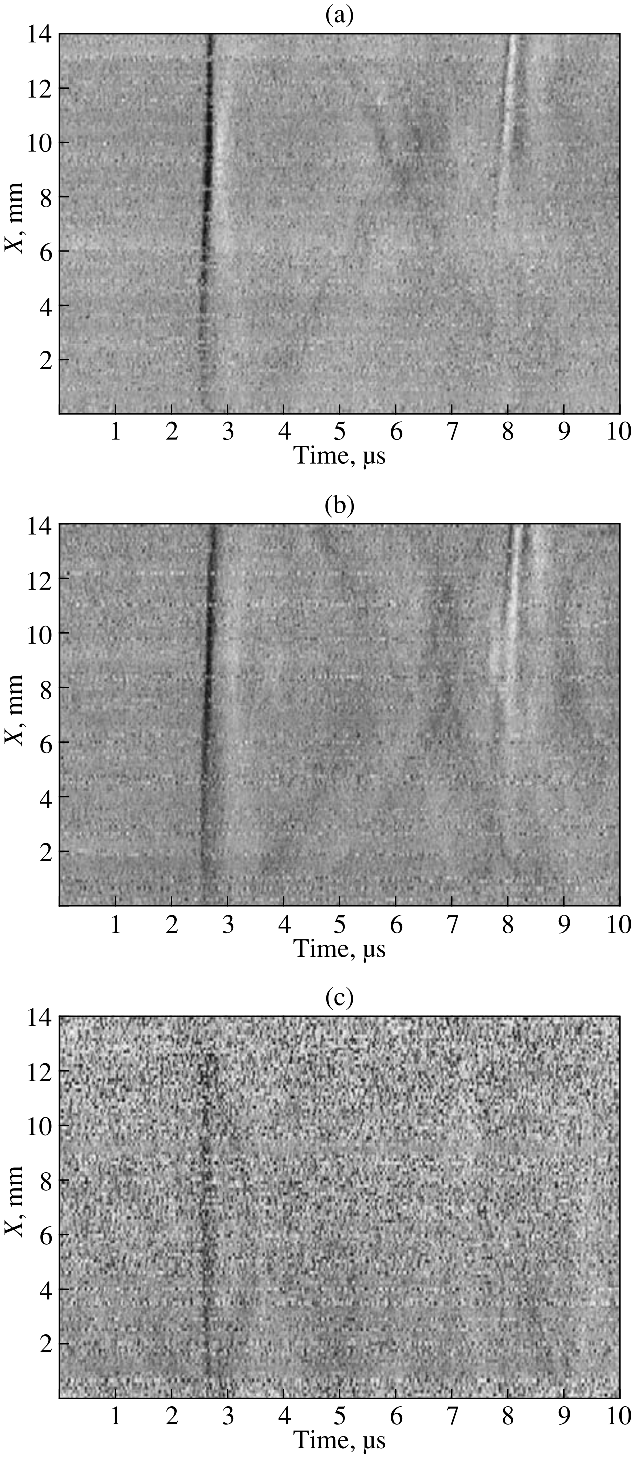

Fig. 3. Type B scans for the same excitation conditions as in Fig. 1: (a) original image constructed for the cross section $X = 8$ mm and (b) image filtered with the Sym8 wavelet function and four expansion levels.

Type B scans can be used to visualize the shape of the wave front. It can also be useful to optimally choose the time interval for the type C scan. Figure 3a shows a type B scan created under the same excitation conditions as that in Fig. 1 for $Y = 8$ mm = const, whose value is chosen from the type C scan in Fig. 1a. The abscissa in Fig. 3a represents time in microseconds (10 μs) during which the interferometer response was recorded. The Y axis represents the distance along the chosen vertical or horizontal line in millimeters. The cross section shown in Fig. 3a passes through the central part of the beam. The vertical lines near 2.5–3.5 μs and 7.5–8.5 μs correspond to wave fronts of the first and second pulses. Less clear-cut oblique lines are produced by the beams reflected from the lateral surfaces of the sample.

The image in Fig. 3a is contaminated with noise. This image was also filtered with the use of the Sym8 function and four expansion levels. The result is shown in Fig. 3b. It is clearly seen that the signal-to-noise ratio has improved. After filtering, even a heavily contaminated image gives information about the acoustic parameters, in particular, about the shape of the wave front.

CONCLUSIONS

Thus, ultrasonic pulse fields in aluminium single crystals are studied. Measurements using an ultrasonic laser interferometer are performed. The amplitude distributions of elastic displacements in ultrasonic pulse beams are obtained, and the shape of the wave front is determined.

Filtering algorithms for the time response of the laser interferometer (pulsed ultrasonic signals) and for two-dimensional images are developed. It is shown that, in filtering two-dimensional images, good results are obtained by using symlet wavelet functions of a sufficiently large order, for example, Sym8. The number of expansion levels can be limited to four without a sacrifice of precision. Filtering with a constant threshold and soft thresholding gives the best results.

A practically important convenience of the wavelet filtering algorithms is that they do not need to be specially tuned to a specific function to be analyzed. Advantages of the wavelet filtering are realized without manual intervention. On the whole, the algorithms of filtering two-dimensional acoustic signals on the basis of the discrete wavelet transform are a reliable and versatile tool, which is capable of filtering noise of diverse spectral contents out of two-dimensional acoustic field images.

ACKNOWLEDGMENTS

This work was supported by the Russian Foundation for Basic Research, project no. 03-02-16207, and by the program “Russian Foundation for Basic Research-Ural,” project no. 01-02-96410.

We are grateful to Prof. M. Kröning and Dr. B. Köhler for giving us the possibility to perform the measurements on a laser interferometer. We are also grateful to Dr. A.S. Krivonosova for providing us with an aluminum single crystal.

REFERENCES

1. N. M. Astaf’eva, Usp. Fiz. Nauk **166**, 1145 (1996) [Phys. Usp. **39**, 185 (1996)].
2. I. Daubechies, *Ten Lectures on Wavelets*, CBMS-NSF Regional Conference Series in Applied Mathematics, Vol. 61 (SIAM, Philadelphia, 1992; Nauchno–Issled. Tsentr Regularnaya i Khaotich. Dinamika, Izhevsk, 2001).
3. D. V. Perov, A. B. Rinkevich, Ya. G. Smorodinskiĭ, and B. Keler, Defektoskopiya, No. 12, 67 (2001).
4. D. V. Perov and A. B. Rinkevich, Defektoskopiya, No. 4, 78 (2002).
5. A. S. Krivonosova, A. B. Rinkevich, and Ya. G. Smorodinskiĭ, Akust. Zh. **47**, 92 (2001) [Acoust. Phys. **47**, 76 (2001)].
6. D. L. Donoho and I. M. Johnstone, Biometrika **81**, 425 (1994).
7. D. V. Perov, A. B. Rinkevich, and Ya. G. Smorodinskiĭ, Defektoskopiya, No. 12, 3 (2002).

Translated by A. Khzmalyan

Acoustical Physics, Vol. 50, No. 1, 2004, pp. 9–19. Translated from Akusticheskiĭ Zhurnal, Vol. 50, No. 1, 2004, pp. 14–25.
Original Russian Text Copyright © 2004 by Burov, Vecherin, Rumyantseva.

Statistical Estimation of the Spatial Spectrum of Secondary Sources

V. A. Burov, S. N. Vecherin, and O. D. Rumyantseva
Faculty of Physics, Moscow State University, Vorob'evy gory, Moscow, 119992 Russia
e-mail: burov@phys.msu.ru

Received October 17, 2002

Abstract—A statistical problem of estimating the shape and maximum possible width of the spatial energy spectrum of secondary sources is formulated and solved. The secondary sources under consideration are characteristic of the class of scatterers with preset statistical mean parameters. This estimation is important for analyzing the possibility of solving inverse scattering problems, including the question of the uniqueness and stability of the solution and also the correct organization of a tomographic experiment. Results of a computer simulation are presented, and the expected statistical mean spectrum is compared with a particular realization of the spectrum. In the case of a strongly pronounced rescattering, the statistical mean width of the spectrum is mainly determined by the effective velocity contrast in the ensemble of scatterers and depends only weakly on the scale of spatial fluctuations of the scatterers' characteristics. *© 2004 MAIK “Nauka/Interperiodica”.*

1. PRACTICAL IMPORTANCE OF THE ESTIMATION PROBLEM

In this paper, we formulate the problem of a statistical estimation of the effective width of the spatial spectrum of secondary sources for scatterers belonging to a preset class. The practical need for such an estimation is connected with solving the inverse scattering problem, namely, the nonlinear and ill-defined problem of reconstructing the internal structure of an object (scatterer) studied by remote sensing with wave fields. Knowing the size of the localization region of the spatial spectrum of secondary sources, it is possible to estimate the number of the degrees of freedom of these sources. In this way, first, it is possible to analyze the fundamental possibility of obtaining a unique and stable reconstruction of a scatterer of a given strength and to determine the minimal amount of discrete experimental scattering data necessary for this reconstruction [1, 2]. Second, it is possible to choose and set up the most appropriate tomographic system that provides the optimal (among available) amount of data in monochromatic and pulsed modes. For this purpose, in particular, it is necessary to estimate the maximal admissible angular interval of discretization in the data acquisition. For example, in the case of a ring circuit of data acquisition in a two-dimensional monochromatic system, this interval is [3] $\Delta\varphi_{\max} \cong 2\pi/(\chi_I L)$, where L is the linear dimension of the scattering region $\Re$ and χ_I is the linear half-width of the localization region of the spatial spectrum of secondary sources at a fixed incident field. It is well known that an excess of the angular interval over the maximum one leads to a loss of information on the scatterer (irreplaceable at the stage of the numerical reconstruction of the scatterer) and to the inadequacy of the reconstructed image [4]. Finally, proceeding from the available amount of data, it is possible to select the most appropriate techniques for solving the inverse problem, some of which are mentioned in [1].

2. STATISTICAL APPROACH TO ESTIMATION

It is necessary to start by mentioning the effect of broadening of the spatial spectrum of secondary sources of a distributed scatterer by repeating several phrases from [1], where this effect is considered in more detail.

An acoustic scatterer formed in the general case by inhomogeneities of the sound phase velocity, absorption coefficient, and density of a medium is described by the function $\varepsilon(\mathbf{r})$. To reconstruct this function, the scatterer is irradiated by an incident field $U_0(\mathbf{r}, \alpha)$ with the parameters (including the field configuration, direction of incidence, and frequency) described by a single generalized index α. The secondary sources $I(\mathbf{r}, \alpha)$ arise in the scattering region $\Re$ as the result of interaction of U_0 with the scatterer:

$$I(\mathbf{r}, \alpha) \equiv \varepsilon(\mathbf{r}) U(\mathbf{r}, \alpha), \tag{1}$$

where $U(\mathbf{r}, \alpha)$ is the total field obeying in the monochromatic case the Lippmann–Schwinger equation [5]

$$U(\mathbf{r}, \alpha) = U_0(\mathbf{r}, \alpha) + \int G(\mathbf{r} - \mathbf{r}', k_0) \varepsilon(\mathbf{r}') U(\mathbf{r}', \alpha) d\mathbf{r}' \quad \forall \mathbf{r}; \tag{2}$$

and $G(\mathbf{r}, k_0)$ is the Green function of a homogeneous infinite nonabsorbing background medium with a wave number k_0 corresponding to the given index α. From

Eqs. (1) and (2) it follows that secondary sources produce a scattered field $u_{\text{sc}}(\mathbf{r}, \alpha) \equiv U(\mathbf{r}, \alpha) - U_0(\mathbf{r}, \alpha)$. An equation for $I(\mathbf{r}, \alpha)$ is obtained by multiplying Eq. (2) by $\varepsilon(\mathbf{r})$:

$$I(\mathbf{r}, \alpha) = I_{\text{born}}(\mathbf{r}, \alpha) + \varepsilon(\mathbf{r})\int G(\mathbf{r} - \mathbf{r}', k_0) I(\mathbf{r}', \alpha) d\mathbf{r}'. \tag{3}$$

In the single scattering approximation (which is also called the Born approximation), it is assumed that $U(\mathbf{r}, \alpha) \approx U_0(\mathbf{r}, \alpha)$ at $\mathbf{r} \in \mathfrak{R}$. Then, $I(\mathbf{r}, \alpha) \approx I_{\text{born}}(\mathbf{r}, \alpha)$, where $I_{\text{born}}(\mathbf{r}, \alpha) \equiv \varepsilon(\mathbf{r}) U_0(\mathbf{r}, \alpha)$ are the secondary sources in the Born approximation. The Fourier transformation of Eq. (3) with respect to the coordinate $\mathbf{r}$ leads to an expression of the Lippmann–Schwinger type, which connects the spatial spectra of a scatterer $\tilde{\varepsilon}(\vec{\xi}) \equiv \int \varepsilon(\mathbf{r}) \exp(-i\vec{\xi}\mathbf{r}) d\mathbf{r}$ and its secondary sources $\tilde{I}(\vec{\xi}, \alpha)$:

$$\begin{aligned} \tilde{I}(\vec{\xi}, \alpha) &= \tilde{I}_{\text{born}}(\vec{\xi}, \alpha) \\ &+ \frac{1}{(2\pi)^p}\int \tilde{\varepsilon}(\vec{\xi} - \vec{\xi}') \tilde{G}(|\vec{\xi}'|, k_0) \tilde{I}(\vec{\xi}', \alpha) d\vec{\xi}', \end{aligned} \tag{4}$$

where p is the space dimension; the spatial spectrum of the Green function is $\tilde{G}(\vec{\xi}, k_0) = \tilde{G}(|\vec{\xi}|, k_0)$. In the Born approximation, $\tilde{I}(\vec{\xi}, \alpha) \approx \tilde{I}_{\text{born}}(\vec{\xi}, \alpha)$, where

$$\tilde{I}_{\text{born}}(\vec{\xi}, \alpha) = \frac{1}{(2\pi)^p}\int \tilde{\varepsilon}(\vec{\xi} - \vec{\xi}') \tilde{U}_0(\vec{\xi}', \alpha) d\vec{\xi}', \tag{5}$$

and $\tilde{U}_0(\vec{\xi}, \alpha)$ is the spatial spectrum of the incident field.

In the case of a spatially distributed scatterer, the function $\varepsilon(\mathbf{r})$ is considered for a continuum set of values $\mathbf{r} \in \mathfrak{R}$. If the scatterer is sufficiently strong (so that the rescattering of wave fields within $\mathfrak{R}$ is essential), the localization region for the basic part of the spatial spectrum of secondary sources $\tilde{I}(\vec{\xi}, \alpha)$ is broader than that for the scattering spectrum $\tilde{\varepsilon}(\vec{\xi})$. The stronger the scatterer, the stronger the broadening is. It is necessary to keep in mind the aforementioned effect for the adequacy of the discrete mathematical description of the scattering process and its physical essence.

Precisely in connection with the broadening effect, the problem of statistical estimation of the width of the spatial spectrum of secondary sources arises. This problem was formulated and partially investigated in [6]. A statistical approach is connected with the fact that only the average characteristics of an object under investigation (a scatterer) can be known *a priori* in tomographic problems. Moreover in the case of taking into account the rescattering, the spectrum $\tilde{I}(\vec{\xi}, \alpha)$ depends on the scatterer function's nonlinearly, which makes the problem of the exact determination of $\tilde{I}(\vec{\xi}, \alpha)$ very difficult. The nonlinear character can be seen directly in the expansion of Eq. (4), with allowance for Eq. (5), into a power series with respect to the function $\tilde{\varepsilon}(\vec{\xi})$.

Consider an ensemble of scatterers $\{\varepsilon(\mathbf{r})\}$ of a certain class. We make the following assumptions (the sign $\langle\bullet\rangle_\varepsilon$ denotes averaging over all scatterers):

—$\langle\varepsilon(\mathbf{r})\rangle_\varepsilon = 0\ \forall\mathbf{r} \in \mathfrak{R}$ and, therefore,

$$\langle\tilde{\varepsilon}(\vec{\xi})\rangle_\varepsilon = 0\ \forall\,\vec{\xi}; \tag{6}$$

—the mean spectral “energy density” of a scatterer, $\mathcal{E}(|\vec{\xi}|) \equiv \langle|\tilde{\varepsilon}(\vec{\xi})|^2\rangle_\varepsilon$, is known;

—the components $\tilde{\varepsilon}(\vec{\xi})$ are correlated only within the volume $\Delta_\xi \approx (\beta)^p$, where $\beta \approx 2\pi/L$:

$$\langle\tilde{\varepsilon}(\vec{\xi}_1)\tilde{\varepsilon}^*(\vec{\xi}_2)\rangle \approx \begin{cases} \mathcal{E}(|\vec{\xi}_1|), & \text{when } |\vec{\xi}_2 - \vec{\xi}_1| < \beta; \\ 0, & \text{in all other cases;} \end{cases} \tag{7}$$

—the probability density of the deviation of the function $\tilde{\varepsilon}(\vec{\xi})$ from its zero average value is distributed according to the normal law at each fixed $\vec{\xi}$.

Each fixed scatterer from the ensemble is irradiated simultaneously from all directions by the monochromatic fields $U_0(\mathbf{r}, \alpha)$, where α is the index of the incidence direction of a field. The field phase is random and uncorrelated with respect to directions, which yields

$$\begin{gathered} \langle U_0(\mathbf{r}, \alpha)\rangle_\alpha = 0 \quad \forall\mathbf{r} \text{ and, therefore,} \\ \langle\tilde{U}_0(\vec{\xi}, \alpha)\rangle_\alpha = 0 \quad \forall\vec{\xi} \end{gathered} \tag{8}$$

(the sign $\langle\bullet\rangle_\alpha$ denotes averaging over all directions and, correspondingly, over the phases of incident fields). It is necessary to estimate the average spectral energy density of secondary sources $J(|\vec{\xi}|) \equiv \langle|\tilde{I}(\vec{\xi}, \alpha)|^2\rangle_{\varepsilon, \alpha}$, if the estimate of this density in the Born approximation $J_{\text{born}}(|\vec{\xi}|) \equiv \langle|\tilde{I}_{\text{born}}(\vec{\xi}, \alpha)|^2\rangle_{\varepsilon, \alpha}$ is known. Averaging $\langle\bullet\rangle_{\varepsilon, \alpha}$ has a twofold character: over all scatterers and all directions α. This corresponds to statistically maximal broadening of the spatial spectrum of secondary sources.

An equation for $J(|\vec{\xi}|)$ is obtained from Eq. (4):

$$\tilde{I}(\vec{\xi}, \alpha) - \tilde{I}_{\text{sc}}(\vec{\xi}, \alpha) = \tilde{I}_{\text{born}}(\vec{\xi}, \alpha), \tag{9}$$

where the term

$$\tilde{I}_{\text{sc}}(\vec{\xi}, \alpha) = \frac{1}{(2\pi)^p}\int \tilde{\varepsilon}(\vec{\xi} - \vec{\xi}') \tilde{G}(|\vec{\xi}'|, k_0) \tilde{I}(\vec{\xi}', \alpha) d\vec{\xi}' \tag{10}$$

(in the operator form $\tilde{I}_{sc} = \hat{\tilde{\varepsilon}}\hat{\tilde{G}}\tilde{I}$) describes the part $\varepsilon(\mathbf{r})u_{sc}(\mathbf{r}, \alpha)$ of secondary sources that is produced by the scattered field. The multiplication of the left-hand and right-hand sides of Eq. (9) by the complex conjugate quantities and the application of the averaging operation $\langle\bullet\rangle_{\varepsilon,\alpha}$ leads to the equation

$$\begin{gathered}\left\langle\left|\tilde{I}(\vec{\boldsymbol{\xi}}, \alpha)\right|^2\right\rangle_{\varepsilon,\alpha} + \left\langle\left|\tilde{I}_{sc}(\vec{\boldsymbol{\xi}}, \alpha)\right|^2\right\rangle_{\varepsilon,\alpha} \\ -2\mathrm{Re}\langle\tilde{I}(\vec{\boldsymbol{\xi}}, \alpha)\tilde{I}^*_{sc}(\vec{\boldsymbol{\xi}}, \alpha)\rangle_{\varepsilon,\alpha} = \left\langle\left|\tilde{I}_{born}(\vec{\boldsymbol{\xi}}, \alpha)\right|^2\right\rangle_{\varepsilon,\alpha}.\end{gathered} \tag{11}$$

According to Eq. (10), the expression for $\tilde{I}_{sc}(\vec{\boldsymbol{\xi}}, \alpha)$ involves the spectral components $\tilde{I}(\vec{\boldsymbol{\xi}}', \alpha)$ at different spatial frequencies. Therefore, in the general case, a rigorous solution of a nonlinear equation (11) seems difficult, and a simplification of the problem requires a transition to approximate estimates. The point is that, strictly speaking, the probability density for the random quantity $\tilde{I}(\vec{\boldsymbol{\xi}}, \alpha)$ does not have the form of a normal distribution at each fixed $\vec{\boldsymbol{\xi}}$. Only the quantity $\tilde{I}_{born}(\vec{\boldsymbol{\xi}}, \alpha)$ has a normal distribution by virtue of definition of Eq. (5), the assumption on the normal distribution of the quantity $\tilde{\varepsilon}$, and the cross-independence of the functions ε and U_0. If we also take into account the effect of rescattering, the distribution for $\tilde{I}$ becomes different from the normal law. This follows from the expansion of Eq. (4) into the Born–Neumann series in powers of the functions $\tilde{\varepsilon}$. In this case, $\tilde{I}$ is formed by the sum of terms, for each of which a distribution law is, generally speaking, different from the normal law. Moreover, these terms are not statistically independent, i.e., each two terms whose product contains an even number of functions $\tilde{\varepsilon}$ correlate with each other. Therefore, even in the case of a strongly pronounced rescattering, when the number of effective terms is large, the distribution for $\tilde{I}$ does not tend to a normal one. In this connection, the first approximation in the process of solving Eq. (11) is the following estimate of the term $\langle|\tilde{I}_{sc}|^2\rangle_{\varepsilon,\alpha}$, which will be rigorous only in the case of a normal distribution of both quantities $\tilde{\varepsilon}$ and $\tilde{I}$:

$$\begin{gathered}\langle|\tilde{I}_{sc}|^2\rangle_{\varepsilon,\alpha} \equiv \langle\hat{\tilde{\varepsilon}}\hat{\tilde{G}}\tilde{I}(\hat{\tilde{\varepsilon}}\hat{\tilde{G}}\tilde{I})^*\rangle_{\varepsilon,\alpha} \\ \cong \langle\hat{\tilde{\varepsilon}}\hat{\tilde{G}}\tilde{I}\rangle_{\varepsilon,\alpha}\langle\tilde{I}^*\hat{\tilde{G}}^*\hat{\tilde{\varepsilon}}^*\rangle_{\varepsilon,\alpha} + \langle\hat{\tilde{\varepsilon}}\hat{\tilde{\varepsilon}}^*\rangle_{\varepsilon}\langle\hat{\tilde{G}}\tilde{I}\tilde{I}^*\hat{\tilde{G}}^*\rangle_{\varepsilon,\alpha} \\ + \langle\hat{\tilde{\varepsilon}}\tilde{I}^*\hat{\tilde{G}}^*\rangle_{\varepsilon,\alpha}\langle\hat{\tilde{G}}\tilde{I}\hat{\tilde{\varepsilon}}^*\rangle_{\varepsilon,\alpha} = \langle\hat{\tilde{\varepsilon}}\hat{\tilde{\varepsilon}}^*\rangle_{\varepsilon}\langle\hat{\tilde{G}}\tilde{I}\tilde{I}^*\hat{\tilde{G}}^*\rangle_{\varepsilon,\alpha} \\ = \langle\hat{\tilde{\varepsilon}}\hat{\tilde{\varepsilon}}^*\rangle_{\varepsilon}\hat{\tilde{G}}\langle\tilde{I}\tilde{I}^*\rangle_{\varepsilon,\alpha}\hat{\tilde{G}}^*.\end{gathered} \tag{12}$$

Here, we use the fact that

$$\begin{gathered}\langle\tilde{I}(\vec{\boldsymbol{\xi}}, \alpha)\rangle_{\alpha} = 0, \quad \langle\tilde{I}_{born}(\vec{\boldsymbol{\xi}}, \alpha)\rangle_{\alpha} = 0, \\ \langle\tilde{I}_{sc}(\vec{\boldsymbol{\xi}}, \alpha)\rangle = 0 \quad \forall\vec{\boldsymbol{\xi}},\end{gathered} \tag{13}$$

since $\tilde{I}$, $\tilde{I}_{born}$, and $\tilde{I}_{sc}$ are linear functions of the field and condition (8) is valid. Therefore, Eq. (12) takes into account that both $\tilde{\varepsilon}$ (see Eq. (6)) and $\tilde{I}$ have zero average values and the cofactors of the type of $\langle\hat{\tilde{\varepsilon}}\hat{\tilde{G}}\tilde{I}\rangle_{\varepsilon,\alpha} = \hat{\tilde{G}}\langle\hat{\tilde{\varepsilon}}\langle\tilde{I}\rangle_{\alpha}\rangle_{\varepsilon}$ are equal to zero due to Eq. (13).

The second approximation in the process of solving Eq. (11) consists of ignoring the term $2\mathrm{Re}\langle\tilde{I}(\vec{\boldsymbol{\xi}}, \alpha)\tilde{I}^*_{sc}(\vec{\boldsymbol{\xi}}, \alpha)\rangle_{\varepsilon,\alpha}$; i.e., we approximately assume that

$$\begin{gathered}\langle\tilde{I}(\vec{\boldsymbol{\xi}}, \alpha)\tilde{I}^*_{sc}(\vec{\boldsymbol{\xi}}, \alpha)\rangle_{\varepsilon,\alpha} \equiv \langle\tilde{I}(\hat{\tilde{\varepsilon}}\hat{\tilde{G}}\tilde{I})^*\rangle_{\varepsilon,\alpha} \\ \equiv \frac{1}{(2\pi)^p}\int\tilde{G}^*(|\vec{\boldsymbol{\xi}}'|, k_0) \\ \times\langle\tilde{I}(\vec{\boldsymbol{\xi}}, \alpha)\tilde{I}^*(\vec{\boldsymbol{\xi}}', \alpha)\tilde{\varepsilon}^*(\vec{\boldsymbol{\xi}} - \vec{\boldsymbol{\xi}}')\rangle_{\varepsilon,\alpha}d\vec{\boldsymbol{\xi}}' \approx 0.\end{gathered} \tag{14}$$

Condition (14) is valid in the case of weak scatterers. Indeed, for them, we have $|u_{sc}(\mathbf{r}, \alpha)| \ll |U_0(\mathbf{r}, \alpha)|$ ($\forall\mathbf{r} \in \mathfrak{R}$, $\forall\alpha$), and, therefore, $\left|\tilde{I}_{sc}(\vec{\boldsymbol{\xi}}, \alpha)\right| \ll \left|\tilde{I}(\vec{\boldsymbol{\xi}}, \alpha)\right|$ $\forall\vec{\boldsymbol{\xi}}$. In this case, $\tilde{I} \approx \tilde{I}_{born} = \hat{\tilde{\varepsilon}}\tilde{U}_0$, $\tilde{I}_{sc} \approx \hat{\tilde{\varepsilon}}\hat{\tilde{G}}\tilde{I}_{born} = \hat{\tilde{\varepsilon}}\hat{\tilde{G}}\hat{\tilde{\varepsilon}}\tilde{U}_0$ (in the operator form), and $\langle\tilde{I}\tilde{I}^*_{sc}\rangle_{\varepsilon} \approx 0$ as a third order moment with respect to $\hat{\tilde{\varepsilon}}$. For an ensemble of stronger scatterers, condition (14) is admittedly not valid at high spatial frequencies $\vec{\boldsymbol{\xi}}$, at which the components are almost absent in the Born spectrum $\tilde{I}_{born}(\vec{\boldsymbol{\xi}}, \alpha)$ but are present in $\tilde{I}(\vec{\boldsymbol{\xi}}, \alpha)$ due to the effects of rescattering. At these frequencies, $\tilde{I}_{sc}(\vec{\boldsymbol{\xi}}, \alpha) \equiv \tilde{I} - \tilde{I}_{born} \approx \tilde{I}(\vec{\boldsymbol{\xi}}, \alpha)$ and $\langle\tilde{I}\tilde{I}^*_{sc}\rangle_{\varepsilon,\alpha} \approx \langle\tilde{I}\tilde{I}^*\rangle_{\varepsilon,\alpha} \neq 0$. In the case of a rigorous consideration, we cannot ignore the term $2\mathrm{Re}\langle\tilde{I}(\vec{\boldsymbol{\xi}}, \alpha)\tilde{I}^*_{sc}(\vec{\boldsymbol{\xi}}, \alpha)\rangle_{\varepsilon,\alpha}$ or any other pairwise correlation of the spatial spectra $\tilde{I}$, $\tilde{I}_{born}$, and $\tilde{I}_{sc}$, because all three spectra are correlated with each other.

Finally, rigorous equation (11) with allowance for Eqs. (12), (14), and (7) is reduced to an approximate equation with respect to $J(|\vec{\boldsymbol{\xi}}|)$:

$$\begin{gathered}J(|\vec{\boldsymbol{\xi}}|) + \frac{1}{(2\pi)^{2p}}\int\varepsilon_0(|\vec{\boldsymbol{\xi}} - \vec{\boldsymbol{\xi}}'|)\left|\tilde{G}(|\vec{\boldsymbol{\xi}}'|, k_0)\right|^2 \\ \times J(|\vec{\boldsymbol{\xi}}'|)d\vec{\boldsymbol{\xi}}' = J_{born}(|\vec{\boldsymbol{\xi}}|),\end{gathered} \tag{15}$$

where

$$J_{\text{born}}(|\vec{\xi}|) \cong \frac{1}{(2\pi)^{2p}}\int \varepsilon_0(|\vec{\xi}-\vec{\xi}'|)W(|\vec{\xi}'|)d\vec{\xi}'; \qquad (16)$$

$W(|\vec{\xi}|) \equiv \langle |\tilde{U}_0(\vec{\xi}, \alpha)|^2 \rangle_\alpha$ is the average spectral energy density of the incident field; and $\varepsilon_0(|\vec{\xi}|) \equiv \varepsilon(|\vec{\xi}|)\Delta_\xi$ is the average spectral energy of a scatterer within the volume Δ_ξ with the center at the point $\vec{\xi}$.

The approximate character of Eq. (15) is reflected in the solution obtained from it. In particular, if the components at some high spatial frequencies $\vec{\xi}$ are absent in $J_{\text{born}}(|\vec{\xi}|)$, the components at the same frequencies $\vec{\xi}$ cannot appear in the estimate $J(|\vec{\xi}|)$ obtained from Eq. (15) (since, according to Eq. (15), $J(|\vec{\xi}|)$ is the difference of $J_{\text{born}}(|\vec{\xi}|)$ and the knowingly positive integral term). This error is a consequence of the aforementioned increasing violation of condition (14) for such $\vec{\xi}$. Nevertheless, the results of the numerical simulation given below demonstrate that, for the range of spatial frequencies that is reflected in $J_{\text{born}}(|\vec{\xi}|)$ at least weakly, Eq. (15) gives estimates that are quite acceptable for the practical purposes indicated above.

A major advantage of Eq. (15) is its linearity with respect to the unknown function $J(|\vec{\xi}|)$. Moreover, due to the omnidirectional irradiation of a scatterer, the functions $\varepsilon(|\vec{\xi}|)$, $J(|\vec{\xi}|)$, and $W(|\vec{\xi}|)$ depend only on $|\vec{\xi}|$. Hence, the integration over the whole $\vec{\xi}$-space in Eq. (15) is rediced to a one-dimensional integral with respect to $d|\vec{\xi}'|$. In this case, the quantities characterizing the average spectral energy density of secondary sources, which, in a two-dimensional case, is contained in a ring with radius $|\vec{\xi}|$ and thickness β and, in a three-dimensional case, in a spherical layer with radius $|\vec{\xi}|$ and thickness β, are informative:

$$\begin{aligned} J'_{\text{born}}(|\vec{\xi}|) &\equiv 2\pi|\vec{\xi}|\beta J_{\text{born}}(|\vec{\xi}|), \\ J'(|\vec{\xi}|) &\equiv 2\pi|\vec{\xi}|\beta J(|\vec{\xi}|), \quad \vec{\xi} \in R^2; \\ J'_{\text{born}}(|\vec{\xi}|) &\equiv 4\pi|\vec{\xi}|^2\beta J_{\text{born}}(|\vec{\xi}|), \\ J'(|\vec{\xi}|) &\equiv 4\pi|\vec{\xi}|^2\beta J(|\vec{\xi}|), \quad \vec{\xi} \in R^3. \end{aligned} \qquad (17)$$

However, in the problem statement under examination, the width of spectrum $J(|\vec{\xi}|)$ can be estimated only in the radial direction $|\vec{\xi}|$. In the angular direction (along a circle or sphere with a fixed radius $|\vec{\xi}|$), averaging over all directions of incident fields occurs. Therefore, a spectrum broadening in the angular direction in the case of one-directional irradiation is the subject of a different problem statement and needs additional consideration.

Setting of the average linear dimension L of the scattering region $\Re$ and the maximal accountable value $|\vec{\xi}| = \xi_{\max}$ can be treated as an *a priori* physical limitation in solving Eq. (15). These parameters determine the steps of discretization of continuous quantities, the number of discrete samples, and the selection of the cutoff radius R_G of the Green function $G(\mathbf{r}, k_0)$ in the coordinate space. The cutoff assumes the utilization of the function $G_{R_G}(\mathbf{r}, k_0) = \{G(\mathbf{r}, k_0)$ at $|\mathbf{r}| < R_G$; 0 at $|\mathbf{r}| \geq R_G\}$ (the coordinate origin is positioned at the center of the region $\Re$). Indeed, since the supports of the functions $\varepsilon(\mathbf{r})$ and $I(\mathbf{r}', \alpha)$ in Eq. (3) are strictly finite and coincide with the scattering region $\Re$, the integrand is nonzero only for $\mathbf{r}, \mathbf{r}' \in \Re$, i.e., when $|\mathbf{r} - \mathbf{r}'| < L$. Therefore, in the case of using the Green function with any cutoff radius $R_G \geq L$, the deterministic equation (3) stays rigorous. However, in contrast to Eq. (3), in the case of transition to $\vec{\xi}$-space and subsequent statistical averaging of quantities, the explicit information on the linear dimension L is lost, because scatterers with different support dimensions L can have equal spectral energy characteristics. Therefore, it is necessary to take into account the dimension L in solving Eq. (15) by assuming $R_G = L$ and calculating from $G_{R_G = L}(\mathbf{r}, k_0)$ the values of $|\tilde{G}_L(|\vec{\xi}'|, k_0)|^2$ that are used as $|\tilde{G}(|\vec{\xi}'|, k_0)|^2$ in Eq. (15). In this case, the maximal admissible step of discretization in $\vec{\xi}$-space must not exceed $2\pi/(2R_G) = \pi/L$. Therefore, in the case of a fixed maximal value $\xi_{\max}$ of the quantities $|\vec{\xi}|$ and $|\vec{\xi}'|$, the dimension of the discrete set of equations to be solved (an analog of Eq. (15)) grows proportionally to the increase in L.

Numerical simulation of Eq. (15) was performed for an ensemble, where each random realization of a scatterer $\varepsilon(\mathbf{r})$ is represented in the form of a manifold of M inhomogeneities of phase velocity, which uniformly fill the region $\Re$ and do not overlap. Each fixed inhomogeneity has a certain sign of velocity contrast and a characteristic spatial dimension $\cong l$, which is the same for all inhomogeneities. In this case, the spatial spectrum of a scatterer has a width $\cong 2\pi/l$ and an amplitude proportional to $\sqrt{M}$. The average linear dimension of the region $\mathfrak{R}$ of spatial localization of a scatterer is $L \cong \sqrt[p]{M}\, l$, where $\sqrt[p]{M}$ is the average number of inhomogeneities along one axis. For different random realizations, inhomogeneities are shifted in their positions with respect to each other by a distance no greater than $\cong l$, and the satisfaction of condition (6) presumes the presence of inhomogeneities with different signs of contrast in the ensemble. This model of an ensemble of scatterers $\{\varepsilon(\mathbf{r})\}$ can be considered as a spatially homogeneous normal random process within the region $\mathfrak{R}$.

The average (effective) volume V_{eff} occupied by a single inhomogeneity and the linear dimension of an inhomogeneity l are estimated as $V_{\text{eff}} \cong \frac{1}{M}\left\langle \left(\int_{\mathfrak{R}} |\varepsilon(\mathbf{r})|^2 d\mathbf{r}\right) \Big/ \left(\frac{1}{2}\max_{\mathbf{r}} |\varepsilon(\mathbf{r})|^2\right)\right\rangle_{\varepsilon}$, $l \cong \sqrt[p]{V_{\text{eff}}}$. The rms value of the scatterer amplitude $\bar{\varepsilon}$ can be determined through the contrast $\Delta c/c_0 \equiv (c - c_0)/c_0$ of an effective scatterer (c_0 is the velocity in the background medium and c is the characteristic velocity within the effective scatterer):

$$\bar{\varepsilon} \cong \sqrt{\langle \max_{\mathbf{r}} |\varepsilon(\mathbf{r})|^2 \rangle_{\varepsilon}} \cong k_0^2 |A_0|,$$

where [5]

$$A_0 \cong 1 - c_0^2/c^2 = (\Delta c/c_0)(2 + \Delta c/c_0)/(1 + \Delta c/c_0)^2.$$

In this case, the average phase shift at a scatterer is

$$\sigma_{\text{phase}} \cong 2\sqrt[p]{M}\, l k_0 |1 - c_0/c| \\ = 2\sqrt[p]{M}\, l k_0 (|\Delta c|/c_0)/|1 + \Delta c/c_0|.$$

It is necessary to note that the possible range of values of A_0 has asymmetric limits: $A_0 \in (-\infty, 1]$. For example, $A_0 \longrightarrow -\infty$ at $c \longrightarrow 0$ (i.e., $\Delta c/c_0 \longrightarrow -1$), $A_0 \longrightarrow 1$ at $c \longrightarrow \infty$ (i.e., $\Delta c/c_0 \longrightarrow \infty$), and $A_0 = -1$ at $\Delta c/c_0 \approx -0.2929$. Therefore, we can consider condition (6), from which Eq. (15) was derived, as satisfied in the following cases. If the effective contrast $\Delta c/c_0$ is such that $A_0 \in [-1; 1]$, condition (6) can be satisfied in the case of equality of the average number of inhomogeneities with a fixed sign of their contrast and an average number of inhomogeneities with another sign of contrast. If $A_0 \in (-\infty; 1]$, condition (6) can be valid only on account of the dominance of the average number of inhomogeneities with positive contrast over the average number of inhomogeneities with negative contrast.

In practice, the average spectral energy density $\boldsymbol{\varepsilon}(|\vec{\boldsymbol{\xi}}|)$ can be obtained from experiment. The characteristic width of this function is close to the value $\cong 2\pi/l$, and the amplitude is proportional to $M\bar{\varepsilon}^2$. The quantity $\boldsymbol{\varepsilon}_0 \equiv \boldsymbol{\varepsilon}\Delta_{\xi}$ in Eq. (15) does not depend on M, since $\boldsymbol{\varepsilon} \sim M$ but $\Delta_{\xi} \approx (2\pi/L)^p \sim 1/M$. Therefore, in the numerical simulation, it was estimated as the spectral energy of an effective scatterer in the form of a single inhomogeneity $\varepsilon_1^{\text{eff}}(\mathbf{r}) = \bar{\varepsilon}\exp(-\mathbf{r}^2/D^2)$. In this case, by virtue of average statistical spatial homogeneity of the medium at the distances of the order of magnitude of l, we have $\boldsymbol{\varepsilon}_0(|\vec{\boldsymbol{\xi}}|) \cong (2\pi)^p \left|\tilde{\varepsilon}_1^{\text{eff}}(\vec{\boldsymbol{\xi}})\right|^2 / V_{\text{eff}}$.

In the case of a two-dimensional space ($p = 2$), for which the results of numerical simulation are given below, we have

$$V_{\text{eff}} \cong \pi D^2, \quad l \cong \sqrt{\pi} D,$$

$$\boldsymbol{\varepsilon}_0 |\vec{\boldsymbol{\xi}}| \cong E_0 \exp(-\vec{\boldsymbol{\xi}}^2 D^2/2), \text{ where } E_0 = (2\pi)^2 \bar{\varepsilon}^2 \pi D^2.$$

Equation (15) takes on the form

$$\begin{aligned} &J(|\vec{\boldsymbol{\xi}}|) + \frac{E_0}{(2\pi)^3} \int |\vec{\boldsymbol{\xi}}'| \cdot \exp\left[-\frac{1}{2}(|\vec{\boldsymbol{\xi}}|^2 + |\vec{\boldsymbol{\xi}}'|^2) D^2\right] \\ &\times I_0(|\vec{\boldsymbol{\xi}}| \cdot |\vec{\boldsymbol{\xi}}'| \cdot D^2) \cdot |\tilde{G}(|\vec{\boldsymbol{\xi}}'|, k_0)|^2 J(|\vec{\boldsymbol{\xi}}'|) d|\vec{\boldsymbol{\xi}}'| \\ &= \frac{E_0}{(2\pi)^3} \int |\vec{\boldsymbol{\xi}}'| \cdot \exp\left[-\frac{1}{2}(|\vec{\boldsymbol{\xi}}|^2 + |\vec{\boldsymbol{\xi}}'|^2) D^2\right] \\ &\times I_0(|\vec{\boldsymbol{\xi}}| \cdot |\vec{\boldsymbol{\xi}}'| \cdot D^2) W(|\vec{\boldsymbol{\xi}}'|) d|\vec{\boldsymbol{\xi}}'|, \end{aligned} \tag{18}$$

where I_0 is the Infeld function of the zero order.

Initially, Eq. (15) in the form of Eq. (18) was investigated for eigenvectors and eigenvalues. In this case, we assume that, on the right-hand side of Eq. (15), we have

$$J_{\text{born}}(|\vec{\boldsymbol{\xi}}|) \approx \nu J(|\vec{\boldsymbol{\xi}}|), \tag{19}$$

and Eq. (15) transforms to the equation

$$\begin{aligned} &J(|\vec{\boldsymbol{\xi}}|) + \frac{1}{(2\pi)^{2p}} \int \boldsymbol{\varepsilon}_0(|\vec{\boldsymbol{\xi}} - \vec{\boldsymbol{\xi}}'|) \cdot |\tilde{G}(|\vec{\boldsymbol{\xi}}'|, k_0)|^2 \\ &\times J(|\vec{\boldsymbol{\xi}}'|) d\vec{\boldsymbol{\xi}}' = \nu J(|\vec{\boldsymbol{\xi}}|), \end{aligned} \tag{20}$$

or, in the operator form, $(\hat{E} + \hat{\boldsymbol{\varepsilon}}_0 \hat{\tilde{G}} \hat{\tilde{G}}^{+}) J = \nu J$, where $\hat{E}$ is a unit matrix and $\hat{\tilde{G}}^{+}$ is the Hermitian conjugate operator. The physical meaning of the substitution of Eq. (19) is as follows. It is assumed that a scatterer is irradiated from all directions by various incoherent monochromatic incident fields, including inhomogeneous ones. This is a limiting case corresponding to the statistically maximum possible broadening of the spatial spectrum of secondary sources in comparison with the spectrum of the scatterer. In this case, it is appropriate to consider stationary spatial energy spectra, when the average energy spectra of secondary sources and irradiation fields are self-consistent. Namely, the problem is reduced to searching for configurations of secondary sources that have self-sustained spatial energy spectra, i.e., that do not change their shapes and widths "sustaining" (repeating) themselves at each new act of rescattering.

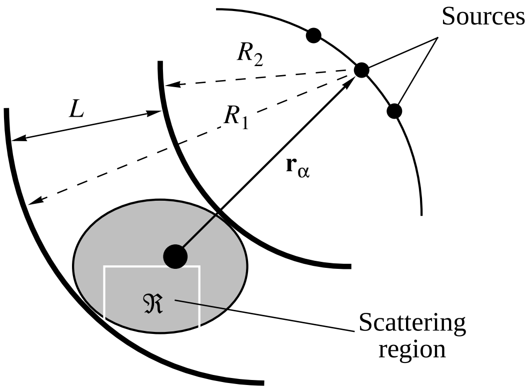

Fig. 1. Geometry of the scatterer irradiation.

Only the limitations $\nu > 0$ and $J(|\vec{\xi}|) \geq 0\ \forall\vec{\xi}$ are imposed on the solution to Eq. (20) by virtue of the physical meaning of the quantity $J(|\vec{\xi}|)$. Numerical simulation of Eq. (20) demonstrated that all its eigenvalues ν are positive and all eigenvectors $J(|\vec{\xi}|)$ are real quantities. However, the solution turned out to be very unstable with respect to insignificant changes in the preset parameters of the problem (L, $\xi_{\max}$, and the discretization step in the $\vec{\xi}$-space). The instability is connected with the structure of the matrix $\hat{E} + \hat{\varepsilon}_0\hat{\tilde{G}}\hat{\tilde{G}}^+$ at the unknowns J in Eq. (20). The matrix basis is the unit matrix $\hat{E}$, for which all vectors are eigenvectors. Therefore, the degeneracy is eliminated only on account of the operator additive $\hat{\varepsilon}_0\hat{\tilde{G}}\hat{\tilde{G}}^+$. The maximum value of the additive can be different depending on the effective contrast in the ensemble of scatterers under consideration. However, since $\hat{\varepsilon}_0\hat{\tilde{G}}\hat{\tilde{G}}^+$ has a structure close to the structure of a diagonal matrix, with the diagonal values decreasing considerably at the diagonal "edges," the conditionality of the matrix $\hat{\varepsilon}_0\hat{\tilde{G}}\hat{\tilde{G}}^+$ is poor.

In connection with instability of the problem with respect to eigenvectors, further investigation of the solution to Eq. (15) in the form of Eq. (18) was connected with presetting a specific model for the average spectral energy density $W(|\vec{\xi}|)$ of the incident field, the calculation of $J_{\text{born}}(|\vec{\xi}|)$ from Eq. (16), and a further estimation of the spectrum width for the given model. In the case of a fixed width of the function $\tilde{\varepsilon}(\vec{\xi})$, the width and shape of the spatial spectrum $\tilde{I}_{\text{born}}(\vec{\xi}, \alpha)$ depend on the form of $U_0(\mathbf{r}, \alpha)$, and, therefore, $\tilde{J}_{\text{born}}$ depends on the type of incident fields. On the other hand, it is necessary to estimate the increase (due to the effect of rescattering) in the number of the degrees of freedom of secondary sources in comparison with the number of degrees of freedom of a scatterer. Therefore, it is convenient for comparison to form, additionally, the Born's secondary sources in such a way that the role of the degrees of freedom of the field U_0 be reduced to its minimum. The model $W(|\vec{\xi}|) = W^0(|\vec{\xi}|)$ corresponding to cylindrically isotropic noise incident omnidirectionally upon a scatterer meets this requirement:

$$W^0(|\vec{\xi}|)(d\vec{\xi}) \cong M\delta(|\vec{\xi}| - k_0)(d\vec{\xi}), \tag{21}$$

for which $J_{\text{born}}(|\vec{\xi}|) = J^0_{\text{born}}(|\vec{\xi}|)$ is determined from Eq. (16) and $J'^0_{\text{born}}(|\vec{\xi}|) \equiv 2\pi|\vec{\xi}|\beta J^0_{\text{born}}(|\vec{\xi}|)$ is calculated at $p = 2$ according to Eq. (17). The function $J'^0_{\text{born}}(|\vec{\xi}|)$ has approximately the same half-width as the function $2\pi|\vec{\xi}|\beta\varepsilon(|\vec{\xi}|)$, since the number of degrees of freedom describing each of these functions are equal. In this case, it is possible to judge on the increase of the number of degrees of freedom of secondary sources in the radial direction by comparing the widths of the functions $J'(|\vec{\xi}|)$ and $J'^0_{\text{born}}(|\vec{\xi}|)$. It is necessary to point out that J' is obtained from Eq. (15) for its model $W(|\vec{\xi}|)$ other than $W^0(|\vec{\xi}|)$ with the corresponding $J_{\text{born}}(|\vec{\xi}|)$. The use of W^0 in solving Eq. (15) leads (if the processes of rescattering are not negligible) to a nonphysical solution oscillating near zero. This result can be explained by the fact that the integral term responsible for taking into account the rescattering processes on the left-hand side of Eq. (15) contains the function $|\tilde{G}(|\vec{\xi}|, k_0)|^2 = |\tilde{G}_L(|\vec{\xi}|, k_0)|^2$, where the cutoff radius $R_G = L$ of the Green function in the coordinate space is taken into account. The model W^0 does not take into account the finite dimension L of the scattering region, and, therefore, it serves only to form J'^0_{born} for further comparison but cannot be used directly to solve Eq. (15).

The indicated inconsistency of model (21) is eliminated by matching the right-hand and left-hand sides of Eq. (15) through taking into account the finite dimension L in them. A model of a real tomographic experiment, where point sources of the incident field are located at the points $\{\mathbf{r}_\alpha\}$, corresponds to the purpose of matching. In this case, the size L is taken into account by the fact that a ring with thickness L, which contains the scattering region $\mathfrak{R}$, is cut out for each $U_0(\mathbf{r}, \alpha)$. The ring center is located at the point $\mathbf{r}_\alpha$ and its external and internal radii are equal to R_1 and R_2, and $R_1 - R_2 = L$ (Fig. 1). Since U_0 is scattered only within $\mathfrak{R}$, $U_0(\mathbf{r}, \alpha)$

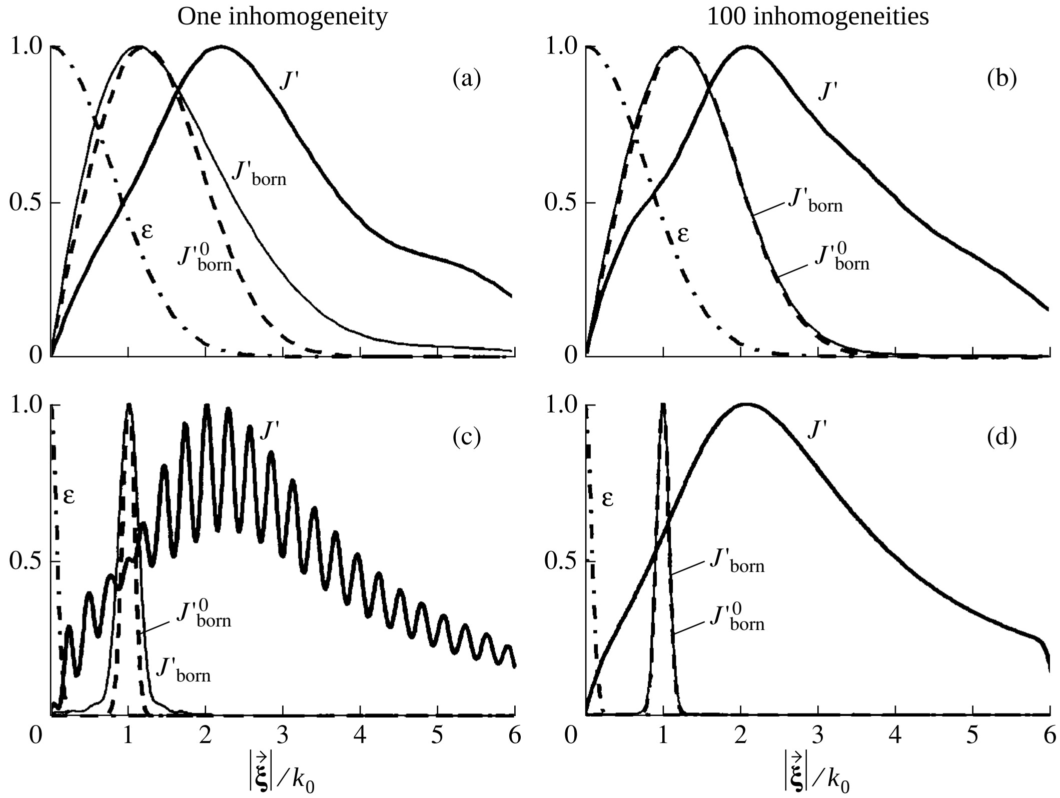

Fig. 2. Average spatial energy spectrum of secondary sources: $J'^{0}_{\text{born}}(|\vec{\xi}|)$ and $J'_{\text{born}}(|\vec{\xi}|)$ correspond to the single scattering approximation without and with allowance for the finite spatial dimensions of the scattering region; $J'(|\vec{\xi}|)$ is the estimate with allowance for rescattering. The average spatial energy spectrum of an ensemble of scatterers $\varepsilon(|\vec{\xi}|)$ is preset for the effective contrast $\Delta c/c_0 = -0.6$ and the characteristic spatial half-width of the scattering inhomogeneities D/λ_0 = (a, b) 0.2 and (c, d) 2. The scatterer consists of (a, c) a single inhomogeneity and (b, d) a manifold of 100 inhomogeneities.

is assumed to be different from zero only within the ring and is formed as the difference of the Green functions with cutoff radii R_1 and R_2, respectively:

$$U_0(\mathbf{r}, \alpha) \sim G_{R_1}(\mathbf{r}-\mathbf{r}_\alpha, k_0) - G_{R_2}(\mathbf{r}-\mathbf{r}_\alpha, k_0);$$
$$W(|\vec{\xi}|) \cong \sqrt[p]{M}\left|\tilde{G}_{R_1}(|\vec{\xi}|, k_0) - \tilde{G}_{R_2}(|\vec{\xi}|, k_0)\right|^2. \qquad (22)$$

The factor $\sqrt[p]{M}$ is introduced to take into account the finite linear size L (proportional to $\sqrt[p]{M}$) of the region $\mathfrak{R}$ in the direction perpendicular to the direction toward the incident field source (i.e., perpendicular to $\mathbf{r}_\alpha$). The finiteness of the size L of the region $\mathfrak{R}$ in the direction $\mathbf{r}_\alpha$ is already taken into account by the introduction of the cutoff radii R_1 and R_2.

A numerical simulation of Eq. (15) demonstrated that the choice of various values of $\{R_1, R_2\}$ at fixed $R_1 - R_2 = L$ almost does not influence the solution. Various cases were examined, starting from the case of positioning the sources of the incident field near the surface of the region $\mathfrak{R}$ to the case of the local plane wave approximation, when the deviation of the wave front from a plane within region $\mathfrak{R}$ can be ignored. Moreover, the function $W(|\vec{\xi}|)$ of the form of Eq. (22) was averaged at a fixed L over different pairs $\{R_1, R_2\}$. Finally, even a "nonphysical" setting of the experiment, i.e., the consideration of all possible positions of point sources of primary fields with a random phase within the region $\mathfrak{R}$, little affected the result. Thus, the model under consideration is valid for a rather arbitrary (but omnidirectional) positioning of the sources of the incident field with respect to the scattering region. Therefore, we assume further that $R_1 = L + 6\lambda_0$, $R_2 = R_1 - L = 6\lambda_0$, and $|\mathbf{r}_\alpha| = R_0 = L/2 + 6\lambda_0\ \forall\alpha$ (Fig. 1). Figures 2a–2d present the normalized (to their maximum values) functions ε, J'^{0}_{born}, and J'_{born} and the solution J' ($\xi_{\max} = 6k_0$) for various ensembles of scatterers, which have the same effective contrasts $\Delta c/c_0 = -0.6$. The normalized function J'^{0}_{born} is close to the normalized function ε shifted from the center $|\vec{\xi}| = 0$ to the distance $|\vec{\xi}| = k_0$. Figure 2a corresponds to an ensemble of scatterers, where each scatterer is represented by a single small-scale inhomogeneity with the characteristic spatial half-width D: $D/\lambda_0 = 0.2$, $M = 1$, $L = l = \sqrt{\pi}D$, and $\sigma_{\text{phase}} \approx 1.2\pi$. As compared to J'_{born}, a shift of the maximum of the function J' towards greater $|\vec{\xi}|$ is observed, evidence of a considerable effect of rescattering. Figure 2b corresponds to an ensemble of scatterers, where each scatterer is represented in the form of $M = 100$ small-scale inhomogeneities (on the average, ten inhomogeneities along each direction): $D/\lambda_0 = 0.2$; $L = 10l$, and $\sigma_{\text{phase}} \approx 3.8\pi$, which is $\approx\sqrt{10}$ times greater than for a single inhomogeneity. Here, J'_{born} and J'^{0}_{born} almost coincide, since the size $L \approx 3.5\lambda_0$ is sufficiently large.

Figures 2c and 2d are analogous to Fig. 2a and 2b, but the inhomogeneities are large-scale, i.e., $D/\lambda_0 = 2$. Figure 2c corresponds to $M = 1$, $L = l$, and $\sigma_{\text{phase}} \approx 12\pi$ (oscillations of the function $J'(|\vec{\xi}|)$ not affecting the estimate of its width are connected with the sharp cutoff of the Green function at the given specific parameters). Figure 2d corresponds to $M = 100$, $L = 10l$, and $\sigma_{\text{phase}} \approx 38\pi$. It is necessary to note that the widths of the functions J' in Figs. 2a and 2c are almost equal, although the mechanisms of the broadening of the spatial spectra are different. For example, small-scale inhomogeneities have a wide spatial spectrum of secondary sources already in the Born approximation, while the number of rescattering events is small. On the contrary, large-scale inhomogeneities have a narrow spatial spectrum, and the strong broadening of the spectrum of secondary sources in comparison with the Born approximation is caused by a great number of rescattering events.

3. ESTIMATION BY WEIGHTED SUMMATION OF DETERMINISTIC SOLUTIONS

In connection with the approximate character of Eq. (15), the estimates obtained by the described statistical method were compared with the result of weighted summation of deterministic solutions to the direct problem. In particular, a model sample of 14 scatterers, which approximately simulated the ensemble statistics, was considered. The scatterers were grouped into seven pairs for convenience. Each scatterer was preset in the form of a single inhomogeneity of Gaussian shape with the half-width $D/\lambda_0 \approx 0.82$ at the level of $1/e$. The amplitude of the function $\varepsilon(\mathbf{r})$ for one inhomogeneity in each pair of scatterers is equal to $k_0^2 A_0$ and corresponds to the contrast $\Delta c/c_0$ of a certain sign. For another inhomogeneity, the amplitude is equal to $-k_0^2 A_0$ and corresponds to the contrast of the opposite sign. For each fixed $\varepsilon(\mathbf{r})$, the direct problem is solved rigorously: the spatial spectrum of secondary sources $\tilde{I}(\vec{\xi}, \alpha)$ is determined from Eq. (4). The simplest iteration technique used for solving Eq. (4) imposes certain restrictions upon the limiting contrast, since it is convergent (at the indicated D/λ_0) only in the case $\Delta c/c_0 \geq -0.28$. Therefore, it was assumed that the contrast of the first pair was $\Delta c/c_0 = -0.28$ and 2.75, which leads to the amplitudes $\mp k_0^2|A_0|$, where $k_0^2|A_0|/\bar{\varepsilon} = 2$. The contrast of each next pair corresponds to a decrease in $|A_0|$ by a factor of $\sqrt{2}$. The quantity $\bar{\varepsilon}$ is the rms amplitude of scatterers of a given model sample, which is set by the effective contrast $\Delta c/c_0 = -0.174$.

The averaging of $|\tilde{I}(\vec{\xi}, \alpha)|^2$ over α (i.e., over the directions φ_0 of the wave vector $\mathbf{k}_0 = \{k_0, \varphi_0\}$ of the incident plane wave U_0) for the sake of estimation was replaced by equivalent averaging over the directions φ_ξ of the vector $\vec{\xi} = \{|\vec{\xi}|, \varphi_\xi\}$ at a fixed $\varphi_0 = 0$. The curves $I'(|\vec{\xi}|) \equiv \left\langle \left|\tilde{I}(\vec{\xi}, \varphi_0 = 0)\right|^2 \right\rangle_{\varphi_\xi} 2\pi|\vec{\xi}| \cdot (d|\vec{\xi}|)$ analogous to relation (17) are given in Fig. 3a for each inhomogeneity (in the numerical simulation, the unit length was taken to be $\lambda_0/8 = 1$; a discrete analog of the quantity $d|\vec{\xi}|$ was $k_0/8$). Curves *3* in Fig. 3a, which correspond to a pair of inhomogeneities with amplitudes $\mp k_0^2 A_0 = \mp(\bar{\varepsilon})$, are shown by thick lines. Inhomogeneities with $\Delta c/c_0 > 0$ are "defocusing." The localization region of the spatial spectrum of their secondary sources is shifted (with respect to the value $|\vec{\xi}| = k_0$) towards low $|\vec{\xi}|$ (the dashed lines in Fig. 3a), since the local value of the wave number in an inhomogeneity is smaller than k_0. For "focusing" inhomogeneities ($\Delta c/c_0 < 0$), the shift occurs towards higher $|\vec{\xi}|$ (the solid lines in Fig. 3a).

Finally, the functions $I'(|\vec{\xi}|)$ are averaged (i.e., summed with weight) over the scatterers by taking into account the normal probability density of the scatterer distribution in A_0. Figure 3b presents the normalized result of weighted summation of the curves $I'(|\vec{\xi}|)$ in Fig. 3a, which is an analog of the quantity $J'(|\vec{\xi}|)$ (the solid line). In the single scattering approximation, this result is an analog of the quantity $J'^{0}_{\text{born}}(|\vec{\xi}|)$ (the dashed line). Figure 3c gives, for comparison, the estimates obtained from the solution of the statistical problem for an ensemble of scatterers with the same values of $\bar{\varepsilon}$ and D/λ_0 as in the model sample. The curves J' and J'^{0}_{born} in Figs. 3b and 3c are close in their shape and width. In both cases, the shift of the maximum of the function J' towards greater $|\vec{\xi}|$ is observed. The widths $2\chi_J$ and

$2\chi^0_{\rm born}$ of the normalized functions J' and $J'^0_{\rm born}$ (respectively) in both cases are $2\chi_J \approx 0.8k_0$ and $2\chi^0_{\rm born} \approx 0.45k_0$ at the level of 0.5 and $2\chi_J \approx 1.2k_0$ and $2\chi^0_{\rm born} \approx 0.7k_0$ at the level of 0.2. Thus, we obtained a good agreement of the average deterministic and statistical solutions. A difference is observed only for the maximum values of the functions $J'^0_{\rm born}$ and J': it is equal to ≈1.4 in the average deterministic case and ≈2.7 in the statistical case. This difference can be explained by both the approximate character of Eq. (15) and the absence of very strong scatterers in the model sample.

Thus, as the results of numerical simulation demonstrated, the elimination of the term $2{\rm Re}\langle \tilde{I}\tilde{I}^*_{\rm sc}\rangle_{\varepsilon,\alpha}$ from Eq. (11) manifests itself first of all by a slightly reduced value of the amplitude of the resulting estimate J'. However, the most interesting applied characteristic, i.e., the width of the function J' is estimated to a precision quite acceptable for applications. This conclusion is true at least for an ensemble of medium-strength scatterers. More rigorous estimates of J' can be obtained only taking into account (to a certain precision) the term $2{\rm Re}\langle \tilde{I}\tilde{I}^*_{\rm sc}\rangle_{\varepsilon,\alpha}$. The results of the attempts to estimate the effect of this term are as follows. An iteration refinement of the quantity $\langle \tilde{I}\tilde{I}^*_{\rm sc}\rangle_{\varepsilon,\alpha}$ expressed through $\langle \tilde{I}\tilde{I}^*\tilde{\varepsilon}^*\rangle_{\varepsilon,\alpha}$ (see Eq. (14)) on the basis of the approximate value $J \equiv \langle |\tilde{I}|^2\rangle_{\varepsilon,\alpha}$ is impossible, since $\langle \tilde{I}\tilde{I}^*\tilde{\varepsilon}^*\rangle_{\varepsilon,\alpha}$ is not expressed directly through J. Therefore, in the first method of estimation, the functions $\tilde{I}$ and $\tilde{I}_{\rm sc}$ were expanded on the basis of Eq. (4) into the Born–Neumann series in powers of the function $\tilde{\varepsilon}$. In this case, the correlation $\langle \tilde{I}\tilde{I}^*_{\rm sc}\rangle_{\varepsilon,\alpha}$ also acquires the form of a series, which, in the case of real scatterers, is expressed only through known energy characteristics ε_0 and $J_{\rm born}$. This series converges for the ensembles of medium-strength scatterers, which allows one to estimate $\langle \tilde{I}\tilde{I}^*_{\rm sc}\rangle_{\varepsilon,\alpha}$ in this case. However, the convergence in the case of ensembles where strong scatterers play a considerable role is not evident and needs a separate study by numerical simulation. It is impossible to determine an analytical expression for the sum of this series and obtain in this way a uniform expression eliminating the problem of convergence.

The second method studied was based on using Eq. (9) for constructing (by multiplication of Eq. (9) by corresponding functions) all possible equations with respect to seven independent functional unknowns: $\langle |\tilde{I}|^2\rangle_{\varepsilon,\alpha}$, $\langle \tilde{I}\tilde{I}^*_{\rm born}\rangle_{\varepsilon,\alpha}$, $\langle \tilde{I}^*\tilde{I}_{\rm born}\rangle_{\varepsilon,\alpha}$, $\langle \tilde{I}\tilde{I}^*_{\rm sc}\rangle_{\varepsilon,\alpha}$, $\langle \tilde{I}^*\tilde{I}_{\rm sc}\rangle_{\varepsilon,\alpha}$, $\langle \tilde{I}_{\rm born}\tilde{I}^*_{\rm sc}\rangle_{\varepsilon,\alpha}$, and $\langle \tilde{I}^*_{\rm born}\tilde{I}_{\rm sc}\rangle_{\varepsilon,\alpha}$, which are the second-order correlation moments of the quantities

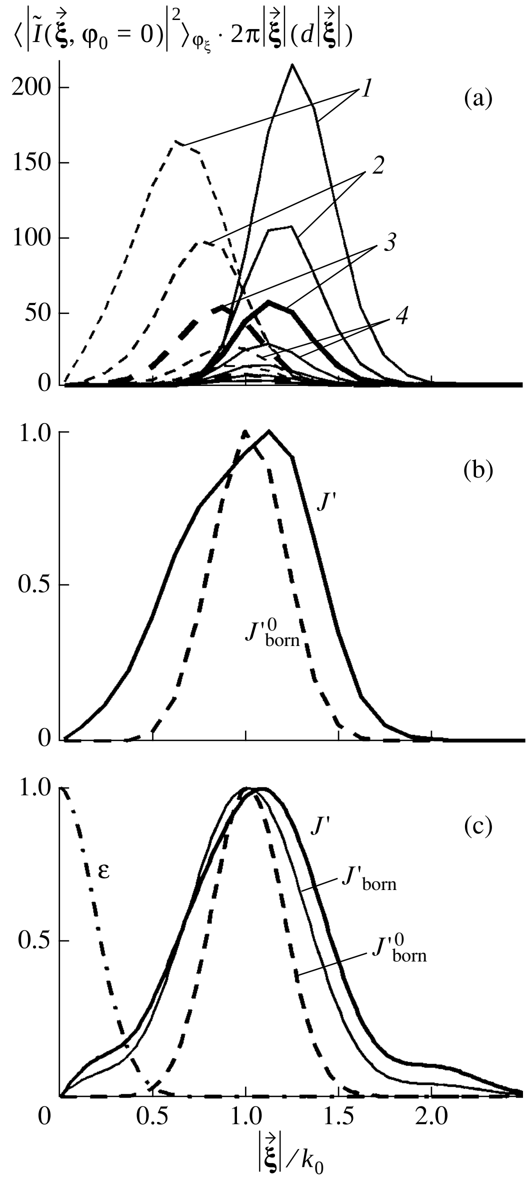

Fig. 3. Comparison of the statistical estimate of the spatial energy spectrum of secondary sources with the result of a weighted summation of deterministic solutions: (a) spectra of secondary sources that are averaged over the incident field directions for seven pairs of inhomogeneities (their half-width is $D/\lambda_0 \approx 0.82$) with positive (the dashed line) and negative (the solid line) sound velocity contrasts. The pair of curves *1* corresponds to inhomogeneities of equal strength with contrasts $\Delta c/c_0 = 2.75$ and –0.28. Each subsequent pair of curves corresponds to a decrease in the inhomogeneity amplitude by a factor of $\sqrt{2}$. (b) The result of weighted summation of the curves shown in Fig. 3a (solid line) in comparison with the result obtained in the single scattering approximation (dashed line). (c) The statistical estimate of the spatial spectrum of secondary sources for an ensemble of scatterers with the effective strength corresponding to the summation of deterministic solutions that is given in Fig. 3b. Notations are the same as in Fig. 2.

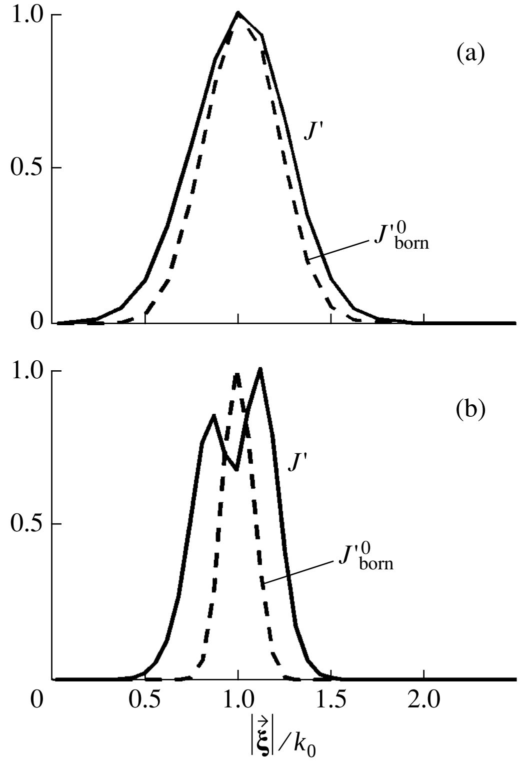

Fig. 4. Result of weighted summation of the spatial energy spectra of secondary sources that was obtained analogously to the result shown in Fig. 3b. The sets of inhomogeneities producing the spectra differ in their spatial half-width $D/\lambda_0 \approx$ (a) 0.82 and (b) 2 while the contrasts are equal. The width of the curves J' is seen to be almost the same in both cases.

$\tilde{I}$, $\tilde{I}_{\text{born}}$, and $\tilde{I}_{\text{sc}}$. The quantity $\langle|\tilde{I}_{\text{sc}}|^2\rangle_{\varepsilon,\alpha} \cong \hat{\varepsilon}_0\hat{G}\hat{G}^+\langle|\tilde{I}|^2\rangle_{\varepsilon,\alpha}$ is expressed according to Eqs. (12) and (7) through $\langle|\tilde{I}|^2\rangle_{\varepsilon,\alpha}$, and, therefore, is not treated as a separate unknown. The known quantities are $\langle|\tilde{I}_{\text{born}}|^2\rangle_{\varepsilon,\alpha}$ and ε_0. Finally, a linear system of 23 integral equations with respect to the desired second-order moments is obtained. However, its rank is equal to five, i.e., it is smaller than the number of unknowns. Five independent equations are obtained, for example, by sequential multiplication of the left-hand side of the equation $\tilde{I}(\vec{\xi}, \alpha) - \tilde{I}_{\text{born}}(\vec{\xi}, \alpha) - \tilde{I}_{\text{sc}}(\vec{\xi}, \alpha) = 0$ by $(\tilde{I} - \tilde{I}_{\text{born}} - \tilde{I}_{\text{sc}})^*$, $\tilde{I}^*$, and $\tilde{I}^*_{\text{born}}$ and also by the complex conjugation of the last two equations. Since the system of five independent equations is linear, it can be resolved analytically with respect to the real quantity $\langle|\tilde{I}|^2\rangle_{\varepsilon,\alpha}$ (the parameter most important for practical purposes). The result coincides with the rigorous Eq. (11). Since Eq. (11) is a single integral equation with two functional unknowns $\langle|\tilde{I}|^2\rangle_{\varepsilon,\alpha}$ $\text{Re}\langle\tilde{I}\tilde{I}^*_{\text{sc}}\rangle_{\varepsilon,\alpha}$, the last of which can be of alternating sign, it is possible to speak only about a solution with the minimal norm. This solution already obeys the numerically simulated Eq. (15) with the right-hand side J_{born} replaced by $J_{\text{born}}/2$, which does not affect the estimate of the shape and width of the function $J \equiv \langle|\tilde{I}|^2\rangle_{\varepsilon,\alpha}$.

Thus, the question on the method of estimating the term $2\text{Re}\langle\tilde{I}\tilde{I}^*_{\text{sc}}\rangle_{\varepsilon,\alpha}$ and its influence proves to be nontrivial and has no answer now.

4. DETERMINING EFFECT OF THE VELOCITY CONTRAST ON THE WIDTH OF SPATIAL SPECTRUM OF SECONDARY SOURCES

The widths of the functions J' given in Figs. 2a–2d for various ensembles with the same value of $\Delta c/c_0$ are almost equal. In this connection, we analyzed the dependence of this width on the effective contrast in an ensemble of scatterers $\Delta c/c_0$ on the characteristic wave dimension l/λ_0 of a single inhomogeneity and on the number of inhomogeneities M. It is evident that, for weak scatterers, the width of the function $J' = J'_{\text{born}}$ is inversely proportional to l/λ_0 (see J'_{born} in Figs. 2a, 2c). If the rescattering from a single inhomogeneity is strong (estimates showed that the average additional phase shift of a wave at a single inhomogeneity must exceed $\approx(\pi–2\pi)$), the width of spectrum J' is determined mainly by the value of $\Delta c/c_0$.

To confirm this dependence, we compared the results of weighted summation of deterministic solutions for two model samples of scatterers. These samples, analogous to the ones described above, differ in the characteristic widths of inhomogeneities ($D/\lambda_0 \approx$ 0.82 for the first sample and $D/\lambda_0 = 2$ for the second one) at equal effective contrast values $\Delta c/c_0 \approx -0.12$ corresponding to $k_0^2|A_0| = \bar{\varepsilon}$. The contrasts of separate inhomogeneities (equal for both samples) were preset in the way described above. The result of weighted summation of deterministic solutions is given in Figs. 4a and 4b. The dip in the central part of $J'(|\vec{\xi}|)$ in Fig. 4b can be explained by the insufficient number of inhomogeneities with the amplitudes about the value $k_0^2|A_0| = \bar{\varepsilon}$ in the sample. The widths of the normalized functions $J'(|\vec{\xi}|)$ in both figures are close in their values: $2\chi_J \approx 0.6k_0$ at the level of 0.5 for $D/\lambda_0 \approx 0.82$ and $2\chi_J \approx 0.5k_0$ for $D/\lambda_0 = 2$. At the same time, the widths of the corresponding Born spectra J'^{0}_{born} inversely proportional to the wave dimension D/λ_0 differ by a factor of more than two: $2\chi^0_{\text{born}} \approx 0.48k_0$ for $D/\lambda_0 \approx 0.82$ and $2\chi^0_{\text{born}} \approx 0.2k_0$ for $D/\lambda_0 = 2$.

This conclusion is valid only in the case of the simultaneous satisfaction of the following conditions for an ensemble of nonabsorbing scatterers with a zero average value of $\varepsilon(\mathbf{r})$. First, as it was already mentioned, the rescattering must be sufficiently strong. Second, the effect considered is attained due to the averaging of energy spectra of secondary sources over all directions of irradiation and inhomogeneities with contrasts of opposite signs. Third, we considered a model of an ensemble of scatterers with equal dimensions l of spatial fluctuations. In these conditions, the independence of the width of the function J' of l/λ_0 can be explained as follows. The maximum of the spatial spectrum of secondary sources for a single strong inhomogeneity with a certain sign of contrast is shifted relative to the value $|\vec{\xi}| = k_0$. The shift direction depends on the contrast sign, and the shift value is determined primarily by the local value of the wave number and almost does not depend on l. In this case, the spectra of secondary sources of two inhomogeneities with opposite signs of contrast are shifted in different directions (Fig. 3a). Therefore, if strong inhomogeneities with the shift of the spectrum of their secondary sources greater than the width of the spectrum itself, which depends on l, play an essential role in an ensemble of scatterers, the dimension l does not influence considerably the total width of the spectrum of secondary sources J', and this width depends mainly on the effective contrast in the ensemble $\Delta c/c_0$.

The fact that the width of the normalized function J' does not depend on the average number of inhomogeneities M also has a physical explanation. For each fixed scatterer, the low-frequency components of the spatial spectrum of its secondary sources that correspond to $|\vec{\xi}| < k_0$ do not radiate at all. The spectral components corresponding to $|\vec{\xi}| = k_0$ and $|\vec{\xi}| > k_0$ (but near k_0) form plane waves, which differ little from the plane waves with a random phase that are incident upon a scatterer. The radiation at these spatial frequencies determines the amplitude of J', which grows with increasing M. The high-frequency components at $|\vec{\xi}| \gg k_0$ produce rapidly decaying inhomogeneous waves, which do not take part in rescattering. In this case, the parts of region $\mathfrak{R}$ that are close in their size form secondary sources almost independently. Therefore, as the number M of the inhomogeneities of the same type, which constitute the scatterer, grows, the total power of secondary sources increases but the shape and width of their spatial energy spectrum J' almost does not change at $L > (2–3)\lambda_0$.

ACKNOWLEDGMENTS

This work was supported by the Russian Foundation for Basic Research, project no. 01-02-16282, and the RF Presidential grant for Scientific Schools no. 1575.003.2.

REFERENCES

1. V. A. Burov and O. D. Rumyantseva, Akust. Zh. **49**, 590 (2003) [Acoust. Phys. **49**, 496 (2003)].
2. V. A. Burov and O. D. Rumiantseva, Acoust. Imaging **22**, 107 (1996).
3. V. A. Burov and O. D. Rumyantseva, Akust. Zh. **39**, 793 (1993) [Acoust. Phys. **39**, 419 (1993)].
4. I. Johansen, L.-J. Gelius, B. Spjelkavik, *et al.*, Acoust. Imaging **19**, 17 (1992).
5. A. A. Goryunov and A. V. Saskovets, *Inverse Scattering Problems in Acoustics* (Mosk. Gos. Univ., Moscow, 1989), p. 152.
6. V. A. Burov, S. A. Morozov, O. D. Rumiantseva, *et al.*, Acoust. Imaging **24**, 73 (2000).

Translated by M. Lyamshev

Acoustical Physics, Vol. 50, No. 1, 2004, pp. 91–94. Translated from Akusticheskiĭ Zhurnal, Vol. 50, No. 1, 2004, pp. 106–110.
Original Russian Text Copyright © 2004 by Sabirov, Semenov, Utarova.

Sound Propagation and Relaxation Processes in the Isotropic Phase of Cholesteryl Miristate

L. M. Sabirov, D. I. Semenov, and T. M. Utarova
Navoi State University, Samarkand, Universitetskii bul'v. 15, Samarkand, 703004 Uzbekistan
e-mail: sabirov@uni.uzsci.net

Received January 5, 2003

Abstract—The propagation and absorption of high-frequency sound in the isotropic phase of cholesteryl miristate is studied in a wide frequency range using the data of both Brillouin spectroscopy and acoustooptic measurements. The parameters of the relaxation process associated with the volume viscosity relaxation are calculated using the experimental data on the velocity and absorption of sound. © *2004 MAIK "Nauka/Interperiodica".*

INTRODUCTION

Studies of acoustic characteristics of a medium usually include the measurements of the relaxation time. Although not everything is known about the dynamic behavior of cholesterics on the molecular level, it is possible to specify the main groups of relaxation processes for the isotropic phase of a cholesteric medium.

The first group consists of relaxation processes connected with the relaxation of fully developed fluctuations of the order parameter. In the isotropic phase, there is no long-range ordering in the direction of different molecular axes, and the tensor of the order parameter is equal to zero. However, on relatively small space–time scales, local ordering exists at a certain distance ξ, which is called the correlation length. In the Landau–de Gennes approximation [1], the temperature dependence of ξ has the form $\xi(T) \approx l[T^*/(T-T^*)]^{\frac{1}{2}}$, where l is the molecule length, T is the temperature in kelvins, and T^* is the critical temperature. This dependence agrees with experimental data for the light scattering intensity in the isotropic phase of nematics [2]. In the immediate vicinity of the phase transition, a deviation from the linear temperature dependence is observed for the reciprocal of the integral intensity of light scattering because of the fluctuation additions [3, 4]. A greater deviation from the linear dependence of this quantity occurs in the isotropic phase of cholesteryl miristate [5]. The relaxation times of the order parameter fluctuations in nematics lie within the range 10^{-8}–10^{-6} s, and they are an order of magnitude greater in cholesteryl miristate (10^{-7}–10^{-5} s) [5].

The second group of relaxation processes is connected with molecule rotation around the long axes and the translational self-diffusion. The relaxation times of such processes are connected to a large extent with the viscosity of the medium and depend little on the closeness to the phase transition point (in comparison with the relaxation processes of the first group). The estimated values of relaxation times for these processes lie within 10^{-12}–10^{-11} s.

One more group of relaxation processes in the isotropic phase of liquid crystals consists of the processes of intramolecular relaxation, which are connected with the motion of the end molecular groups. These processes also have a weak temperature dependence of the relaxation time, the values of which lie within 10^{-8}–10^{-11} s. For example, the intramolecular relaxation time for MBBA nematics is 10^{-8} s [6].

We conducted a study of the propagation velocity and absorption of sound in the isotropic phase of cholesteryl miristate in a wide range of frequencies (from 22 MHz to 7 GHz) and temperatures (from 100 to 82°C) to obtain information on high-frequency relaxation processes. We performed ultrasonic experiments at $f = 22$ MHz by using a pulsed technique. Sound was detected using the diffraction of light. In the frequency band from 1.1 to 7 GHz, the Brillouin spectroscopy was used. The investigations were conducted using a single sample of cholesteryl miristate.

EXPERIMENT

To determine the propagation velocity and the coefficient of ultrasonic absorption, we used an acoustooptic technique based on the phenomenon of light diffraction by ultrasound. The technique was modified for operation in a pulsed mode. Such a modification is necessary to conduct the measurements near phase transitions, where the susceptibility of liquid crystals is very high. A detailed description of the technique and the results of measuring the propagation velocity and the absorption coefficient at ultrasonic frequencies is given in our previous paper [7]. The ultrasonic propagation velocity was determined according to the diffraction

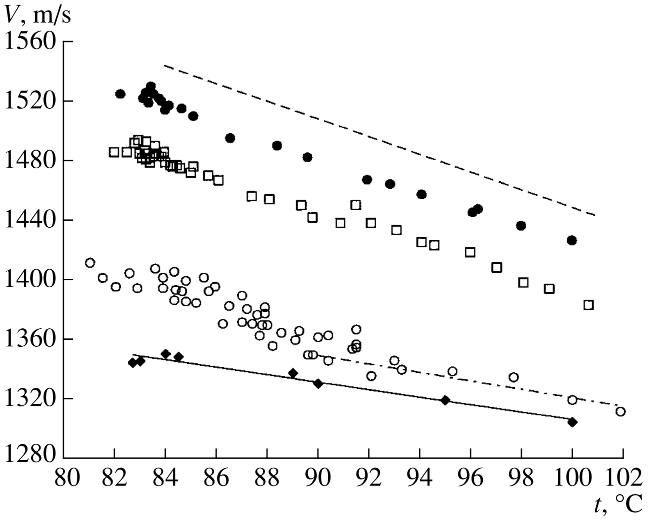

Fig. 1. Temperature dependence of the sound velocity for (◆) 22 MHz, (○) 1.1–1.04 GHz, (□) 4.9–4.5 GHz, and (●) 7–6.5 GHz. The solid line shows the result of averaging for a frequency of 22 MHz, the dashed line corresponds to V_∞ calculated according to [8], and the dash-and-dot line represents the linear part of the temperature dependence of sound velocity at a frequency of 1.1 GHz for $t > 90$°C.

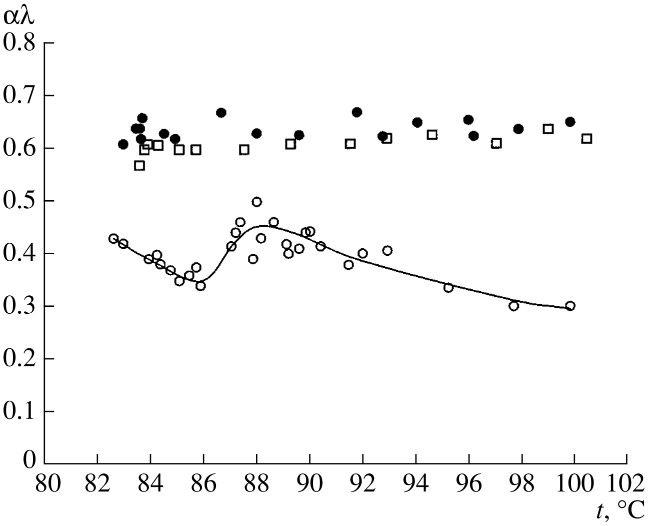

Fig. 2. Temperature dependence of the quantity $\alpha\lambda$ for (○) 1.1–1.04 GHz, (□) 4.9–4.5 GHz, and (●) 7–6.5 GHz. The solid line is plotted for illustration (as guide line).

angle, and the ultrasonic absorption, according to the intensity of the diffracted light pulse, depending on the distance to the piezoelectric transducer. The precision of measurements for the propagation velocity and the ultrasonic absorption was 0.5% and 10%, respectively. The cell with the sample of cholesteryl miristate was placed in an electronic thermostat, which stabilized the temperature within ±0.05°C.

The hypersonic velocity and absorption in the frequency band 1–7 GHz were determined according to the shifts and widths of the Brillouin spectral components [8]. The spectra were recorded under the light scattering angles of 19.6° ± 0.2°, 90° ± 0.2°, and 167° ± 0.2° by a setup with a double-pass Fabry-Perot interferometer (a detailed description of the setup is given in [9]). The contrast of the interference pattern was 5×10^4, and the sharpness was 35. The double-pass mode of operation provided an opportunity to investigate the spectra of the Brillouin scattering near the isotropic liquid–cholesteric liquid crystal phase transition. The precision of the determination of the sound velocity and absorption depended on the scattering angle and varied from 1 to 0.5% for the velocity and from 20 to 10–15% for the absorption coefficient. As the scattering angle increases, the errors decrease.

The sample of cholesteryl miristate was subjected to a dust removal procedure by forcing it in vacuum through a filter with a pore diameter of 0.2 μm and then sealing it in a cylindrical cell. The cell with the sample was placed into an electronic thermostat, which stabilized temperature within ±0.01°C. The sample studied had the following characteristics: the clearing point t_c on heating the cholesteric phase was 83.1 ± 0.02°C, and the mist phase on cooling appeared at 83.6 ± 0.02°C. The measurements were conducted from higher to lower temperatures, and with overcooling it was possible to reach a temperature of ~81°C.

RESULTS AND DISCUSSION

The results of measuring the temperature dependence of the hypersonic propagation velocity for three angles of light scattering in cholesteryl miristate are given in Fig. 1. The results of measuring the ultrasonic velocity at a frequency of 22 MHz are also presented here. Figure 2 demonstrates the temperature dependences of the absorption coefficient multiplied by the sound wavelength for three frequencies corresponding to three angles of light scattering.

From Fig. 1 one can see that the hypersonic velocities in the frequency bands 4.5–4.9 GHz and 6.5–7 GHz increase as the temperature decreases with close temperature coefficients $dV/dt \approx 3$ m s^{-1} deg^{-1}. In the frequency band (1.04–1.1) GHz, the hypersonic velocity changes with approximately the same temperature coefficient within the temperature interval from 100 to 90°C. At $t < 90$°C, the behavior of the sound velocity in this frequency band has a more complex character.

In the ultrasonic frequency region, the value of the velocity for $f = 22$ MHz coincides with the values of V_∞ obtained in [10]. The order of magnitude of the relaxation time indicated in [10] assumes that this process is connected with the motion of the end molecular groups.

The experimental results given in Fig. 1 show that a considerable dispersion of the velocity of high-frequency sound (about 10%) is observed in cholesteryl miristate in the temperature range from 100 to 82°C. This value of dispersion is retained, within the experi-

Parameters of the relaxation processes related to the volume viscosity relaxation in the isotropic phase of cholesteryl miristate

t, °C	A, cm^{-1} s^2	C, cm^{-1} s^2	V_∞, m/s	f_r, Hz	τ, s
100	5×10^{-17}	17×10^{-17}	1448	2.0×10^9	8×10^{-11}
95			1470	1.7×10^9	9×10^{-11}
90			1500	2.3×10^9	7×10^{-11}
Ultrasound [10]					
79	40.5×10^{-14}	1.9×10^{-14}	1360	5.3×10^6	3.0×10^{-8}
90.2	11.3×10^{-14}	1.4×10^{-14}	1324	7.3×10^6	2.2×10^{-8}

mental error, in the whole temperature interval for the frequencies 1.1, 4.9, and 7 GHz, except the temperature region $t < 90$°C for the frequency 1.1 GHz.

This order of magnitude of dispersion and also its relative independence of temperature are usually observed in low-viscosity liquids and attributed to a single relaxation process due to the volume viscosity relaxation [8]. The analysis of the experimentally observed dispersion of the velocity and absorption of high-frequency sound was carried out for $t > 90$°C, and this allowed us to assume that the contribution of the sound energy dissipation through the interaction of orientation and sound modes near the isotropic liquid–cholesteric liquid crystal transition can be ignored (the transition temperature for our sample was $t_c = 83.1$°C). To estimate the parameters of the relaxation process responsible for the 10% dispersion of sound velocity in the hypersonic frequency range, we used the expressions describing the dispersion of sound velocity and the sound absorption that are caused by a single relaxation process according to the Mandel'shtam–Leontovich relaxation theory [11]:

$$\frac{\alpha}{f^2} = \frac{A}{1 + (\omega\tau)^2} + C, \qquad (1)$$

$$\frac{V_\omega^2 - V_0^2}{V_\infty^2 - V_0^2} = \frac{\omega^2\tau^2}{1 + \omega^2\tau^2}, \qquad (2)$$

where α is the coefficient of sound absorption, f is the sound frequency, $\omega = 2\pi f$, τ is the relaxation time, V_∞ is the velocity value at $\omega \longrightarrow \infty$, V_0 is the velocity value at $\omega \longrightarrow 0$, V_ω is the velocity value at the frequency ω, and A and C are constants for this process.

The values of A, C, τ, V_∞, and V_0 for the ultrasonic frequency range are given in [10]. In the hypersonic interval, we determined these values from experimental data on the velocity and absorption of hypersound.

Calculation of the parameters of the relaxation process observed in the hypersonic frequency range was conducted at the following conditions: the values of V_0 were taken equal to the value of ultrasonic velocity at a frequency of 22 MHz (note that the values of V_∞ for the ultrasonic relaxation process [10] coincide with our values for V_0). Since we conducted the measurements in the hypersonic region at three frequencies, it is possible to construct a set of equations for the determination of the parameters V_∞ and τ. In view of the fact that the temperature behavior of the sound velocity at the frequency of 1.1 GHz has a complex character, for the calculation we used the velocity values corresponding to $t > 90$°C. In addition, from the experimental values of α/f^2 for three frequencies, it is possible to calculate τ and the coefficients A and C by Eq. (1). The average values of the absorption coefficient (which can be estimated from the values of $\alpha\lambda$), velocity V, and frequency f were used for the calculation.

As the result of calculations using the velocity dispersion and the hypersonic absorption, the values of the relaxation frequencies were obtained for cholesteryl miristate. These values are given in the table.

Thus two relaxation processes with essentially different relaxation times are observed in the isotropic phase of cholesteryl miristate. The calculated parameters provide an opportunity to take into account in the general case the contributions of these processes to both absorption and dispersion of sound velocity. The results of calculating V_∞ for the hypersonic range are plotted in Fig. 1 by the dashed line. Our calculations demonstrate that the total dispersion of hypersonic velocity has weak temperature dependence: at 100°C, it is equal to ≈11%, and at 86°C, its value grows up to ≈13%. A small increase in the dispersion of hypersonic velocity with decreasing temperature apparently reflects the fact of the interaction of the order parameter fluctuations with the sound wave.

The calculated values of V_∞ correspond to the hypersonic frequency not exceeding 7.5 GHz. Therefore, the range of the frequencies studied in our experiment almost completely covered the relaxation process of interest.

Thus, two relaxation processes are observed in the frequency interval from 1 MHz to 7 GHz in the isotropic phase of cholesteryl miristate away from the isotropic liquid–cholesteric liquid crystal transition. The low-frequency intramolecular relaxation process [10] with relaxation time $\tau \approx 3 \times 10^{-8}$ s is apparently related to the motion of molecular end groups. The high-frequency relaxation process with relaxation time $\tau \approx 7 \times 10^{-11}$ s and the parameters presented in this paper is evidently related to the molecular rotation around the long axes and the translational self-diffusion.

One can see from Fig. 2 that the temperature behavior of the value of $\alpha\lambda$ at a frequency of 1.1 GHz noticeably differs from the one observed at higher frequencies. As seen from Fig. 2, a small peak is observed near the temperature of ~87°C, while in the temperature region $t < 85°C$, the absorption multiplied by the sound wavelength increases. The temperature region of the peak coincides with the region of peculiarity of the sound velocity behavior at a frequency of 1.1 GHz, which consists in the deviation from a linear temperature dependence (see Fig. 1).

The temperature dependences of the absorption coefficient and the propagation velocity of sound at the frequency of 1.1 GHz suggests that, on the background of the relaxation process of volume viscosity with a large dispersion of sound velocity (about 12%), one more relaxation process with the parameters depending on the closeness to the isotropic liquid–cholesteric liquid crystal transition manifests itself. The nature of this process is apparently connected with the interaction of the sound mode with the fluctuations of the order parameter. Since, at the isotropic liquid–cholesteric liquid crystal transition, the fluctuations of the order parameter are in fact the fluctuations in the distribution of the axes of anisotropic molecules of cholesteryl miristate, it is necessary to involve the data on the temperature dynamics of the width of the Rayleigh line wing [8] and the theory of interacting modes [12, 13] in the study of the characteristics of this process.

REFERENCES

1. *The Physics of Liquid Crystals*, Ed. by P. de Gennes (Clarendon Press, Oxford, 1974; Mir, Moscow, 1977).
2. T. W. Stinson and J. D. Litster, Phys. Rev. Lett. **30**, 688 (1973).
3. L. V. Adzhemyan, L. Ts. Adzhemyan, A. Yu. Val’kov, *et al.*, Zh. Éksp. Teor. Fiz. **87**, 1244 (1984) [Sov. Phys. JETP **60**, 712 (1984)].
4. M. A. Anisimov, E. E. Gorodetskiĭ, and V. É. Podnek, Pis’ma Zh. Éksp. Teor. Fiz. **37**, 352 (1983) [JETP Lett. **37**, 414 (1983)].
5. V. Yu. Lerman, L. M. Sabirov, R. L. Sabirov, and T. M. Utarova, J. Mol. Struct. **348**, 201 (1995).
6. A. P. Kapustin and O. A. Kapustina, *Acoustics of Liquid Crystals* (Nauka, Moscow, 1986).
7. V. Yu. Lerman, Sh. A. Kadyrov, and L. M. Kashaeva, Uzb. Fiz. Zh., No. 3, 22 (1997).
8. I. L. Fabelinskiĭ, *Molecular Scattering of Light* (Nauka, Moscow, 1965; Plenum, New York, 1968).
9. V. Yu. Lerman, L. M. Sabirov, and T. M. Utarova, Fiz. Zhidk. Sostoyaniya, No. 14, 22 (1989).
10. A. P. Kapustin, *Electrooptical and Acoustic Properties of Liquid Crystals* (Nauka, Moscow, 1973).
11. L. I. Mandel’shtam and M. A. Leontovich, Zh. Éksp. Teor. Fiz. **7**, 437 (1937).
12. H. Imura and K. Okano, Chem. Phys. Lett. **19** (3), 387 (1973).
13. I. A. Kozhevnikov and I. A. Chaban, Akust. Zh. **21**, 421 (1975) [Sov. Phys. Acoust. **21**, 262 (1975)].

Translated by M. Lyamshev

Acoustical Physics, Vol. 50, No. 1, 2004, pp. 95–99. Translated from Akusticheskiĭ Zhurnal, Vol. 50, No. 1, 2004, pp. 111–115.
Original Russian Text Copyright © 2004 by Studenichnik, Glotov.

Sound Velocity in Shallow Water Bodies with Gas-Saturated Water–Bottom (Ice) Interfaces

N. V. Studenichnik[†] **and V. P. Glotov**

Andreev Acoustics Institute, Russian Academy of Sciences,
ul. Shvernika 4, Moscow, 117036 Russia

e-mail: bvp@akin.ru

Received August 27, 2002

Abstract—Sound velocity variations in shallow water bodies with gas-saturated water–bottom (ice) interfaces are investigated. The effect of air inclusions in water and water-like bottoms (ice) on the velocity of longitudinal sound waves is qualitatively and quantitatively estimated. It is shown that changes in the sound velocity are mainly governed by the radial resonance, which at low frequencies depends on the quality factor of the zeroth mode of bubble oscillation. For real concentrations of bubbles, the velocity of longitudinal waves may become very low. This may lead to considerable distortions of boundary conditions at rough surfaces and, hence, to enhancement of scattering and absorption of sound waves and additional leakage of acoustic energy into the bottom (ice), as well as considerable changes in the sound velocity profile in surface layers with a change of sign of the velocity gradient from negative to positive, which results in the formation of a subsurface channel or an increase in its power. It is found that water-like bottoms (sediments) and ice ("liquid" ice), which are characterized by shear wave velocities of an order of 15 m/s or less, behave in the kilohertz range almost as a vacuum ($C_l \longrightarrow 0$) when the air content in them reaches several percent. As a result, the propagation of first normal modes in shallow water or in subsurface layers of arctic and oceanic waveguides noticeably changes. © *2004 MAIK "Nauka/Interperiodica".*

This study opens up possibilities for establishing previously unknown physical criteria for the excitation of surface and shear waves that lead to abnormally large absorption and scattering of sound by rough interfaces; for explaining such paradoxical empirical facts as the negative steps in sound velocity at interfaces in deep-water and shallow-water regions; and for estimating the considerable increase in the critical frequencies of modes in a waveguide, which affects the channel propagation of low frequencies and leads to other poorly understood effects.

1. In the problem of sound propagation in shallow water (rivers, lakes, and shallow seas), the estimate of real properties of the bottom and the ice cover occupies a central position. In particular, of special interest are such objects as porous bottom and ice saturated with air, which are characterized by low propagation velocities of longitudinal and shear waves, as well as the upper ocean layer saturated with air bubbles. The low velocity ($n > 1$, where n is the refractive index) shifts the angle of total internal reflection to the region of steep grazing angles of modes (water rays). This leads to the deformation of the processes of sound attenuation and scattering by rough interfaces (changes in the boundary conditions), which previously were not taken into account.

Below, we consider the sound velocity variations for water-like bottoms and ice with a small shear modulus ($\mu/\lambda \ll 1$, where μ and λ are the Lame constants) that occur in the Arctic basin and other water bodies.

2. For studying sound velocity variations in a liquid dispersive medium, we use the Rytov formula [1]

$$n^2 - 1 = 4\pi N/ik^3 \sum L_m(\omega)(iK/k)^m, \qquad (1)$$

where K is the sound wave number in the dispersive medium, k is the wave number in pure water, N is the number of particles (bubbles) in 1 cm^3, $L(\omega)$ is the diffraction scattering amplitude, m is the number of the mode of oscillation, and ω is the circular frequency.

Formula (1) was obtained for a liquid dispersive medium, but it is also valid for elastic dispersive media, since it takes into account multiple scattering of a longitudinal wave by small spherical particles. As a result of interference of incident and scattered waves, the sound velocity changes.

Using formula (1), we estimated the magnitude of a negative step in the velocity of longitudinal waves in deep-water regions of the ocean, for which Hamilton generalized extensive experimental data [2]. It was

---

[†] Deceased.

shown that the negative step in velocity reaches a magnitude of an order of 5–10% (in agreement with the field data) and is observed for the bottom density $\rho \leq 2$ g/cm^3 [2]. For bottoms (ice) with air bubbles, literature data are absent, but it is known that, in low-frequency sound propagation in shallow water, the velocity of longitudinal waves in the bottom drastically decreases down to the sound velocity in the atmosphere (a strong negative step). No convincing interpretation of this phenomenon appeared until now, although it was qualitatively clear that it may be related to the effect of air bubbles saturating the shallow-water bottom (the sea depth was about 4 m). Really, formula (1) allows the estimation of the magnitude of the negative step at low frequencies (100 Hz), at which the bubble is not in resonance because of its small size: in nature, only small bubbles are observed with resonance frequencies higher than 0.5–1 kHz (with radii $a = 0.15$–0.3 cm). However, fundamental difficulties arise in determining the number of terms in formula (1) for the oscillation modes. For a small hard spherical particle, it will suffice to take into account only two terms: the zeroth and dipole modes of oscillations, if we restrict our consideration to weak emulsions and porous bottoms [1, 2]. In the case of a dispersive medium containing bubbles with other boundary conditions at the radially compressible surface, it is necessary to solve the diffraction problem anew by following the method of [1].

Solving the problem of a plane wave diffraction by a compressible spherical particle that is small compared to the sound wavelength, we arrive at the following result:

$$L_0 = -ka(\kappa/\kappa_1 - 1)/(ka + i(1 - 3\kappa/\kappa_1)/k^2a^2), \quad (2)$$

$$L_1 = 1/3(ka)^3(\gamma - 1)B(\gamma, \omega), \quad (3)$$

where $B(\gamma, \omega)$ is the Kenig function for the velocity of particle oscillations [2]; $\gamma = \rho/\rho_0$ (ρ_0 is the water density); κ_1 and κ are the compressibilities of the medium inside and outside the particle, respectively; and a is the radius of the particle. Formulas (2) and (3) are valid for small spherical particles of any compressibility. For $\kappa_1/\kappa \longrightarrow \infty$ (absolutely hard particle), Eqs. (2) and (3) exactly lead to theoretical results obtained in [2, 3] and are confirmed by experimental data (emulsion of mercury in water, porous bottoms). For gas-saturated bottoms at low frequencies ($f \ll f_0 = 330/a$ Hz), from Eqs. (2) and (3) we obtain

$$L_0 = i(ka)^3Q^2, \quad (4)$$

$$L_1 = -(ka)^3, \quad (5)$$

where f_0 is the resonance frequency, f is the operating frequency, and Q is the quality factor of radial oscillations.

For a radially compressible sphere, the dipole diffraction parameter L_1 coincides with a similar parameter for an absolutely incompressible sphere (with a precision of a factor of 3), because the oscillations occur without deformation of the shape and, therefore, depend only on the ratio of densities of particle and water. In particular, for an air bubble, the velocity of oscillations is three times greater than that for a hard particle of the same size. Therefore, sound velocity oscillations related to dipole oscillations are almost three times greater than for a heavy particle (this is reflected in Eq. (5)). From Eqs. (4), (5), and (1) it follows that the contribution of the dipole term is Q^2 times smaller than that of the radial term (the zeroth mode). Since the quality factor for real bubbles is very large (in the frequency range of 1–5 kHz and lower, $Q = 80$), the inclusion of the dipole term, as well as higher modes of oscillation, in Eq. (1) is not obligatory, because the main contribution to the variations of the sound velocity is made by the zeroth mode of oscillation (radial oscillations). In addition, from Eq. (1) it follows that the effect of the scatterer interactions (by radiation) manifests itself only in the small dipole term (in contrast to the zeroth mode, dipole scattering takes place into a dispersive medium—see velocity C in Eq. (1)). Thus, we may conclude that a strong negative step can be obtained at a rather high concentration of bubbles, which almost do not interact with one another due to symmetry (the zeroth mode) but generate a strong scattered field at the surface of any bubble in the dispersive medium through reradiation of acoustic energy by the exciting plane wave. According to Eq. (1), we have

$$C = C_0/(1 + 3\beta Q^2)^{1/2} \sim C_0/Q(3\beta)^{1/2}, \quad (6)$$

because $3\beta Q^2 \gg 1$, where C_0 is the sound velocity in pure water and β is the volume concentration of bubbles. From Eq. (6) it follows that, at a moderate volume concentration of bubbles, we can obtain (because of the large quality factor) a low sound velocity commensurable with its atmospheric value. For example, setting $\beta = 7 \times 10^{-3}$ (0.7%) and $Q = 80$ (resonance frequencies of 1–5 kHz and lower), we obtain $C = 150$ m/s (for the atmosphere, $C = 340$ m/s). For smaller bubbles ($f_0 > 10$ kHz), the quality factor is less than 80 (it is determined mainly by the incomplete heat exchange with surrounding water), however, their volume concentration in natural media is rather low and almost does not influence the estimate obtained above. Formula (6) is valid not only for a fixed size but also for any mixture of bubbles in a dispersive medium (the main contribution is given by the bubbles with constant quality factor in the range of resonance frequencies within 1–5 kHz and lower). In this case, it is necessary to take into account the total concentration determined in experiments (see Fig. 2).

3. The limiting concentration of bubbles β is determined, as usual, from the condition of probable approach of the bubbles to one another to a distance of the order of the effective diameter formed by the bubble radius and the influence of the added mass of the surrounding medium. As a result, we have $\beta_1 = N^*V_1$, where $V_1 = 8V_{\text{eff}}$. The effective volume of the bubble with allowance for the added mass of water equals $V_{\text{eff}} = 3V$, where V is the volume of the bubble. Then, we obtain $\beta_1 = 24\beta$. The limiting concentration is determined from the close packing condition $\beta_1 = 1$. Finally, we have

$$\beta_{\text{lim}} = 1/24 = 0.05\ (5\%). \tag{7}$$

For concentration $\beta > \beta_{\text{lim}} = 5\%$, the initial dispersion formula (1) is not valid, since it does not take into account the interaction of particles by the added mass. In nature, the maximum concentration of bubbles $\beta = 0.1$ [4] is recorded in oceanic water at a depth of 0.1 m (a wind speed of 15 m/s); in arctic ice, β is of the order of 3% [5] (Fig. 2). Therefore, the above-mentioned results are quite realistic. If in Eq. (6) we set the limiting possible concentration ~ 5% and $Q = 80$, we obtain $C = 50$ m/s (this result does not change for gas-saturated bottom (ice) with velocity of shear waves $C_t < 13.5$ m/s).

4. Now, let us take into account the elastic properties of bottom and ice. Following Sivukhin [7] and Isakovich [8], we conclude that an air bubble (vacuole) introduced in an elastic medium has resonances at the zeroth and dipole modes. However, these resonances are significant for longitudinal waves (a shear wave is not considered because of its smallness) only for rather small ratios $\mu/\lambda < 10^{-3}$, i.e., for water-like bottoms and ice. The resonance of the zeroth mode (radial oscillations) is determined by the elastic properties of the surrounding medium (mainly by modulus μ) and by the elasticity of air inside the bubble, which depends on the atmospheric pressure. The resonance dipole mode is determined only by the modulus μ for different boundary conditions at the surface of the bubble (vacuole): for vacuoles frozen into ice (bottom) and for sliding vacuoles [8]. In both cases, the resonances at the natural frequency are different for the dipole and zeroth modes (the ratio of frequencies is $\sim(\mu/\lambda)^{1/4}$). For the zeroth mode, the resonance is determined from the relation

$$(k_l a) = 2(\mu/\lambda)^{1/2}, \tag{8}$$

where k_l is the wave number of a longitudinal wave in a homogeneous bottom (ice). From Eq. (8) it follows that the resonance frequency of radial oscillations is much higher than in pure water. Setting, for example, $\mu/\lambda = 4 \times 10^{-2}$ ($C_l = 3000$ m/s, $C_t = 600$ m/s), we obtain $f_{0\text{rad}} = 200$ kHz for $a = 0.1$ cm ($f_0 = 3$ kHz in water). For $\mu/\lambda = 4 \times 10^{-4}$ ($C_l = 3000$ m/s, $C_t = 60$ m/s), $f_{0\text{rad}} = 24$ kHz, i.e., 8 times higher than in water.

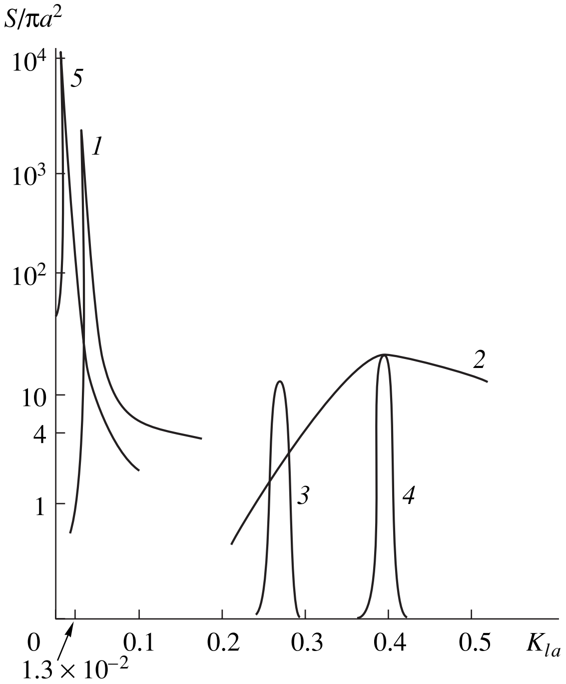

Fig. 1. Scattering cross section, $\sigma s/\pi a^2$, of spherical vacuoles (bubbles) introduced into the bottom (ice) as a function of the parameter K_{la}. $\mu/\lambda = 0.0004$ ((*1*) zeroth and (*3*) dipole modes), 0.04 ((*2*) zeroth and (*4*) dipole modes), and 0 ((*5*) a bubble in water).

The resonance of a dipole mode in an elastic medium is determined by the relation [8]

$$k_l a = [3(\mu/\lambda)^{1/2}(1 + 4(\mu/\lambda)^{1/2})]^{1/2}, \tag{9}$$

where k_l is, as before, the wave number of a longitudinal wave. Here, we do not take into account the small difference between "frozen-in" and "sliding" variants of boundary conditions. Let us estimate the characteristic frequency of the dipole mode. Setting, as before, $a = 0.1$ cm, we obtain $f_{0\text{dip}} = 550$ kHz for $\mu/\lambda = 4 \times 10^{-2}$ and $f_{0\text{dip}} = 120$ kHz for $\mu/\lambda = 4 \times 10^{-4}$. It is seen that the dipole resonance is much higher than the zeroth (radial) one. Its role in the sound velocity variation can be more significant for high elasticity of the medium ($\mu/\lambda \sim 1$). However, this case is beyond our consideration, because the main mechanism (radial resonance) at $\mu/\lambda \sim 1$ is strongly damped and does not affect the velocity of sound waves.

Figure 1 displays the resonance properties, i.e., scattering cross sections (both calculated ($\mu = 0$, a pressure of $P_0 = 1$ atm) and taken from [7]), of individual vacuoles introduced in the bottom (ice) as a function of frequency, size, and ratio μ/λ. These data allow one to estimate the magnitudes of $|L_0|$ and $|L_1|$ and, therefore, the relative contribution to the sound velocity variations (in order of magnitude). From Fig. 1 one can see that the

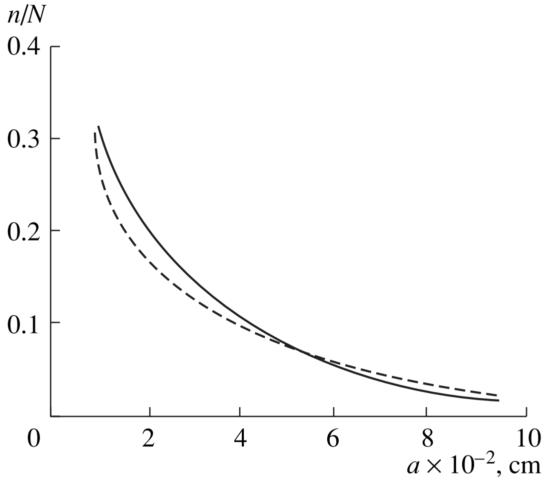

Fig. 2. Distribution of the concentration n/N of air bubbles frozen into ice in a real arctic ice cover. The dashed line represents the function of bubble size distribution $f(R) \sim R^{-1}$.

contribution of the dipole resonance is commensurable with that of the main (radial) resonance already for $\mu/\lambda = 4 \times 10^{-2}$, i.e., for the velocity of the shear waves $C_t > 300$ m/s. As temperature decreases (elastic ice) and hydrostatic pressure increases (deep-water elastic bottom), the velocity of shear wave grows ($\mu/\lambda \sim 1$). The resonances considered above are attenuated (damped), and the sound dispersion becomes insignificant. The role of air inclusions is mainly reduced to a decrease in the density of the medium.

5. Let us estimate the velocity of low-frequency sound in the ice of the Arctic basin. Figure 2 shows the empirical data for the concentration of air bubbles frozen into the ice [5]. The ice density changes within $0.917 \pm 2.5 \times 10^{-2}$ g/cm^3. The statistical size distribution was determined from photographs (transmission geometry) of arctic ice specimens. The volume concentration of air inclusions (bubbles) was about 3%, which far exceeds (by an order of the magnitude) the air bubble concentrations in oceanic foam at a wind speed of 15 m/s [4]. This concentration value (3%) is quite reliable, because measurements on ice specimens (bubbles are frozen in) are more reliable and accurate than measurements in a breaking wave. We will estimate the true value of sound velocity for the longitudinal velocity $C_l = 3000$ m/s and the shear velocity $C_t = 300$ m/s ($\mu/\lambda = 4 \times 10^{-2}$). Such values occur mainly for summer arctic ice and in a "loose" layer at the water–ice boundary. In this case, the ratio of resonance frequencies of the zeroth and dipole oscillations equals 1 : 3; i. e., the ratio of squared decrements is $Q^2_{\text{rad}}/Q^2_{\text{dip}} = 1/9 \cong 0.1$. Therefore, the change in the sound velocity (at frequencies $f \ll f_{0\text{rad}} \ll f_{0\text{dip}}$) will depend almost exclusively on the radial mode. According to Eqs. (1) and (3), we have

$$n^2 - 1 = 3\beta Q^2_{\text{rad}}, \tag{10}$$

where $Q_{\text{rad}} = 0.5(\mu/\lambda)^{-2}$ is the quality factor of the zeroth mode (the influence of air inside the vacuole is neglected).

Substituting the data for arctic ice (Fig. 2): $\beta = 3\%$ (0.03) and $\mu/\lambda = 2 \times 10^{-2}$, we obtain $C_l = 2150$ m/s instead of C_l =3000 m/s for pure ice. For more water-like ice (bottom), at $\mu/\lambda = 4 \times 10^{-4}$ (C_l =3000 m/s and $C_t = 60$ m/s), we obtain $C_l = 400$ m/s. One can see that, in contrast to sound velocity variations in pure water, which are related to the inclusion of air bubbles, the sound velocity in water-like ice (bottom) changes much less. This is explained by the "damping" effect of the elastic medium. Note that, at $\mu/\lambda = 4 \times 10^{-5}$, i.e., for $C_t = 13.5$ m/s ($C_l = 3000$ m/s), the role of the bottom (ice) elasticity is insignificant compared to the role of the elasticity of air inside the bubble (vacuole), and the sound velocity is close to that in the atmosphere [6]. The results obtained agree well with conclusions made by other authors (see, for example, [9]).

CONCLUSIONS

The influence of air inclusions in water and water-like bottoms (ice) on the sound velocity of longitudinal waves is estimated both qualitatively and quantitatively. It is shown that the main role in sound velocity variations is played by the radial resonance, which, at low frequencies, depends on the quality factor of radial oscillations. For real concentrations of bubbles (vacuoles), the velocity of longitudinal waves can reach very low values. This may considerably affect the boundary conditions at rough surfaces and, therefore, cause an enhancement of scattering and absorption of sound waves (additional leakage of acoustic energy into the bottom and ice), as well as other effects, such as a change of sign of the sound velocity gradient in boundary layers, a change in the sound velocity profile, etc. It is shown that water-like bottoms (sediments) and ice ("liquid" ice), in which the velocity of shear waves is about 15 m/s or less, behave almost as a vacuum ($C_l \longrightarrow 0$) for longitudinal waves of kilohertz frequencies when the concentration of air in these media increases to several percent. As a result, the propagation of the first modes in the subsurface layer of the arctic waveguide becomes more difficult or even completely absent because of the increase in the critical frequency. Indeed, from the pole equation [6], we obtain for shallow water $f_{\text{cr1}}/f_{\text{cr2}} = 2$, where f_{cr1} is the critical frequency of a waveguide with a gas-saturated bottom and f_{cr2} is the critical frequency of a waveguide with a conventional bottom. Setting the sea depth $h = 5$ m and the sound velocity in water equal to 1500 m/s, we obtain $f_{\text{cr1}} = 150$ Hz and $f_{\text{cr2}} = 75$ Hz; i.e., a channel propagation in shallow water with a gas-saturated bottom is possible only at frequencies $f > 150$ Hz. In this example, even the zeroth mode can exist, but we do not consider it because of its fast attenuation due to the strong scattering in the dispersive bottom.

ACKNOWLEDGMENTS

This work was supported by the Russian Foundation for Basic Research, project no. 01-02-16636.

REFERENCES

1. S. M. Rytov, V. V. Vladimirskiĭ, and M. D. Galanin, Zh. Éksp. Teor. Fiz. **8** (5), 614 (1938).
2. V. P. Glotov, Akust. Zh. **36**, 1113 (1990) [Sov. Phys. Acoust. **36**, 621 (1990)].
3. E. L. Hamilton, in *Physics of Sound in Marine Sediments*, Ed. by L. Hampton (Plenum, New York, 1974; Mir, Moscow, 1977).
4. V. S. Bezzabotnov, B. O. Bortkovskiĭ, and D. F. Timakovskiĭ, Izv. Akad. Nauk SSSR, Fiz. Atmos. Okeana **22** (1), 1186 (1986).
5. V. P. Gavrilo and B. O. Gaĭtskhoki, Tr. Arkt. Antarkt. Nauchno-Issled. Inst. **295**, 149 (1970).
6. L. M. Brekhovskikh, *Waves in Layered Media*, 2nd ed. (Nauka, Moscow, 1973; Academic, New York, 1980).
7. D. V. Sivukhin, Akust. Zh. **1**, 78 (1955) [Sov. Phys. Acoust. **1**, 82 (1955)].
8. M. A. Isakovich, *General Acoustics* (Nauka, Moscow, 1973), pp. 477–495.
9. T. N. Gardner and G. C. Sills, J. Acoust. Soc. Am. **110**, 1878 (2001).

Translated by Yu. Lysanov